Title
Backgrounds in LUX and LZ: Extending the Sensitivity of LUX to Low-mass Dark Matter

Author
Oliver-Mallory, Kelsey Colleen

Publication Date
2021

Peer reviewed|Thesis/dissertation

Backgrounds in LUX and LZ: Extending the Sensitivity of LUX to Low-mass Dark Matter

by

Kelsey Colleen Oliver-Mallory

A dissertation submitted in partial satisfaction of the

requirements for the degree of

Doctor of Philosophy

in

Physics

in the

Graduate Division

of the

University of California, Berkeley

Committee in charge:

Doctor Kevin T. Lesko, Co-chair
Professor Robert G. Jacobsen, Co-chair
Professor Matt C. Pyle
Professor Kai M. Vetter

Fall 2021

Backgrounds in LUX and LZ: Extending the Sensitivity of LUX to Low-mass Dark Matter

Abstract

Backgrounds in LUX and LZ: Extending the Sensitivity of LUX to Low-mass Dark Matter

by

Kelsey Colleen Oliver-Mallory

Doctor of Philosophy in Physics

University of California, Berkeley

Doctor Kevin T. Lesko, Co-chair

Professor Robert G. Jacobsen, Co-chair

Cosmological and astrophysical phenomena indicate the existence of a class of particles that are dark in the sense that they interact only very weakly with the Standard Model (SM). A strong set of candidates are Weakly Interacting Massive Particles (WIMPs) with masses of $m_\chi \in 10$–$10,000$ GeV. The Large Underground Xenon (LUX) experiment utilized a dual-phase xenon time projection chamber (TPC) to search for this type of dark matter (DM), setting competitive limits on the spin-independent DM-nucleon scattering cross section for $m_\chi \gtrsim 5$ GeV. It's successor, LUX-ZEPLIN (LZ), is currently being commissioned and will improve upon these results. This dissertation presents work extending the sensitivity of both detectors to rare events above and below the energy range of WIMP scattering. It does so, first, through precise management of backgrounds that can hide or mimic higher-energy signals of interest. A particularly challenging set of backgrounds comes from radon and its daughters. The LUX data were used to characterize the distribution of these isotopes throughout the xenon and place limits on the rate at which radon-related surface contamination washes off of TPC walls. To make this work possible, strategies were developed to accurately calibrate the detector and select high-energy decays by mitigating spurious low-energy signals that accompany the primary events. Another significant source of backgrounds is intrinsic contamination of detector components by primordial nuclides and cosmogenically activated isotopes. To best-design the LZ detector, a new facility named the Black Hills Underground Campus (BHUC) was built to house high-purity germanium (HPGe) detectors. These were used to assays potential construction materials and the lowest-activity materials were selected for use in the LZ detector. In addition, LUX components were assayed to refine the background model of this experiment. This dissertation also presents work lowering the LUX energy threshold to gain sensitivity to low-mass DM. This was done by incorporating events containing only ionization signals which remain robust at very-low energies where there are usually no detectable scintillation signals. In this regime, that data are plagued

by backgrounds from radiogenic surface contamination of the grid wires and additional grid electron emissions. A novel machine learning technique was used to mitigate these events based on ionization pulse shape. It was applied to an effective 5 tonne·day exposure from the 2013 LUX science operation to place strong limits on the scattering of low-mass DM particles with $m_\chi \in 0.15$–10 GeV.

Contents

List of Figures

List of Tables

Chapter 1

Dark Matter

The night sky is a vast sheet of black broken by scattered pin pricks of light. These distant infernos—stars, galaxies, and the like—are the only visual evidence of the existence of matter beyond our solar neighborhood. However, there is no real reason to expect the absence of matter in the dark. Why would all remote objects be ablaze? After all, we exist and are not burning at the stake; at least there should be many more planets like ours hidden from sight if only because they are so distant.

The search for this dark matter arguable began with the invention of the telescope in the early 17th century. The device revealed objects that had previously been too dim, absorbing, or distant to be observed through ordinary means. For example, Galileo discovered several of Jupiter's moons shortly after improving his own home-made telescope.

At this time, dark matter would have included planets, dim stars, gas, and dust. Things that are normal in the sense that they are composed of atoms.

Now, these types of objects are mostly well understood. At least, we have constrained their quantity and distribution throughout space to an impressive degree.

The remaining dark matter is something very different. For one, the substance does not interact with the electromagnetic force. It is invisible, not dark. Furthermore, it does not appear to interact much with itself—at least in the same way as baryons. If it did, it would form compact objects that would bend or block the light of background stars more sharply than evidence suggests is happening. It does appear to interact with gravity. It draws luminous objects towards itself, collecting stars to form galaxies then drawing galaxies into massive webs that span the Universe.

In fact, for the cosmos to have evolved into its current state, there must by 5 times as much dark matter as there is normal matter [1]. We therefore know very little about the majority of matter in the Universe. Some of the clues we do have about the identity of this mysterious substance are summarized throughout the rest of this chapter.

1.1 Evidence

Galactic and Intergalactic Dynamics

Perhaps the earliest hints of a dark matter arose at the beginning of the 20th century within the context of dynamical measurements of luminous objects.

In 1932, Jan Oort observed discrepancies in the vertical motion of nearby stars. His model of their velocity dispersion, which treated them as an atmosphere under the influence of gravity, suggested there ought to exist four times more matter than what was visibly present [2]. He attributed his observations to ordinary astrophysical phenomena, such as stars too-dim to be seen.

In 1933, Fritz Zwicky applied the virial theorem to the Coma Cluster and inferred an amount of mass that greatly exceeded predictions made using luminosity [3]. To explain the observation, Zwicky postulated a yet-unobserved type of mass.

Much more striking evidence was found on a smaller scale by Vera Rubin and W Ford in the early 1970s. They observed the rotation speed of stars in spiral galaxies rose near the center of the galaxy then remained constant out to very large radii (r), as is shown in Fig. 1.1. If the majority of mass were contained in the bulge at the center, as they had predicted from luminosity measurements, then Newtonian dynamics would indicate speeds falling as $\sim 1/\sqrt{r}$ [4]. The discrepancy can be ameliorated through addition of a spherical dark matter halo extending to much larger radii than the visible stars.

There is a very different type of measurement in support of the plethora of the dynamical evidence: gravitational lensing. The mass contained in distant galaxies and clusters can be estimated by exploiting the capacity for these objects to distort light from even-more-distant background sources.

For example, gravitational lensing measurements of galactic mass agree with those calculated from rotation curves [6, 7].

Possibly the most famous instance concerns the Bullet cluster, a conglomeration of two colliding galaxy clusters. X-ray imaging was used to locate the baryonic distribution of mass of the system, found to be positioned near the central point of the collision. Conversely, gravitational lensing identified the total distribution of mass was weighted towards the outer edges, as shown in Fig. 1.2. The electromagnetic interactions of the baryons had apparently slowed this component of the mass preventing it from travelling far from the point of collision. Dark matter without electromagnetic interactions would not have suffered this fate leading to the observed behavior [8].

Cosmology

In 1929, Edwin Hubble presented a paper demonstrating extra-galactic nebulae are receding at a speed proportional to their distance from us [9]. It was the first evidence we exist in an expanding Universe of finite age. Extrapolating the relationship backwards in time revealed

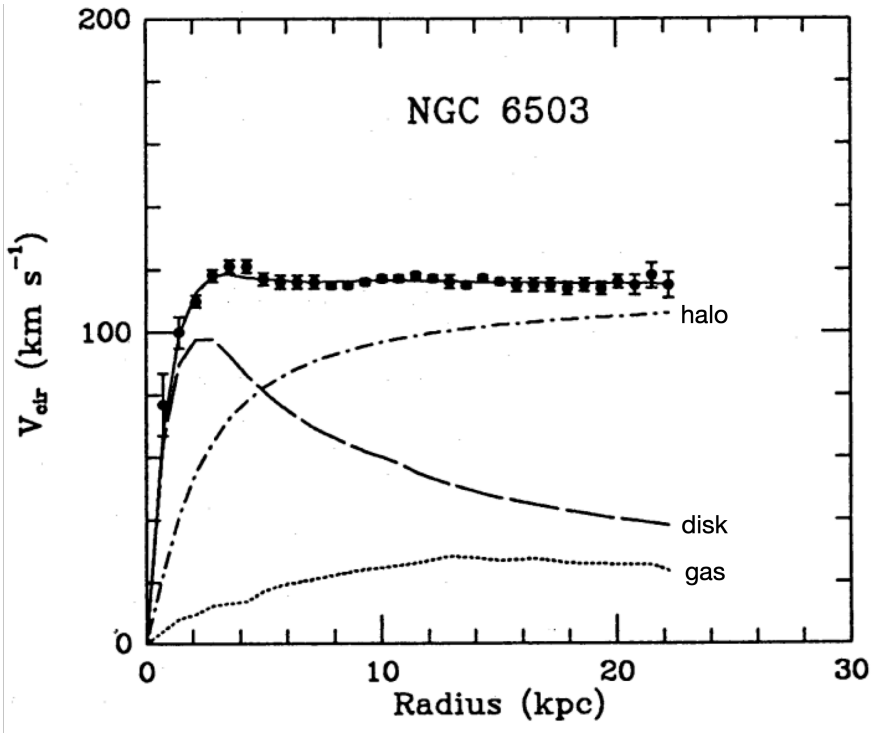

Figure 1.1: Rotation curve of spiral galaxy NGC 6503 indicating contributions to the velocity from halo, disk, and gas components. Figure from [5].

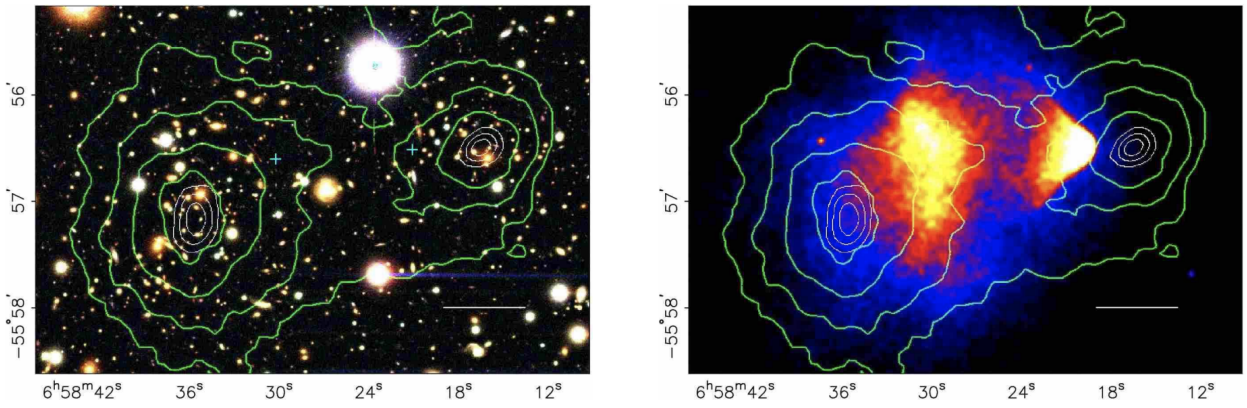

Figure 1.2: Hubble image of the Bullet cluster with the white bar indicating 200 kpc at the distance of the cluster (left). Chandra X-ray Observatory image illustrating the intracluster plasma (right). The green contours outline the distribution of mass inferred from gravitational lensing. Figure from [8].

an increasingly concentrated cosmos beginning as a singularity in which the laws of space and time no longer had any meaning: the Big Bang.

This standard model of cosmology is described by the Friedmann-Lemaitre-Robertson-Walker (FLRW) metric

$$ds^2 = dt^2 - a^2(t)\left(\frac{dr^2}{1-kr^2} + r^2(d\theta^2 + sin^2\theta d\phi^2)\right) \tag{1.1}$$

where (r, θ, ϕ) are comoving spherical coordinates. $a(t)$ is a scale factor that represents the time-dependent expansion of the universe and relates distances between objects ($d(t) = a(t)d_0$) to a reference time ($a(t_0) = 1$), typically the present day. k is a constant representing the curvature of spacetime: $k = 1$ is elliptical, $k = 0$ is Euclidean, and $k = -1$ is hyperbolic.

Combining the FLRW metric with Einstein's field equation results in an expression for the rate of expansion of the Universe,

$$H(t)^2 = \frac{8\pi G_N}{3}\rho - \frac{k}{a^2} \tag{1.2}$$

where $H(t) = \frac{da/dt}{a}$ is the Hubble parameter; G_N is the Newtonian gravitational constant; and $\rho = \rho_M + \rho_R + \rho_R$ is an average energy density divided into components from matter (ρ_M), radiation (ρ_R), and a cosmological constant (ρ_λ). The density of each component evolves differently with a. According to the equation of state for a fluid filling the Universe: $\rho_M \propto a^{-3}$, $\rho_R \propto a^{-4}$, and $\rho_\lambda \propto$ *constant*—assuming a cosmological constant.

Redshift measurements of very-distant Type-Ia supernovae reveal the Universe is expanding at an accelerating rate and is almost entirely flat ($k = 0$). Plugging the latter result into Equation 1.2, defines a critical energy density to compare with experimental measurements of the components of ρ.

$$\rho_{cr} = \frac{3H_0^2}{8\pi G_N} \equiv \frac{\rho}{\Omega} \tag{1.3}$$

In the above, H_0 is the Hubble parameter defined at the present day and $\Omega = \sum_i \Omega_i$ is the energy density in units of a fraction of the critical density, equal to 1 for a flat universe.

The above framework, along with observations indicating the matter content of the Universe is dominated by a cold (nonrelativistic) dark component, define the widely-excepted ΛCDM model of cosmology. The evidence supporting this model and the existence of cold dark matter is best understood in the context of the three stages of expansion of the Universe.

- Within the first picosecond of time, referred to as the *very-early Universe*, the four fundamental forces emerged—first gravitation then electromagnetic, weak, and strong interactions. During this period, there were quantum fluctuations of an inflationary field that mapped out future structure formation.

- From 1 picosecond to 370,000 years, the *early Universe*, various subatomic particles were formed within a hot dense plasma. As the universe expanded and cooled, quarks

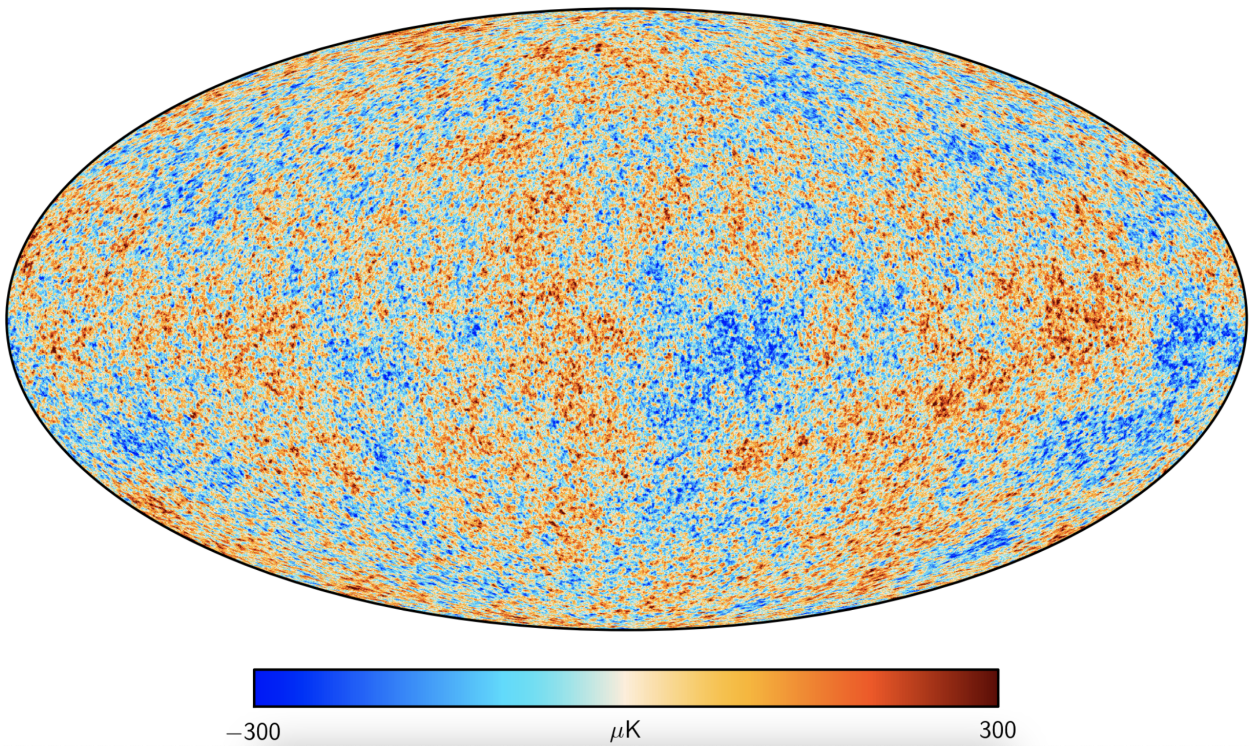

Figure 1.3: CMB temperature fluctuations in data from the Planck satellite. Figure from [12].

bound together as hadrons, the lightest stable hadrons (protons and neutrons) began nucleosynthesis, and electrons recombined with nuclei to form neutral atoms.

- From 370,000 to 1 billion years, *the dark ages*, clouds of hydrogen collapsed very slowly to form stars and galaxies. Galaxy clusters and superclusters emerged over additional time.

During the recombination epoch, the Universe very suddenly became transparent to photons, which did not interact as readily with neutral atoms compared to their unbound constituents. The photons still exist today, though their energy has greatly reduced, corresponding to an average blackbody temperature of 2.7 K [10]. This cosmic microwave background (CMB) radiation is mostly isotropic and homogeneous, to a factor of $\sim 10^{-5}$ [11], but has minor anisotropies that contain a huge amount of information concerning the geometry and energy content of the Universe. A map of the anisotropies, from data of the Planck satellite, is shown in Fig. 1.3.

The CMB is studied by satellite missions such as COBE, WMAP, or Planck—since photons of these energies are absorbed by the atmosphere precluding the use of ground based telescopes. On small scales, where the curvature of the Universe can be neglected, the

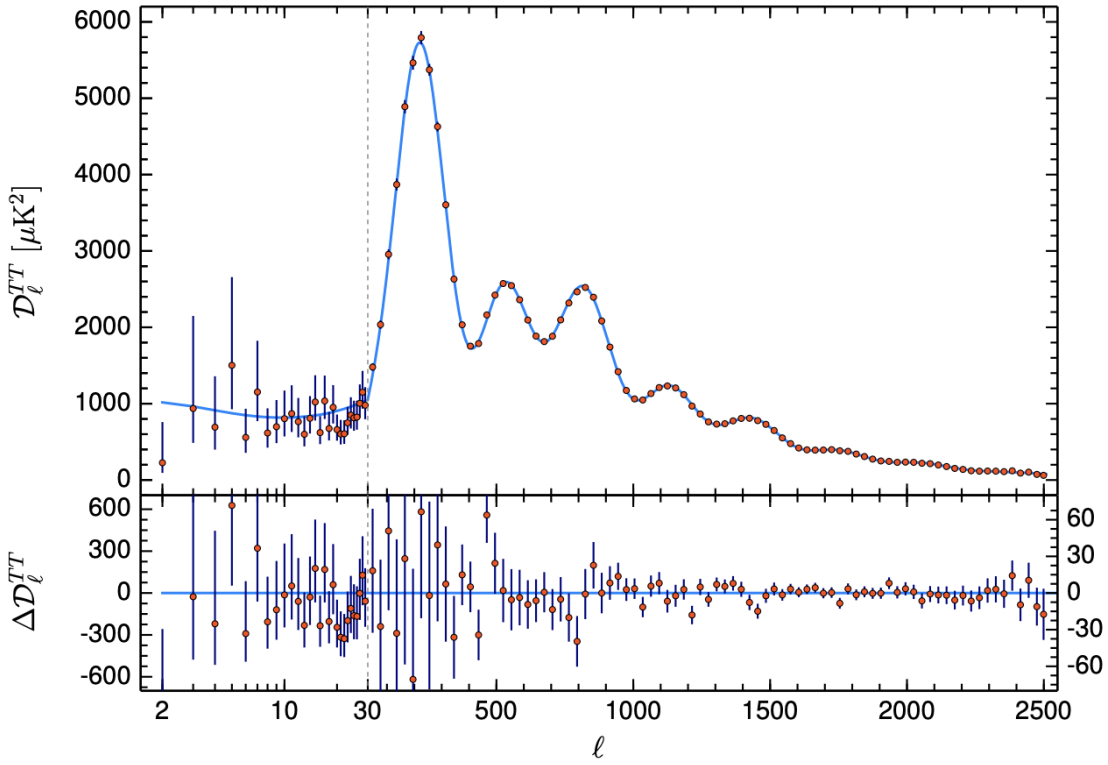

Figure 1.4: CMB power spectrum measured by Planck (red points) and best fit ΛCDM model (blue). The grey dashed line marks a change in logarithmic to linear scale, on the horizontal axis. Figure from [13].

data is expanded in spherical harmonics, $Y_{\ell m}(\theta, \phi)$, and a Fourier analysis is used to extract the wave numbers, ℓ, which are inversely related to the separation angle of fluctuations in the data, $\theta = 2\pi/\ell$. The result is a power spectrum, shown in Fig. 1.4, with peaks that are sensitive to the curvature, dark energy, baryon density, and matter density. Fig. 1.5 shows the results of a simulation varying these parameters; apparently, the ratio of second and third peaks is particularly sensitive to the matter density and its baryonic content.

The origin of these anisotropies dates all the way back to the very-early Universe where ripples had formed in the inflationary field. As the Universe evolved, the ripples transformed into matter density fluctuations that gravitationally attracted additional matter. Baryons in these regions would experience a photon-interaction pressure that pushed them back outward in waves that were again pulled inward by gravity. Conversely, particles that had no electromagnetic interactions, i.e. dark matter, would have remained in the overdense regions producing a different density pattern. The "baryon acoustic oscillations" (BAO) continued through recombination at which time the photons decoupled becoming a photograph of the Universe at that time. Table 1.1 summarizes measurements of cosmological parameters

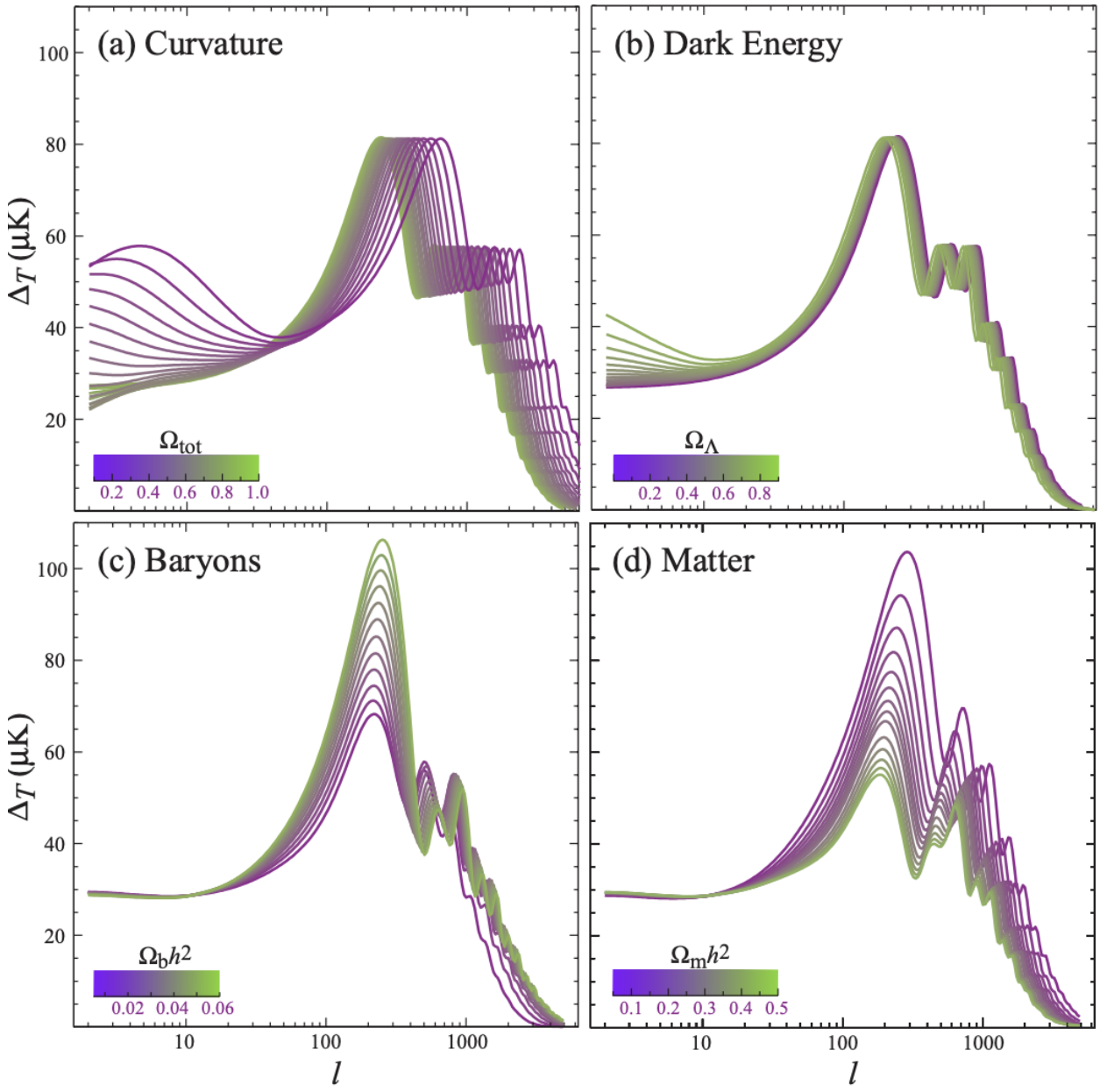

Figure 1.5: Simulated sensitivity of the CMB power spectrum to curvature k (a), dark energy Ω_Λ (b), baryon density Ω_b (c), and matter density Ω_m (d). Models constrained to a total of $\Omega = 1$. Figure from [14].

Parameter	Symbol	Value
Baryonic Matter Density	Ω_b	0.0490 ± 0.0003
Cold Dark Matter Density	Ω_c	0.2606 ± 0.0020
Dark Energy	Ω_Λ	0.6889 ± 0.0056

Table 1.1: A selection of constraints on the ΛCDM model generated by the Planck collaboration [1].

extracted from the Planck data. Most noteably, cold dark matter is 5 times more prevalent the baryonic matter.

In the dark ages, the oscillations became sites that gravitationally attracted clouds of hydrogen eventually nucleating stars and galaxies followed by conglomeration of these objects into galaxy clusters and super clusters. The patterns of large-scale objects are therefore another measure of the quantum fluctuations, thus the energy content of the Universe. The maximum possible distance an acoustic wave could travel before recombination is a particular striking feature visible as a bump in the large-scale correlation function of luminous red galaxies measured by the Sloan Digital Sky Survey (SDSS), shown in Fig. 1.6.

1.2 Candidates

There is an abundance of hypothetical dark-matter particles.

Historically, the candidates have been structures composed of the normal matter we see in our immediate surroundings, in other words, baryons. Examples are gas or Massive Compact Halo Objects (MACHOs), such as the dim-stars postulated by Jan Oort. The quantity and properties of this type of dark matter have been tightly constrained through decades of scientific pursuit, a success that is to be expected because baryons do interact electromagnetically and there are striking physical consequences of this fact. For example, the cooling effect of photon exchange between baryons causes a tendency for them form compact objects which can act as lenses magnifying background stars. Not to mention the effect of baryons on the CMB and their roll in the BAO described in the previous section.

The majority of contemporary dark candidates are entirely theoretical. They are particles that can be extracted from extensions to the standard model Lagrangian and have properties necessary for them to comprise the relic density of dark matter, according to Big Bang cosmology. Almost all of the candidates have self interactions inappreciable to those of electromagnetism thus would not form compact objects; they would produce the more subtle gravitational signatures of elementary particle clouds.

Figure 1.7 illustrates the masses spanned by leading dark candidates. This dissertation focuses on Weakly Interacting Massive Particles (WIMPs), an attractive solution to the problem first put fourth in the 1970s [15], as well as newer hidden sector alternatives: hidden thermal relics/WIMPless, asymmetric, and freeze-in DM. The latter are a set of well

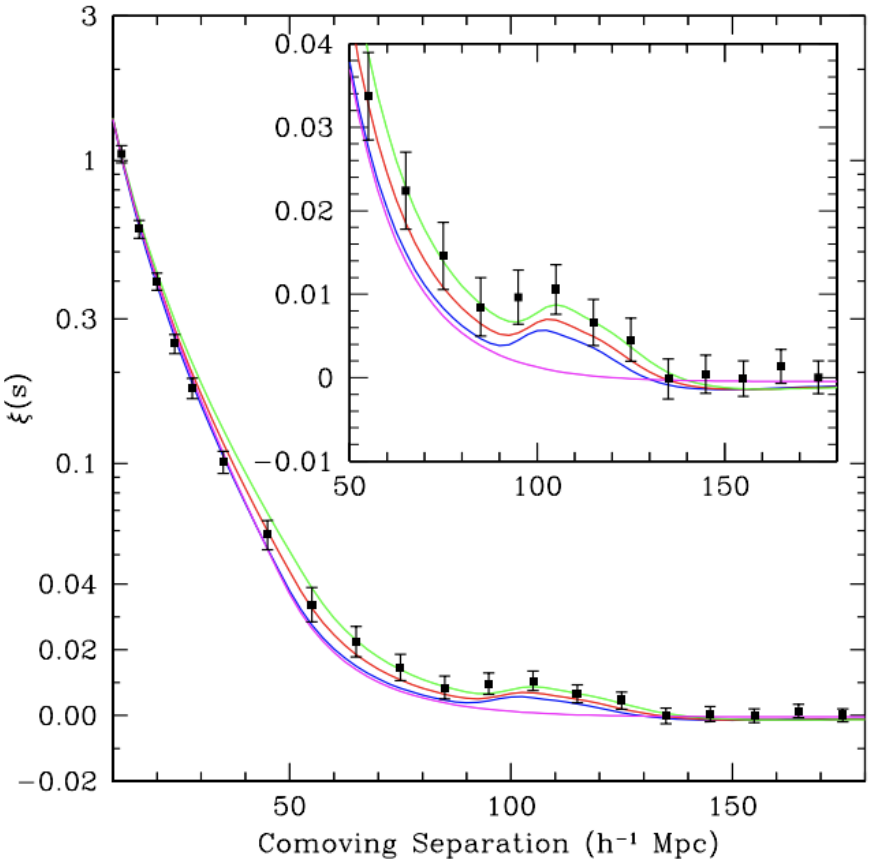

Figure 1.6: Large-scale correlation function of luminous red galaxies from the Sloan Digital Sky Survey. $\xi(s)$ is the redshift. The bump at $\sim$ 100 h^{-1}Mpc is a statistically significant feature corresponding to the maximum distance that an acoustic wave could have traveled before the epoch of recombination. The green, red, and blue lines are models with different relic dark matter density. The magenta line is a pure CDM model. Figure from [13].

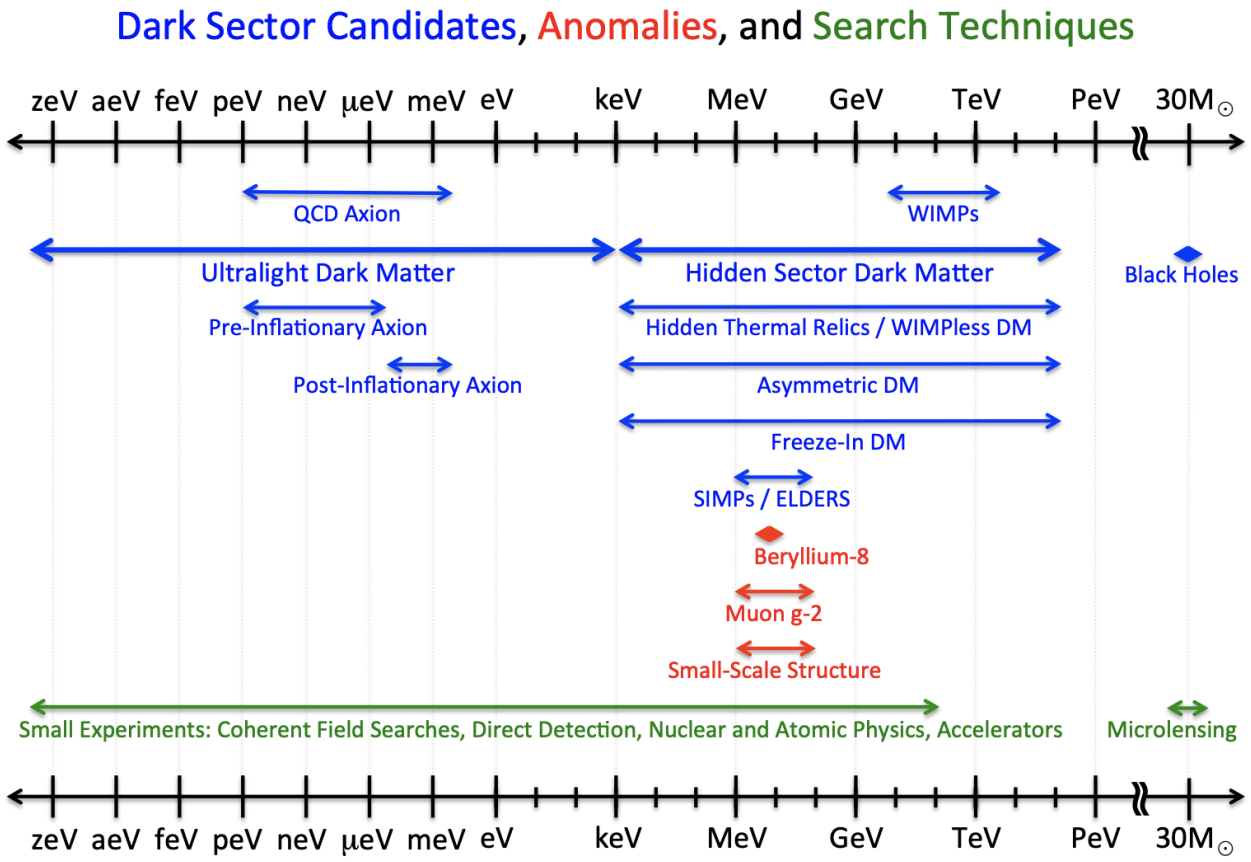

Figure 1.7: Dark matter candidates and their mass ranges compared to current physical anomalies and search techniques. Reproduced from [16].

motivated classes of dark particles with masses extending above and below the edges of the WIMP range. In particular, these models are favored as low-mas DM candidates. Each of the candidates is discussed in the following two subsections.

WIMPs

In the hot dense plasma of the early Universe, particles speed through space frequently colliding with neighbors undergoing reactions of the form

$$p_1 + p_2 \rightleftharpoons p_3 + p_4. \tag{1.4}$$

Initially, the forward and reverse rates of such reactions were equal, and the particles were said to have been in thermal equilibrium. Their number densities are given by solutions to

the Boltzmann equation,

$$n_i^{eq} = \begin{cases} g_i \frac{T^3}{\pi^2} & \text{for } m_i c^2 \ll kT \\ g_i \left(\frac{m_i T}{2\pi}\right)^{3/2} e^{\frac{-m_i c^2}{kT}} & \text{for } m_i c^2 \gg kT, \end{cases} \tag{1.5}$$

where g_i is a statistical weight accounting for the number of states of particle species i, m_i the mass, T the temperature, and k the Boltzmann constant. The two branches of the solution quantify the effect that occurs the thermal energy (kT) of the plasma drops below the mass of a heavy species. Annihilation of the species into lighter products continues but the reverse reaction slows as the products loose the kinetic energy necessary to produce their heavier counterpart. The number density of the heavy species becomes suppressed according to the $m_i c^2 \gg kT$ branch of the equation.

If equilibrium were to be maintained, all species would annihilate into particles of the lowest possible mass; however, equilibrium can be broken by expansion of the Universe. As the rate of a reaction drops below the rate of expansion, annihilation of the heavier species will abate leaving a relic number of these particles, a process known as "freeze out". The moment where this occurs is calculated, approximately, from the Hubble constant

$$H(t) > \Gamma_i = n_i \langle \sigma_i \nu \rangle \tag{1.6}$$

where Γ_i is the reduction rate of particle species i and $\langle \sigma_i \nu \rangle$ is the thermally-averaged effective annihilation cross section, σ_i, taking into account all possible reactions of species i, and relative particle velocity, ν.

Freeze out of standard model particles is predicted to have occurred on several occasions: for example, neutrons and protons decoupled from leptons before nucleosynthesis and photons from electrons shortly after recombination. Naturally, one might speculate as to whether this mechanism generated the abundance of dark matter we observe in the Universe today.

Imagine a dark matter species, χ, in thermal equilibrium with quarks, q, via reaction

$$\chi + \overline{\chi} \rightleftharpoons \mathrm{q} + \overline{\mathrm{q}}. \tag{1.7}$$

If the quarks remain in equilibrium with other Standard Model particles, while the dark matter freezes out through the above interaction, the Boltzmann equation can be solved numerically to find the dark-matter number density as it depends on temperature of the Universe and $\langle \sigma_\chi \nu \rangle$, shown for a 100 GeV particle in Fig. 1.8. Larger effective annihilation cross sections result in smaller relic density according to

$$\Omega_\chi h^2 \approx \frac{0.1 \text{ pb} \cdot c}{\langle \sigma_\chi \nu \rangle} \tag{1.8}$$

where pb is the unit picobarns and c is the speed of light. For interactions mediated by the weak force, the effective annihilation cross section is $\sim \frac{g_{weak}^4}{m_\chi^2}$ with $g_{weak} \simeq 0.65$ and m_χ in

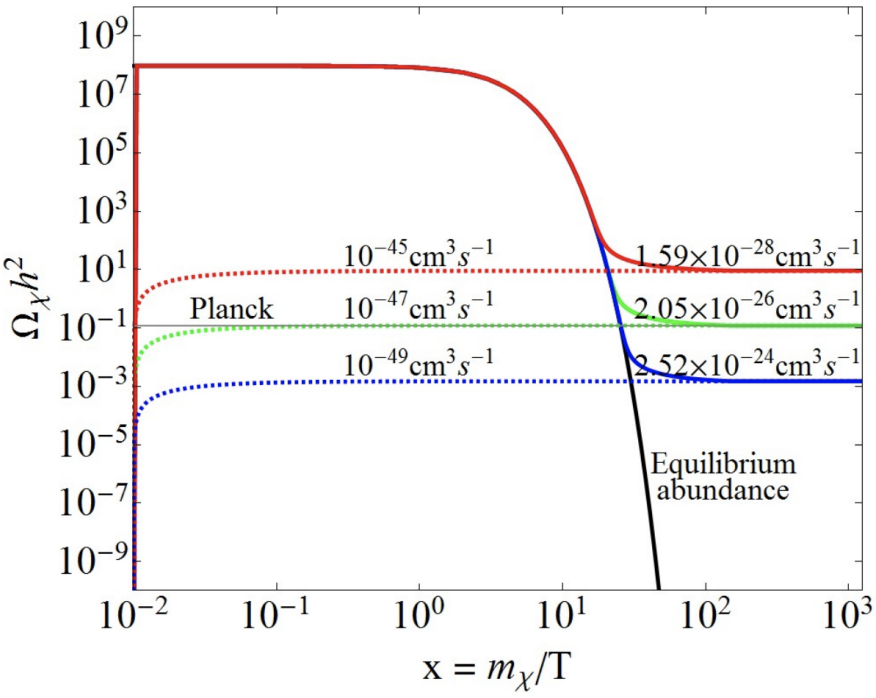

Figure 1.8: Relic density ($\Omega_\chi h^2$) of a 100 GeV DM particle as a function of $x = m_\chi/T$, where m_χ is the DM mass and T the temperature of the Universe. The solid/dashed red, green, and blue lines correspond to the freeze-out/freeze-in mechanisms with three different average effective cross sections. The solid black line shows the density of particles that stay in thermal equilibrium. The thin grey line indicates the relic DM density calculated from Planck data [19]. Reproduced from [20].

the weak range (100–1,000 GeV), an expression that yields approximately the correct relic density [17, 18].

Dark matter candidates predicted by freeze out to have the above characteristics are referred to as Weakly Interacting Massive Particles (WIMPs) [17, 18]. Originally, the name was reserved for species with interactions at the weak scale, traditional WIMPs, but experiments have since ruled out this region of parameter space and the definition has been extended to species with interactions below this range [21]. The class is generally precluded to particles interacting via Standard Model forces: hidden sector dark matter, neutral under such forces, is discussed in the following subsection [16].

The leading WIMP candidates come from the theory of R-parity-conserving supersymmetry, a long-favored extension of the Standard Model. The theory predicts the existence of heavier superpartners for every Standard Model particle with spin differing by a half integer. It solves the hierarchy problem due to the superpartners introducing quadratically-divergent loop corrections that would exactly cancel those of the Standard Model particles in the

renormalisation of the Higgs mass, thus yielding a finite value. It also provides a path to grand unification of the forces at $\sim 10^{19}$ GeV. Most versions of supersymmetry predict a stable particle, usually the lightest superpartner, with a mass and annihilation cross section similar to a WIMP, a coincidence referred to as the "WIMP miracle" [22]. Detection of such a particle would be a fortunate event in the field of particle physics.

Hidden Sector Dark Matter

All robust evidence for dark matter is, thus far, gravitational. Perhaps the simplest hypothesis is that it consists of particles neutral under all SM forces—not simply electromagnetism—but charged under additional forces that remain hidden.

Dark matter could arise in a "hidden valley" of light particles charged under a new non-abelian gauge group [23]. Such theories are compatible with supersymmetry—and other solutions to the hierarchy problem—but could have a significant impact on its phenomonology, possibly one that would obscure searches for supersymmetry at the LHC contributing to continued null results [24].

It is also viable for hidden sector dark matter to have absolutely no interactions with the SM eliminating its connection to supersymmetry or other solutions to the central problems of particle physics. However, there is a strong motivation to search for such interactions. Symmetry arguments allow construction of "portals" between the hidden and standard sectors produced by radiative corrections, for example, the vector and Higgs portals [16]. These interactions are generally consistent with a broad set of cosmological production mechanisms, including, but not limited to the freeze out mechanism that applies to WIMPs. These are described in the points below.

- *Hidden Thermal Relics*

  WIMPs with masses below ~ 2 GeV are forbidden by the Lee-Weinberg bound. They would have larger annihilation cross sections according to $\langle \sigma_\chi \nu \rangle \sim \frac{g^4_{weak}}{m^2_\chi}$ thus would freeze out earlier and at higher temperatures. The relic density would be correspondingly higher and result in overclosure of the Universe [25].

  If the DM is part of hidden sector interacting through a new dark force coupling g_D, this circumstance can be avoided. The DM can undergo "secluded" annihilation to hidden mediator particles followed by mediator decays to SM particles—as long as m_χ is greater than the mediator mass. The effective average cross section would have proportionality $\langle \sigma_\chi \nu \rangle \sim \frac{g^4_D}{m^2_\chi}$ and lower DM masses would be allowed as long as g_D is reduced together with $sqrtm_\chi$. Correct cosmological conditions can be realized with a vector mediator for DM masses $\gtrsim 1$ GeV and a scalar mediator for sub-GeV masses [16].

The DM can also interact "directly" with SM fermions through a vector s-channel mediator. The annihilation cross section would have proportionality $\langle \sigma_\chi \nu \rangle \sim \frac{g_D^2 g_{SM}^2 m_\chi^2}{m_{med}^4}$ where g_{SM} is a standard model coupling and m_{med} the mass of the mediator [16].

Hidden thermal relics have also been a topic of discussion in relation to the 511 keV emission line from the center of the Milky Way [26]. Light scalar dark matter of $m_\chi \sim 100$ MeV, interacting through a hidden neutral gauge boson [27, 28, 29], could annihilate to electron-positron pairs and the subsequent positron annihilate could produce the observed excess of γ rays [30]. However, there is more recent work demonstrating classical sources of positrons can also explain the excess [31].

- *Asymmetric Dark Matter*

  If there had been no primordial asymmetry favoring matter over antimatter, these particles would have been created and destroyed at equal rates for the first fraction of a second following the big bang, after which there would only exist leftover energy. However, about one in a billion baryons survived annihilation with antibaryons resulting in the current Universe composed of $\sim 5\%$ normal matter.

  With this in mind, its quite a coincidence the relic abundance of DM is of the same order of magnitude as that of SM particles: $\Omega_\chi \simeq 5\Omega_b$. Its plausible the DM relic density has its origin in a similar—or the same—asymmetry as that of the baryons.

  In such a scenario, if the hidden and standard sectors were in chemical equilibrium in the early Universe, then the abundances of these classes of particles are related by $\Omega_\chi \sim r\Omega_b \frac{m_\chi}{m_p}$, where $m_p \simeq 1$ GeV is the mass of the proton and r a number of order $\mathcal{O}(1)$ that depends on the interaction maintaining equilibrium [32, 33]. Considering the observed ratio of dark and normal matter, this relationship motivates DM masses of a few GeV. In models where hidden sector is out of equilibrium, r is much less than 1 and DM masses far below that of the proton are probable.

  Asymmetric DM production requires the existence of interactions that depopulate the symmetric component of the DM density. Considering freeze out, appropriately-large annihilation cross sections require the existence of a hidden force. Both secluded and direct annihilation processes are possible [32], and the former would imply a minimum coupling that can be probed by near-future accelerator and direct-detection experiments [34].

  A special case is mirror DM in which the hidden sector is an exact copy of the standard sector. The DM particles would interact with one another through similar, or exactly the same, dynamics as ordinary particles and would have an asymmetry that generated the relic density of mirror antibaryons, which could be connected to the SM counterpart [35, 36]. The two sectors could interact through photon-mirror photon and Higgs-mirror Higgs kinetic mixing, processes that are observable by direct-detection and accelerator experiments, respectively [37].

- *Freeze In Dark Matter*

  DM with very weak couplings to the SM would never reach thermal equilibrium with the standard sector in the early Universe. In this circumstance, a relic density of DM could freeze in through SM annihilations or decays at temperatures near the DM mass—although these interactions would be very rare. Initially, there would be negligible quantities of DM; as the universe evolved, SM interactions would gradually generate DM at a rate that is exponentially suppressed by the decreasing temperature; eventually, decoupling of the DM would set the relic density [38, 16, 39]. These stages are visible in Fig. 1.8.

  Freeze in implies DM-SM interaction cross sections that are orders of magnitude below those of freeze out, and correspondingly-low couplings. Despite this fact, there are some models that can be probed by laboratory experiments. Primarily, if the DM-SM mediator is much lighter than the DM particle, then scattering cross sections are enhanced above those of annihilation [16].

  Freeze in avoids the Lee-Weinberg limit applied to WIMPs because lower-mass particles with smaller cross sections would reduce the predicted relic density. As a consequence, the allowed mass range of freeze-in DM naturally extends far below that of WIMPs. Fig. 1.9 illustrates the extended DM mass range and allowed annihilation cross sections for both freeze-in and hidden-thermal-relic freeze-out scenarios.

1.3 Direct Detection of Dark Matter

Gravitational effects reveal a great deal about the galactic and large-scale characteristics of dark matter but little about the particle nature of the substance. In this pursuit, it is necessary to search for more-powerful interactions incorporating SM or hidden force carriers.

There are three experimental approaches to accomplishing this task: production of DM, indirect detection of DM annihilation products, and direct detection of DM scattering on SM particles. They are summarised by the schematic shown in Fig. 1.10.

Production could occur when SM particles are collided into one another at an accelerator such as the Large Hadron Collidor (LHC) at the European Center for Nuclear Research (CERN). The collisions would produce DM at a much lower rate than other SM particles and the DM would usually travel through a surrounding detector without interacting. For these reasons, searches are performed by measuring energy and momentum of the SM collision products to identify a missing quantity of momentum that can be attributed to the DM. Neutrinos can leave a similar absence in the detector, thus it is advantageous to require the events contain no leptons. Examples of such searches are $p\overline{p} \rightarrow \chi\overline{\chi} + jets$, γs, or other particles in the ATLAS detector, which have thus far yielded null results [41, 42].

Annihilation could occur in appreciable quantities within objects that have a large gravitational potential or other cosmological features where DM density is very high, for example: the galactic center, dwarf galaxies, or the center of the Sun. Satellite and earth-based tele-

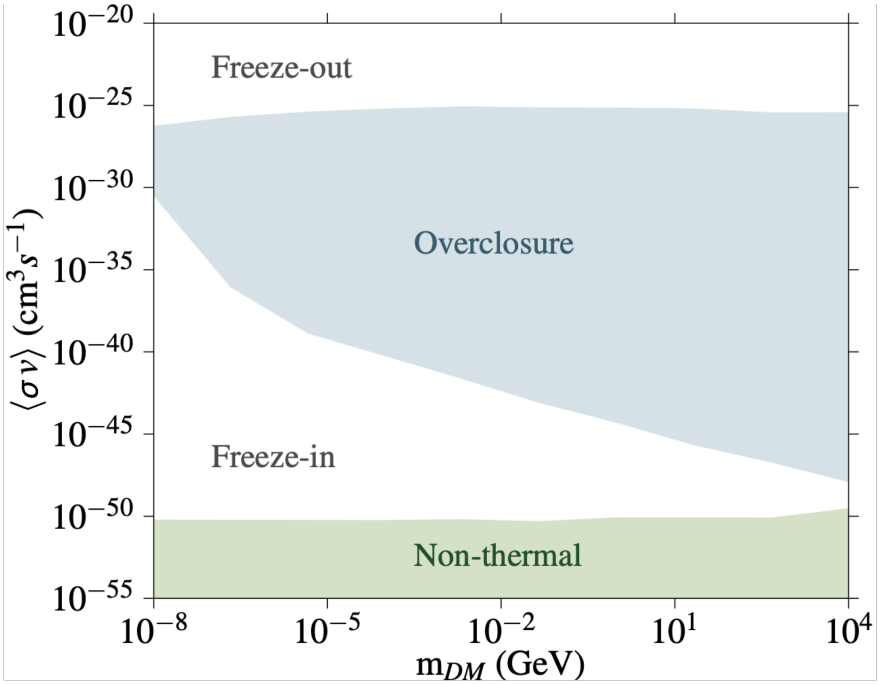

Figure 1.9: Annihilation cross section ($\langle\sigma\nu\rangle$) dark matter mass (m_{DM}) combinations allowed for thermal freeze-in and hidden-thermal-relic freeze-out scenarios. The blue shaded region is excluded by a constraint requiring relic densities that do not cause overclosure of the Universe. The green shaded region indicates the regime of non-thermal DM. Figure adapted from [20].

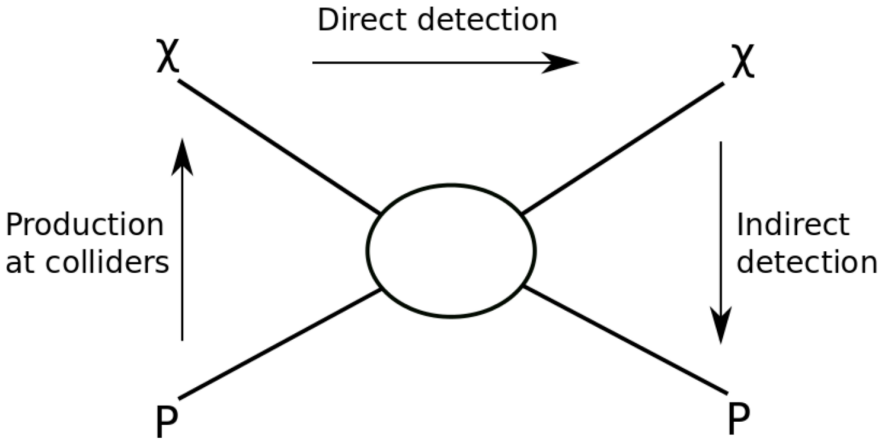

Figure 1.10: Schematic of the three dark matter detection channels. Reproduced from [40].

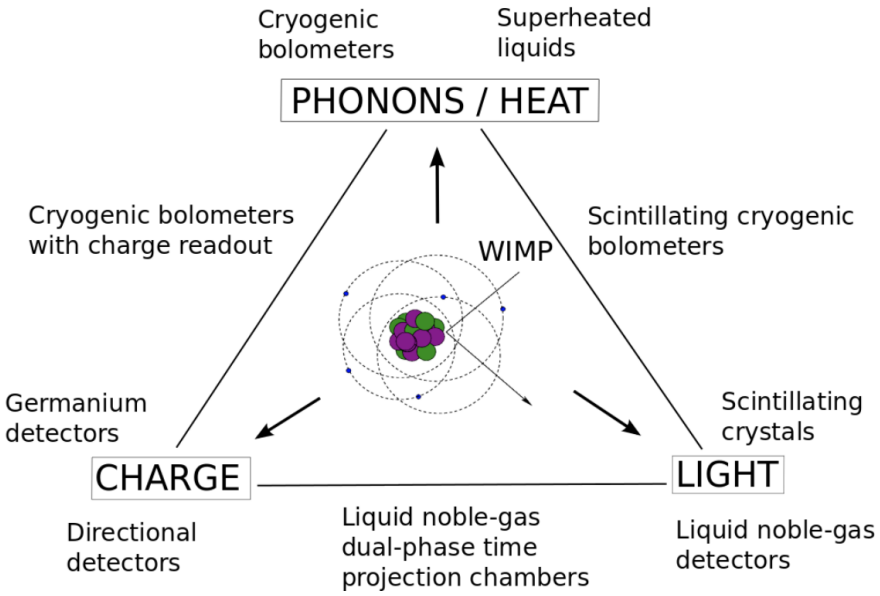

Figure 1.11: Categories of direct dark matter detectors with respect to the quanta of energy that they measure. Reproduced from [40].

scopes can be used to detect gamma rays and positron annihilation remnants from $\chi\overline{\chi} \to \gamma\gamma$ and $\chi\overline{\chi} \to e^+e^-$, and high-energy neutrino detectors can observe products from $\chi\overline{\chi} \to \nu\overline{\nu}$ [43, 44]. Indirect searches like these are a challenge due to an abundance of known background sources that are difficult to model with high fidelity [45].

Direct detection experiments search for DM that passes through our local environment because of our motion through the Milky Way halo. The strategy of these experiments is to construct a very precise detector that can be left waiting for passing DM to scatter on the SM particles of its medium. In these interactions, the DM transfers a quantity of energy to the particle then travels out of the detector without further interactions, due to its modest coupling to the SM. The particle will recoil and rapidly loose its kinetic energy in further interactions with its neighbors producing ionisation, scintillation, and phonons. Detectors are designed to measure one or a combination of these quanta; for example, dual-phase noble-gas time projection chambers (TPCs) are instrumented to measure freed electrons and photons [46]. Figure 1.11 summarizes the detector technologies with respect to the signals they observe. As with indirect searches, backgrounds are the primary challenge for direct detection experiments. Detectors are usually placed underground to avoid interference of cosmic rays and built from radiopure materials to reduce the rate of events from radioactive decay products scattering in the medium [40].

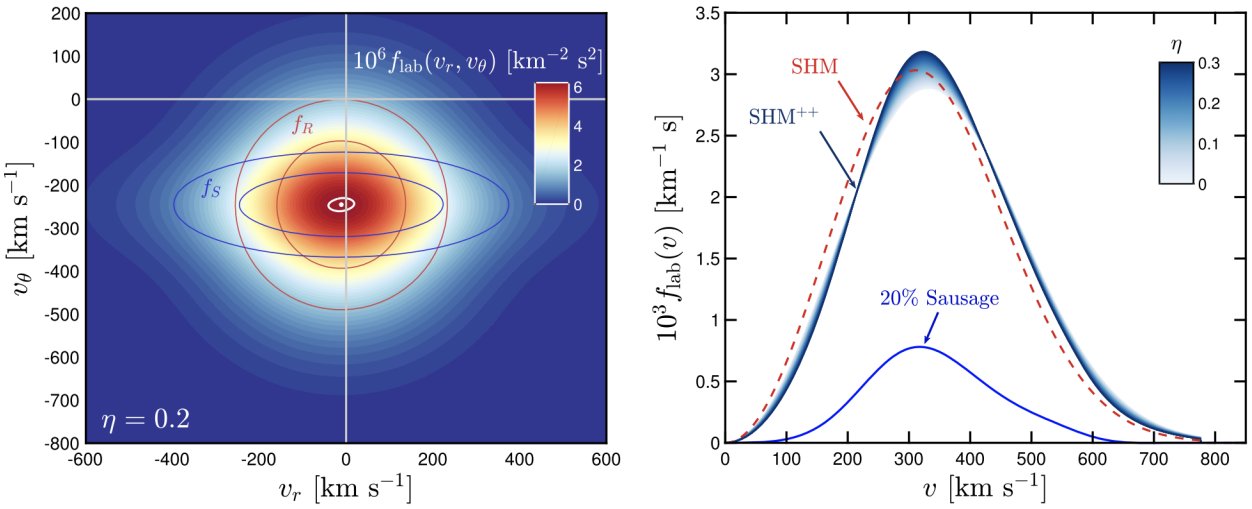

Figure 1.12: On the left is the earth frame velocity distribution, f_{lab}, of the Milky Way halo DM in the radial, r, and horizontal, θ, directions. The round and Gaia-sausage components, f_R and f_S, are outlined in red and blue. The white point and line are the inverse of the Sun's velocity (LSR + peculiar motion) and evolution of the Earth's velocity over the length of a year. On the right is the Earth frame DM speed distribution for SHM and SHM^{++} models drawn by dashed red a solid blue lines. η is the fraction of the DM distribution belonging to the sausage, with a best fit value of 0.2. Reproduced from [48].

Dark Matter Differential Interaction Rate

The calculation of the DM differential interaction rate in a direct detection experiment is presented in this subsection.

The process begins with an estimate of the DM velocity distribution at the location of the earth within the Milky Way. The canonical model—the standard halo model (SHM)—spreads the DM particles throughout an isotropic isothermal sphere that extends greatly beyond the baryonic disk. This type of model can produce the asymptotically flat rotation curves presented in Sec. 1.1, but is an idealization; there exist more complicated models that have better agreement with n-body simulations [47]. In particular, data from the Gaia satellite suggests a substantial fraction of the DM lies in a radially anisotropic population, the "Gaia sausage", resulting in an discrepant component of the velocity distribution [48], shown in Fig. 1.12 (left).

The SHM predicts a Maxwell-Boltzmann speed distribution truncated at the value beyond which DM would escape the Milky Ways gravitational potential ($v_{esc} = 544$ km/s), as is shown below:

$$f(\mathbf{v}) = \frac{1}{(2\pi\sigma_v^2)^{3/2} N_{esc}} e^{\left(\frac{-|\mathbf{v}|^2}{2\sigma_v^2}\right)} \times \Theta(v_{esc} - |\mathbf{v}|). \tag{1.9}$$

N_{esc} is a constant that renormalizes $f(\mathbf{v})$ after truncation by the step function $\Theta(v_{esc}-|\mathbf{v}|)$. $\mathbf{v}$ is the galactic frame velocity of the DM and σ_v is the isotropic velocity dispersion calculated from the local speed of rest (LSR), $v_0 = \sqrt{2}\sigma_v = 220 \pm 20$ km/s. More recent and precise estimates of v_0 and v_{esc} are 233 ± 3 km/s and 528^{+24}_{-25} [48, 49], though most direct detection experiments use the former values for consistent comparison of results [50, 51, 52, 53]. The SHM speed distribution is plotted in Fig. 1.12 (right) and compared to that of SHM^{++}.

In the Earth's frame, the energy imparted to a target particle from the scatter of a DM particle is given by

$$E_R = \frac{1}{2} m_\chi u^2 \frac{4 m_\chi m}{(m_\chi + m)^2} \cos^2(\theta) \tag{1.10}$$

where m_χ and m are the DM and target masses, $u = |\mathbf{v} - \mathbf{v_0} - \mathbf{v_S} - \mathbf{v_E}|$ is the DM velocity ($\mathbf{v_S}$ being the Sun's peculiar motion about the LSR, and $\mathbf{v_E}$ being the Earth's motion about the Sun—on average ~ 30 km/s), and θ is the recoil angle with respect to the original direction of the DM particle [54]. E_R is greatest when $m_\chi \gtrsim m$ and the recoil angle in the center of mass frame $\theta_{CM} = \cos^{-1}(1 - 2\cos^2(\theta)) = \pi$, that is, for backscattering. Plugging this into 1.11 and solving for u gives the lowest speed that can generate a recoil of energy E_R,

$$u_{min} = \sqrt{\frac{E_R m}{2} \left(\frac{m + m_\chi}{m_\chi m} \right)^2}. \tag{1.11}$$

The differential interaction rate is a product of the number of particles in the detection medium ($\frac{M}{m}$ where M is the total medium mass), the DM flux ($\frac{\rho_0}{m_\chi}$ where $\rho_0 = 0.3$ GeV/cm^3 is the local DM density [55]), and the differential scattering cross section ($\frac{d\sigma}{dE_R}$):

$$\frac{dR}{dE_R} = \frac{M}{m} \frac{\rho_0}{m_\chi} \int_{u_{min}}^{|\mathbf{v_{esc}} + \mathbf{v_s} + \mathbf{v_E}|} u f(\mathbf{u}) \frac{d\sigma}{dE_R} d^3u. \tag{1.12}$$

The characteristics of the particular DM model under consideration and the target particle on which the DM is scattering determine the implementation of $\frac{d\sigma}{dE_R}$.

The number of DM interactions occurring in a detector is given by

$$N = e \int_{E_{thr}}^{E_{max}} \epsilon \frac{dR}{dE_R} dE_R \tag{1.13}$$

where $e = M \times \textit{livetime}$ is the exposure, ϵ is the normally energy-dependent efficiency, E_{thr} is the energy threshold, and E_{max} is the kinematically-determined maximum recoil energy, specifically Equation 1.11 evaluated at $\cos^2(\theta) = 1$.

DM-nucleus Scattering Cross Section

DM scattering on target nuclei is considered in this subsection—though scattering on electrons is also possible and would produce more substantial signals when m_χ is much less than the mass of a nucleon, according to kinematics of Equation 1.11.

DM-nucleus interactions that are mediated by a heavy particle can be described with a general set of effective field theory (EFT) operators. Direct detection experiments use two standard cases, spin independent (SI) and spin dependent (SD) coupling described by a scalar $(\overline{\chi}\chi\overline{q}q)$/vector $(\overline{\chi}\chi\overline{q}q)$ and axial vector $(\overline{\chi}\gamma^{\mu}\gamma_5\chi\overline{q}\gamma^{\mu}\gamma_5 q)$ models, respectively [56]. The differential cross section for the two couplings is written as

$$\frac{d\sigma}{dE_R} = \frac{m_A}{2u^2\mu_A^2}\left(\sigma_{SI}F_{SI}^2(E_R) + \sigma_{SD}F_{SD}^2(E_R)\right) \tag{1.14}$$

where m_A is the mass of the nucleus and μ_A is the reduced mass of the DM-nucleus system [57].

F_{SI} and F_{SD} are form factors that incorporate the relationship between the size of the target nucleus and the momentum of the DM (p), or the momentum transfer through the mediator (q). At low energies, when the DM particle's de Broglie wavelength ($\gamma = h/p$) is long compared to the breadth of the nucleus, the DM scatters off of the nucleus as a coherently whole and the form factors tend toward a constant value of 1—they are designed to do so. At high energies, coherence is lost and the form factors are necessary to approximate the nucleon density as a function of position. A usual choice for SI scattering is the Helm form factor which represents a smooth solid sphere of radius r_A that dwindles toward 0 over a skin thickness of s,

$$F_{Helm}^2(q) = \left(\frac{3j_1(qr_A)}{qr_A}\right)^2 e^{(-qs)^2/2}. \tag{1.15}$$

where $j_1(qr_A)$ is the spherical Bessel function of the first kind [58]. Calculation of form factors for SD scattering require a more complex approach that accounts for the quark content of the nucleus [59, 60].

The SI cross section, σ_{SI}, is given by

$$\sigma_{SI} = \sigma_0\frac{\mu_A^2}{\mu_0^2}\frac{(f_pZ + f_n(A-Z))^2}{f_n^2} \rightarrow \sigma_0\frac{\mu_A^2}{\mu_0^2}A^2 \tag{1.16}$$

where μ_A/μ_0 are the DM-nucleus/DM-nucleon reduced masses, A is the nucleus mass number, and Z is the proton number. σ_0 is the DM-nucleon cross section introduced to compare the results of experiments utilizing different target nuclei. f_p/f_n are coupling strengths to protons and neutrons that most models predict are near equal [61]. If this is the case, σ_{SI} simplifies to the expression on the right, which is proportional to A^2 and implies that heavier target nuclei should have higher DM interaction rates. However, this effect is accompanied by lower recoil energy E_R, thus a larger fraction of the DM interactions will fail to produce an above-threshold signal.

The SD cross section, σ_{SD} is given by

$$\sigma_{SD} = 8G_F^2\mu_A^2\frac{J+1}{J}\left(\alpha_p\langle S_p\rangle + \alpha_n\langle S_n\rangle\right)^2 \tag{1.17}$$

where G_F is the Fermi constant, J is the total nuclear spin, α_p/α_n are spin-dependent couplings to individual protons/neutrons, and $\langle S_p \rangle / \langle S_n \rangle$ are expectation values of the total spin operators of protons/neutrons in the target nucleus of interest [62]. Unlike the SI case, heavy nuclei have no A^2 enhancement to SD interactions; instead, the cross section depends only on the nucleus' spin structure. The coupling occurs primarily with unpaired nucleons, thus only specific isotopes with this quality grant sensitivity. For example, ^{129}Xe and ^{131}Xe (26% and 21% abundance) have unpaired neutrons that make these isotopes a viable SD DM-neutron interaction target.

Outline

This dissertation is a contribution to the subfield of direct DM detection. The contents began to develop as the Large Underground Xenon (LUX) experiment was publishing its third and final limits on the scattering cross sections of WIMP dark matter. The experiment had acquired a year's worth of data that could potentially be used to search for other rare signals. It's successor LUX-ZEPLIN (LZ) was in the design phase and thought was being put toward optimizing its sensitivity to many processes of interest. At the same time, a broader range of dark candidates was gaining interest from the wider community.

The following chapter describes the fundamentals of DM detection in dual-phase xenon time projection chambers (TPCs), specifically LUX and LZ.

The remaining chapters focus on extending the sensitivity of both detectors to rare events above and below the narrow energy range of WIMP scattering. The work enlarges the sensitivity window of LUX and LZ to enable additional searches for DM and other physics, and handles some residual issues with the standard WIMP analysis.

The chapters pursue these objectives first through precise management of backgrounds that can hide or mimic higher-energy signals of interest [such as: DM coupling through a complete basis of effective field theory operators (the standard WIMP signal is induced through only one such operator), two-neutrino double electron capture of ^{124}Xe, and neutrinoless double beta decay of ^{134}Xe and ^{136}Xe]. Chapters 3 and 4 present data selection and calibration strategies used to study radon in Chapter 5, one of the most challenging backgrounds in this type of detector. Chapter 6 presents work on construction of a material screening facility [the Black Hills Underground Campus (BHUC)] used to select radiopure materials used to build LZ.

A second avenue of investigation is followed in Chapter 7. It presents a search for low-mass DM using the most powerful analysis technique for lowering the threshold of dual-phase xenon TPCs: a scintillation agnostic analysis.

Chapter 2

Dark Matter Detection in Dual-phase Xenon Time Projection Chambers

The previous chapter recounts the current astrophysical evidence for the existence of particle dark matter (DM) relating it to theories of the early universe such as to motivate WIMPs and a set of low-mass DM models. With masses $m_\chi \in 10\text{–}10,000$ GeV, WIMPs immediately suggest the use of xenon as a detection medium due to its similar heavy mass, ~ 131 GeV, which would promote large transfers of energy in elastic DM-nucleus collisions according to Equation 1.11.

This chapter outlines the basics of DM detection via dual-phase xenon time projection chambers (TPCs) such as Large Underground Xenon (LUX) and LUX-ZEPLIN (LZ) around which the work presented in this dissertation is centered. It details signal production mechanisms in liquid xenon and discusses how these motivate the design of dual-phase TPCs. It continues by describing the LUX experiment and analysis of its data, which was used to produce multiple world leading WIMP-nucleon scattering limits [63, 64, 52]. The chapter introduces the strategies used to lower energy thresholds and mitigate electron backgrounds so that dual-phase TPCs can be used to search for low-mass DM. It concludes with a summary of the LZ experiment, the successor of LUX. Detailed discussions of backgrounds common to this type of detector are provided throughout the text because of their relevance to preparations for the future experiment and extension of its reach to low-mass DM.

2.1 Signal Production in Xenon

Xenon Microphysics

When a particle travels through a xenon detector it can interact coherently with a whole xenon atom or scatter on an individual atomic electron. The atom will recoil with a kinetic energy equal to that lost by the primary particle (E)—the electron would do so with E less its atomic binding energy—but will rapidly lose that energy through ionisation, elec-

tronic excitation, and elastic collisions with neighboring atoms that heat the medium. When averaged over many events, the distribution of energy among these three channels can be described by [65, 46]

$$E = W_i n_i + W_{ex} n_{ex} + E_{heat} \tag{2.1}$$

where $n_{i/ex}$ are the average number of ionised/excited atoms, $W_{i/ex}$ the average energy required to produce a single ionised/excited atom, and E_{heat} the average energy dissipated through elastic collisions. Dual-phase xenon TPCs do not measure heat, thus the remainder of this chapter considers only the first two channels.

Ordinary thermal motion of the liquid causes the excited atoms to scatter repeatedly on other nearby atoms. Three body collisions bind each excited atom (Xe^*) with a second atom as a third carries away excess energy. The resulting diatomic molecules are initially in electronically and vibrationally excited states ($Xe_2^{*\nu}$), but rapidly undergo two body collisions that relax their vibrational mode (Xe_2^*). The electronic state is one of the two lowest energy excimers, ${}^3\Sigma_u{}^+$ and ${}^1\Sigma_u{}^+$, which differ only in the singlet or triplet spin quantum number of their electrons. Each decays to the ground state, ${}^1\Sigma_g{}^+$, by emission of a ~ 175 nm [66, 67] scintillation photon. The minima of the excimer potentials are located at short interatomic distances where the ground state potential is repulsive, thus transition to the ground state causes dissociation of the diatom.

$$\begin{aligned} Xe^* + 2Xe &\longrightarrow Xe_2^{*\nu} + Xe \\ Xe_2^{*\nu} + Xe &\longrightarrow Xe_2^* + Xe \\ Xe_2^* &\longrightarrow 2Xe + \gamma \end{aligned} \tag{2.2}$$

Three body collisions between the ions and nearby neutral atoms form positively charged diatomic molecules promptly after the interaction of the primary particle. Additional scintillation is formed when a fraction of the freed electrons recombine with these diatoms. Following neutralisation, the diatoms will dissociate with one atom in a highly excited electronic state (Xe^{**}) and the other in the ground state. Two body collisions relax the highly excited atom to one of the two lowest energy excited states (Xe^*) after which the atom takes part in the scintillation producing steps detailed in the previous paragraph.

$$\begin{aligned} Xe^+ + 2Xe &\longrightarrow Xe_2^+ + Xe \\ Xe_2^+ + e^- &\longrightarrow Xe^{**} + Xe \\ Xe^{**} + Xe &\longrightarrow Xe^* + Xe + heat \end{aligned} \tag{2.3}$$

The total numbers of scintillation photons and free electrons are given by

$$n_\gamma = n_{ex} + r n_i = (\alpha + r) n_i \tag{2.4}$$

$$n_e = (1 - r) n_i \tag{2.5}$$

where $\alpha \equiv \frac{n_{ex}}{n_i}$ is the average ratio of excitons to ions present before recombination has taken place and r is the fraction of recombining ions.

α is approximately constant for the physical conditions and energy ranges considered in xenon dark matter experiments; however, its value depends on whether an incident particle interacted coherently with a whole xenon atom or scattered on an individual atomic electron. In the former case, the xenon nucleus and surrounding electrons recoil together dissipating kinetic energy through excitation and ionisation of bound electrons, but also coherent elastic scatters on whole neighboring atoms (i.e. heat). These so called nuclear recoils (NRs) result in a relatively large ratio of excitons to ions of ~ 1 [68, 69]. In the latter case, the electron recoil (ER) dissipates energy through only excitation and ionisation—elastic scattering is negligible. The ratio of excitons to ions is theoretically predicted to be 0.06 although ~ 0.2 is more consistent with experimental data [70, 71].

r depends on the interaction type, amount of transferred energy, and xenon density; but varies most notably with the magnitude of an applied electric field [68, 71, 72, 73]. Larger field magnitudes drift electrons away from their liberation site more quickly reducing the chance that they recombine with a nearby Xe_2^+ molecule. This is particularly true for ERs which produce clusters of ion-electron pairs that are not as dense as those from NRs, thus have a lower probability for each electron to meet and recombine with Xe_2^+ molecule at any particular instance in time. As an example, the r of 100 keV ERs rises by a factor of ~ 1.5 between electric field magnitudes of 98 and 180 V/cm[74, 75], while the r of 100 keV NRs rises by the same amount between 100 and 2000 V/cm [76].

Equations 2.4 and 2.5 can be used to write Equation 2.1 in terms of the number of scintillation photons and free electrons remaining after recombination:

$$E_{ee} = W(n_\gamma + n_e). \tag{2.6}$$

The result has the additional simplification $W_i = W_{ex} = W$, an approximation found accurate in the keV to MeV range. Experiments utilising dual-phase, xenon TPCs rely on a measurement described in [68] that places the value of W at 13.7 ± 0.2 eV/quantum[1]. The subscript ee stands for "electron equivilant" and indicates the equation only holds for ER events. To account for elastic scattering, NR events require the modification

$$E_{nr} = A{E_{ee}}^\gamma \tag{2.7}$$

where $A = 0.173$ and $\gamma = 1.05$ are experimentally determined parameters that quantify the fraction of energy transformed into heat and its energy dependence [73].

Dual-phase Xenon TPCs

Dual-phase xenon TPCs have several common design features that allow them to count scintillation photons and freed electrons. They are vats of liquid xenon with a thin layer of vapor at the top; they are equipped to produce a uniform electric field throughout the bulk

[1] A single-phase xenon TPC using avalanche photodiodes to detect photons, instead of PMTs, has measured $W = 11.5 \pm 0.5$ eV/quantum [77], but the reason for its inconsistency with that measured in [68] is not yet known.

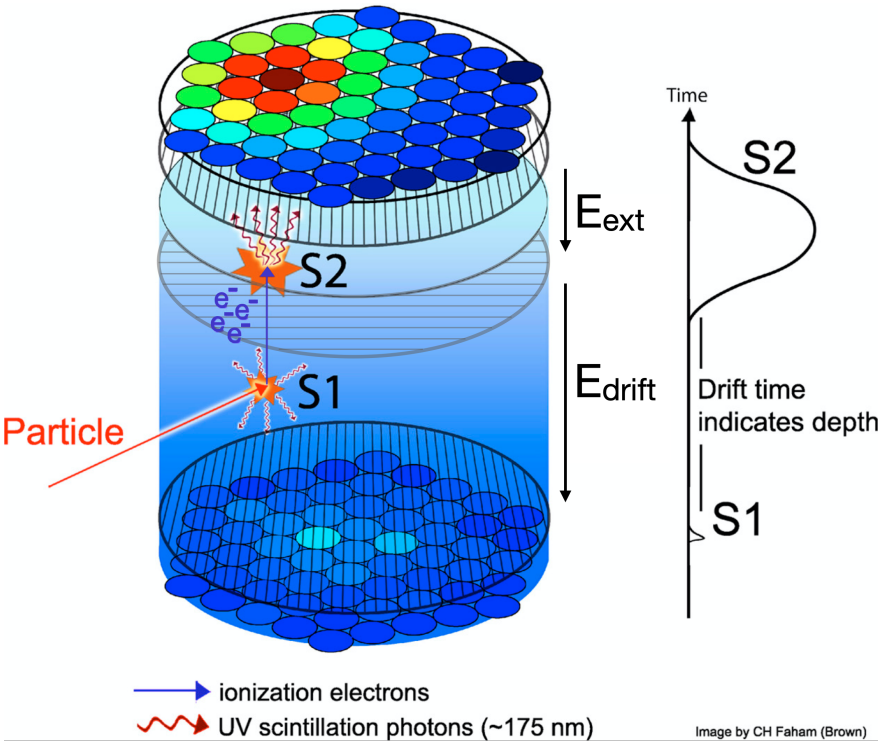

Figure 2.1: Schematic of the LUX detector highlighting the detection principles of dual-phase xenon TPCs. A particle enters the detector and scatters in the liquid xenon generating scintillation photons and ionizing atoms. The photons are detected by PMTs located in arrays at the top and bottom of the TPC producing what is named the $S1$. The free electrons are drifted upward toward the liquid-vapor interface by an electric field, E_{drift}. A stronger electric field, E_{ext}, extracts the electrons into the vapor where they generate electroluminesence that is also detected by the PMTs producing the $S2$. The vertical position of the interaction is calculated from the time difference between the $S1$ and $S2$ and the drift speed of the electrons, while the horizontal position is inferred from the pattern of electroluminescence in the top PMTs. Modification of a figure by Carlos Faham.

of the liquid ($\vec{E}_{drift}$) and a stronger electric field across the liquid-vapor interface ($\vec{E}_{ext}$); and they are instrumented with devices that count photons, usually located in arrays at the top and bottom of the detector. Fig. 2.1 contains a schematic drawing of the LUX detector highlighting these elements.

After a particle scatters in the liquid, scintillation photons travel away from the interaction site toward the edges of the detector where they might encounter one of the photon counting devices. They are detected promptly after the primary interaction due to the short time scales of all processes involved: singlet and triplet excimers have experimentally measured decay constants of 2–4 and 21–28 ns [78, 79, 80], ions undergo three body collisions that

form diatomic ions within $\sim ps$ [70, 81], measurements and an empirically driven formula indicate recombination is best described by an exponential with a < 50 ns time constant [82, 83, 80, 84], and photon transport/instrumentation effects occur on $\sim ns$ timescales [85]. Summing the signals in every photon counting device produces a waveform containing a pulse with a few-nanosecond rise time and tens-of-nanoseconds roughly-exponential decay named the $S1$.

Freed electrons are transported by $\vec{E}_{drift}$ away from the interaction site toward the liquid-vapor interface where they encounter $\vec{E}_{ext}$. The magnitude of $\vec{E}_{drift}$ is tuned for optimal ER/NR discrimination—a topic discussed in the following section. The magnitude of $\vec{E}_{ext}$ is bipartite due the different relative dielectric constants in the liquid and gas phases: $\varepsilon_{r,liq} = 1.95$ and $\varepsilon_{r,gas} = 1$. Its value in the liquid must be increased above a few kV/cm to induce a significant fraction of the electrons to overcome the potential barrier at the liquid surface [86]. The magnitude in the vapor, $|\vec{E}_{ext,vap}| = \frac{\varepsilon_{r,liq}}{\varepsilon_{r,gas}}|\vec{E}_{ext,liq}|$, must also be sufficient for each extracted electron to produce several hundred electroluminesence photons, a condition usually met at several kv/cm in this type of detector. These photons are produced when the field accelerates electrons to energies great enough to excite and ionise surrounding atoms which subsequently undergo the processes outlined in Equations 2.2 and 2.3. Newly freed electrons are also accelerated producing additional photons and free electrons. The corresponding "$S2$" pulse has a roughly Gaussian shape with a several μs width determined by the initial shape of the electron distribution, the longitudinal diffusion experienced by the electrons while drifting, and effects associated with extraction and electroluminesence.

Fig. 2.1 highlights the methods used to calculate the three dimensional position of an interaction given observation of a single $S1/S2$ pair. The (x, y) position can be calculated from the pattern of electroluminesence detected in the array of photon counting devices directly above the vapor. The z position can be calculated from the product of electron drift velocity and time delay between $S1$ and $S2$.

The number of scintillation photons and free electrons are related to the size of the $S1$ and $S2$ signals by

$$n_\gamma = \frac{S1}{g_1} \qquad\qquad n_e = \frac{S2}{g_2} \tag{2.8}$$

where g_1 and g_2 are parameters that encompass detector specific efficiencies and gains discussed in detail in Chapter 4. These conversions can be used to express the energy of an ER event, Equation 2.6, entirely in terms of observables and predetermined quantities as is shown below.

$$E_{ee} = W\left(\frac{S1}{g_1} + \frac{S2}{g_2}\right) \tag{2.9}$$

2.2 The LUX Experiment

Detector

The LUX detector was a dual-phase xenon TPC operated 4850 ft underground in the Davis cavern of the Sanford Underground Research Facility (SURF) in Lead, South Dakota. Fig. 2.2 shows the subsystems and supportive infrastructure as it was laid out in the cavern while data was being collected. The clean room was used by members of the LUX collaboration to build sensitive detector components during the construction phase and the control room was used to operate the detector during the data collection phase. Also shown in the illustration are: a breakout system containing components such as signal/high voltage cables, the liquid nitrogen (LN) system used to cool the xenon, a bladder installed to recover the xenon in the event of a total operation failure, and the cryostat which contained the TPC [87]. Items discussed later in this section, in the context of calibrations and background reduction, are the gas system and the water tank. A view of the water tank from the corner of the cavern is shown in Fig. 2.3.

The vital components of the LUX detector are shown in Fig. 2.4. There were two nested titanium cryostats between which was vacuum that thermally isolated the inner cryostat from the surrounding environment. Top and bottom thermosyphons were used to cool the inner chamber and the internal TPC components to temperatures that allowed formation of liquid xenon. There was a 48 cm tall by 49 cm diameter drift region located between gate and cathode wire grid electrodes that contained 250.9 ± 2.1 kg of liquid xenon [88]. Formation of a uniform $\vec{E}_{drift}$ in this region was aided by 48 copper field-shaping rings ascending a resistive ladder linking the two electrodes. An anode wire grid electrode 1 cm above the gate defined the extraction region. Two additional grids shielded top and bottom arrays of 61 Hamamatsu R8778 photomultiplier tubes (PMTs) [89] from electrons freed by interactions in the xenon. Polytetrafluoroethylene (PTFE) panels were fitted over the copper rings to reflect scintillation and electroluminesence photons toward the faces of the PMTs [87]. The detector, fully constructed inside the water tank, is shown in Fig. **??**.

The LUX PMTs, like most PMTs, were evacuated glass receptacles containing a photocathode, several dynodes, and an anode connected through a resistor chain with a voltage applied across the whole circuit. When a photon struck the photocathode it could eject one or more electrons into the vacuum of the PMT via the photoelectric effect. The electrons were then focused by the electric field toward the emissive surface of the first dynode where they would cause emission of secondary electrons upon contact. All the electrons were then accelerated toward each successive dynode where this process would repeat multiplying their numbers by orders of magnitude. The amplified signal was collected by the anode. The described components are outlined in the PMT schematic shown in Fig. 2.6. The top PMT array, installed inside the TPC, is shown in Fig. 2.7.

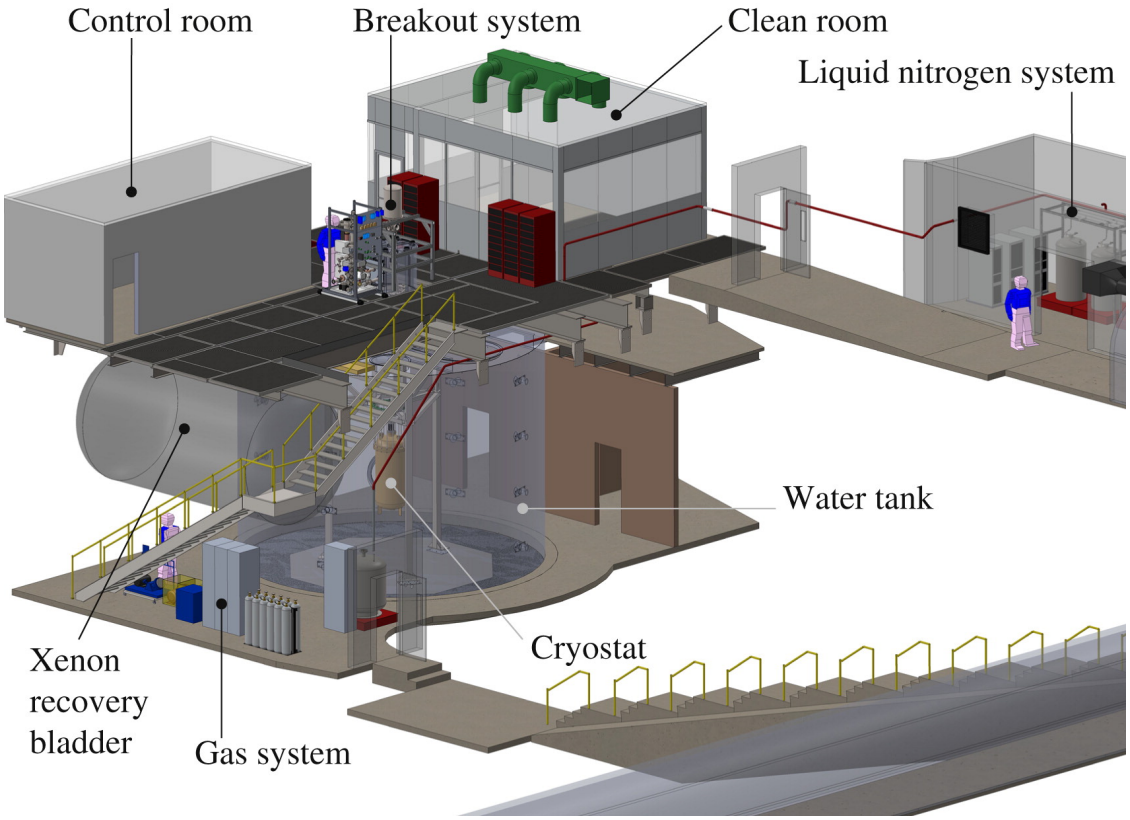

Figure 2.2: Layout of the LUX experiment within the Davis cavern of the Sanford Underground Research Facility (SURF). Figure from [87].

Science Datasets

The LUX collaboration collected data in two science runs occurring from April 2013–Sep 2013 and Sep 2014–May 2016. Because the primary purpose of each run was to perform a WIMP search (WS) analysis, the two runs and corresponding datasets were named WS2013 and WS2014-16 [64, 52].

In preparations for WS2013; the cathode, gate, and anode voltages were varied in order to optimise $\vec{E}_{drift}$ and $\vec{E}_{ext}$ within limits imposed by field induced electrostatic breakdown of the grid wires. $\vec{E}_{ext}$ could only be increased far enough to achieve a $49 \pm 3\%$ efficiency for extracting electrons from the liquid into the gas [52], which is less than the desired $\sim 100\%$ extraction efficiency (EE) that would enable the most precise calibration of the electron signals. Table 2.1 lists the voltages selected for use in WS2013 based on the results of this experimentation.

After WS2013, a grid conditioning campaign was carried out to smooth microscopic surface imperfections on the wires that were hypothesised to cause the observed breakdown

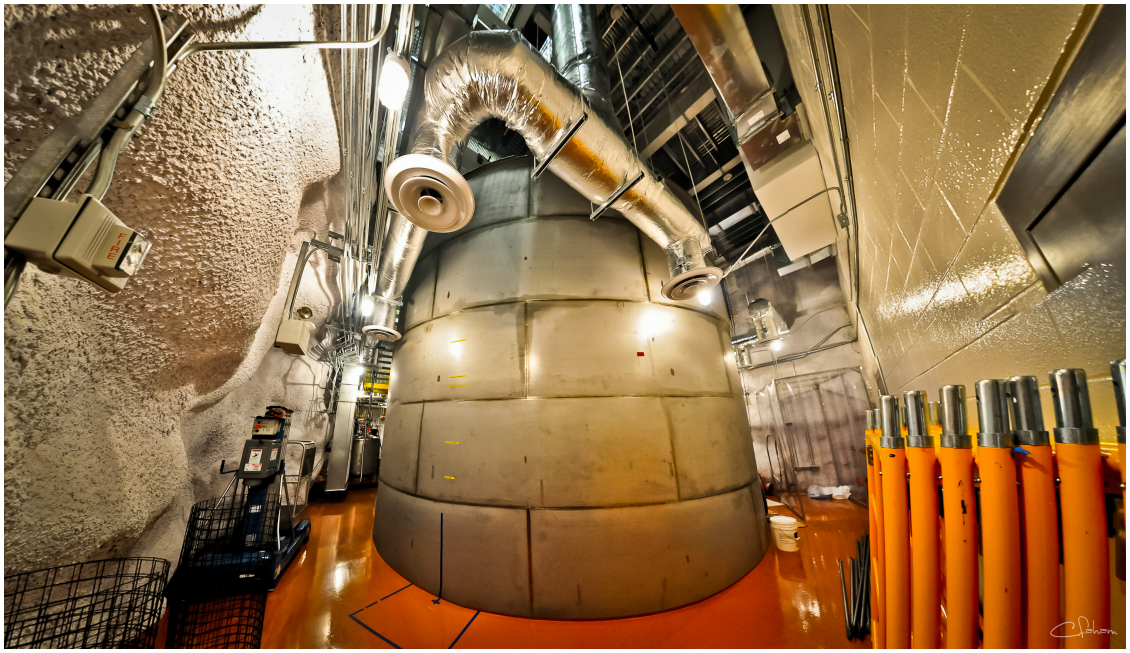

Figure 2.3: Image of the LUX water tank from the corner of the Davis cavern.

	Grid Voltages (kV)				
Dataset	Bottom Shield	Cathode	Gate	Anode	Top Shield
WS2013	-2	-10	-1.5	3.5	-1
WS2014-16	-2	-8.5	1	7	-1

Table 2.1: Grid electrode voltages applied during WS2013 and WS2014-16. $\vec{E}_{drift}$ is determined by the voltage drop between the cathode and gate while $\vec{E}_{ext}$ is determined by the voltage drop between the gate and anode. Data are from [90].

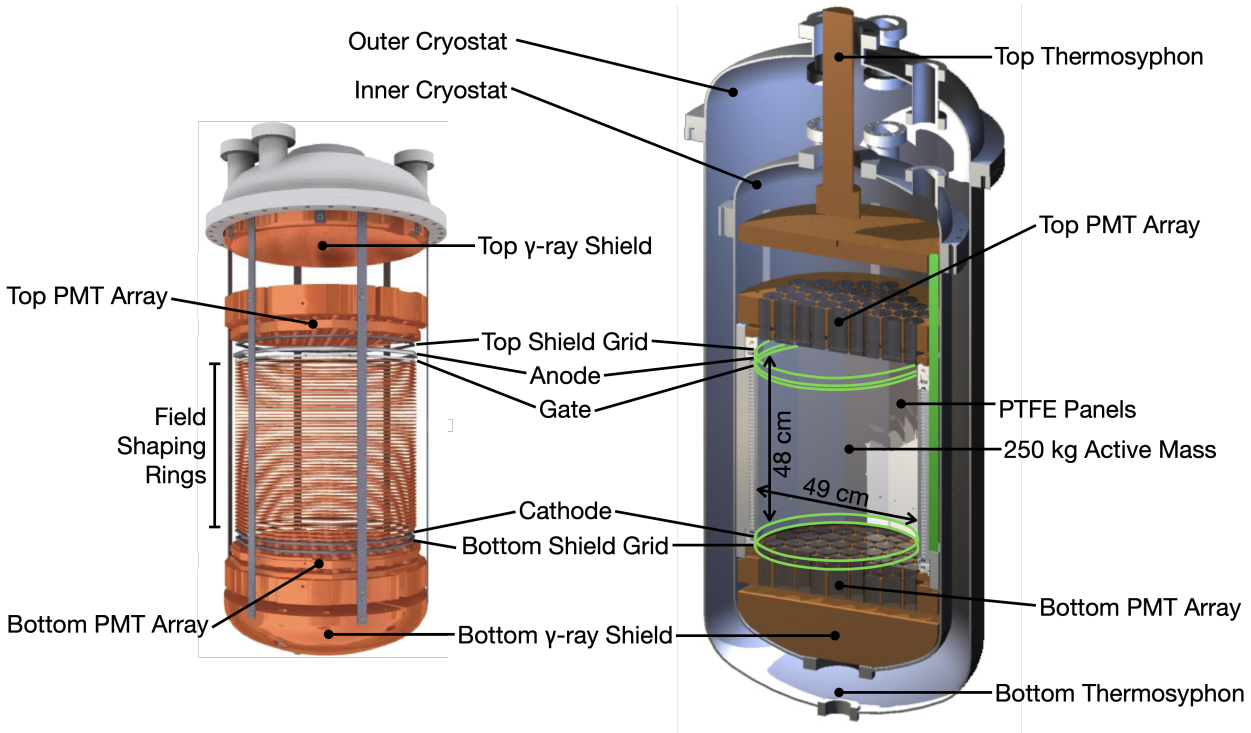

Figure 2.4: Vital components of the LUX detector. Figures adapted from [87].

behavior. With the detector filled by xenon gas, each grid was brought to a potential just above the onset of sustained electrical discharge and maintained at this point for many days. The campaign allowed $\vec{E}_{ext}$ to be increased in WS2014-16, raising the EE to $73 \pm 4\%$ [52]; however, it had the pernicious side effect of negatively charging the PTFE panels. Electron drift trajectories in the liquid Xe were no longer near-vertical paths but instead arched away from the panels toward the center of the xenon. Fig. 2.8 plots the raw radial coordinate [calculated from the pattern of electroluminesence in the top PMT array (r_{S2})] and drift time (t_{drift}) of the edges of TPC as reconstructed from ^{83m}Kr calibration data. A significant inward bias was observed at the beginning of WS2014-16 and its angle increased throughout the run. The data from WS2013 shows a much smaller inward bias [90].

The COMSOL Multiphysics software package was used to produce an electric field model for the WS2014-16 dataset [91, 90]. It found the field magnitude varied most-significantly along the vertical coordinate increasing from approximately 100 to 400 V/cm from the bottom to the top of the liquid xenon [90]. Four drift-time bins were defined to encapsulate features of the data that correlated with the field magnitude at different depths; the average field for each bin is plotted in Fig. 2.9. Because the average fields varied significantly over time periods of several months, shown in Fig. 2.10, four date bins were defined to capture coevolving features of the data. Finally, the electric field model was used to produce a set of

Figure 2.5: Image of the LUX detector fully constructed inside the water tank.

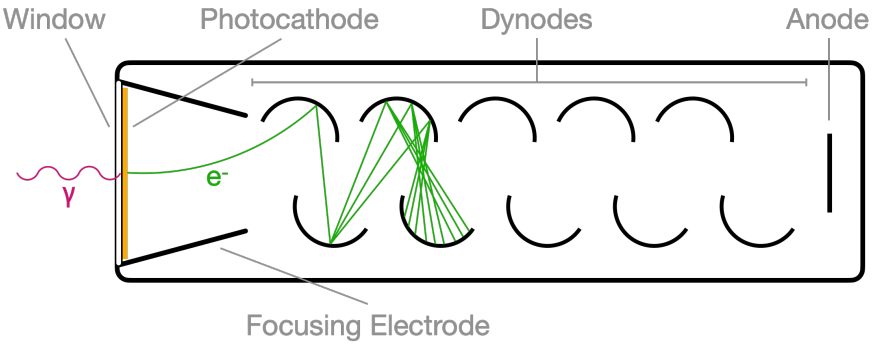

Figure 2.6: Schematic of a photomultiplier tube. The photocathode, focusing electrode, dynodes, and anode are connected through a resistor chain and a voltage is applied across the whole circuit. Photoelectrons from the photocathode are accelerated toward the first dynode producing additional electrons upon collision. These electrons are then accelerated toward the next dynode and the process repeats. At the end of the chain, the amplified signal is collected by the anode.

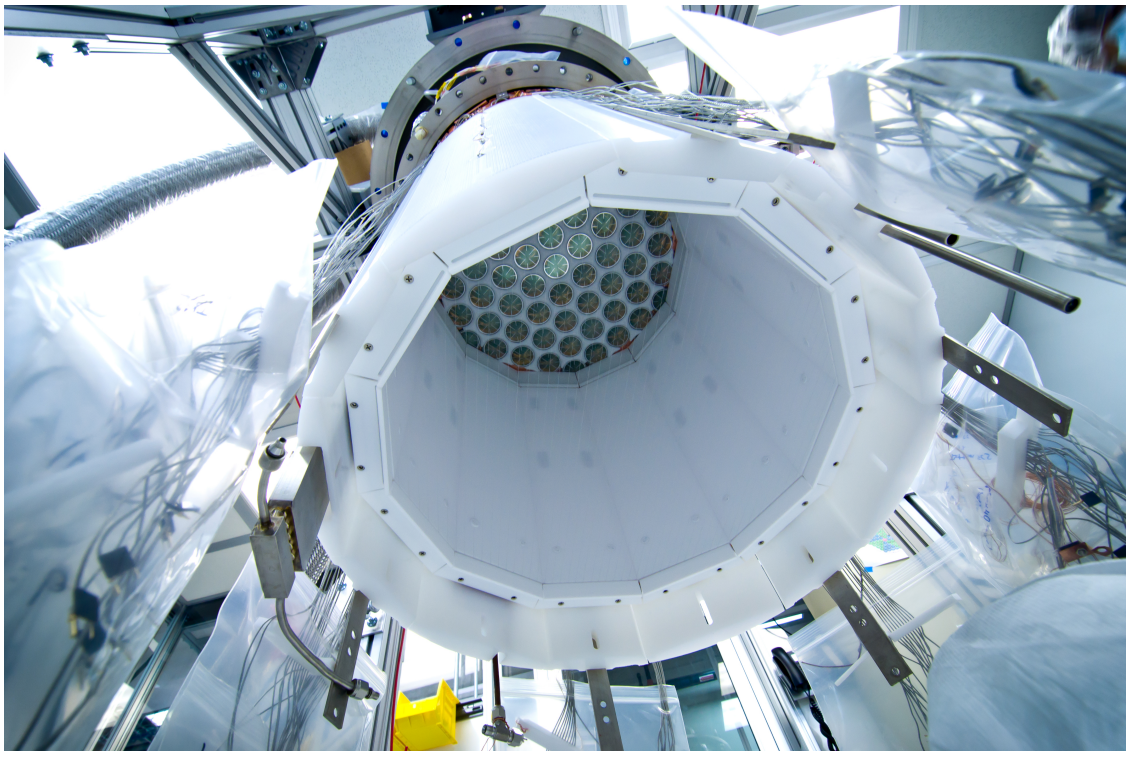

Figure 2.7: Image of the top PMT array installed inside the LUX TPC.

corrected position coordinates (x, y, r, and z) used instead of the raw position coordinates (x_{S2}, y_{S2}, r_{S2}, and t_{drift}) in some analyses.

Data Processing

Data analysis in LUX began with digitisation of signals observed in the PMTs. Afterward, the resulting waveforms were input through an automated data processing framework (DPF) that calculated a set of reduced quantities (RQs). A final filter was used to classify events based on information stored in the RQs.

Digitisation of PMT Signals

PMT signals were pre- and post-amplified to $\sim$ mV scales before being sent through two data streams. In the first, signals were digitised at 100 MHz by analog to digital converts (ADCs) controlled by a field programmable gate array (FPGA). Operating in pulse only digitisation (POD) mode, the FPGA rejected baseline noise with a 1.5 mV threshold that each digitised sample of a PMT waveform was required to exceed in order to be saved in the data acquisition (DAQ) computer. In the second data stream, the individual PMT channels

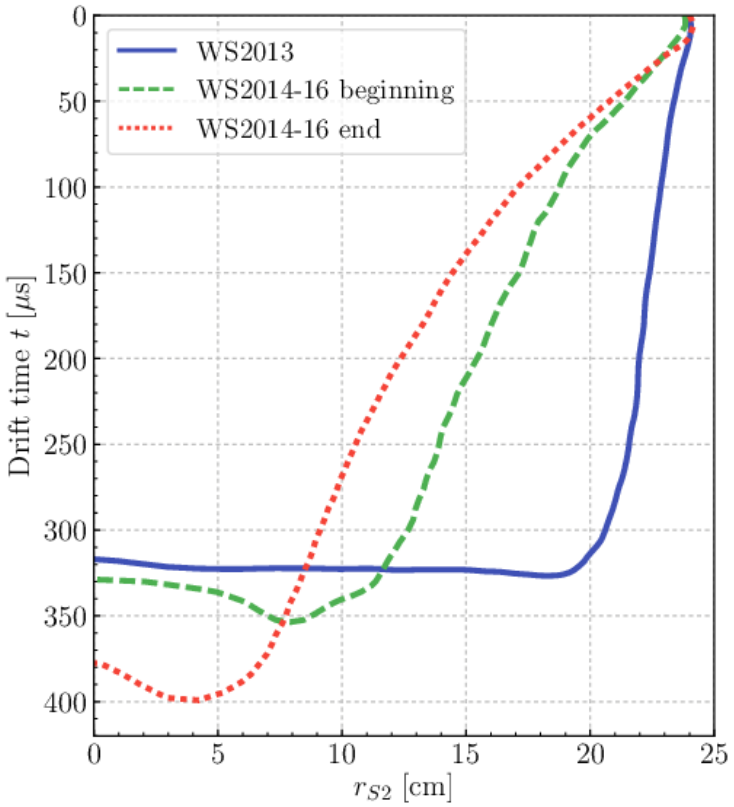

Figure 2.8: Radial coordinate and drift time of the edges of the TPC in WS2013 and WS2014 as reconstructed from ^{83m}Kr calibration data. The radial coordinate is calculated from the pattern of electroluminesence in the top PMT array (r_{S2}). Figure from [90].

were summed into 16 groups before being sent to a trigger system with two internal filters. Acting as integrators, the filters produced responses proportional to the area of input pulses. The first filter was tuned to the shape of $S1$s and the second to the shape of $S2$s [92].

Offline software was used to build distinct events from digitised waveforms occurring within a specified window surrounding a trigger pulse. The software could be used in trigger modes accepting events based on $S1$ information, $S2$ information, or a combination of both. In WS2013 and WS2014-16, the trigger software used $S2$ information [92, 93]. An example of a distinct event is provided in Fig. 2.11.

Data Processing Framework

The LUX DPF accepts digitised waveforms that have been sorted into distinct events and calculates a set of approximately 400 RQs. A schematic of the DPF modules is shown in Fig. 2.12, and the function of each module is summarised in the bullet points below [88].

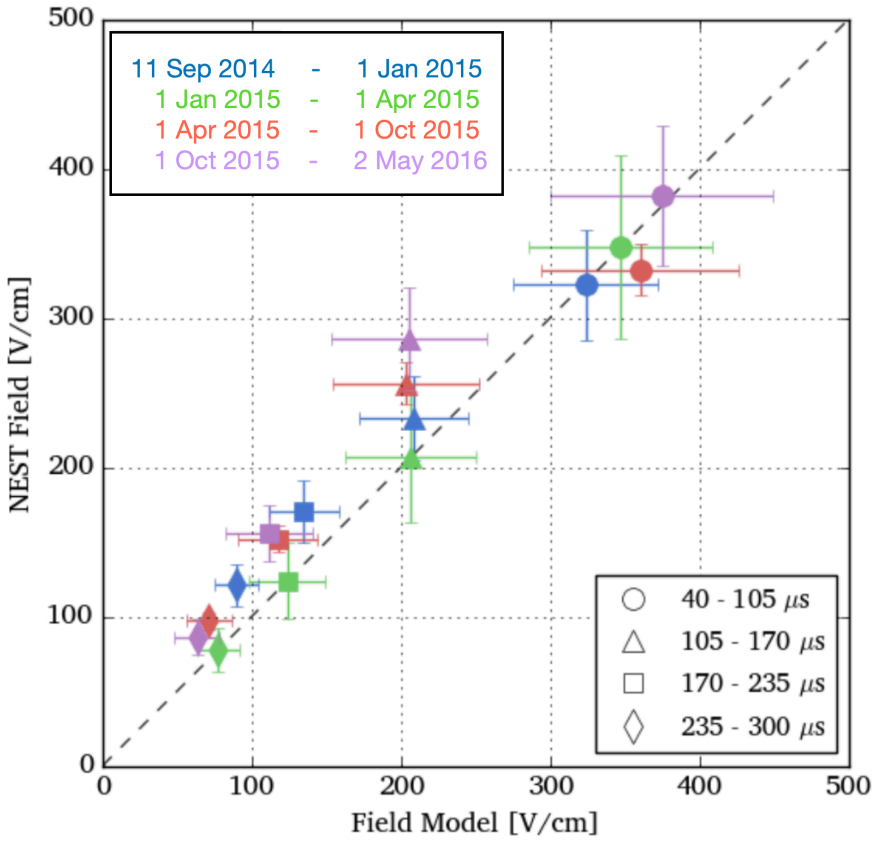

Figure 2.9: Average electric field magnitude within four drift-time bins and four date bins occurring throughout WS2014-16. The horizontal axis has values calculated using the COMSOL Multiphysics software package. For comparison, the vertical axis has values calculated using the Noble Element Simulation Technique (NEST) to predict the response of the detector to radioactive decays, discussed later in the chapter. Figure from [90].

- *Initialization* of RQ files.
- A PMT *signal calibration* converting from mV to photons detected (phd) per 10 ns sample.
- A *pulse finding* algorithm that selects up to 10 pulses in an event and returns start and end times for those pulses. The algorithm prioritises a combination of the largest pulses in an event and those appearing before the very largest pulse of an event.
- A *pulse feature reduction* routine that returns RQs calculated solely from the pulse waveforms. For example, there are: integrated area, metrics of rise time and width, and times at which the pulse reaches x% of its total area.

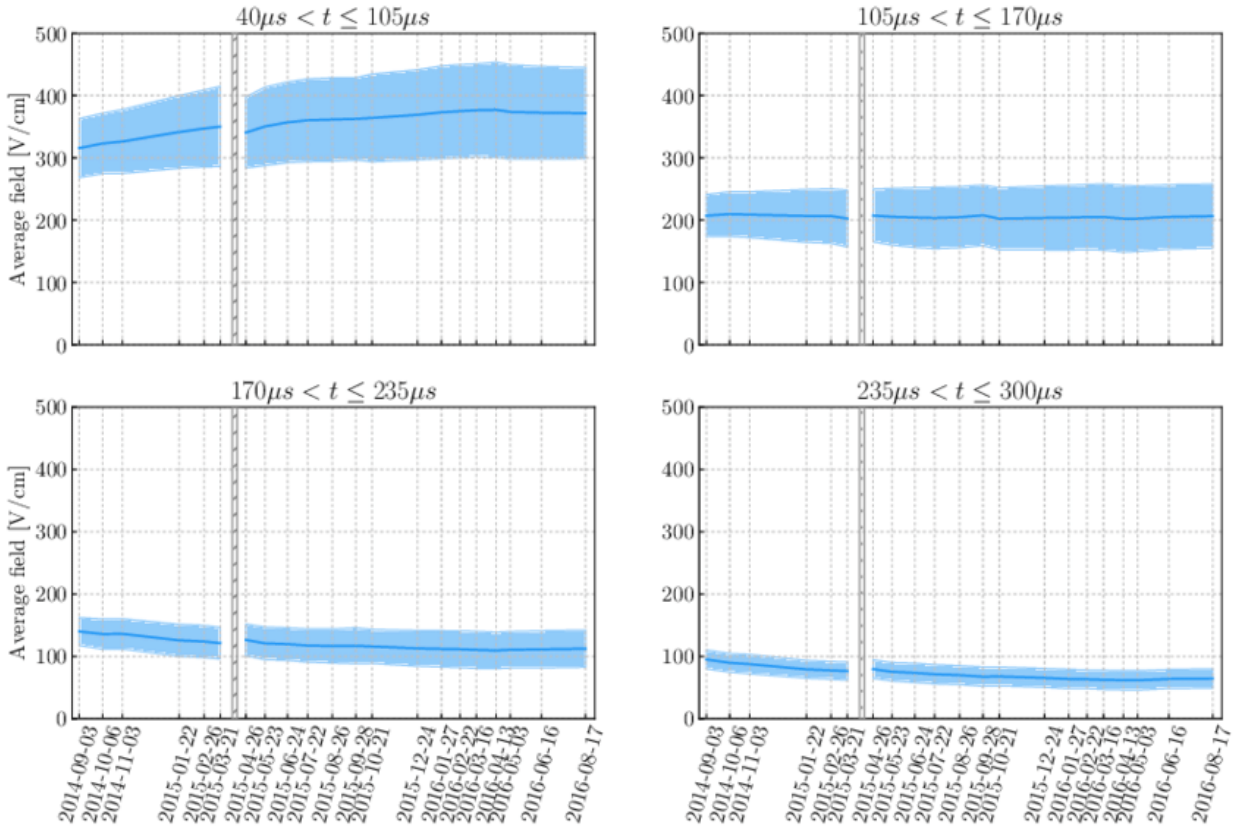

Figure 2.10: Time dependence of the average electric field magnitude within four drift-time bins throughout WS2014-16. Figure from [90].

- A *pulse classification* algorithm that labels each pulse as a: single photoelectron (SPE), $S1$, single electron (SE), $S2$, or *Other*. The algorithm begins by dividing pulses into $S1$-like or $S2$-like categories using RQs that quantify differences in pulse shape. $S1$s are much thinner, have a much shorter rise time, and are asymmetric compared to $S2$s. There is also a cut on the asymmetry in light collected by the top and bottom PMT arrays. Since electoluminesence occurs very high in the detector, above the liquid surface, $S2$s have a greater fraction of light in the top PMTs. Additionally, there are threshold cuts defined to separate SPEs and SEs from $S1$s and $S2$s, since these small pulses are usually backgrounds. $S1$s are required to have a two PMT coincidence to distinguish them from thermionic PMT dark counts and PTFE fluorescence photons (discussed in further detail in the context of backgrounds). $S2$s are required to have an area of > 33 phd to distinguish them from rogue single electrons from a variety of sources discussed in chapters 3 and 7. The cut was chosen to be $1 \cdot \sigma$ above the average area of a single extracted electron in WS2013: 24.5 phd. Finally, *Other*

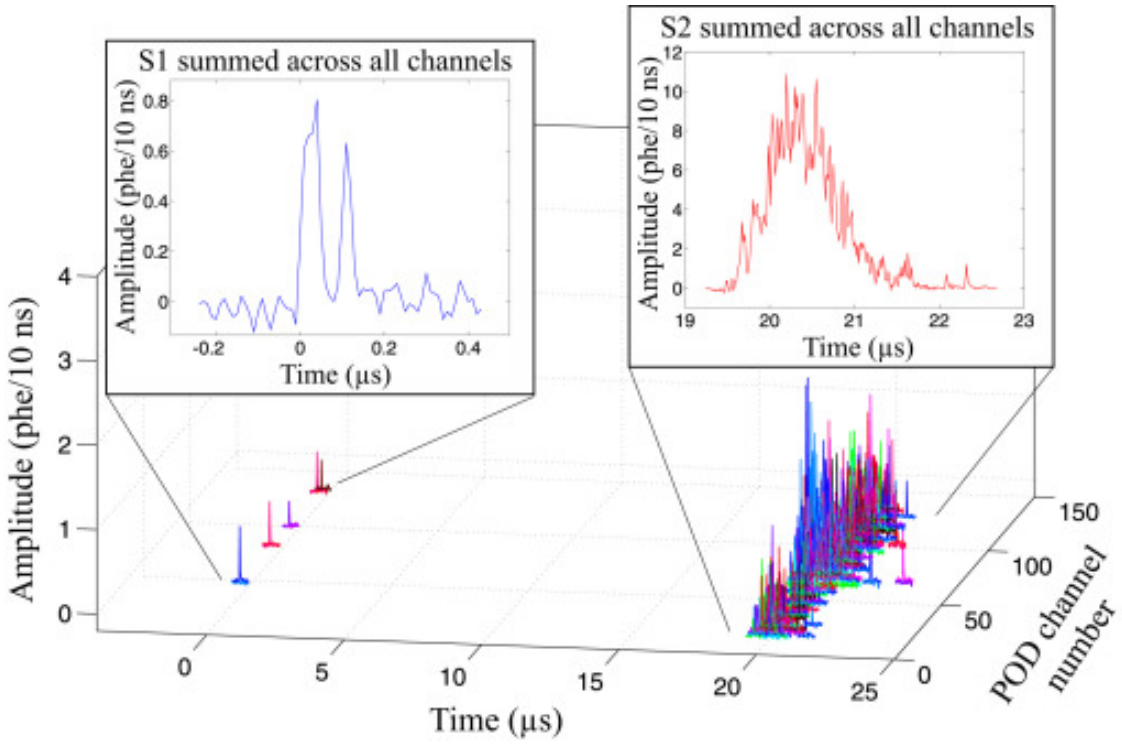

Figure 2.11: The PMT waveforms of a 1.5 keV$_{ee}$ event and their sum. Figure from [92].

pulses are divided from the first four categories with a similar combination of RQ cuts.

- An *event classification* algorithm that separates single scatters with one $S1$ succeeded by one $S2$ from other interaction patterns, for example γ-ray multiple scatters with one $S1$ succeeded by multiple $S2$s. Most hypothetical types of dark matter would scatter at most once while traversing the xenon, due to their small cross section with normal matter, while the LUX data contains numerous multiple scatter backgrounds as discussed later in this section.

- A *position reconstruction* routine that calculates the (x_{S2}, y_{S2})-coordinates of an interaction using the pattern of electroluminesence detected in the top PMTs. It employs the Mercury algorithm which iteratively calculates PMT light response functions from estimates of the position of photon emission until a maximum likelihood convergence condition is met [94].

- A routine that calculates $(x_{S2}, y_{S2}, t_{drift})$ dependent *detector response corrections* to the areas of $S1$ and $S2$ pulses using the ^{83m}Kr calibration data as discussed later in the section. Hereafter, the uncorrected areas are represented with variables $S1$ and $S2$, and the corrected areas with $S1_c$ and $S2_c$.

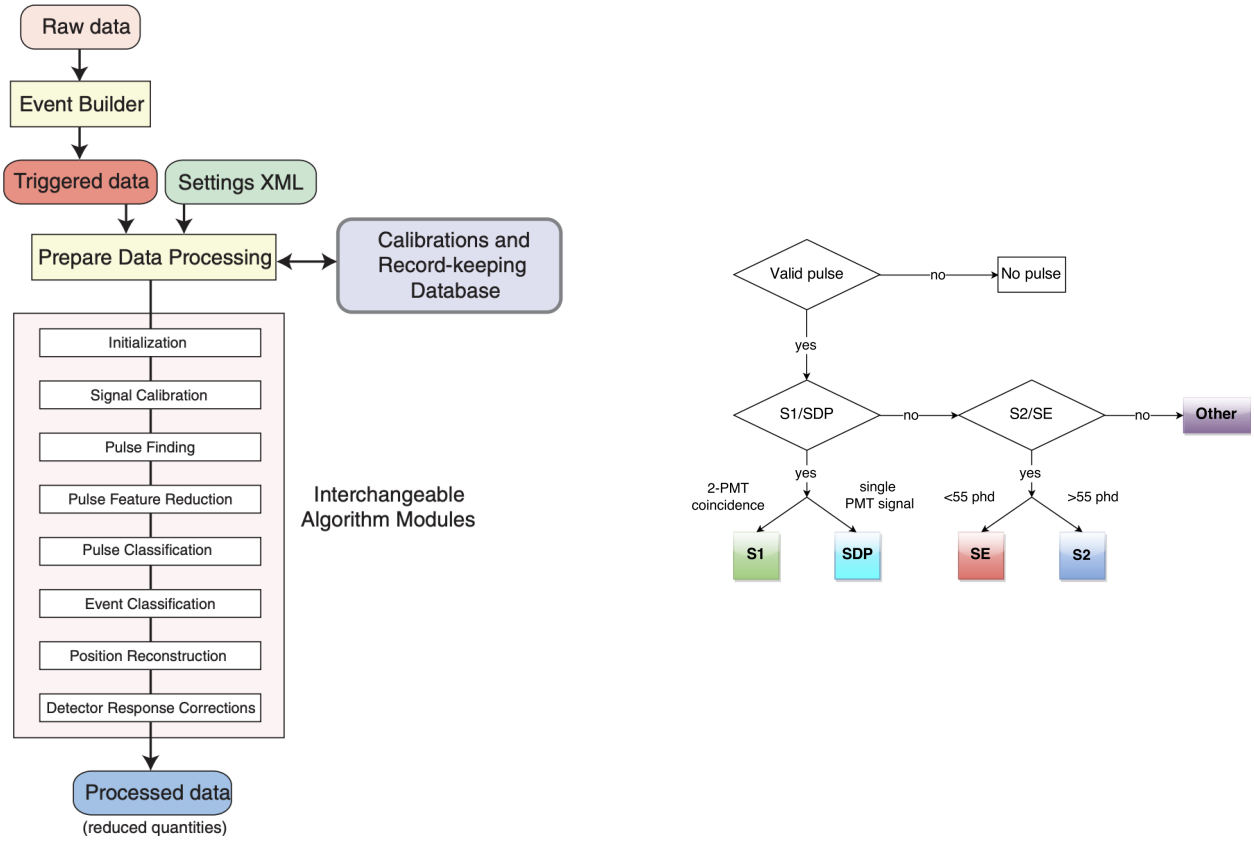

Figure 2.12: Left, schematic depicting modules in the LUX data processing framework. Right, diagram of logic programmed into the version of the event filter used in WIMP analyses. Figures from [88].

Filter

The LUX filter iterates through the output of the DPF to consolidate events based on the results of the event classifier. Additionally, it pairs down the number of RQs leaving only those useful to higher level analyses. If a user were to request single scatter events, the filter would return an n-tuple containing a subset of RQs from events with just one $S1$ and one $S2$.

A second job of the filter is to correct mistakes made by the event classifier due to neglect of "secondary processes" that create small, incidental $S1$s and $S2$s in addition to those from a primary interaction. An example would be the photoelectric effect of scintillation light on the gate causing emission of electrons that produce a small $S2$ shortly after an $S1$. The intensity and size of secondary $S1$s and $S2$s increases with the energy of the primary interaction; consequently, the filter employed an algorithm that depended on energy. The version of the algorithm used for the WIMP search analyses, extending up to ~ 10 keV$_{ee}$,

contained the single scatter definition shown in Fig. 2.12. It reclassifies $S2$s with < 55 spikes in their pulse waveform as SEs [88] (note that spike count is simply an alternative method of measuring pulse size sometimes used in place of area in sparse pulses). Chapter 3 extends this definition to the total range of interaction types and energies observed in LUX.

A final job of the filter is calculating the electric field corrected position coordinates (x, y, r, and z) used by some analyses of the WS2014-16 dataset.

Calibrations

The LUX collaboration carried out a myriad of calibrations used to exactly characterise the $S1$s and $S2$s observed in WS2013 and WS2014-16. This subsection summarises four overarching categories of calibrations: PMT, detector response corrections, energy reconstruction, and light/charge yield.

Photomultiplier Tubes

The Hamamatsu R8778 PMTs are characterised by a photon detection efficiency (DE) and gain. DE is a product of the quantum efficiency ($QE = \frac{\#\,of\,emitted\,photoelectrons}{\#\,of\,incident\,photons}$) and collection efficiency of photoelectrons on the first dynode (CE). The QE encompasses probabilities of four processes: (1) photon transmission through the quartz window, (2) photon absorption by the photocathode resulting in production of an electron, (3) diffusion of the electron toward the vacuum, and (4) conveyance of the electron across the potential barrier at the photocathode-vacuum interface. It depends on the incident photon wavelength and angle as well as temperature and quality of the window material, since electrons scatter off lattice imperfections and phonons. The overall gain is a product of the PMT gain and analog amplification. The former is the number of electrons observed at the end of the dynode chain for every photoelectron emitted into the vacuum, tuned by raising and lower the differential voltage between the photocathode and anode. It can be given in apparent units of electrons per photoelectron, or area of a pulse generated across a 50 Ω resister used to measure high frequency signals from the anode. The analog amplification is determined by the properties of pre- and post-amplifiers located between the PMTs and analog to digital converters. Table 2.2 summarises typical magnitudes of each calibration effect for ~ 175 nm scintillation/electroluminesence photons at normal incidence to a LUX PMT at cryogenic temperatures.

The LUX collaboration performed multiple measurments of every PMT's DE and gain during both the construction and operation phases of the experiment. Before installing PMTs in the detector, calibrations were performed in a dedicated external setup using 430 nm photons from a light emitting diode (LED). DE and PMT gain were also periodically monitored in situ with a system of 12x 430 nm LEDs. The LED results were corroborated with measurements using $\sim$ 175 nm scintillation/electroluminesence photons produced during tritiated methane and ^{83m}Kr calibrations (discussed in the next subsection) [88].

Effect		Magnitude	Citation
DE	QE	$33 \pm 2\%$	[95]
	CE	$\sim 90\%$	[87]
Gain	PMT Gain	3.3×10^6 (13 mV·ns)	[92]
	Analog Amplification	11.6 (151 mV·ns)	[92]
DPE		17%	[96]

Table 2.2: Typical magnitudes of LUX PMT calibration effects for $\sim$ 175 nm scintillation/electroluminesence photons incident on a PMT at cryogenic temperatures. The QE value listed here was measured by the manufacturer at normal photon incidence.

PMT calibrations can be performed in units of photoelectrons (phe) or photons detected (phd). The difference between the two units is a consequence of the double photoelectron effect (DPE) whereby photons incident on PMT photocathodes eject two photoelectrons into the vacuum instead of just one [97, 98]. Figure 2.13 points out single and double photoelectron distributions in the spectral response of a Hamamatsu R11410 PMTs (those selected for use in the LZ TPC) to 175 nm photons. LUX takes this double photoelectron effect into account by using units of phd to measure $S1$ and $S2$ pulse areas. Figure **??** shows a measurement of DPE probability versus photon wavelength for the PMT models used in LUX and LZ. A 175 nm photon incident on a LUX Hamamatsu-R8778 PMT will cause emission of two photoelectron with a probability of 18%—normalized to the total number of photons that cause an emission of any type.

Detector Response Corrections

There are effects that cause the detection efficiency for individual scintillation photons and freed electrons, thus the size of $S1$s and $S2$s, to vary with position of an interaction in the TPC. Scintillation photons can reflect on the internal or external surface of the liquid, encounter impurities in the xenon, and come in contact with absorptive components of the TPC such as the grids. Furthermore, the refractive index of the PMT windows is more similar to that of liquid xenon than gaseous xenon, causing the average QE of the bottom PMTs to be greater than that of the top PMTs. The combined result of these effects is that $S1$s from the bottom and radial center of the detector are larger than those at the top and sides. Similarly, electrons travelling through the xenon can encounter and sometimes become captured by an impurity. The probability of such an occurrence increases with time spent drifting through the xenon as described by $P = e^{-t_{drift}/\tau_e}$, where τ_e is the purity dependent lifetime of a drifting electron. Furthermore, deflection of the gate wires toward the anode wires, due to the force of E_{ext}, can cause the EE to vary over the (x_{S2}, y_{S2})-plane, most notably with the radial coordinate. These effects—in addition to all those described for scintillation photons since electroluminesence photons also encountered such effects—cause

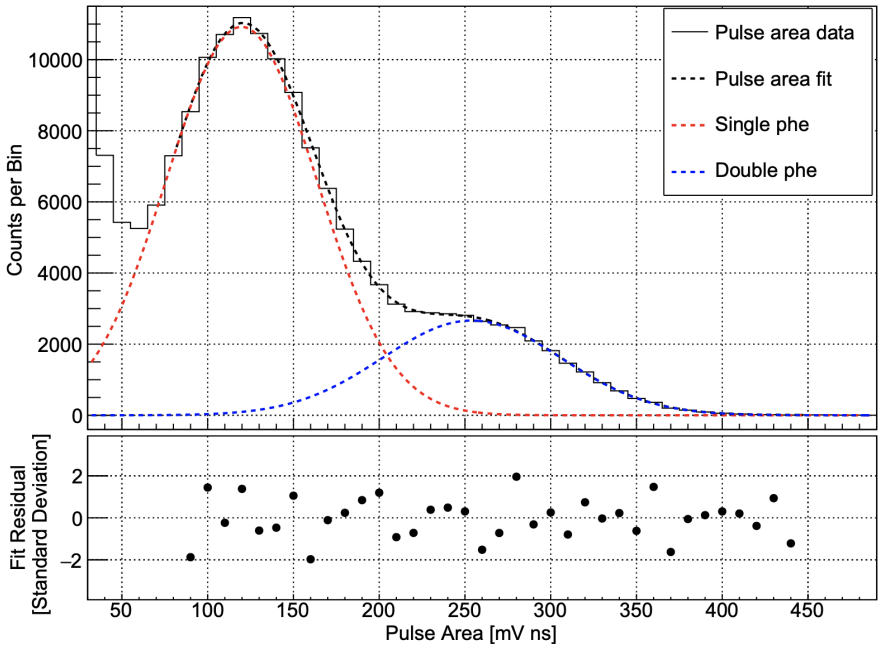

Figure 2.13: Spectral response of a Hamamatsu R11410 PMT to 175 nm photons. The fit to the data accounts for the probabilities of one or two photoelectron emission into the PMT vacuum. Figure from [97].

$S2$s from the top and radial center of the detector to be larger than those at the bottom and sides. Fig. 2.15 depicts the trends described in this paragraph.

Position dependent pulse area corrections were calculated using data from biweekly ^{83m}Kr calibrations. This source was injected from a containment system holding charcoal laden with its longer lived parent isotope ^{83}Rb (half-life of 86 days). Because krypton is a noble element with similar inter-molecular forces to those of xenon, the ^{83m}Kr rapidly dissolves itself throughout the liquid and gas in the TPC [99]. Its short half-life, 1.83 hr, and relatively high decay energy, 41.56 keV, prevented it from becoming a background in the lower energy WIMP search analysis. Consequently, it was possible to perform high rate 10–100 Bq injections necessary to derive corrections while in the midst of taking WIMP search data.

Fig. 2.16 shows the qualitative improvement in $S1$ and $S2$ resolution obtained by applying position dependent pulse area corrections. $S1$s were normalised to the center of the TPC with corrections computed from three dimensional maps of ^{83m}Kr $S1$ area, like that shown in Fig. 2.15. $S2$s were first scaled for the effect of electron lifetime using a correction calculated from plots of ^{83m}Kr $S2$ area verses t_{drift} before applying a second correction normalising pulses to the center of the (x_{S2}, y_{S2})-plane. The original $S1$ and $S2$ distributions are shown in blue, the t_{drift} corrected versions are shown in red, and the (x, y, t_{drift}) versions are shown in black. Figure from [99].

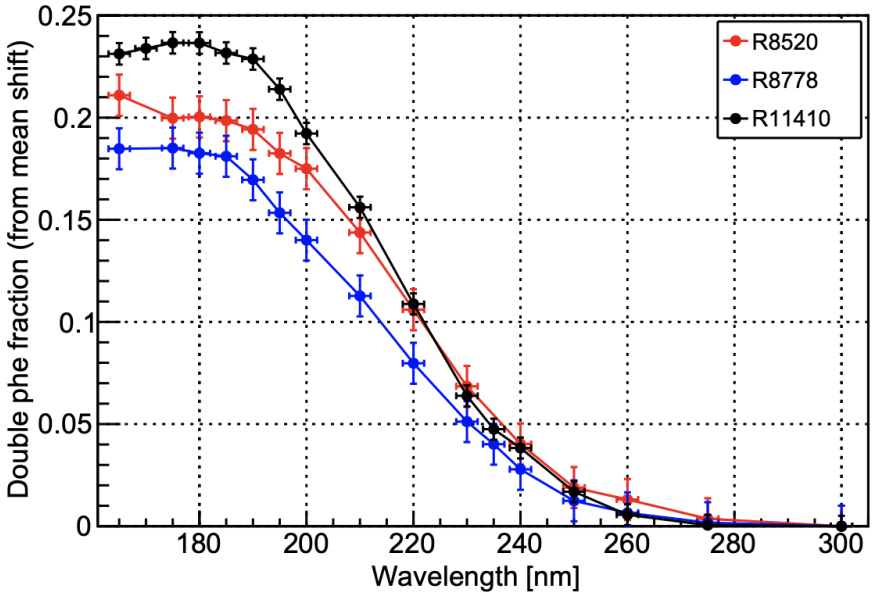

Figure 2.14: Double photoelectron (DPE) probability for three models of PMTs used in LUX and LZ. Figure from [97].

In WS2014-16, calculation of the pulse area corrections was complicated by the highly position dependent electric field observed in the TPC during this time. In addition to the $S1$ and $S2$ size variation from the aforementioned detection efficiency effects, which the corrections are designed to mitigate, there is inherent variation caused by electric field dependence of recombination, i.e. n_γ and n_e. The latter effect was detangled from the former by exploiting the two-step decay scheme of ^{83m}Kr, shown in Fig. 2.17. First, ^{83m}Kr emits 32.1 keV in an internal conversion (IT) decay to a metastable state with 154 ns half life. It then emits 9.4 keV in a second IT to the ground state. Usually the short intermediate half life results in a single $S1/S2$ pair; however, a small, yet significant fraction of the time there are two $S1$s, $S1a$ and $S1b$ corresponding to 32.1 and 9.4 keV, respectively. In these instances, it is reasonable to assume the electrons/ions from the first decay have drifted sufficiently far away from the interaction site that they do not affect the microphysics of the second decay; specifically the amount of recombination occurring after each decay is representative of separate 32.1 and 9.4 keV events. The ratio $\frac{S1b}{S1a}$ should then rise in positions with higher electric field magnitude due to significant field dependence of recombination for interactions of energy > 10 keV$_{ee}$. If there were no field variation present, the ratio would be constant because detection efficiency effects would act on both pulses equally.

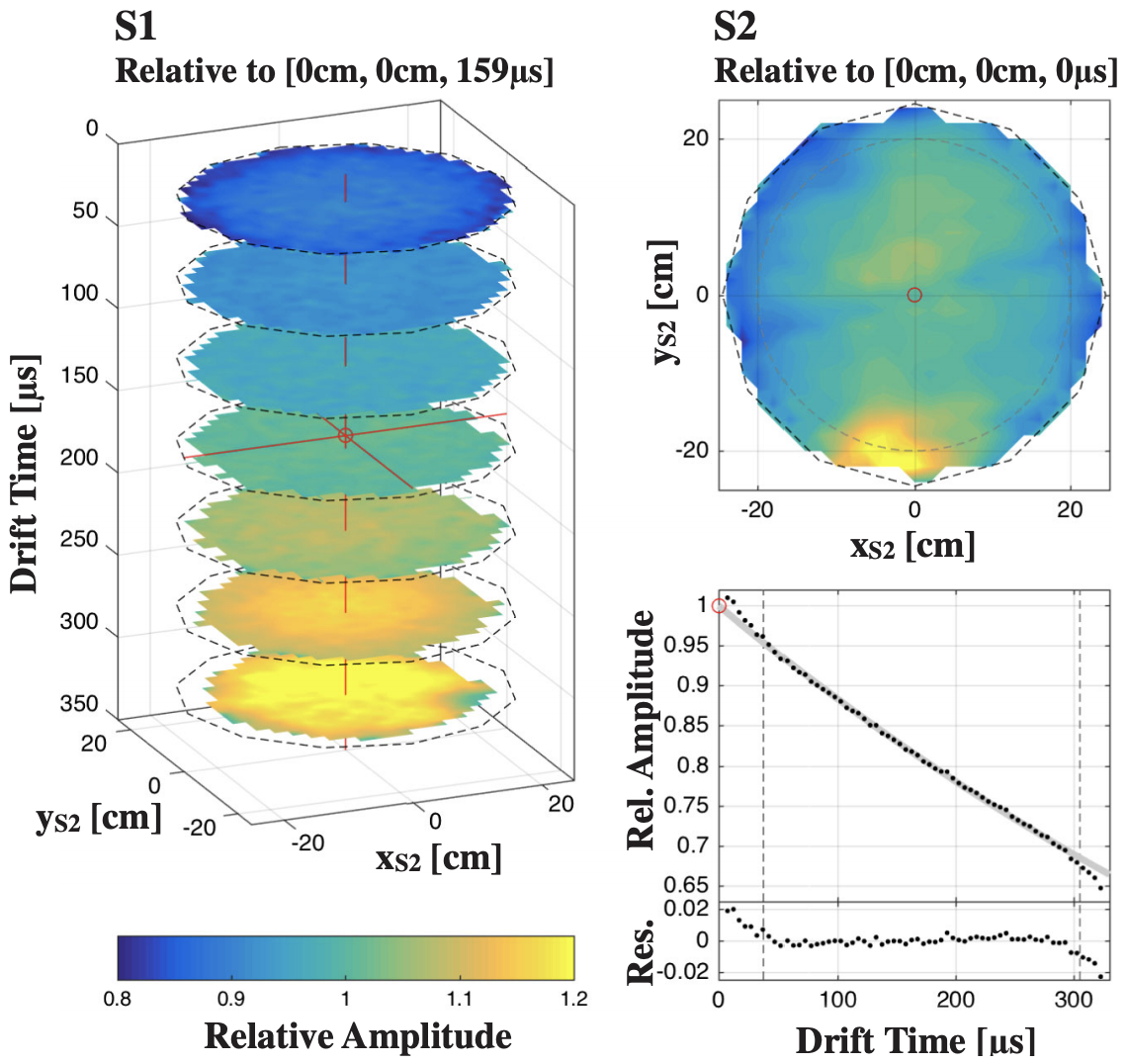

Figure 2.15: Position dependence of $S1$ and $S2$ amplitudes derived using ^{83m}Kr calibration data. Figure from [99].

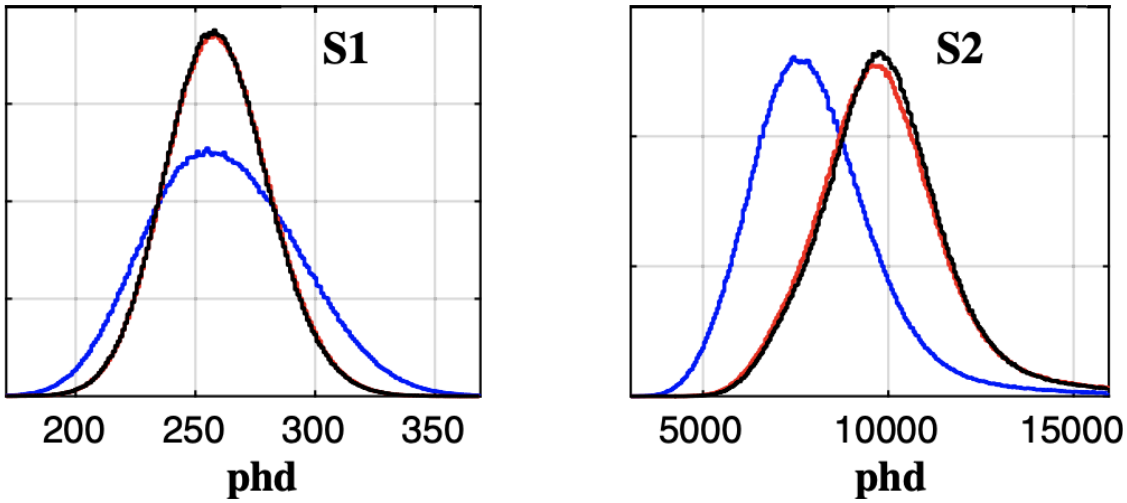

Figure 2.16: Qualitative improvement in $S1$ and $S2$ resolution obtained in WS2013 by applying position dependent pulse area corrections to ^{83m}Kr calibration data. Figure from [99].

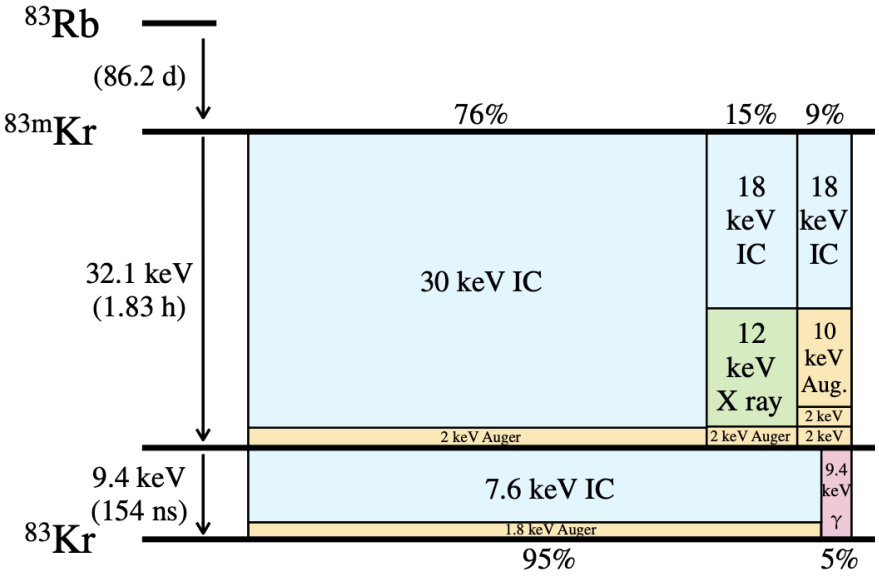

Figure 2.17: Two step decay scheme of ^{83m}Kr with intermediate metastable state of 154 ns half-life. Figure from [99].

Energy Reconstruction

In order to reconstruct the energy of interactions in dual-phase xenon TPCs, it is necessary to measure parameters g_1 and g_2 which appear in Equation 2.9. This task is generally accomplished using the "Doke" method in which Equation 2.9, is rewritten as

$$\frac{S1_c}{E_{ee}} = \frac{g_1}{W} - \left(\frac{g_1}{g_2}\right)\frac{S2_c}{E_{ee}} \tag{2.10}$$

a linear equation in variables $\frac{S2_c}{E_{ee}}/\frac{S1_c}{E_{ee}}$ entirely determined by parameters g_1/g_2 and quantity W, which is measured independently. The equation is fit to data from radiogenic decays with energies corresponding to distinct mean recombination fractions ($\langle r \rangle$), thus a variety of $\left(\frac{S2_c}{E_{ee}}, \frac{S1_c}{E_{ee}}\right)$ combinations.

In LUX WS2013, the Doke analysis data were selected from ^{83m}Kr and ^{137}Cs calibrations; ^{127}Xe, ^{131m}Xe, and ^{129m}Xe cosmic ray activated xenon isotopes; and γ rays emitted by ^{214}Bi contamination in the TPC components (summarized in Table 2.3). Fig. 2.18 shows the fit to these data used to determine $g_1 = 0.117 \pm 0.003$ phd/photon and $g_2 = 12.1 \pm 0.8$ phd/electron [88].

Table 2.3: Sources used in the WS2013 Doke analysis. The column "Energy" refers to the total decay energy or Q-value. The column "Feature" refers to the energy of corresponding features observed in the LUX data—sometimes different then "Energy" due to some decay products depositing energy outside of the active xenon volume.

Isotope	Event Type	Halflife	Energy (keV)	Features (keV)
^{83m}Kr	IT	1.83 h	41.6	41.6
^{127}Xe	EC	36.4 d	662	5.5/208/236/408
^{131}Xe	IT	11.8 d	164	164
^{129}Xe	IT	8.9 d	236	236
^{214}Bi	$beta^- + \gamma$s	19.7 m	3269	609
^{137}Cs	$beta^- + \gamma$s	30 d	1176	662

In WS2014-16, there were fewer sources available for the Doke analysis. The cosmic ray activated xenon isotopes had decayed away because of their short half-lives and the two highest energy decays (of ^{137}Cs and ^{214}Bi) were producing $S2$s large enough to saturate PMTs due to the higher EE occurring throughout this run. However, there were data from continued ^{83m}Kr calibrations and several deuterium-deuterium (DD) neutron beam calibrations which produced ^{129m}Xe and ^{131m}Xe as byproducts. The $\langle r \rangle$s of decays from these sources were not varied enough to tightly constrain a linear fit. Instead, it was necessary to exploit the dependence of $\langle r \rangle$ on electric field magnitude which, as discussed in the previous sections, varied significantly throughout the TPC during this run. This adapted Doke analysis, is the subject of Chapter 4.

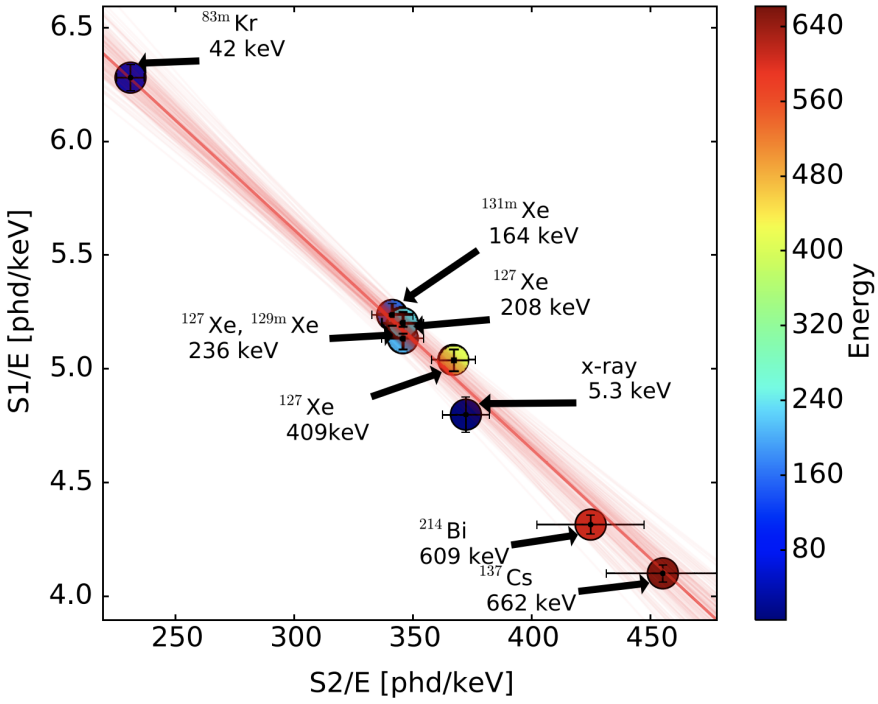

Figure 2.18: WS2013 "Doke plot" with linear fit used to calculate $g_1 = 0.117 \pm 0.003$ phd/photon and $g_2 = 12.1 \pm 0.8$ phd/electron. Figure from [88].

Light and Charge Yield

Light and charge yield (L_y and Q_y) are parameters that quantify the number of scintillation photons and electrons produced per unit energy transferred to a medium:

$$n_\gamma = L_y E \tag{2.11}$$
$$n_e = Q_y E. \tag{2.12}$$

Under the conditions observed in xenon dark matter experiments, L_y and Q_y vary primarily with the fraction of recombining ions which depends on interaction type (ER or NR), amount of transferred energy, xenon density, and electric field magnitude as described in Sec. 2.1. It is therefore necessary to calibrate ER and NR L_y/Q_y for the specific conditions observed in the LUX TPC at any particular point in time.

To this end, the LUX collaboration performed multiple L_y/Q_y measurements with several different calibration sources under a variety of detector conditions. Fig. 2.19 presents those relevant to Chapter 7 of this dissertation, low energy ER and NR Q_y measurements performed under detector conditions comparable to those present during WS2013. There are two ER calibrations performed using 0.186–33.2 keV ^{127}Xe and 1.3–17 keV tritiated methane data [100, 74], and a NR calibration performed using 0.7–74 keV DD neutron beam data [101].

Fig. 2.19 compares the results of these LUX calibrations with relevant measurements made by independent dual-phase xenon TPC experiments [102, 103, 104]. The black solid curves drawn in each plot are analytical models used by the Noble Element Simulation Technique (NEST) to predict Q_y given the exact conditions present during this run. NEST is discussed in further detail in the context of simulations, in the next subsection.

Backgrounds

Dual-phase xenon TPCs observe a variety of backgrounds that complicate searches for DM; however, this type of detector offers a set of mitigation strategies that can be used to eliminate the vast majority of these events. Those backgrounds and mitigation strategies relevant to LUX are described in the following sections.

Background Sources

LUX observed backgrounds from cosmic radiation [53]; radiocontamination of the laboratory environment, detector components, detector component surfaces, and xenon [107]; as well as accidental coincidences of rogue $S1$s and $S2$s [52]. These categories are detailed in the itemised points below.

- *Cosmic*
  - Galactic charged nuclei incident on the earth interact in the upper atmosphere producing a rain of secondary subatomic particles. Below the earths surface, the most abundant are muons and neutrinos; although, there are smaller numbers of nucleons, electrons/positrons, and pions [55]. In xenon, the *cosmic ray muons* continuously lose energy at rates of ∼MeV/cm through radiative processes—Bremstrahlung, photonuclear interactions, and e^+/e^- pair production—and elastic scattering on atomic electrons.
  - *Atmospheric neutrinos*, deposit ∼keV quantities of energy through coherent elastic scattering on xenon nuclei (CEνNS).
  - Distant core-collapse supernovae produce a glow of *diffuse supernova neutrinos* (DSN) which also deposit energy via CEνNS.
  - Nuclear fusion proton-proton (pp), ^{7}Be, and carbon-nitrogen-oxygen (CNO) reactions in the sun produce lower energy *solar neutrinos* that interact via neutrino-electron scattering. There are also ^{8}B and helium-proton (hep) reactions that produce higher energy neutrinos which interact via CEνNS.
- *Laboratory Environment*
  - Muon induced *electromagnetic and hadronic cascades in the water tank and rock walls* of the Davis cavern can produce neutrons energetic enough to travel the

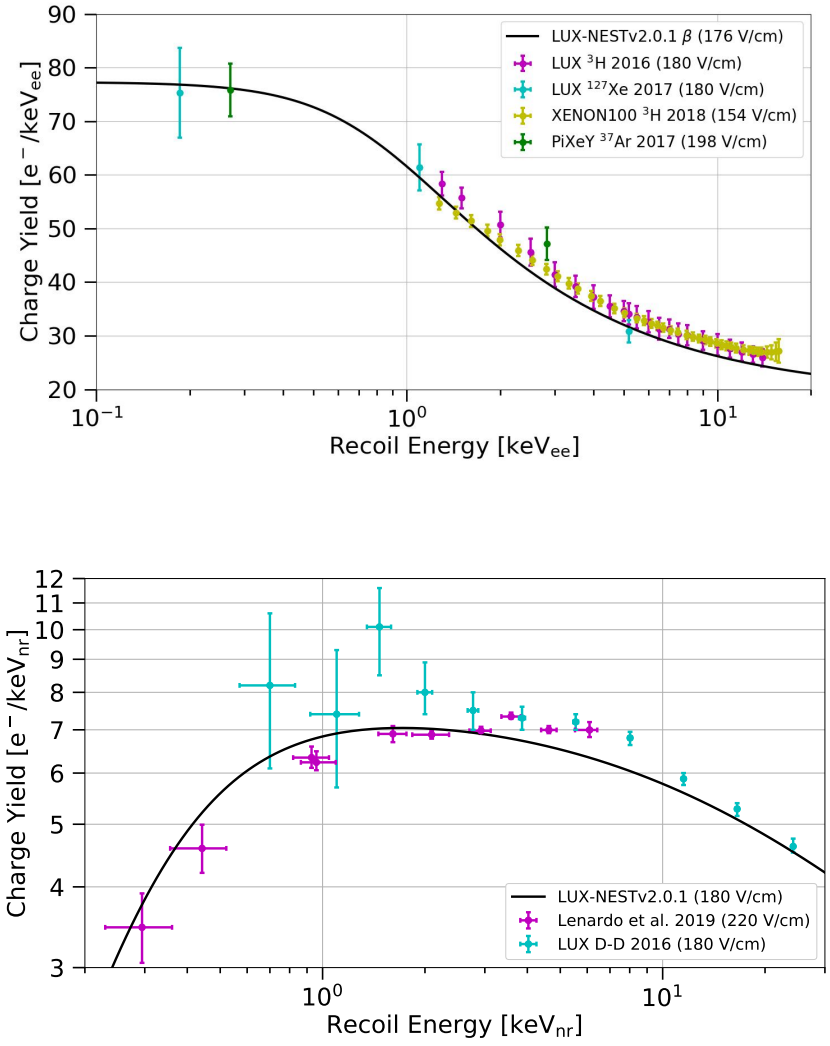

Figure 2.19: ER and NR charge yield (Q_y) measurements performed under detector conditions comparable to those present during WS2013. Data are from LUX publications [100, 74, 101] and independent dual-phase xenon TPC experiments [102, 103, 104]. The black solid curves drawn in each plot are analytical models used by the Noble Element Simulation Technique (NEST) to predict Q_y given the exact conditions present during this run [105]. Figure from [106].

distance through the rock wall and water tank into the TPC. These neutrons can elastically scatter on xenon nuclei one or multiple times depositing ∼keV quantities of energy.

- ^{238}U, ^{232}Th, and ^{40}K *radiocontaminates in the cavern walls* (primarily the shotcrete that covers the rock) can undergo β or electron capture (EC) decays to excited nuclear states that de-excite by emission of γ rays with energies extending up to ~ 2614 keV [108]. The can also undergo α decays that interact with surrounding nuclei through (α, γ) reactions. Those energetic enough to travel into the TPC can interact one or multiple times via Compton scattering and photoconversion on xenon atomic electrons, or e^+/e^- pair production in the xenon atomic and nuclear electric fields. Each interaction transfers all or part of the γ rays energy to the xenon resulting in a spectrum of ERs in range 0–2614 keV.

- *Detector Components*

  - ^{238}U, ^{232}Th, and ^{40}K *radiocontaminates in the detector components* produce additional ERs. Because the detector components are much closer to the active xenon volume than the cavern walls, and not shielded by water, they are a much more significant source of backgrounds. Fig. 2.20 plots the simulated spectrum of events from these sources and the observed spectrum of events for comparison.
  - Some of the ^{238}U and ^{232}Th daughters decay by emission of an α particle. As a consequence, ^{238}U and ^{232}Th contamination in the reflective panels can produce neutrons through $^{19}F(\alpha,n)^{22}Ni$ *interactions in the PTFE*. The outgoing neutrons will deposit ∼keV quantities of energy via single or multiple coherent scatters on xenon atoms.
  - While the LUX detector was being built above ground, neutron cosmic rays *activated components* through ^{63}Cu(n,α)^{60}Co and ^{46}Ti(n,p)^{46}Sc scattering processes. Both ^{60}Co and ^{46}Sc have 5.3 year and 84 day half-lives which are long enough to ensure these isotopes were still present after the detector was installed underground. They each β decay to an excited nuclear state that de-excites through emission of 1173 and 1332 keV or 889 and 1120 keV γ rays, respectively.

- *Detector Component Surfaces*

  - During construction, LUXs components, including the reflective panels and grids which contacted the active volume, were exposed to air containing typical (undoors, 100–1000 Bq/m^3 [109]) quantities of ^{222}Rn. This isotopes daughters precipitated onto the uncovered surfaces in a process called *radon daughter plate-out*. Afterwards, the short-lived daughters quickly decayed away leaving only ^{210}Pb, with a 22-year half-life, and its two daughters, ^{210}Bi and ^{210}Po. ^{210}Pb and ^{210}Bi β decay emitting a set of photons and electrons with energies up to their Q-values of = 63.5 and = 1162 keV. Each individual decay product has some probability

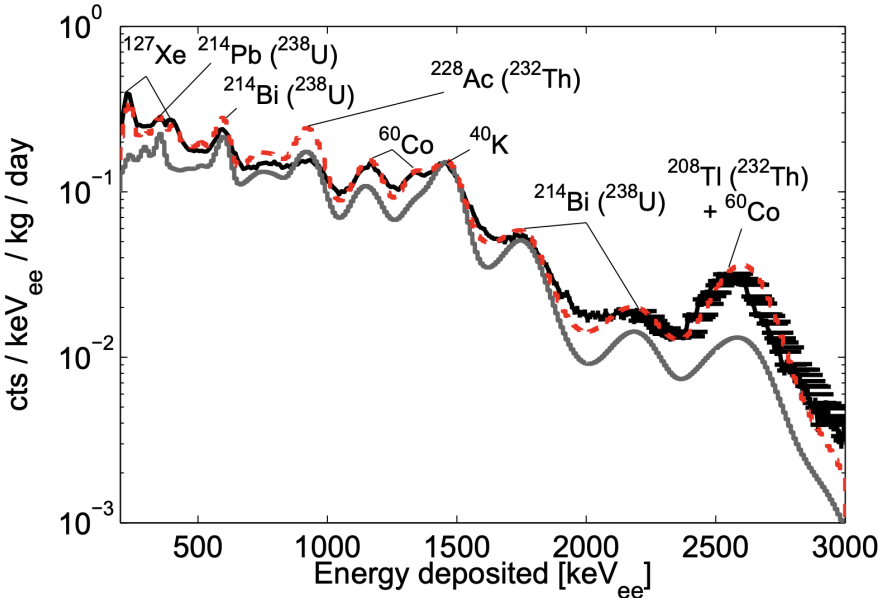

Figure 2.20: Spectrum of γ ray events from ^{238}U, ^{232}Th, ^{40}K, and ^{60}Co contamination of the detector components simulated at activities measured during assays of the component materials or predicted from cosmic ray exposure above ground (solid grey). The observed spectrum of events in the TPC is shown for comparison (black), along with the result of fitting the simulated spectrum to the data (dashed red). Figure from [107].

of travelling away from its surface of origin into the xenon where it will produce an ER. ^{210}Po decays by emission of an α particle after which either the recoiling ^{206}Pb daughter nucleus or α particle can travel into the xenon. The ^{206}Pb nucleus will deposit energy in a manor very similar to that of xenon NR, thus will produce a similar $S2/S1$ ratio, while α recoils will produce many more photons compared to electrons and lose less energy to heat.

- Radon daughter plate-out on the reflective panels produces additional $^{19}F(\alpha,n)^{22}Ni$ *interactions from* ^{210}Po *on the surface of the PTFE.*

- *Xenon*
  - ^{238}U/^{232}Th atoms in the detector components decay through long chains of daughters of which one is ^{220}Rn/^{222}Rn. These isotopes can emanate from the components and become absorbed in the xenon due to their similar inter atomic forces, both being noble elements. The *absorbed radon* and its daughters travel with the xenon through the circulation system, which includes a getter that removes some but not all of the contamination, into the TPC where their β and α decays produce backgrounds.

- Upon receipt, the LUX xenon contained 130 ppb g/g natural krypton which was independently estimated to have 2×10^{-11} g/g concentrations of ^{85}Kr, an isotope which β decays emitting an electron with energy up to its Q-value of 687 keV. Although LUX passed the xenon through a krypton removal system prior to it being shipped to SURF, the ^{85}Kr remained in the xenon in small concentrations during operation. Additional small amounts leaked into the xenon from the PTFE.
- LUX data revealed an unanticipated background from ^{37}Ar, an isotope that can be produced from spallation of xenon atoms. It decays via EC emitting photons and electrons out to 2.8 keV [2].
- While above ground, the xenon was exposed to a flux of secondary cosmic rays great enough to produce significant quantities of *activated xenon isotopes*: ^{127}Xe, ^{133}Xe, ^{129m}Xe, and ^{131m}Xe. Furthermore, DD neutron generator calibrations produced additional isotopes ^{125m}Xe, ^{129m}Xe, and ^{131m}Xe of which ^{125m}Xe decayed to ^{125}Xe then ^{125}I. The set of activated xenon isotopes undergo EC, β, isomeric transition (IT) decays that emit photons and electrons with energies out to 427 keV, the Q-value of ^{133}Xe.

- *Isolated $S1s$ and $S2s$ Contributing to Accidental Coincidences*
  - During WS2013, the PMTs had an average, in situ single photoelectron rate of $\sim$ 11 Bq [96]. These pulses are phenomenologically consistent with thermionic dark counts from the PMT photocathode and fluorescence of the reflective panels occurring after xenon luminescence photons are absorbed by the PTFE [96, 111]. If *single photoelectrons* were to appear in two or more PMTs at once, the resulting pulse waveform would pass the two PMT coincidence threshold defined in the pulse classification algorithm and the DPF would identify it as an $S1$.
  - The electric field in the region between the cathode and bottom shield grid points upward causing electrons in this region to drift downward away from the vapor where they would otherwise produce electroluminesence, thus $S2$s. However, scintillation photons emitted in this region are detected with a similar efficiency to those in active volume, thus usually do produce $S1$s. These *reverse field $S1s$* have a wide range of sizes determined primarily by the amount of energy deposited by radioactive decays in this region and in nearby components.
  - The density of the xenon vapor at the top of the TPC is a factor of 100–200 less than that of the liquid (according to the Antoine equation for xenon [112]), thus photon mean free paths in this region are 100–200 times greater than those below the surface. Often times, this disparity causes photons produced at the top of the detector to travel entirely through the vapor, but interact shortly after passing the liquid surface. Electrons from these events are almost immediately extracted

[2] ^{37}Ar contamination is of special interest to near-future experiments, because it is a viable explanation for the XENON1T low-energy excess [110].

causing electroluminsence to be produced only 0–100 ns after scintillation. The resulting waveforms usually contain completely or partially overlapping scintillation and electroluminesence signals which are grouped by the pulse finding algorithm into a single pulse that is labelled an $S2$ by the pulse classification algorithm. These *liquid surface* $S2s$ have a wide range of sizes determined primarily by the energy of photons emitted in atomic de-excitation processes within the vapor, and radioactive decays in the vapor and nearby components.

- Electron emission by cathodic electrodes, such as the gate and cathode, has been observed in LUX and other dual-phase xenon TPCs [113, 114, 111]. This mechanism produces a substantial rate of few electron $S2$s.
- Radioactive decays on and within the grid wires generate scintillation photons and free electrons very close to the wire surfaces. A significant fraction of the photons are absorbed by the wire generating isolated $S2$s and, because 84% of field lines around cathode wires arch toward the bottom shield grid [106], electrons near the cathode surface often travel downward generating isolated $S1$s. The range of sizes of these pulses is determined by the energy spectrum of decay products of ^{210}Pb/^{210}Bi/^{210}Po surface contamination and ^{238}U/^{232}Th contamination inherent to the grid wires.
- Radiocontamination on and within the reflective panels surrounding the detector generates *isolated wall* $S1s$ in a manner similar to events originating on or within the cathode. The electrons from these events can become trapped on the panel surface as they drift due to the electron affinity of the PTFE. The scintillation photons often travel into the central xenon volume or are reflected by the PTFE in this direction.

Learning from experience with the LUX, the LZ collaboration was able to significantly improve its backgrounds. Some of the most significant improvements were in reducing the fixed contamination levels in the PMTs and the titanium cryostat. Additional reductions were obtained in stainless steel components and in all of the welded components. During assemble of the TPC, LZ rigorously control surface deposition of radioactivity with strict cleanroom protocol and the use of radon-reduced air. Surface deposition on insulated parts were reduced with deionizing fan-filter units. These improvements are presented in [115].

Background Mitigation Strategies

The LUX DM search was optimised by installing infrastructure and employing analysis techniques that minimised backgrounds. The most crucial were detector shielding and event rejection based on the number of $S1$s and $S2$s, energy, position, and $S2/S1$ ratio described in [87, 63, 64, 52]. These background mitigation strategies are summarised in the numbered points below.

- *Shielding*

  - The LUX detector was installed in the Davis Cavern at SURF which is 4850 feet below the earths surface, 4.3 kilometers water equivalent. At this *underground location*, the cosmic ray muon flux is reduced by a factor of $\sim 10^6$ [107]; and nucleon, electron/positron, and pion cosmic rays are practically non-existent.
  - The 300 tonne *water tank*, and a 20 tonne steel pyramid placed below the tank, act as passive shielding against neutrons and γ rays produced in the rock walls of the cavern. These structures reduce the neutron flux by a factor of ~ 100 and the γ ray flux by a factor of $\sim 10^{10}$ [107].

- *Event Rejection*

  - Small, weak scale cross sections close to guarantee WIMPs would scatter only once in the xenon before travelling out of the detector. This is unlike many radiogenic decay products which have higher cross sections causing them to frequently scatter multiple times: for example, there are muons, γ rays, and neutrons. By applying a basic *single scatter cut*, requiring waveforms contain at most one $S1$ succeeded by one $S2$, many of these backgrounds can be rejected.
  - WIMP scatters produce xenon atom recoils with energy of a few keV. Although γ rays, β decays, α decays, and muons produce some events within this energy range; they produce many more at $\sim$MeV scales that can be rejected with an *energy cut*. A WIMP search energy range of approximately 1.1–40 keV$_{nr}$ removes the majority of these backgrounds.
  - Xenon's high density, $\sim$3 g/cm^3, causes most γ rays from external sources to interact within centimeters of entering the xenon. Furthermore, radon daughter plate-out backgrounds are sequestered to the surfaces of components, for example the reflective PTFE panels and the gate/cathode. As shown in Fig. 2.21, this attenuation causes the background rate near the edges of the xenon to be a factor of 10^2–10^4 greater than in the center. An approximately cylindrical fiducial volume cut can be used to select a low event rate region at the center of the TPC.
  - ERs, such as those produced by γ ray and β decay backgrounds, produce relatively fewer scintillation photons and more free electrons than DM NRs for a given observed signal size. In the graphical space defined by $\frac{S2}{S1}$ and $S1$, the result is a distinguishable ER band appearing above a NR band, as outlined in Fig. 2.22. 99.6% of ER backgrounds could be removed by requiring events fall below the 50% chord of the NR band. This cut could also be used to remove accidental backgrounds which, by nature, do not follow ER or NR bands. In general, *ER/NR discrimination* is performed within the profile likelihood ratio (PLR) statistical analysis used to search for DM, since it compares predicted DM signal distributions in $S1$, $S2$, and other parameters to the observed data.

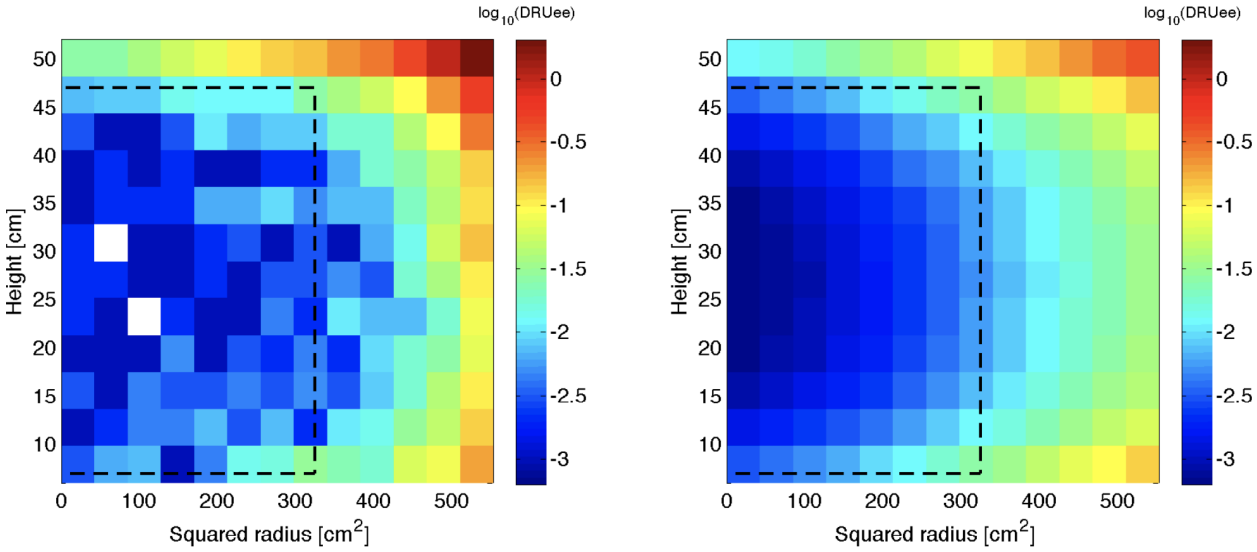

Figure 2.21: ER background events in the range 0.9–5.3 keV. Figure from [107].

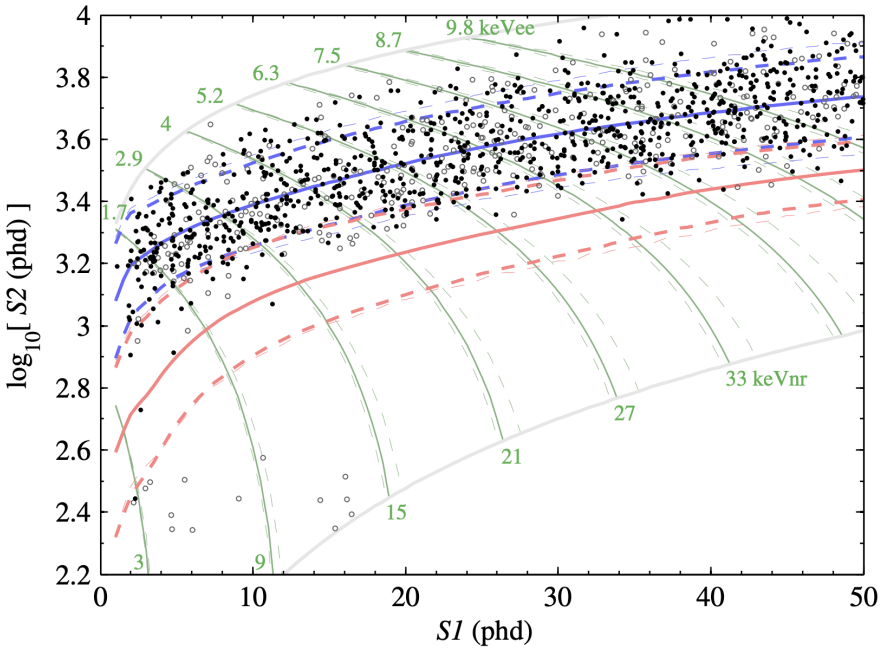

Figure 2.22: LUX WS2014-16 data. 50% contour of the ER and NR bands are indicated in thick blue and red lines, respectively. 10% and 90% contours of the bands are indicated in thick dashed lines. Figure from [52].

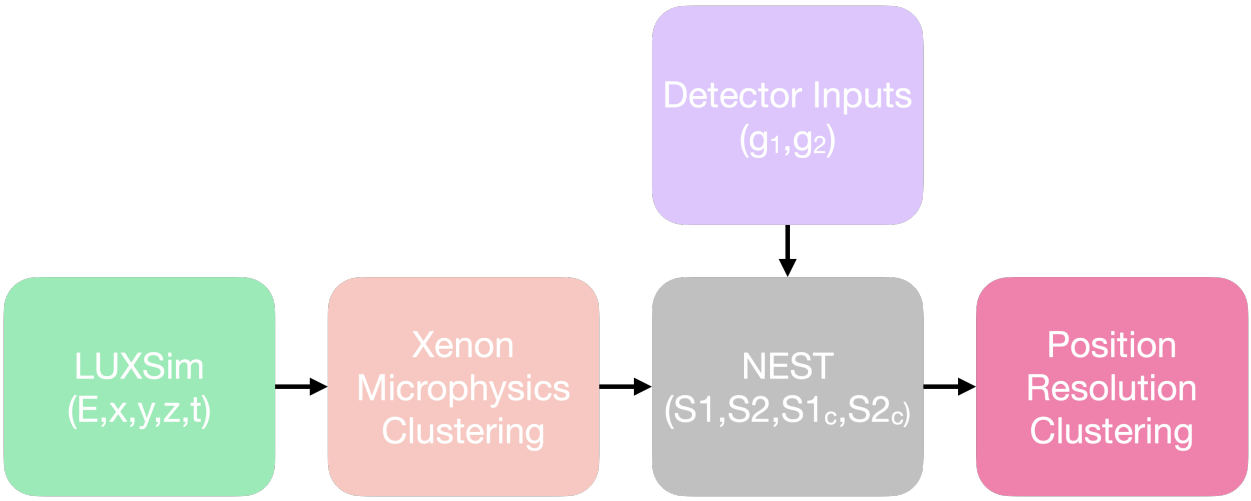

Figure 2.23: Primary steps in the LUX simulation framework used to model DM and background signal distributions.

Simulations

Fig. 2.23 shows the primary steps in the LUX simulation framework used to model DM and background signal distributions within the detector.

The GEANT4-based LUXSim software package [116, 117] was used to simulate radiogenic processes and the passage of particles through matter. The software contains a detailed model of the LUX TPC and water tank geometries produced from engineering CAD designs. It was used to track particles incident on the detector, such as DM and radioactive decay products, and calculate precise position and time coordinates of energy depositions in the xenon. It stopped short of modeling the xenon microphysics of signal production, specifically atomic excitation/de-excitation, ionisation, and formation of excitons.

The energy depositions output by LUXSim were distributed into clusters distant enough from one another to have independent xenon microphysics phenomena. The Noble Element Simulation Technique (NEST) [105] was then used to calculate the number of scintillation photons and freed electrons that would be associated with each cluster using a set of analytical models that predict L_y/Q_y given a specified interaction type, amount of energy, and conditions present in the detector during WS2013 and WS2014-16. This software was also used to predict the $S1/S2$ and $S1_c/S2_c$ signal sizes considering independently measured g_1 and g_2 values. The output of NEST was then clustered once more, based on the position resolution of the detector.

Table **??** summarises the WS2013 and WS2014-16 simulation results for the background sources found to contribute significant quantities of events after application of all event rejection techniques other than ER/NR discrimination. The most significant, by far are γ ray, β decay, ^{127}Xe, and ^{37}Ar backgrounds which all produce ERs that the PLR can readily

	WS2013 counts		WS2014-16 counts	
Parameter	Constraint	Fit	Constraint	Fit
γ	247 ± 106	228 ± 19	511 ± 77	590 ± 34
Low-z-origin γ	172 ± 74	165 ± 16	94 ± 19	99 ± 14
β	55 ± 22	84 ± 15	468 ± 140	499 ± 39
^{127}Xe	91 ± 27	78 ± 12	-	-
PTFE surface	24 ± 7	22 ± 4	14 ± 5	12 ± 3
^{37}Ar	-	12 ± 8	-	-
Accidental	-	-	1.3 ± 0.4	1.6 ± 0.3

Table 2.4: WS2013 and WS2014-16 simulation results for the background sources found to contribute significant quantities of events after application of all event rejection techniques other than ER/NR discrimination. Data from [64, 52].

distinguish from WIMP signals. They are compared with the best fit results of the profile likelihood ratio (PLR) test described in the next sub-section.

WIMP Search Results

The LUX collaboration used a PLR—a frequentist significance test used by many recent particle physics experiments [55, 118]—to place limits on spin-independent (SI) WIMP-nucleon cross sections given the data observed in WS2013 and WS2014-16 [52]. The null hypothesis was presence of a galactic halo WIMP signal and background composed of the constituents listed in Table 2.2. For a set of WIMP masses and cross-sections, the PLR uses the simulation framework to generate a suite of pseudo experiments with characteristics of the signal+background model. For each WIMP mass, it placed a limit at the cross-section where 90% of the pseudo experiments were more compatible with the null hypothesis than the observed data.

The 90% confidence level limits for the sole WS2013 and combined WS2013+WS2014-16 datasets are drawn in Fig. 2.24. At the time of publication, both results were the most stringent SI WIMP-nucleon cross-section limits yet measured.

2.3 Techniques to Search for Low-mass DM

The LUX collaboration has made a distinctive effort to expand its scientific reach beyond WIMPs by developing analysis techniques to probe low-mass DM models. LUX has exploited exotic scattering processes, devised novel methods for lowering the detectors energy threshold/utilized already existing ones, and advanced low-threshold methods by crafting novel procedures to mitigate backgrounds in this energy regime. The first two categories of techniques are summarised in the following subsections, while the very last technique is the

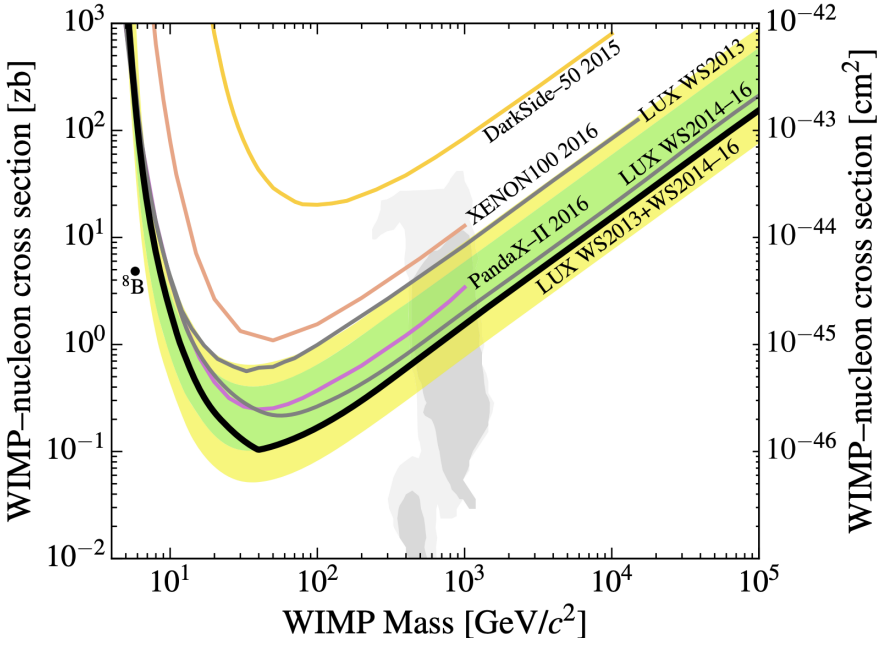

Figure 2.24: LUX limits on SI DM-nucleon cross section limits calculated from WS2013 and WS2014-16 data. Figure from [52].

subject of Chapter 7 of this dissertation: "Improving sensitivity to low-mass dark matter in LUX using a novel electrode background mitigation technique".

Exotic Scattering Processes

Xenon NRs produce fewer scintillation photons and freed electrons than ERs of the same energy because they often scatter coherently on other xenon atoms dissipating a significant fraction of energy as heat. As a consequence, NRs in LUX were less likely to pass the lower $S1/S2$ thresholds than comparable ERs. Additionally, the 50% detection efficiency for NRs occurred at 3.3 keV, while that for ERs occurred at 1.24 keV.

This disparity in xenon, and other detection mediums, has prompted researchers to consider rare scattering processes whereby a recoiling nucleus can produce a concurrent ER. They arise because of a delay between the recoil of the nucleus and movement of its surrounding electron cloud. For an instant the atom is polarised sometimes inducing emission of a Bremsstrahlung photon [119], other times changing the atomic energy levels promoting ionisation or excitation of the atom through what is called the Migdal effect [120][3]. Although

[3]Bremsstrahlung and Migdal effects in DM-nucleon scattering have been formulated in [119] and [120]; however, both effects have yet to be verified experimentally.

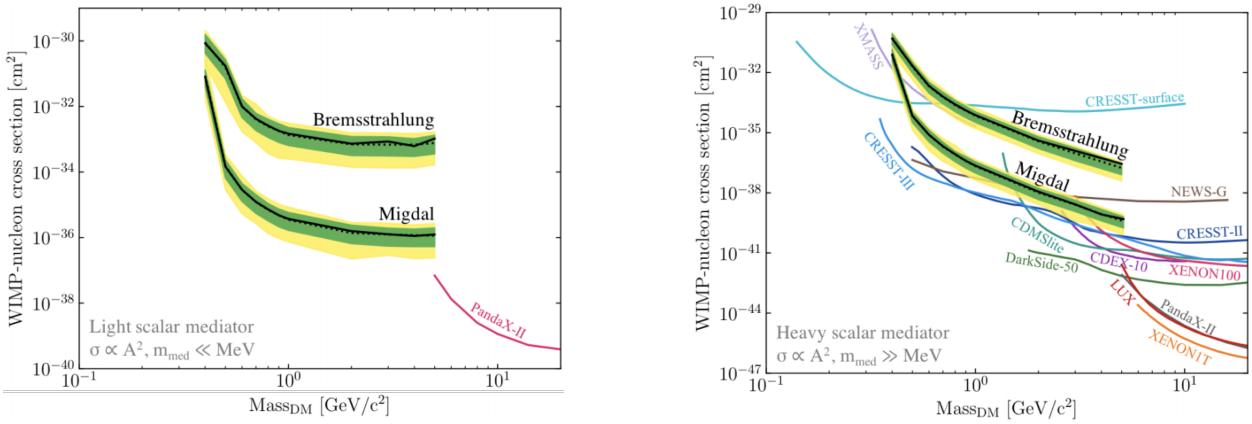

Figure 2.25: LUX limits on SI DM-nucleon cross section limits calculated from WS2013 data by incorporating Bremsstrahlung and Migdal scattering processes. Figure from [121].

the NR component of the event may produce sub-threshold numbers photons and electrons, the ER is often in the ∼keV range where it is detectable.

In 2018, LUX published analyses of the WS2013 data considering both Bremmstrahlung and Migdal signal types in [121]. The paper reported limits on SI DM-nucleon scattering for masses of 0.4–5 GeV that were competitive with world leading limits from experiments designed specifically to probe this mass range. These limits are shown in Fig. 2.25.

Analysis Methods for Lowering the Energy Threshold

Historically, dual-phase xenon TPCs have had asymmetric scintillation photon and freed electron detection efficiencies of (~ 0.1) and (~ 1), respectively. Because of this condition, low energy scatters that drive production of only a handful of these quanta often produce a photon pulse which fails the lower $S1$ threshold cut, but an electron pulse that passes the lower $S2$ threshold. Analysis techniques used to lower dual-phase xenon TPC energy thresholds focus on including events with this trait in DM searches.

LUX developed one such technique which exploited the $\sim 17\%$ probability that a Hamamatsu R8778 PMT photocathode emit two photoelectrons after contact by a scintillation photon, the double photoelectron effect (DPE) [97, 96]. First, the $S1$ threshold, requiring at least two photon signals in different PMTs, was dropped to one photon signal in a single PMT. This choice included lower energy scatters, but also many accidental coincidence background events in which the $S1$ was a single thermionic dark count or PTFE fluorescence photon. To reduce the background rate, single PMT $S1$s were required to have areas of approximately 2–4 phd consistent with the signal of a single scintillation photon which has induced the DPE. This cut removed the majority of events from thermionic dark counts and PTFE fluorescence photons because they appear as single photoelectron signals.

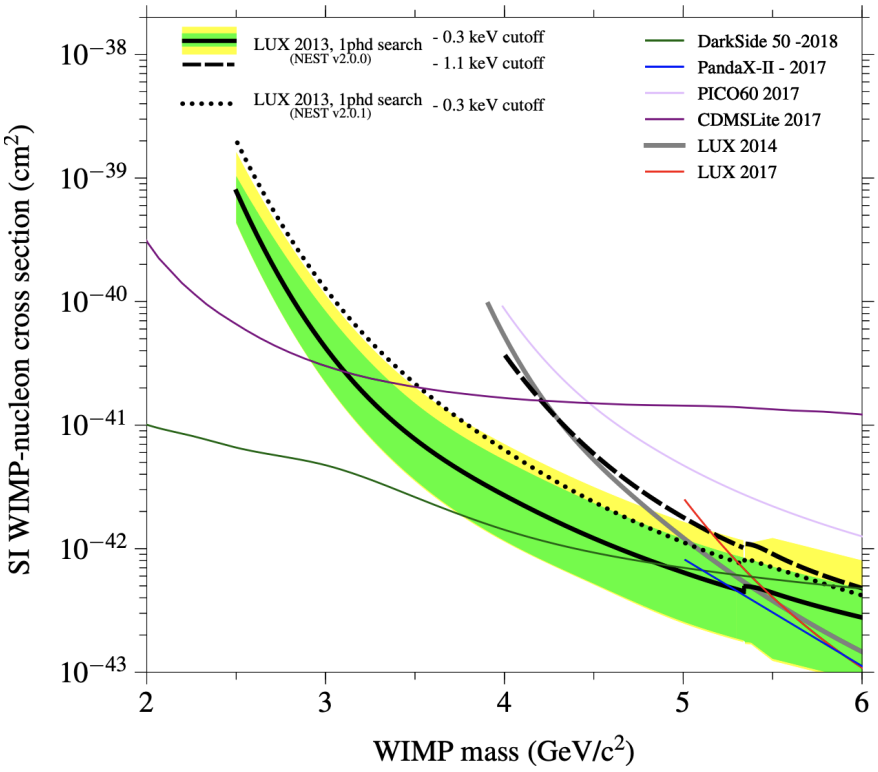

Figure 2.26: LUX limit on the SI WIMP-nucleon cross section calculated from WS2013 data which included single photoelectron $S1$s. Figure from [96].

In 2020, LUX published [96] describing application of the DPE technique to the WS2013 data. The technique allowed the collaboration to produce a competitive limit on SI DM-nucleon scattering down to 2.5 GeV, shown in Fig. 2.26. For comparison, the standard DM analysis, published in 2014, had only been competitive at $\gtrsim 4$ GeV.

LUX also performed an $S1$-agnostic analysis in which no $S1$ threshold was applied to the WS2013 data [106]. In other words, the dataset was expanded to include events with both zero or one $S1$, and one $S2$. This technique was first developed by past dual-phase xenon TPC experiments XENON10 and XENON100 [122, 123]. It has since been adopted by DarkSide-50 [124], a dual-phase argon TPC experiment, and XENON1T [125], the successor of XENON100. For LUX and all the mentioned experiments, the choice to incorporating events with only an $S2$ lead to elevated rates of low-energy background events from multiple sources. As described in Chapter 7, LUX noted that backgrounds from emission of electrons by the gate and cathode were particularly prevalent in the WS2013 data. In reaction, LUX collaborators developed a novel machine learning technique [106] that rejected events based on $S2$ pulse shape, which was observed to differ between $S2$s originating on the electrodes and those originating in the bulk xenon.

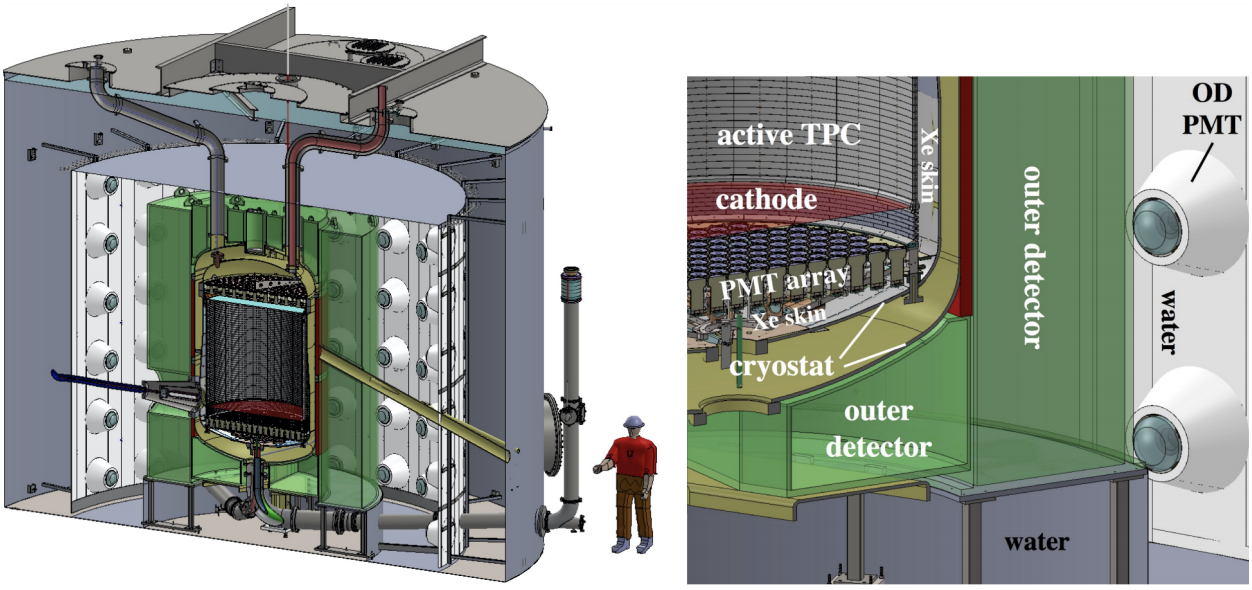

Figure 2.27: The LZ detector. Figure from [53].

2.4 The Future LUX-ZEPLIN Experiment

The LUX-ZEPLIN (LZ) collaboration is a merger between LUX and ZEPLIN (ZonEd Proportional scintillation in LIquid Noble gases) another previous dual-phase xenon TPC experiment based in the United Kingdom [126, 127, 128]. The central LZ detector is ~ 1.6 m diameter and 2.6 m tall dual-phase xenon TPC with a 7 tonne active mass instrumented by 494 Hamamatsu R11410-22 3"-diameter PMTs, shown in Fig. 2.27 and 2.28. It is currently being commissioned in the LUX detectors previous location: at SURF, in the Davis cavern, within the water tank [129, 53].

The central LZ TPC is installed within two surrounding veto detectors used to reduce backgrounds [129]. Just outside the TPC, there is a thin, 2 tonne, xenon skin detector instrumented with 93 R8520 1" PMTs and 38 R8778 2" PMTs. It is used to veto events from γ-ray emitting radiocontamination in the TPC components, considering these photons are usually emitted in coincidence with other γ rays that can scatter in the skin—or in the TPC. Just outside of the outer vessel, there is 17.3 tonnes of gadolinium-loaded liquid scintillator (GDLS) contained within transparent acrylic vessels. The GDLS is viewed by 120 R5912 8" PMTs located on a cylindrical shell within the water tank $\sim$1 m outside of the vessels. The GDLS detector is used to reduce the rate of neutrons from (α, n) interactions in the PTFE surrounding the TPC. After scattering once in the xenon, a neutron can thermalise in the scintillator detector after which it becomes captured by a gadolinium nucleus resulting in emission of several γ rays totally ~ 8 MeV [130]. Fig. 2.29 shows the single scatter event rate in the detector before and after application of both vetoes.

Figure 2.28: The LZ outer cryostat. Photo taken by Matt Kapust.

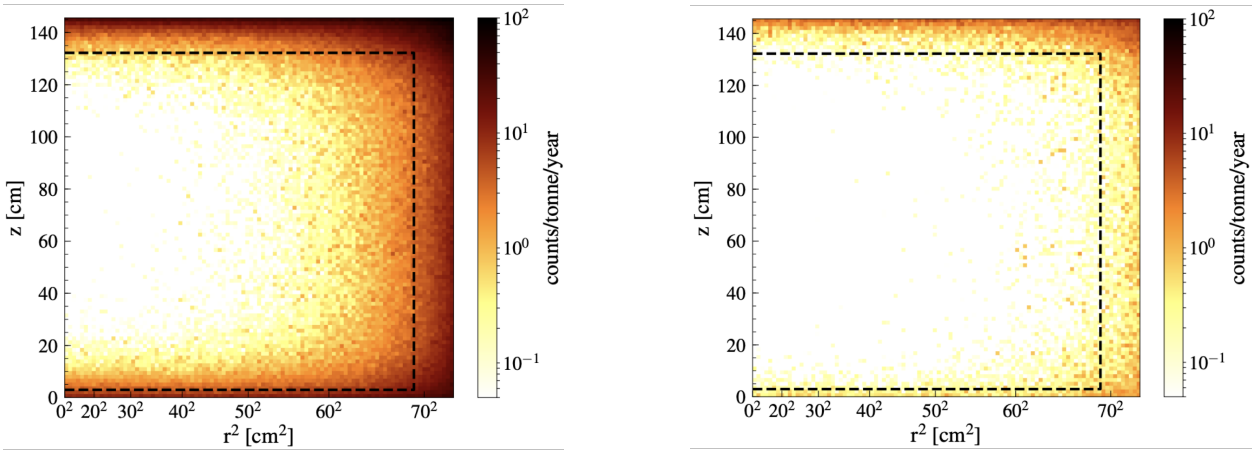

Figure 2.29: Single scatter event rate in the TPC before and after application of xenon skin and GDLS vetoes. Figure from [53].

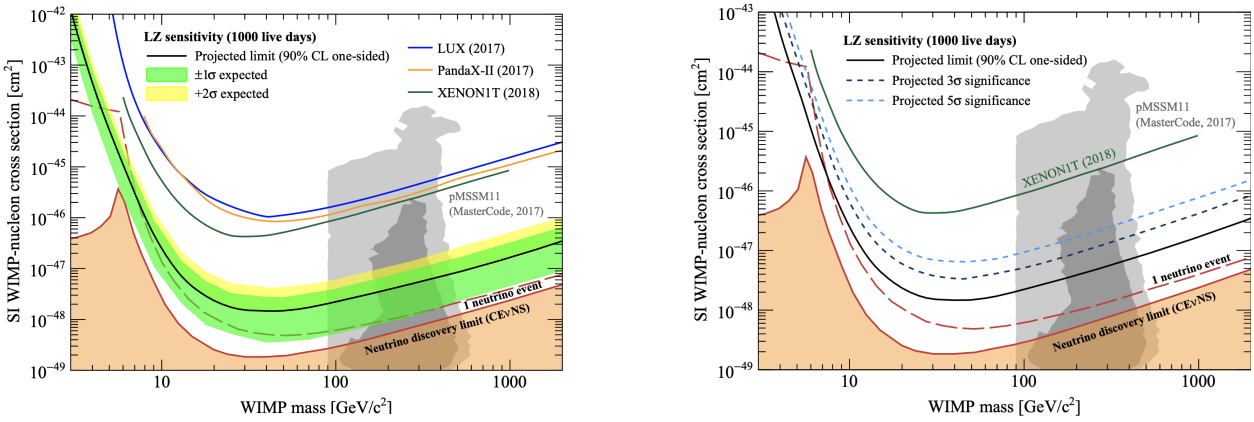

Figure 2.30: The LZ projected 1000 live-day, SI WIMP-nucleon cross-section sensitivity (left) and discovery potential (right). Figures are from [53].

The LZ TPCs massive size alone would advance its scientific reach beyond that of LUX; however, the collaboration has channeled additional effort into optimising the detectors design. This work was performed not only to maximise WIMP sensitivity but also to extend the experiments reach to low-mass DM. For example, a vast material screening campaign was carried out to select construction materials with the lowest possible levels of radiocontamination [131, 115], the subject of Chapter 6. This work resulted in a combined detector component background rate in the WIMP search energy range that is less than 1% of the total background rate [53]. Additionally, experimentation with wire surface treatments was performed to reduce the grid electron emission rate [114], the primary source of isolated, few-electron $S2$s that limit $S1$ agnostic analyses used to look for low-mass DM [111].

The LZ projected, 1000 live-day SI WIMP-nucleon cross-section sensitivity and discovery potential are shown in Fig. 2.30. The second calculation characterizes the ability to exclude the null hypothesis at 3 and 5σ significance as a function of WIMP mass, and is compared to 90% confidence level sensitivities of existing and future dual-phase xenon TPCs.

Chapter 3

High Energy Event Classification

Dual-phase noble-element time projection chambers (TPCs) observe a variety of small signals that mimic $S1$s and $S2$s generated by low-energy (∼few keV) scatters in the target medium [132, 96, 114, 113, 111]. These spurious pulses can be produced by components that carry thermal and/or electrical potential energy which is, occasionally, transformed into detectable emissions of light and charge. They can also be induced by a primary particles interaction in the medium: the scintillation photons and free electrons generated in these events undergo additional interactions as they travel delaying their progress so that they are detected at a later time or producing secondary light and charge emissions. The itemized points below provide a summary of the most probable mechanisms for production of spurious pulses in LUX, dividing them into categories of those generated by "components" or "interactions", and list relevant citations.

- *Produced by Components*
  - Cathodic grid electrodes, such as the LUX gate and cathode, can sometimes emit single electrons and, more rarely, multiple electrons or scintillation due to field effects that can induce electron multiplication processes. The behavior has been shown to be related to the quality of the wire surface concerning corrosion and nature of its oxide layer. The result of this *grid emission* is a prevalence of spurious $S2$s composed of just a few electrons originating from the grid wires, most significantly from hotspots likely caused by imperfections in the wire surface or the presence of impurities at those locations [114, 113, 111].
  - Photomultiplier tube (PMT) photocathodes thermionically emit electrons into their internals producing single photon-like signals called *PMT dark counts*. When two or more of these signals occur in coincidence in differing PMTs they can create a pulse that passes the two PMT coincidence threshold for an $S1$ [96].
  - As photoelectrons cascade from one dynode to the next inside a PMTs vacuum space, they can encounter and ionize residual gas particles causing them to drift along the electric field in the direction opposite of the electrons. The ions can

collide with the photocathode causing emission of additional electrons which travel down the dynode chain themselves, producing *PMT afterpulses*. These signals are most prominent following large $S1$s and $S2$s that generate many photons, thus many PMT photoelectrons. If two or more of the signals occur in coincidence—which is common since they occur at time delays characteristic of each ion, all less than a few microseconds—then they can create a pulse that passes the two PMT coincidence threshold for an $S1$ [132].

- *Induced by Particle Interactions*
  - A fraction of xenon luminescence photons induce *grid photoelectron emission* when they come in contact with a wire surface. The result of this effect is the presence of few-electron spurious $S2$s trailing many-photon $S1$s and $S2$s by a delay equal to the time it takes the electrons to drift from gate or cathode to the liquid surface [111].
  - *Photoionization of impurities* by xenon luminescence generates many single electrons following $S1$s and $S2$s [111]. Many-photon pulses will produce dense trails of electrons, with length equal to the maximum electron drift time, that can be grouped by the waveform processing software into spurious $S2$s of various sizes [111].
  - A fraction of the electrons freed by interactions in the xenon are temporarily captured by impurities then released with delays of up to seconds following a primary $S2$. The waveform processing software groups the electrons from *impurity capture and release* into spurious $S2$s of various sizes [111].
  - Imperfect efficiency for extraction of electrons into the vapor causes some of these quanta to be trapped just below the liquid surface. *Delayed extraction* of the electrons tends to occur in one to hundreds of microsecond wide bursts at delays of up to a tens of milliseconds following a primary $S2$. As with the previous two categories of mechanisms, the waveform processing software groups the electrons into spurious $S2$s of various sizes [111].
  - Xenon luminescence can be absorbed by the reflective PTFE panels which will then fluoresce with a time delay of up to seconds following a primary pulse. The *PMT fluorescence* temporarily raises the rate of single photon-like backgrounds above that from PMT dark counts alone, hence elevates the rate of spurious S1s [96, 111].

The most straightforward complication of spurious signals is that they create low-energy background events that encumber searches for new physics in this regime. Discussion of these events is left to Chapter 7 which details a low-mass dark matter search and supporting background mitigation techniques.

This chapter focuses on a more inconspicuous problem, pathologies from spurious signals occurring within the same event window as high-energy ($\gtrsim$ 40 keV) primary interactions. In

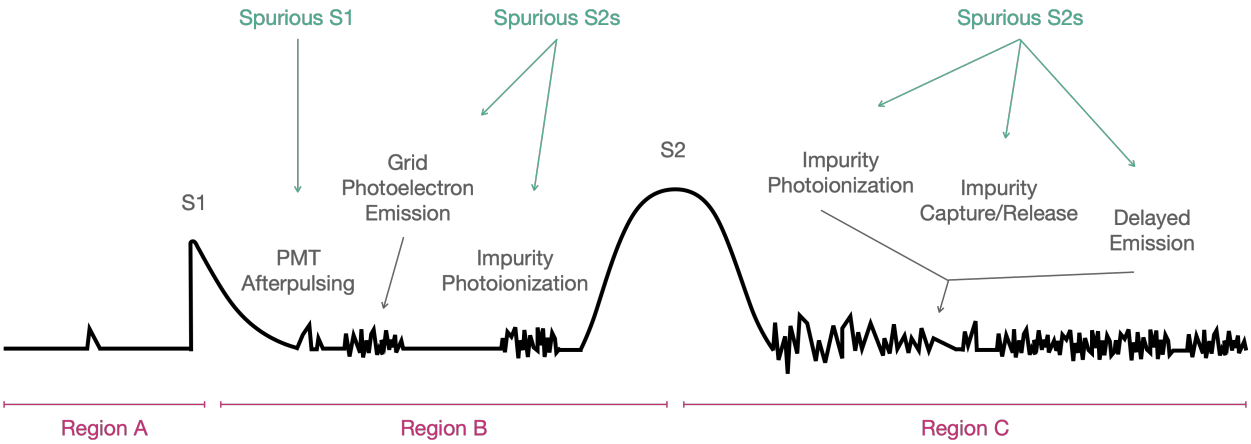

Figure 3.1: Schematic single-scatter high-energy event containing spurious pulses induced by a primary $S1$ and $S2$ pair. In LUX, there were visible populations of PMT afterpulsing $S1$s, grid photoelectron emission $S2$s, and impurity photoionisation $S2$s following primary $S1$s. There were also dense trails of $S2$s from impurity photoionisation, capture and release by impurities, and delayed electron emission following primary $S2$s. The waveform is divided into regions A, B, and C: different cuts were used to mitigate the categories of spurious pulses observed in each region.

this case, a primary $S1$ or $S2$ is the trigger around which the waveform processing software builds a 1 ms long event. During this period of time, the interaction induces smaller spurious $S1$s/$S2$s whose number and size grow with the amount of primary scintillation photons and free electrons. High energy single scatters that generate many of these quanta falsely appear to be multiple scatters because their waveforms contain many $S1$s and/or $S2$s, as illustrated with the toy event shown in Fig. 3.1. Above several hundred keV—the regime of searches for new physics such as neutrinoless double beta decay—there are large numbers of true multiple-scatter background events; consequently, it is essential to design a robust algorithm for selecting single-scatter signal-like events in order to obtain competitive sensitivity in these searches.

The following section characterises the types of spurious signals observed in several energy regimes relevant to LUX. The latter sections describe the construction of an algorithm that identifies single scatters with high fidelity. The work uses calibration sources to measure the algorithm's efficiency at several energies. In regimes where no such sources are available, conservative cuts are implemented. As a valuation, the reduction in background rate is measured at the ^{134}Xe and ^{136}Xe $0\nu\beta\beta$ energies, processes of interest not only to LUX, but also its predecessor LZ.

3.1 Spurious Pulses

It would be interesting to systematically characterise the energy, intensity, and timing of spurious signals to better understand their underlying mechanisms. Unfortunately, this is not possible using LUX's standard waveform processing machinery relied on throughout this dissertation. It records only 10 pulses in an event window prioritising a combination of the largest pulses and small pulses occurring before the largest pulse [88]. Compare this to the handful of primary $S1$s/$S2$s and dozens of spurious $S1$s/$S2$s observed in many high energy waveforms. Almost all primary pulses are stored because of their low numbers and large size, but most spurious pulses are neglected.

The data processing machinery can, however, be used to get a general understanding of the high energy pathologies. As the size of the primary $S1$s/$S2$s increases, populations of spurious pulses with specific size, intensity, and timing distributions begin to emerge. They can be characterized using calibration and background sources that sample the range of event energies expected in the WS2013 and WS2014-16 data. The list includes ^{83m}Kr, ^{133}Xe, ^{131m}Xe, ^{238}U/^{232}Th β decays/γ rays, ^{222}Rn and ^{218}Po with decay energies of 42, 81–427, 164, 0–2614, 5590, and 6115 keV.

The first step of this analysis was to obtain high purity selections of events from the isotopes of interest. Graphical cuts were designed to select the features of each isotope visible in $\left(\sum_i^9 S1_i, \sum_i^9 S2_i\right)$ space, shown in figures 3.2, 3.3, and 3.4. The sum is over every $S1$ or $S2$ in the event, regardless of whether it is a primary or spurious pulse.

No additional cuts were placed on ^{133}Xe, ^{131m}Xe, ^{222}Rn, and ^{218}Po events, because these isotopes truly do produce single scatters. They decay through one step processes that emit a charged particle (electron or α) which will travel a very short distance through the xenon before losing all of its energy. The result is a single flash of scintillation that produces the primary $S1$ and a small electron cluster that produces the primary $S2$.

The remaining isotopes decay through more complicated processes that require further scrutiny.

^{83m}Kr decays first to a metastable state with 154 ns half life, emitting 32.2 keV. It then decays to the ground state, emitting a final 9.4 keV. Usually the short intermediate half life generates a single primary $S1/S2$ pair. However, a fraction of the time there are two primary $S1$s, two primary $S2$s, or both. These events were required to pass a second cut the ensured a reasonably pure selection of single scatters. Fig. 3.5 shows regions of $S1_i, \sum_{i=1}^9 S1_i$ and $S2_i, \sum_{i=1}^9 S2_i$ space corresponding to the two steps of the ^{83m}Kr decay. Events with an $S1$ or $S2$ in these regions were removed from the analysis. ^{40}K decays were required to pass the cuts $\frac{max(S1)}{\sum_{i=1}^9 S1_i} > 0.9$ and $\frac{max(S2)}{\sum_{i=1}^9 S2_i} > 0.9$.

The ^{238}U/^{232}Th β decays are single scatters—for the same reasons as ^{133}Xe, ^{131m}Xe, ^{222}Rn, and ^{218}Po—but they overlap in $\left(\sum_i^9 S1_i, \sum_i^9 S2_i\right)$ space with the γ rays which can scatter once or multiple times in the xenon depositing a fractions of their energy at each scatter site. Because the gamma ray travels at the speed of light, their scatters occur in such close succession they produce scintillation signals that overlap to form one primary $S1$. However,

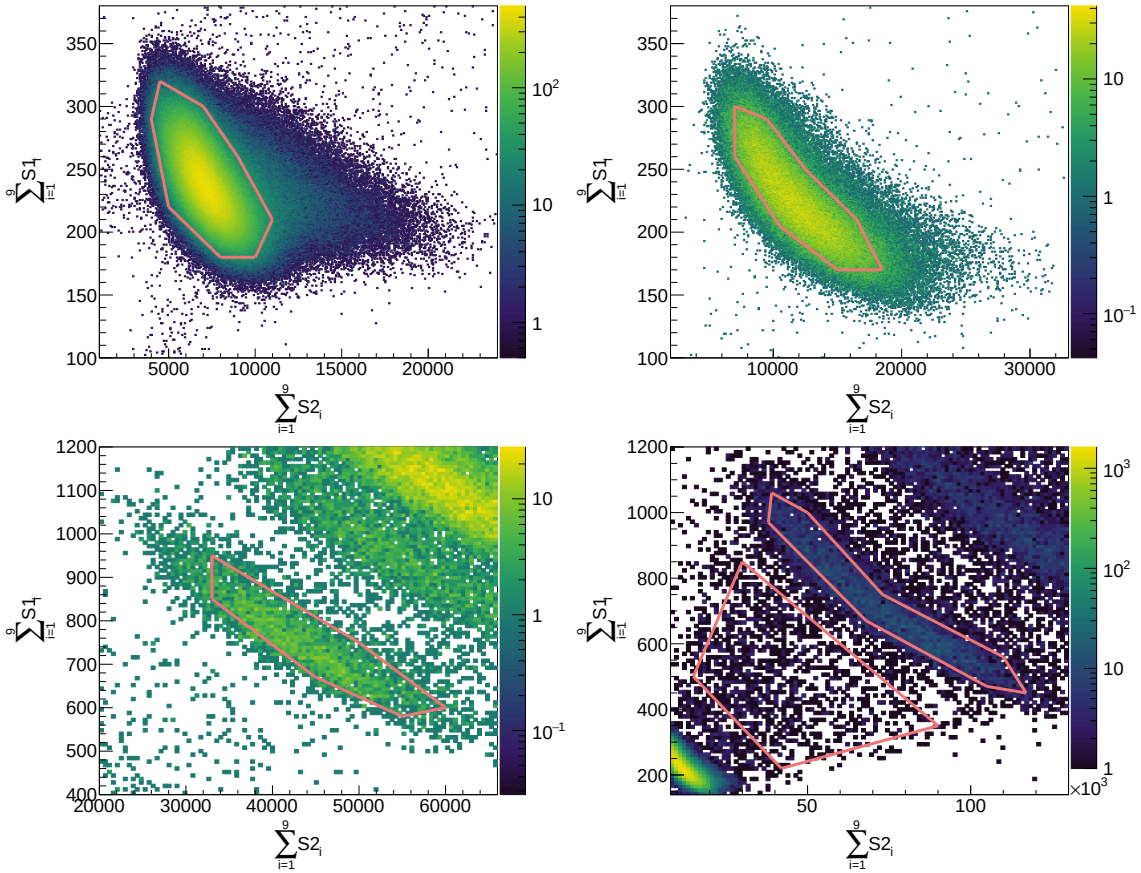

Figure 3.2: Graphical cuts selecting events from calibration sources in WS2013 (left) and WS2014-16 (right). The top plots show the ^{83m}Kr cuts. The bottom plots show the ^{131m}Xe cuts and, for WS2014-16, the ^{133}Xe cut.

if the scatters occur at different depths, the electron clusters will drift for different amounts of time resulting in multiple primary $S2$s. No additional cut was applied to the ^{238}U/^{232}Th events; instead, their populations of primary and spurious $S2$s are separated based on size, in the following sections, and cuts removing the latter are defined conservatively

Events passing all cuts were divided into the three regions as outlined in Fig. 3.1. Region A contains pulses that occur independent of the primary interaction, for example pulses produced by the components or induced by previous interactions, which are not the focus of this analysis. Region B and C contain pulses induced by scintillation photons of the primary $S1$ and region C contains additional pulses induced by free electrons and electroluminesence of the primary $S2$. In most cases, the primary $S2$ is composed of many more energy quanta than the $S1$ thus is responsible for the majority of spurious pulses in Region C.

As you iterate through the sources, in order of increasing in energy, the first significant

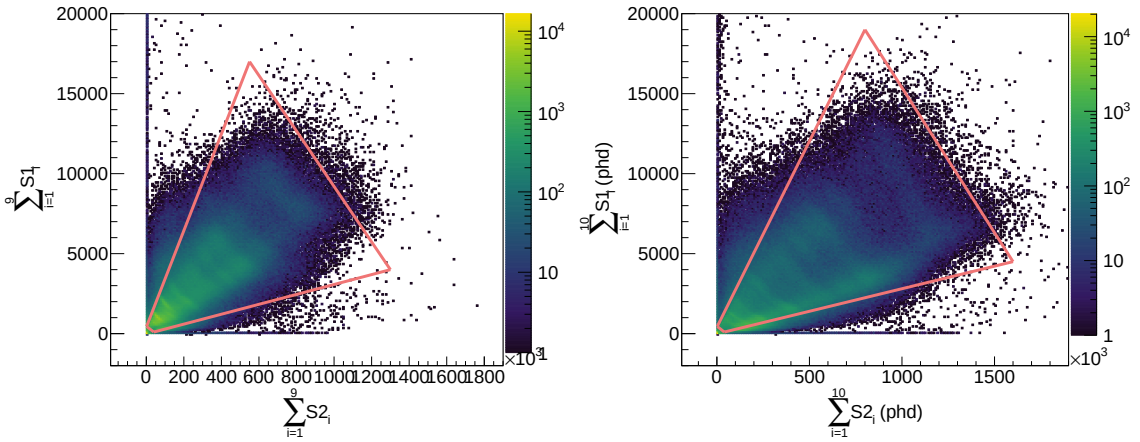

Figure 3.3: Graphical cuts selecting events from high-energy β-decay and γ-ray background sources in WS2013 (left) and WS2014-16 (right).

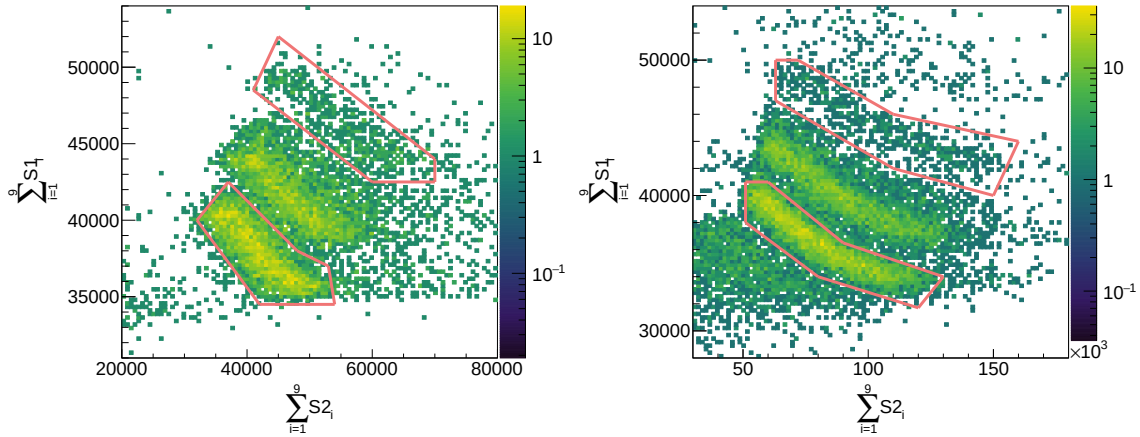

Figure 3.4: Graphical cuts selecting events from α-decay background sources in WS2013 (left) and WS2014-16 (right). The top population is ^{218}Po and the bottom populations are ^{222}Rn.

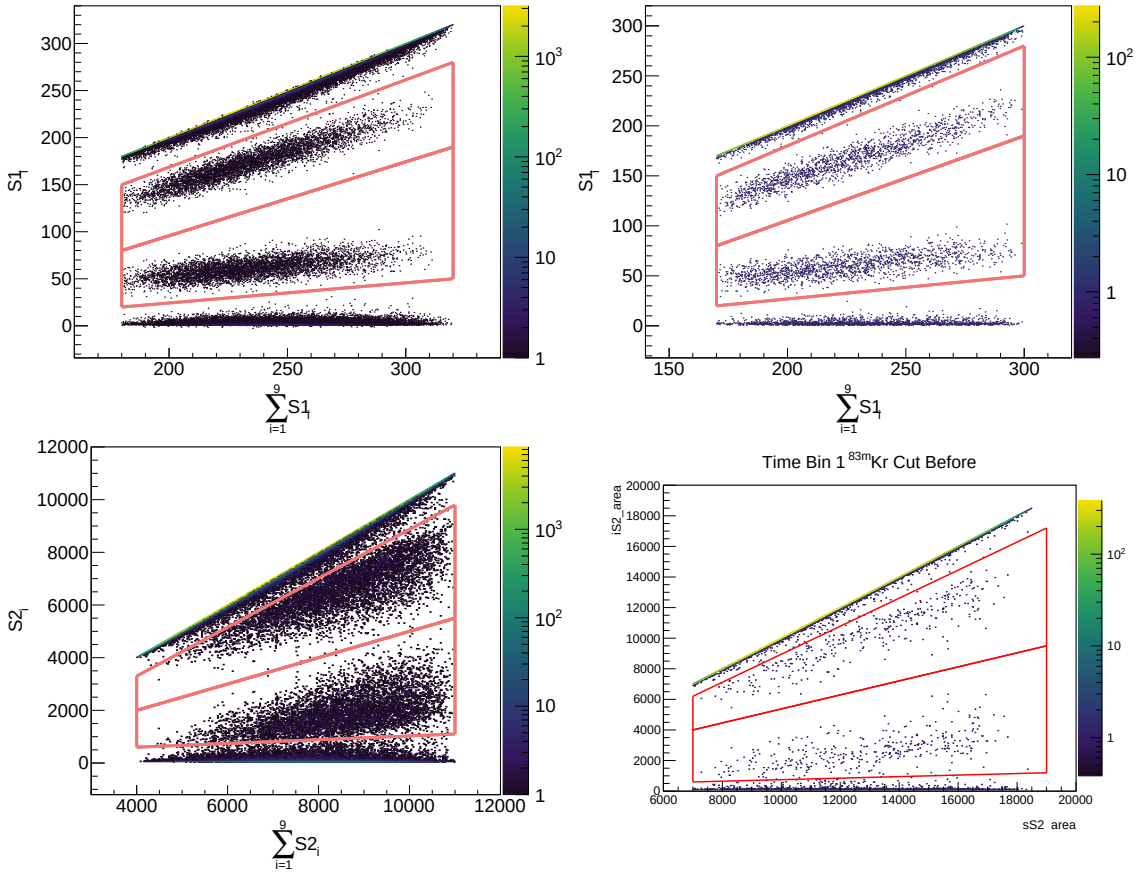

Figure 3.5: Graphical cuts removing ^{83m}Kr events with two $S1$s or $S2$s corresponding to the two-step decay of this isotope. WS2013 and WS2014-16 data are on the left and right, respectively.

populations of spurious pulses arises in the ^{133}Xe data. Fig. 3.6 shows an extended trail of electrons following a ^{133}Xe primary $S2$, which the pulse finder has divided up into several spurious $S2$s. The long time delays of the electrons suggest they are from photoionization of impurities, impurity capture and release of electrons, and delayed extraction of electrons from the liquid.

Fig. 3.7 shows a spurious $S1$ shortly trailing the primary $S1$ of a ^{238}U/^{232}Th β decays or γ ray. This pulse is from a population that trails the primary $S1$s by just a few microseconds. The timing distributions suggests they are produced by the coincidence of PMT afterpulses.

Fig. 3.8 shows two examples of the type of spurious pulses trailing ^{222}Rn $S1$s. There are spurious $S2$s that trail the primary $S1$ by a few microseconds, likely from gate photoelectron emission. There are additional $S2$s at longer time delays, likely from photoionization of impurities.

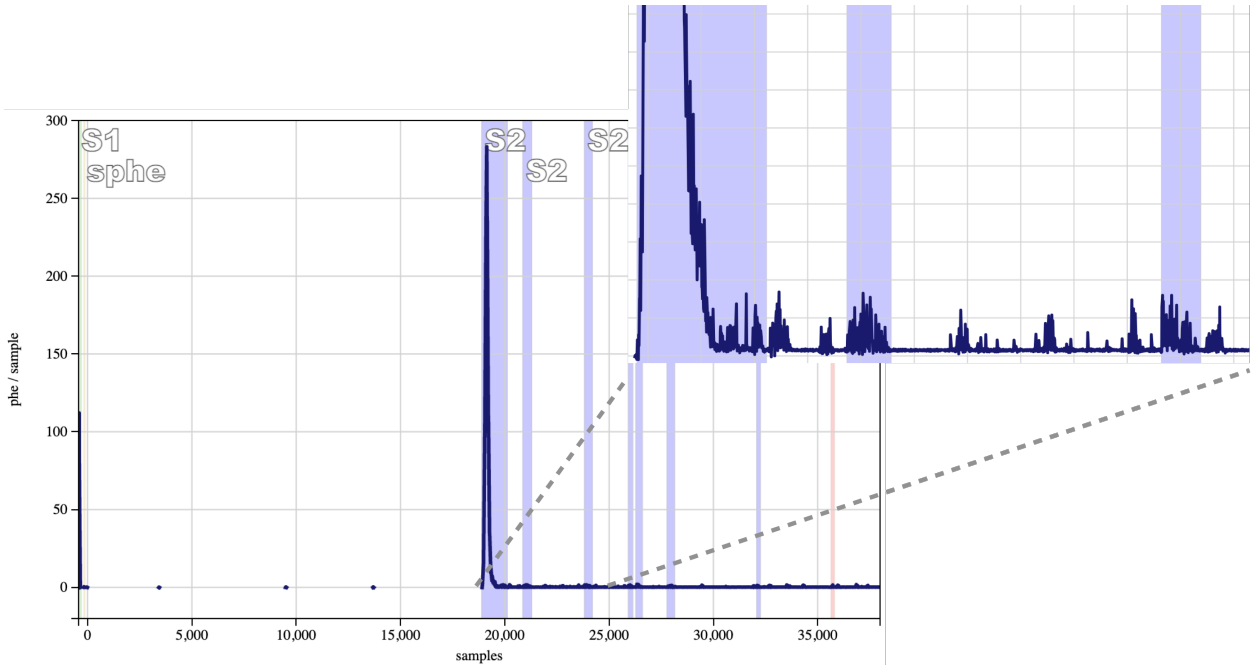

Figure 3.6: Trail of electrons from photoionization of impurities, impurity capture and release, and delayed extraction from the liquid following a ^{133}Xe primary $S2$.

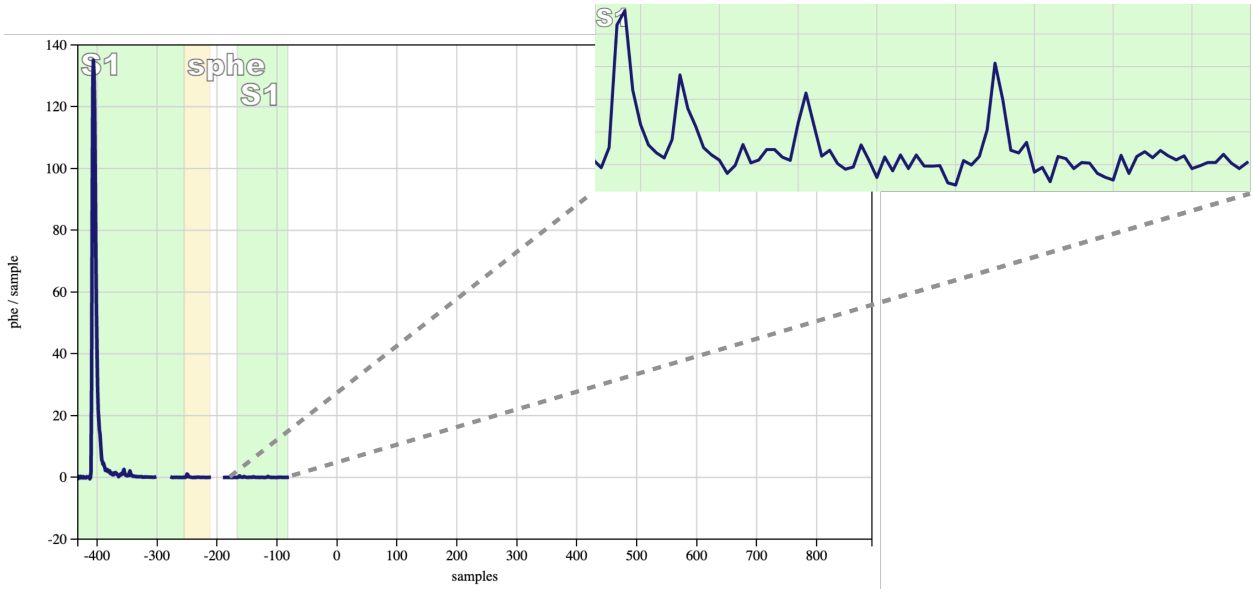

Figure 3.7: PMT afterpulses following a ^{238}U/^{232}Th β decays or γ ray primary $S1$.

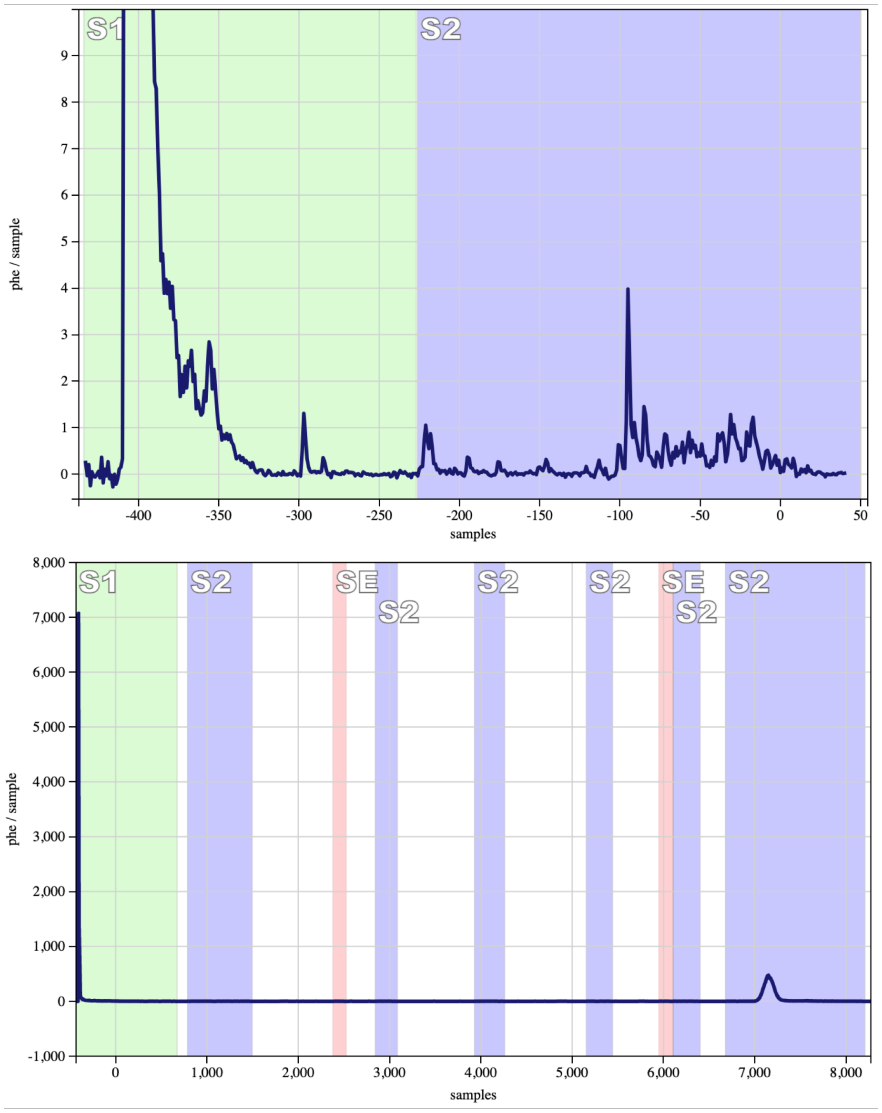

Figure 3.8: Gate photoelectron emission (top) and photoionization of impurities (bottom) following a ^{222}Rn $S1$.

3.2 Event Classification Algorithm

This section describes the algorithm that classifies events by the number of primary $S1$s/$S2$s counted in its waveform. It begins by considering single-scatters with energies out to 164 keV (the decay energy of ^{131m}Xe), then extends the algorithm to any number of primary $S1$s/$S2$s and all interaction energies observed in the LUX data.

Probing to 164 keV with Single Scatter Calibration Sources

The strategy outlined in Sec. 3.1 was used to obtain high purity selections of ^{83m}Kr, ^{133}Xe, and ^{131m}Xe events which were divided into regions A, B, and C.

The top panels in figures 3.9, 3.10, and 3.11 illustrate the energy dependence of spurious pulses, in terms of their size and intensity, appearing in WS2013 and WS2014-16 ^{83m}Kr/^{133}Xe/^{131m}Xe events. Figures 3.9 and 3.10 plot the ith $S1$ and $S2$ in region B versus the size of the maximum $S1$ and Fig. 3.11 plots the ith $S2$ in region C versus the size of the maximum $S2$. The pulses along the line $y = x$ in figures 3.9 and 3.11 are the primary $S1$s and $S2$s of every event: these pulses are are always the largest $S1$ and $S2$ in the waveform. The populations near $y \sim 0$ are composed of spurious pulses. To a lesser extent, Fig. 3.10 has the same spurious features along $y \sim 0$. Also visible are populations from larger primary $S2$s.

The middle panels in figures 3.9, 3.10, and 3.11 draw the thresholds used to identify spurious pulses in both regions. These criteria determine whether or not an event is labelled a single scatter: such events should only contain one $S1$ and $S2$ passing the cuts, ie the largest $S1$ and $S2$. If an event contains a second passing $S1$ or $S2$, than it is labelled as "other".

The bottom panels in figures 3.9, 3.10, and 3.11 plot the single scatter selection efficiency before and after applying each of the spurious pulse thresholds. Prior to performing the cuts removing spurious $S1$s in region B and spurious $S2$s in region C, the efficiency falls significantly as primary $S1/S2$ size increases. This is especially true of spurious $S2$s in region C which lower the efficiency from ~ 1 to ~ 0 across the range of primary $S2$ sizes shown in the plots. After performing all cuts, the efficiency remains at ~ 1 for all primary $S1$ and $S2$ sizes.

The spurious pulse threshold cuts have the potential to mistakenly classify some "other" events as single scatters. For example, if a γ ray scatters at the top of the detector producing a large primary $S2$ then again at the bottom of the detector producing a small primary $S2$, the second pulse could be classified as spurious. For this reason, the thresholds were reduced as far as was possible while maintaining single scatter selection efficiency of 1.

Probing to 2614 keV with Multiple Scatters

As stated earlier, the ^{238}U/^{232}Th γ rays and β decays are a mixture of single and multiple scatters. These events almost always have a one primary $S1$, thus the technique described

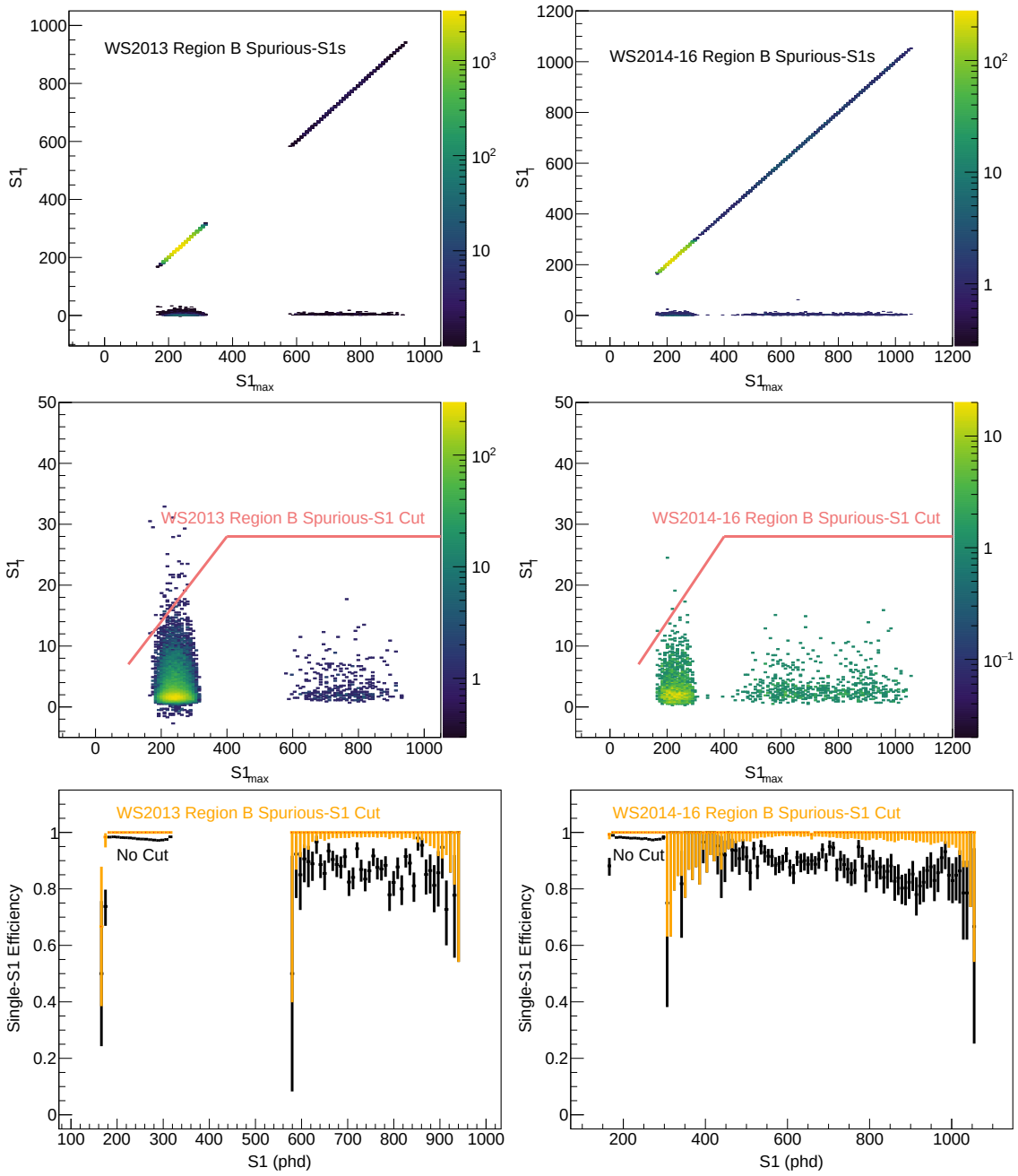

Figure 3.9: The top plots show region-B spurious $S1$s occurring in ^{83m}Kr/^{131m}Xe events for WS2013 (left) and ^{83m}Kr/^{133}Xe/^{131m}Xe events for WS2014-16 (right). The primary $S1$s lie along the line $y = x$ and the spurious $S1$s lie along $y = 0$. The middle plots show a zoomed in view of the spurious pulses and compares them to a threshold cut used to identify them as "spurious". The bottom plots show the efficiency for identify single $S1$ events after application of the threshold cut.

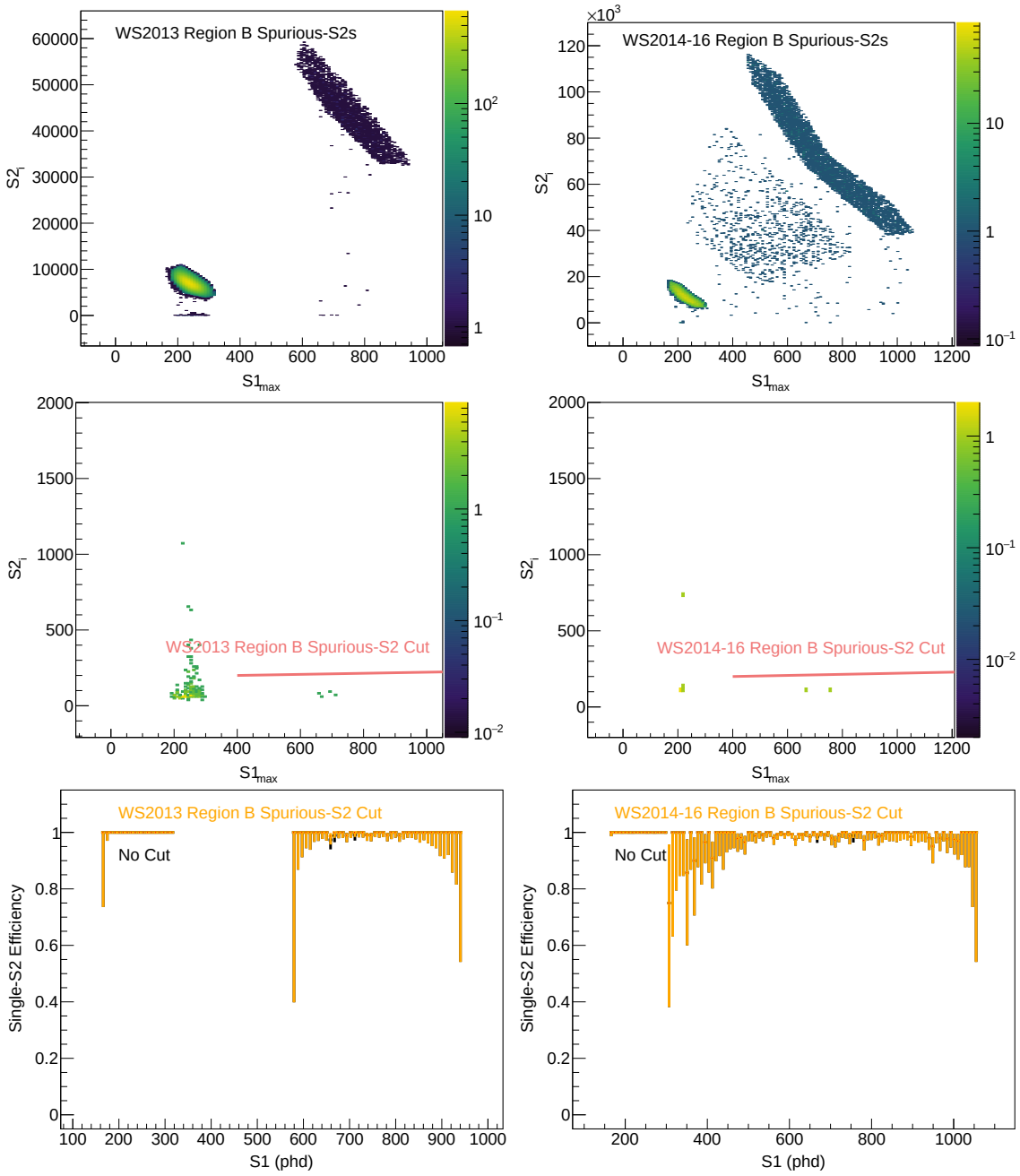

Figure 3.10: The top plots show region-B spurious $S2$s occurring in ^{83m}Kr/^{131m}Xe events for WS2013 (left) and ^{83m}Kr/^{133}Xe/^{131m}Xe events for WS2014-16 (right). The primary $S2$s lie in the center of the plot and the spurious $S1$s lie along $y = 0$. The middle plots show a zoomed in view of the spurious pulses and compares them to a threshold cut used to identify them as "spurious". The bottom plots show the efficiency for identify single $S2$ events after application of the threshold cut.

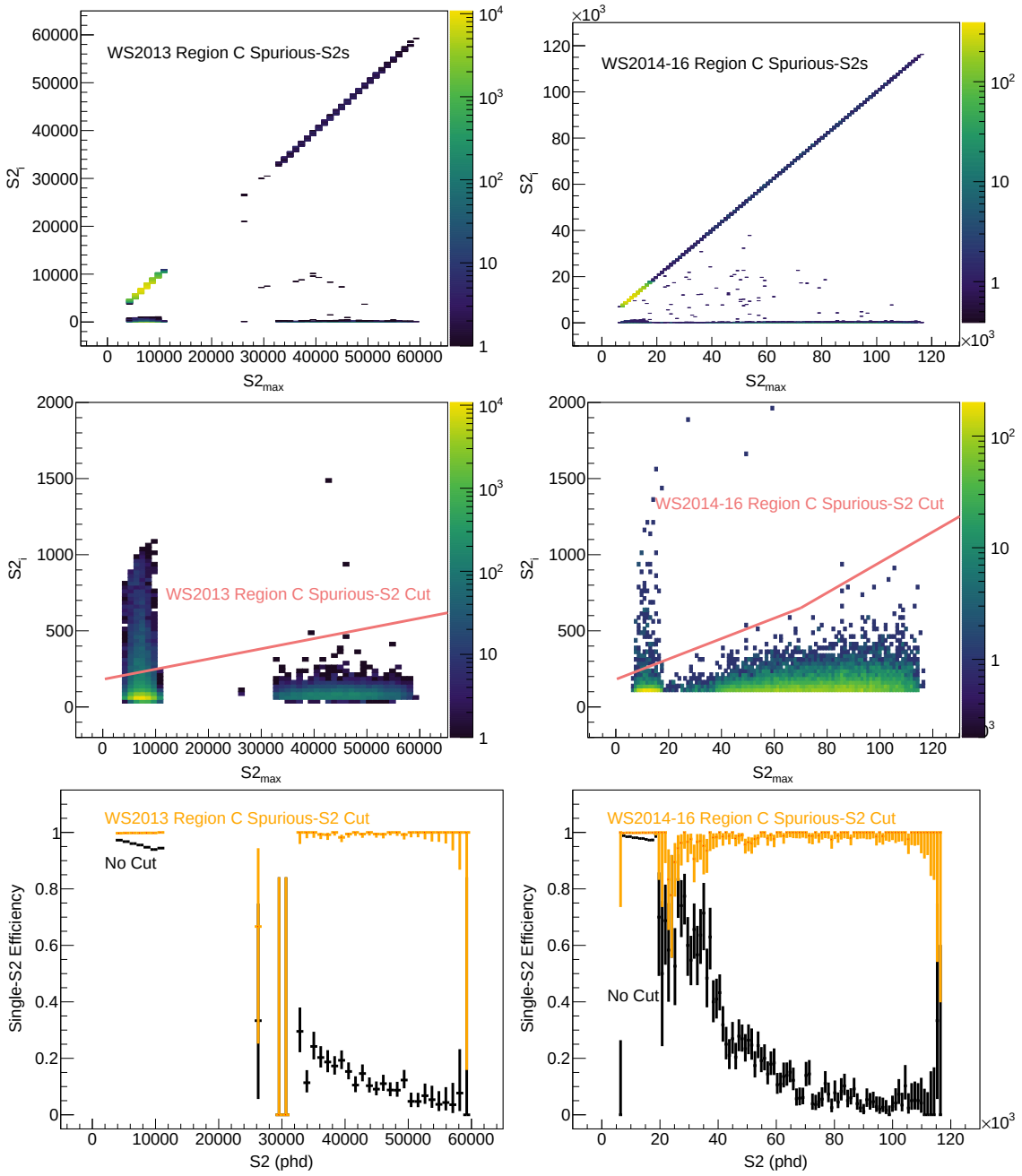

Figure 3.11: The top plots show region-C spurious $S2$s occurring in ^{83m}Kr/^{131m}Xe events for WS2013 (left) and ^{83m}Kr/^{133}Xe/^{131m}Xe events for WS2014-16 (right). The primary $S2$s lie along the line $y = x$ and the spurious $S2$s lie along $y = 0$. The middle plots show a zoomed in view of the spurious pulses and compares them to a threshold cut used to identify them as "spurious". The bottom plots show the efficiency for identify single $S2$ events after application of the threshold cut.

in the previous subsection can be used to make efficiency measurements for the region B spurious S1 cuts. Figure 3.12 illustrates the energy dependence of spurious $S1$s in region B, draws the thresholds used to identify these pulses, and plots the corresponding single scatter selection efficiencies.

Figure 3.13 contains the same set of plots considering spurious $S2$s in region B; however, no efficiency measurements are included because the data contains many multiple scatter events with more than one primary $S2$. In this instance, region B is considered to be the length of time between the primary $S1$ and the first $S2$ large enough to have induced a spurious $S2$; this size is 1350 phd, as determined using the single scatter calibration data. The threshold is conservatively high enough to reject all spurious $S2$s in region B, thus ensure single scatter selection efficiency of ~ 1.

Figure 3.14 contains the set of plots used to characterize spurious $S2$s in region C. They are different from the corresponding plots in the previous section in that they do not use maximum $S2$ size on the x axis, since this parameter is meaningless when considering multiple-scatter data with more than one $S2$. Instead, they use the sum of all primary $S2$s occurring before the ith $S2$. As in region B, the spurious $S2$ threshold in region C was chosen to be conservatively high.

∼MeV $S1$s with ^{222}Rn and ^{218}Po

The technique used to study spurious pulses in single-scatter calibration data was applied to ^{222}Rn and ^{218}Po α decay events (5489 and 6002 keV). α decays have moderately sized $S2$s—similar in size to ^{131m}Xe—but very large S1s. The cuts outlined in the previous subsections are sufficient for removing spurious $S2$s in region C (following the $S2$), but higher thresholds are required to remove the larger more numerous spurious pulses in region B (following the $S1$). Figures 3.15 and 3.16 illustrates the energy dependence of spurious $S1$s/$S2$s in region B, draw the thresholds used to identify these pulses, and plots the corresponding single scatter selection efficiencies.

∼kev $S2$s with Tritium Calibration Source

The current chapter focuses on high energies; however, it is also necessary to characterise the effect of spurious pulse cuts on low-energy WS2013 data used in the low-mass dark-matter search presented in Chapter 7.

At these energies, the only relevant cut is the minimum $S2$ threshold applied in regions A, B, and C; defined in the data processing software as 55 spikes in a pulse waveform. The condition relies on an alternative method of estimating size by counting photons (i.e. "spikes") as opposed integrating the area of a pulse. A single electron extracted from the liquid would produce an average of 24.5 photons, thus the threshold corresponds to an $S2$ of approximately 2.2 detected electrons. Interactions of low-enough energy will often produce $S2$s smaller than this size, thus the single-scatter selection efficiency in this regime will take a hit from application of the cut.

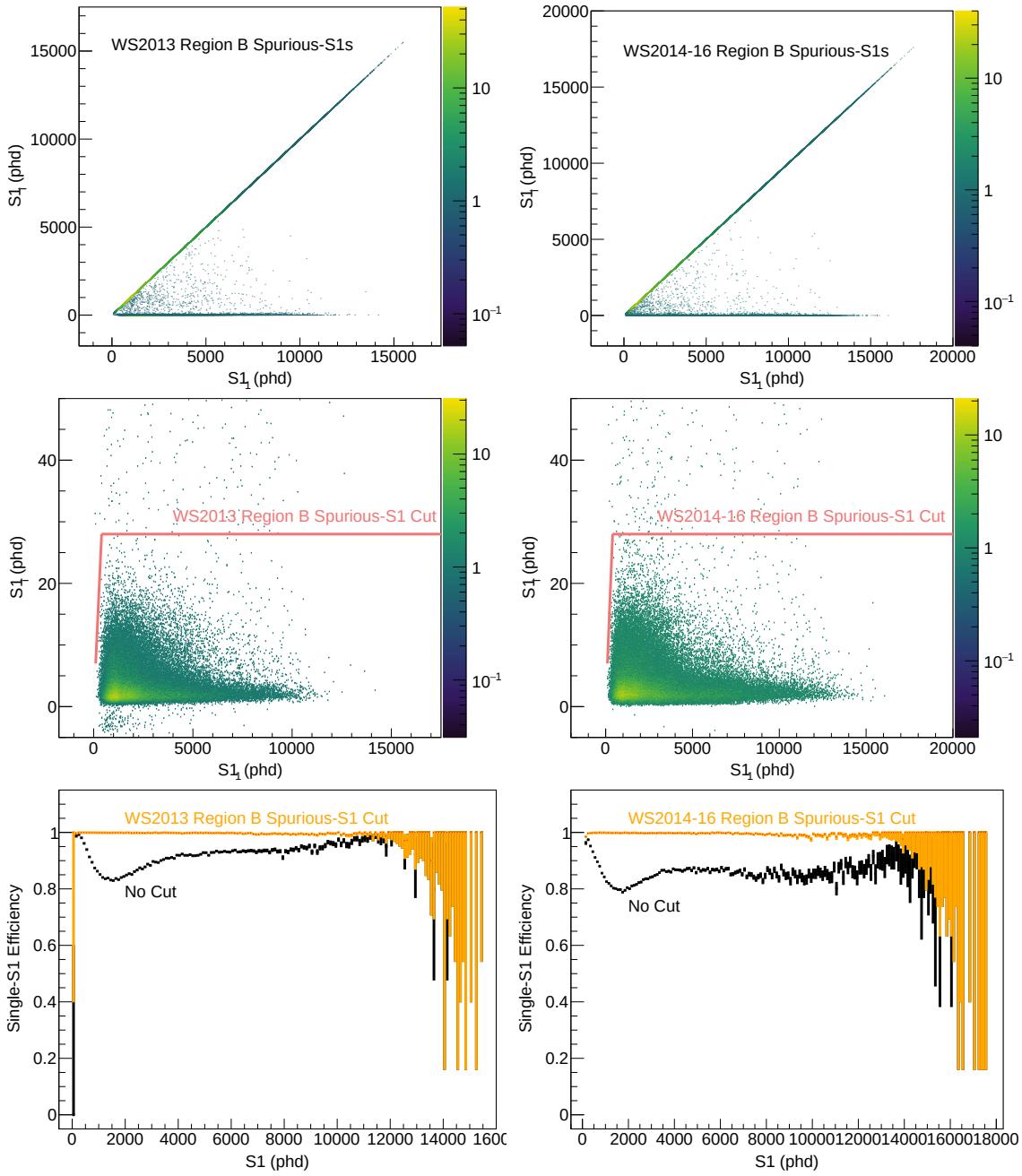

Figure 3.12: The top plots show region-B spurious $S1$s occurring in γ ray and β decay background events for WS2013 (left) and WS2014-16 (right). The primary $S1$s lie along the line $y = x$ and the spurious $S1$s lie along $y = 0$. The middle plots show a zoomed in view of the spurious pulses and compares them to a threshold cut used to identify them as "spurious". The bottom plots show the efficiency for identify single $S1$ events after application of the threshold cut.

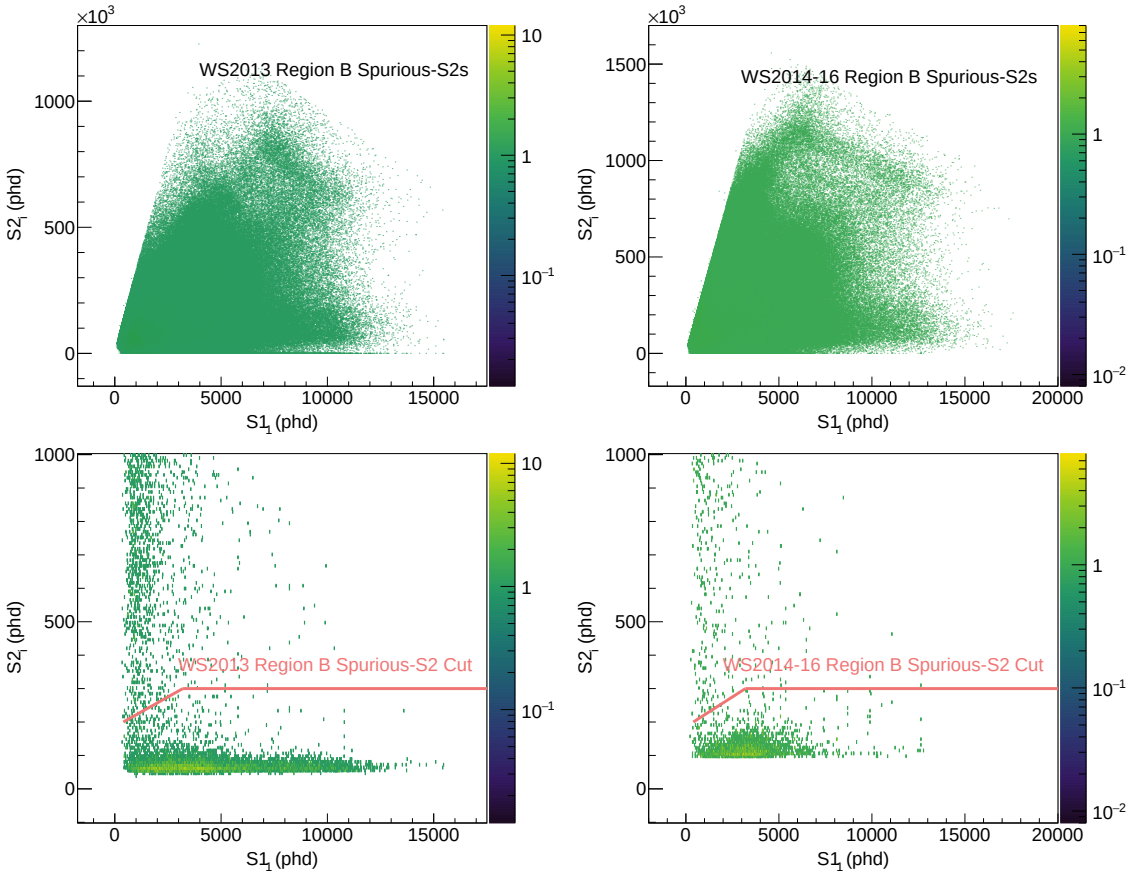

Figure 3.13: The top plots show region-B spurious $S2$s occurring in γ ray and β decay background events for WS2013 (left) and WS2014-16 (right). The primary $S2$s lie in the center of the plot and the spurious $S2$s lie along $y = 0$. The bottom plots show a zoomed in view of the spurious pulses and compares them to a threshold cut used to identify them as "spurious".

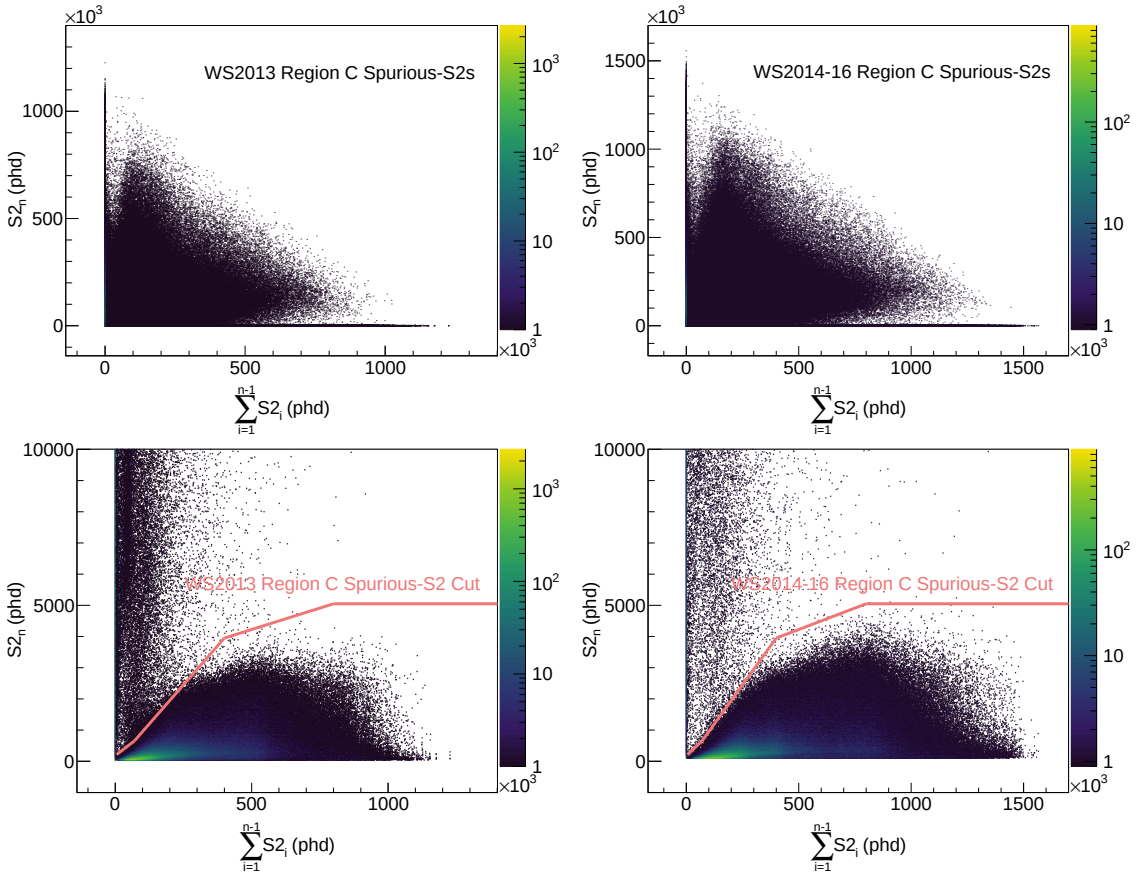

Figure 3.14: The top plots show region-C spurious $S2$s occurring in γ ray and β decay background events for WS2013 (left) and WS2014-16 (right). The primary $S2$s lie in the center of the plot and the line $x = 0$ while the spurious $S2$s lie along $y = 0$. The bottom plots show a zoomed in view of the spurious pulses and compares them to a threshold cut used to identify them as "spurious".

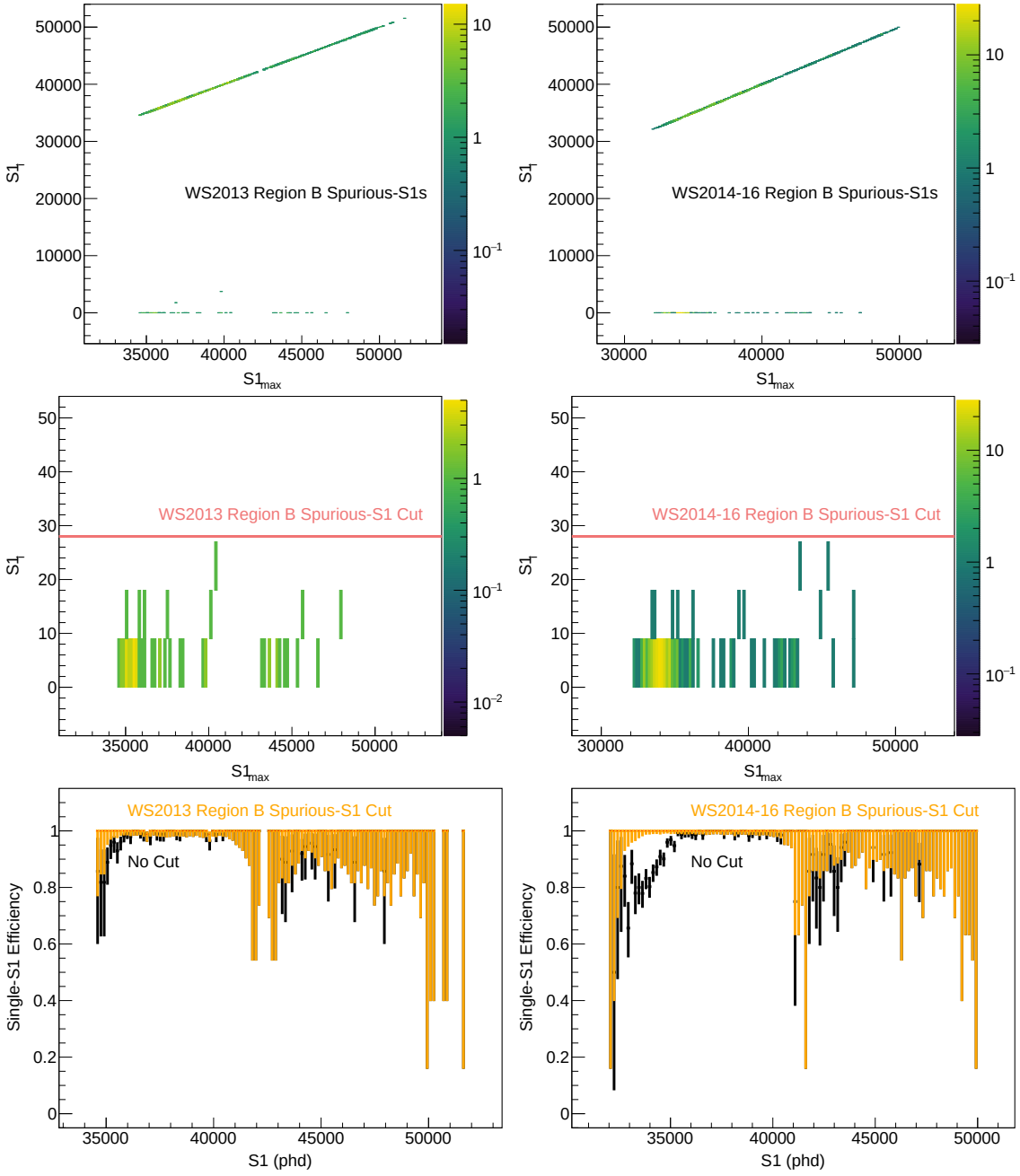

Figure 3.15: The top plots show region-B spurious $S1$s occurring in ^{222}Rn/^{218}Po events for WS2013 (left) and WS2014-16 (right). The primary $S1$s lie along the line $y = x$ and the spurious $S1$s lie along $y = 0$. The middle plots show a zoomed in view of the spurious pulses and compares them to a threshold cut used to identify them as "spurious". The bottom plots show the efficiency for identify single $S1$ events after application of the threshold cut.

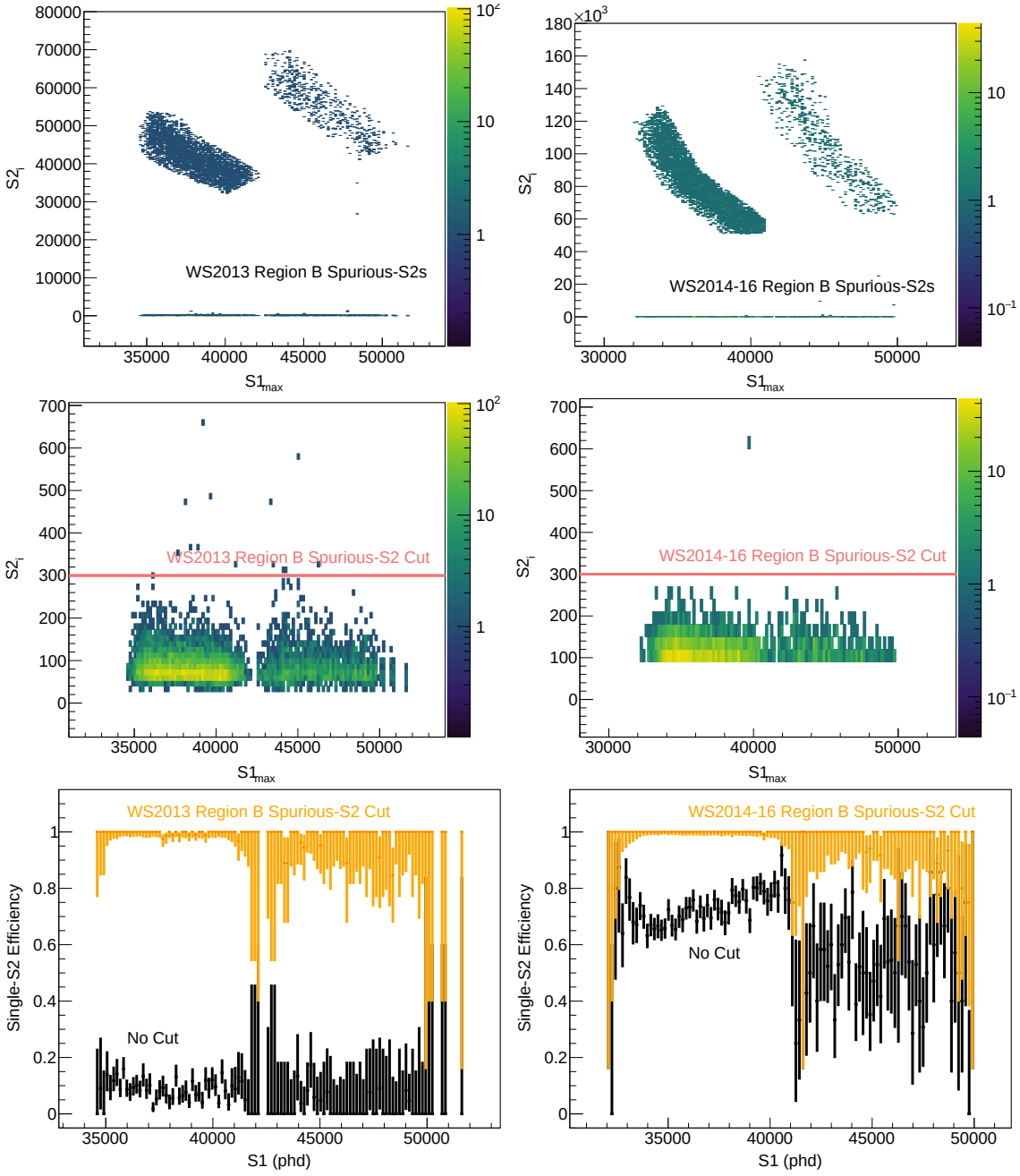

Figure 3.16: The top plots show region-B spurious $S2$s occurring in ^{222}Rn/^{218}Po events for WS2013 (left) and WS2014-16 (right). The primary $S2$s lie in the center of the plot and the spurious $S2$s lie along $y = 0$. The middle plots show a zoomed in view of the spurious pulses and compares them to a threshold cut used to identify them as "spurious". The bottom plots show the efficiency for identify single $S2$ events after application of the threshold cut.

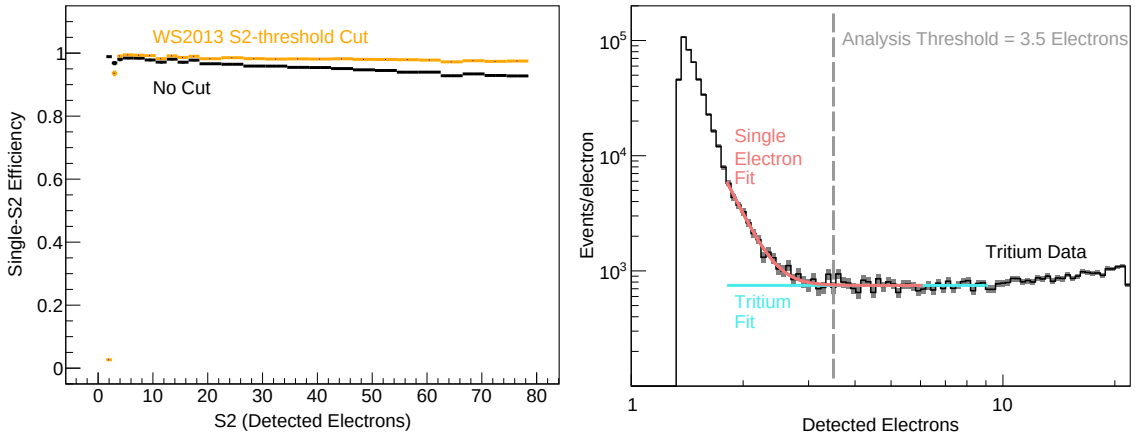

Figure 3.17: Left, the efficiency for selection of single $S2$ events before and after applying the 55 spike count threshold cut used to remove spurious $S2$s, measured using tritium data with a "badarea" cut and a veto following large events. Right, fits of the tritium β decay spectrum and low-energy rise from single-electron backgrounds in the tritium events. The fits were used to estimate the contamination of the above-threshold tritium data by single-electron backgrounds.

Events from a tritium β decay source ($Q = 18$ keV) were used to measure the single-scatter selection efficiency plotted in Fig. 3.17. To obtain a significant quantity of data, waveforms were only required to contain $S2$s, since $S1$s from events of a few are often undetectable. At these energies there are additional backgrounds that can contaminate the calibration data: tritium decays occurring in the gas and spurious $S2$s induced by preceding high-energy interactions. Many vapor events have wide degraded $S2$s and elongated $S1$s that are divided by the pulse finder into many separate pulses. They were mitigate with a cut on a parameter named "badarea" defined as the integrated area of the waveform trace minus the area of the $S1$ and $S2$ pulses. $S2$s induced by preceding high-energy interactions were mitigated with veto was removing livetime after previous large events (described in further detail in Chapter 7).

The veto greatly diminishes the tritium background rate from multiple-electron $S2$s induced by previous events but leaves a significant population of single-electron pulses of the same origin. This condition is visible in Fig. 3.17 (right) as a sharp rise in the $S2$ spectrum at ~ 1 detected electron. The efficiency calculation relies on purity of the tritium data, thus these backgrounds can significantly bias the result in the lowest-energy bins.

To estimate the degree of contamination of the tritium data by single-electron backgrounds, the spectrum was fit with the function $f(S2) = A + Be^{-CS2}$, in which the constant term models the beta decay in the low-energy regime and the exponential approximates the rise in event rate due to backgrounds. The fractional contamination of the data was then

$S2$ Range (detected electrons)	Fractional Contamination
2.5–3.5	0.096
3.5–4.5	0.002

Table 3.1: Fractional contamination of tritium calibration data with single-electron backgrounds induced by previous events, after applying a "badarea" cut and veto following large events.

calculated from $\frac{\int_{S2_{low}}^{S2_{high}} Be^{-CS2}dS2}{\int_{S2_{low}}^{S2_{high}} f(S2)dS2}$ for two ranges of $S2_{low}$–$S2_{high}$, see Table 3.1. In the bin $3.5 > S2 > 4.5$ detected electrons, thus all higher-energy bins, the contamination is $< 1\%$ which introduces a sufficiently-low systematic uncertainty into the efficiency measurement. An analysis threshold is imposed at 3.5 detected electrons to reject events in the low-energy region where the measurement cannot be trusted.

Algorithm

The algorithm employing threshold cuts outlined in Sec. 3.2 used to select events based on the number of primary $S1$s and $S2$s, is illustrated in Fig. 3.18. The same logic is applied to both WS2013 and WS2014-16, although the cuts used to distinguish between primary and spurious pulses vary between the two datasets. The efficiency measurements made using calibration and background data ensure the algorithm can be used to select single-scatter events (one primary $S1$ and $S2$) with near-unitary efficiency over the wide range of interaction energies observed in the LUX data.

3.3 High-energy Single-scatter Spectrum

The event selection algorithm is most useful at energies > 300 keV where incident γ rays—the greatest source of radiogenic backgrounds in the detector—predominately interact via Compton scattering or pair production, processes that result in transfer of only part of the particles energy to the xenon. The remaining energy can be deposited in further interactions, resulting in multiple-scatter events that are inconsistent with signals of interest which produce mostly single-scatters, such as ^{134}Xe and ^{136}Xe $0\nu\beta\beta$ decay. In this regime, many background events can be rejected by using the algorithm to select events with just one $S1/S2$ pair.

To evaluate usefulness of the event selection algorithm, the WS2014-16 spectrum before and after rejecting multiple scatters is plotted in Fig. 3.19. The event rate is reduced by a factor of ~ 3 throughout the region of the spectrum spanned by the ^{134}Xe and ^{136}Xe $0\nu\beta\beta$ decay Q-values, 826 to 2458 keV. The reduction in rate corresponds to an approximately three-fold increases in sensitivity to these hypothetical signals.

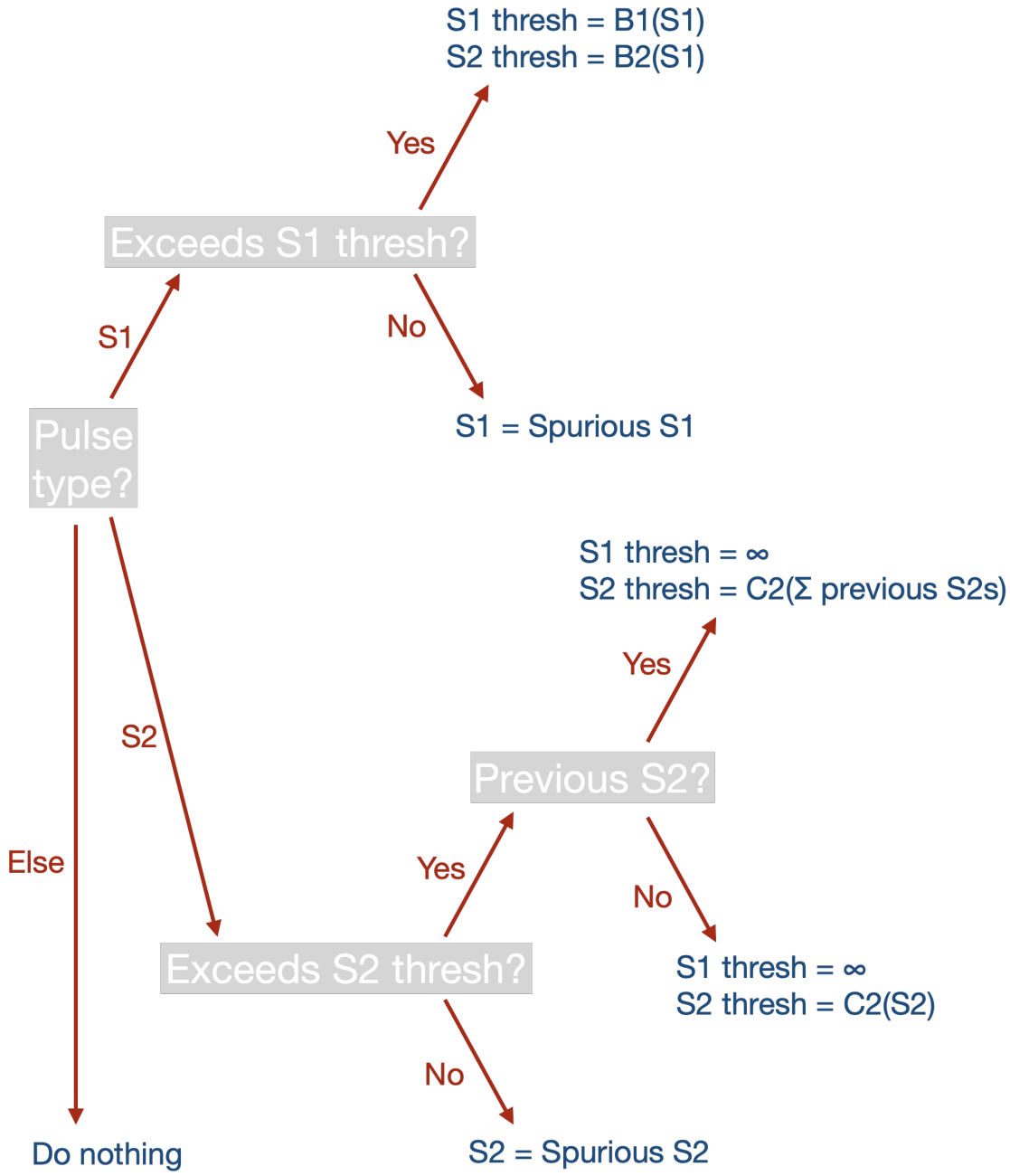

Figure 3.18: The algorithm that labels $S1$s and $S2$ as "primary" or "spurious" and selects events based on the number of primary $S1$s and $S2$s—neglecting the spurious pulses. The algorithm iterates through pulses from the start to the end of an event waveform. When it encounters the first $S1$ it labels it a primary $S1$ then begins applying region B threshold cuts to subsequent pulses labelling them as either primary or spurious. When it encounters the first $S2$ that passes the region B $S2$-threshold cut, it labels it a primary $S2$ then begins applying region C threshold cuts to subsequent pulses.

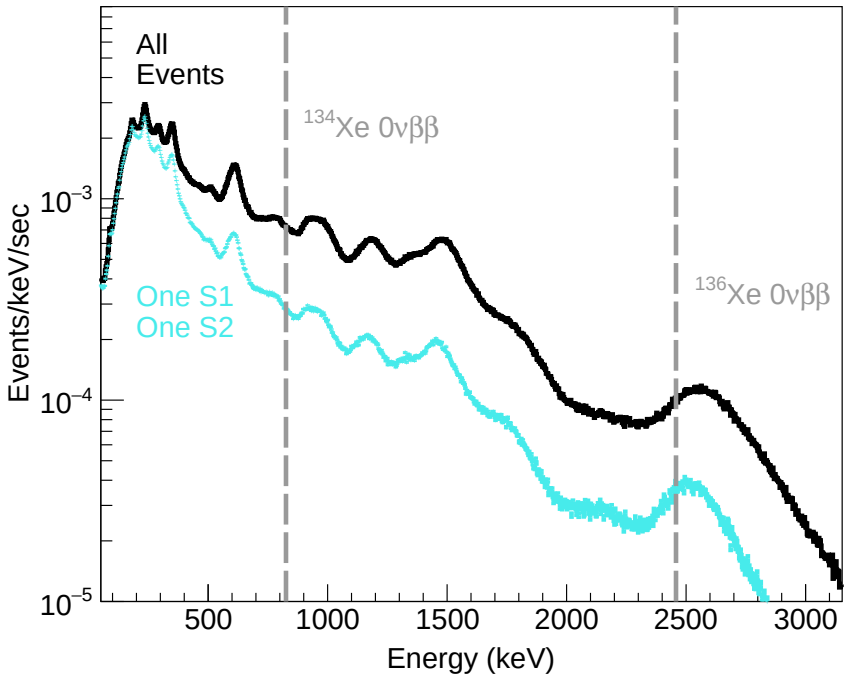

Figure 3.19: Energy spectrum before and after applying the single scatter selection algorithm described in this chapter. The event rate is reduced by a factor of ~ 3 throughout the region of the spectrum spanned by the ^{134}Xe and ^{136}Xe $0\nu\beta\beta$ decay Q-values, 826 to 2458 keV.

Chapter 4

Energy Reconstruction

Chapter 2 outlined the fundamentals of calibration and energy reconstruction with dual-phase xenon time projection chambers (TPCs). Some of these concepts are summarized again here, as they are central to the Doke analysis of the LUX WS2014-16 data presented in this chapter.

To begin, the equation for the energy of an electron recoil (ER) is rewritten below.

$$E = W(n_\gamma + n_e). \tag{4.1}$$

n_γ is the number of scintillation photons, n_e is the number of free electrons, and W is the average energy required to produce one of these quanta (13.7 ± 0.2 eV/quantum)[1].

The scintillation photons and electrons are produced in two processes that accompany the ER. First, the recoiling electron dissipates its energy by exciting and ionizing atoms along its trajectory. All of the excited atoms will decay by emission of scintillation photons that disperse from the recoil site, but only a some of the free electrons will escape this locale. The imbalance occurs because of interference from the second process in which a fraction of the ionized atoms recombine with electrons to produce additional excitation. Consequently, the final numbers of scintillation photons and free electrons can be written as

$$n_\gamma = n_{ex} + r n_i \tag{4.2}$$

$$n_e = (1 - r) n_i \tag{4.3}$$

where n_{ex} is the original number of excited atoms, n_i is the original number of ionized atoms, and r the fraction of recombining ion-electron pairs.

r depends on the energy of the ER and the magnitude of an applied electric field (E_{drift})—among other things [68, 71, 72, 73]. Larger field magnitudes drift electrons away from their liberation site more quickly reducing the chance that they recombine with a nearby ion. In

[1]The W value selected for use in this dissertation is from [68]. The measurement was made in a dual-phase xenon TPC using PMTs to detect photons. A single-phase xenon TPC using avalanche photodiodes has measured a discrepant value, $W = 11.5 \pm 0.5$ eV/quantum [77], but the reason for its inconsistency with the previous result is not yet known.

WS2014-16, there was appreciable nonuniformity of the field, thus the average recombination fraction, $\langle r \rangle$, would have had significant position dependence [90]. For the range of fields observed during this run, 50–400 V/cm, the $\langle r \rangle$ of an ER with a few hundred keV of energy would have varied by a factor of ~ 2 across the detector. In a uniform electric field, for comparison, the r would fluctuate by $\sim 10\%$ due to binomial statistics and other physical effects such as the microscopic structure of the ER track [133, 134].

Promptly after the ER, the scintillation photons are detected by the PMTs at the top and bottom of the TPC producing the $S1$ signal. The free electrons are drifted upward by the force of E_{drift} then extracted from the liquid into the vapor by a stronger electric field, E_{ext}, applied over the interface. Once in the vapor, they generate electroluminescence that is also detected by the PMTs, the $S2$ signal. The numbers of scintillation photons and free electrons are related to the size of the $S1$ and $S2$ signals by

$$n_\gamma = \frac{S1}{g_1} \qquad\qquad n_e = \frac{S2}{g_2} \tag{4.4}$$

where g_1 and g_2 are parameters that encompass the detector specific efficiencies and gains. These conversions can be used to express the energy entirely in terms of observables and predetermined quantities as is shown below.

$$E = W\left(\frac{S1}{g_1} + \frac{S2}{g_2}\right) \tag{4.5}$$

There are effects that cause the detection efficiency for individual scintillation photons and freed electrons, thus the size of $S1$s and $S2$s, to vary with position of an interaction in the TPC. Scintillation photons can reflect on the internal or external surface of the liquid, encounter impurities in the xenon, and come in contact with absorptive components of the TPC such as the grids. Furthermore, the refractive index of the PMT photocathode windows is more similar to that of liquid xenon than gaseous xenon, causing the average quantum efficiency (QE) of the bottom PMTs to be greater than that of the top PMTs. The combined result of these effects is that $S1$s from the bottom and radial center of the detector are larger than those at the top and sides. Similarly, electrons travelling through the xenon can encounter and sometimes become captured by an impurity. The probability of such an occurrence increases with time spent drifting through the xenon as described by $P = e^{-t_{drift}/\tau_e}$, where τ_e is the purity dependent lifetime of a drifting electron (i.e. the "electron lifetime"). Furthermore, deflection of the wire grid electrodes that generate E_{ext}, due to the force of this field, can cause the extraction efficiency to vary over the horizontal plane, most notably with the radial coordinate, r_{S2}. These effects—in addition to all those described for scintillation photons since electroluminesence photons also encountered such effects—cause $S2$s from the top and radial center of the detector to be larger than those at the bottom and sides.

Calibration data is used to define detector response corrections that normalize $S1$s to the center of the TPC and $S2$s to the top and horizontal center (with an electron-lifetime

correction followed by a second horizontal scaling). Equations 4.5 can then be expressed in terms of the corrected pulses $S1_c$ and $S2_c$,

$$E = W\left(\frac{S1_c}{g_1} + \frac{S2_c}{g_2}\right). \tag{4.6}$$

Note that g_1 and g_2 in the above equation are also implicitly defined in terms of the corrected pulses. In this form, they can be expressed in terms of the normalized photon detection efficiency in the liquid (PDE), extraction efficiency (EE), and single electron size (SE), where the latter is the normalized number of detected electroluminescence photons per electron,

$$g_1 = PDE \qquad\qquad g2 = EE \times SE. \tag{4.7}$$

A "Doke" analysis is generally used to calculate g_1 and g_2. Equation 4.6 is written in the form

$$\frac{S1_c}{E} = \frac{g_1}{W} - \left(\frac{g_1}{g_2}\right)\frac{S2_c}{E}. \tag{4.8}$$

a linear equation in variables $\frac{S2_c}{E}/\frac{S1_c}{E}$. Typically, the equation is fit to data from radiogenic decays with energies corresponding to distinct $\langle r\rangle$, thus a variety of $\left(\frac{S2_c}{E}, \frac{S1_c}{E}\right)$ combinations. However, there is another possible method that can be used on WS2014-16 data. The E_{drift} nonuniformity increases the variation in r enough so that data at just a single decay energy can be used to constrain g_1/g_2.

The remainder of this chapter describes a Doke analysis of LUX WS2014-16 data used to measure g_1 and g_2. It takes advantage of the variation in r with both energy and electric field magnitude. An in-depth investigation into the largest sources of systematic uncertainty was performed to evaluate the accuracy of the result. There is evidence that the variation in r introduced a bias into the calculation of the detector response corrections. A modest time dependence of g_1 and g_2 is also noted and possible causes of this behavior are discussed. The results are used to reconstruct the energy of ^{210}Pb events in Chapter 5 and many other LUX analyses not discussed in this dissertation.

4.1 Determination of g_1 and g_2

The radiogenic sources available during WS2014-16, include: a ^{83m}Kr calibration source injected periodically into the xenon (41.5 keV), decays of activated xenon isotopes produced during and shortly after five DD neutron generator calibrations (67–277 keV), and photoabsorptions of γ rays emitted by the decays of radiocontamination in the detector components (235–2614 keV). They are shown in Fig. 4.1.

Only some of the isotopes produced high-quality events that could be used in the Doke analysis used to determine g_1 and g_2.

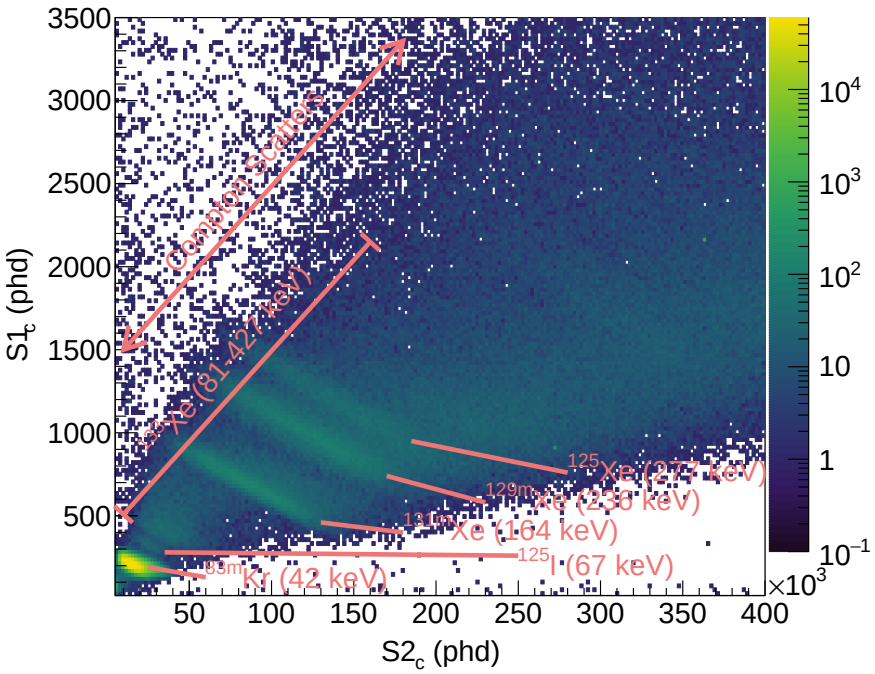

Figure 4.1: Events from background and calibration sources present during WS2014-16. The data in this plot are from the DD calibration beginning in May of 2016.

The ^{83m}Kr data were excluded because of the isotopes two-step decay—going first to a metastable state with 154 ns half life, emitting 32.2 keV, then to the ground state, emitting a final 9.4 keV. ^{83m}Kr data have atypical $S1/S2$ covariance because the underlying number of ions and excitons, as well as the recombination fraction, are more representative of the two separate 9.4 and 32.2 keV events, as opposed to a single 41.5 keV event.

The use of γ rays is precluded by the presence of photomultiplier tube (PMT) saturation which was observed to contort the large $S2$s produced by high-energy events ($E \gtrsim 250$ keV) that generate many free electrons. Once extracted from the liquid, the electrons produce lots of electroluminesence, the majority of which is collected by a few PMTs directly above the horizontal position of the electrons. These PMTs see large signals that often exceed the dynamic range of the digitizer, as is shown in Fig. 4.2.

Fortunately, there is high-quality data from two monoenergetic xenon activation isotopes. ^{131m}Xe and ^{129m}Xe are produced in significant quantities by the DD generator and both have decays of intermediate energy, 164 keV and 236 keV, respectively. Due to the 12 and 9 day half-lives of these isotopes, there are many events during and after each of five the DD calibrations beginning in Sep 2014, Mar 2015, Oct 2015, Feb 2016, and May 2016. The analysis is performed on five datasets composed of livetime during each of the calibrations and the two subsequent weeks.

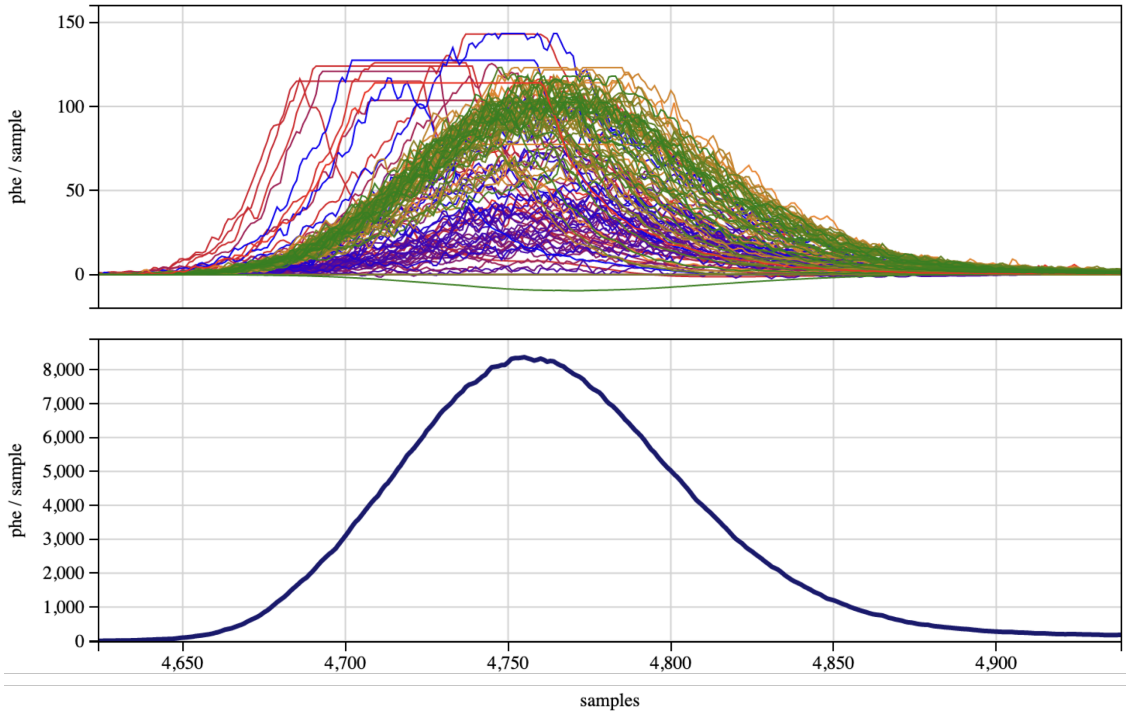

Figure 4.2: Waveform of an $S2$ exhibiting effects from saturation of the dynamic range of the digitizer, which bias the reconstructed energy of events with very large $S2$s downward. The bias becomes significant above $\sim$ 250 keV. Individual PMT waveforms are shown in the top panel; the waveforms that plateau at a specific number of phe/sample are saturated. The sum of the waveforms is shown in the bottom panel.

In $(S1_c, S2_c)$ space, the ^{131m}Xe and ^{129m}Xe populations are surrounded by backgrounds from ^{133}Xe/^{125m}Xe activation isotopes and a continuum of Compton scatters from high-energy γ rays, all identified in Fig. 4.1. To obtain mostly pure selections of ^{131m}Xe and ^{129m}Xe events, the populations were fit with 2-dimensional Gaussian functions that approximate their shape. Elliptical cuts were defined at 1.5σ–2.4σ where σ is the 2-dimensional standard-deviation parameter of the Gaussian. The populations are not exactly elliptical, but instead asymmetrically distributed along the axis of recombination as determined by the prevalence of electric field magnitudes observed in the detector. Additionally, there is a smaller contribution to the asymmetry from recombination fluctuations which themselves are not Gaussian [134]. As a consequence, the elliptical cuts were chosen to be broad enough to encompass the whole asymmetric shape, as illustrated in Fig. 4.3.

^{131m}Xe and ^{129m}Xe events passing the elliptical cuts are plotted in $\left(\frac{S2_c}{E}, \frac{S1_c}{E}\right)$ space in Fig. 4.4. The data are distributed about the line described by Equation 4.8 whose intercepts are $x_{int} = g_1/W$ and $y_{int} = g_2/W$. The objective is to identify the intercepts and the

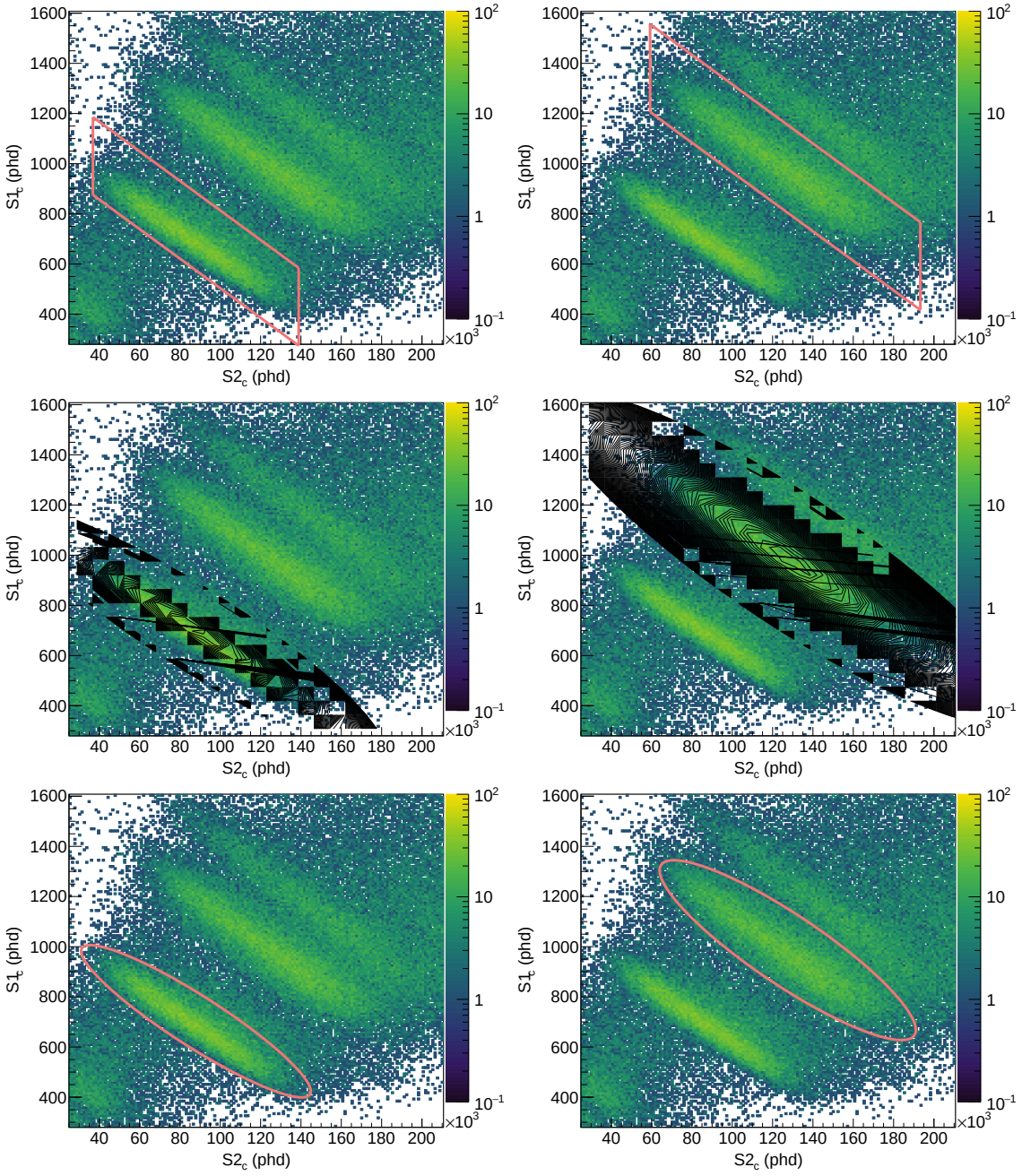

Figure 4.3: The top panels show the rectangular cuts used to isolate populations of ^{131m}Xe (left) and ^{129m}Xe (right) events in the May 2016 data. The middle panels show Gaussian fits to these populations and the bottom panels show the elliptical cuts placed at the 2.3σ (^{131m}Xe) and 2σ (^{129m}Xe) contours of the fits, where σ is the 2-dimensional standard-deviation parameter of the Gaussian. Cuts from other DD calibrations are placed at different contours, ranging from 1.5σ–2.4σ, because of minor variations in the datasets.

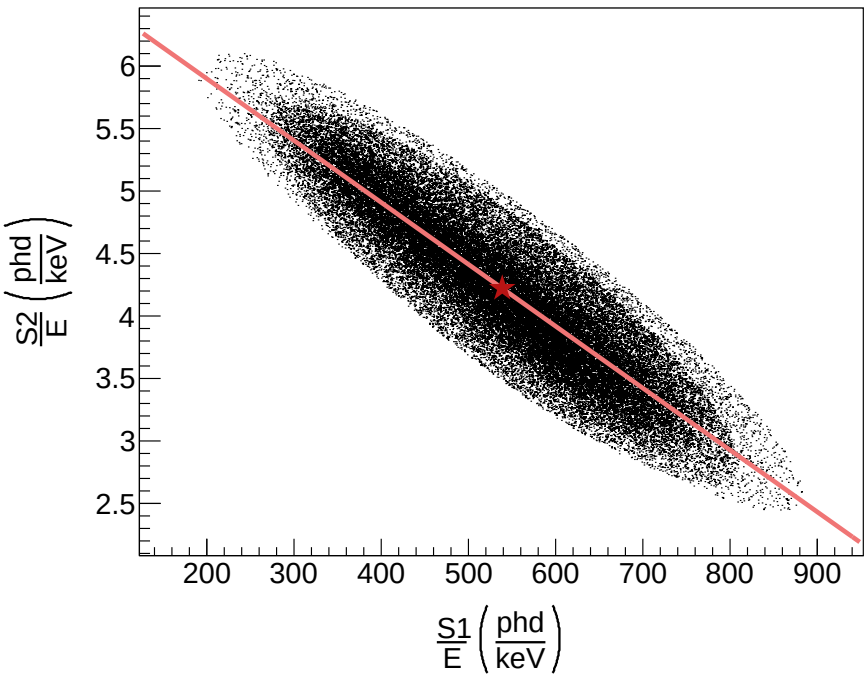

Figure 4.4: Doke plot of the May-2016 ^{131m}Xe and ^{129m}Xe data. A red star is drawn at the center of the data and a pink line is drawn through the first principle component. g_1 and g_2 values are calculated from the intercepts of the line, $x_{int} = g_1/W$ and $y_{int} = g_2/W$.

corresponding statistical error. This was done using a bootstrap technique in which the data were treated as an empirical probability distribution function. In 400 trials, the n datapoints were sampled at random with repetition n times, principle component analysis was used to find the direction that maximizes the variance of the sample, the result was used to construct the equation of a line passing through the center of the sample, and g_1/g_2 were calculated from the intercepts of the line. The resulting distribution of g_1/g_2 values is plotted in Fig. 4.5. The 50th percentiles of the distribution were adopted as the final g_1 and g_2 values, given in Table 4.1. The upper and lower statistical uncertainty were calculated from the 86th and 14th percentiles: $g^i_{1,2}(86\%) - g^i_{1,2}(50\%)$ and $g^i_{1,2}(50\%) - g^i_{1,2}(14\%)$, respectively.

4.2 Systematic Uncertainty

There are several systematic uncertainties associated with the measurements of g_1 and g_2 presented in the previous section. The linear fits for these parameters can be skewed by the small fraction of background events accepted by the elliptical cuts outlining the ^{131m}Xe and ^{129m}Xe populations. The detector response corrections can have a residual dependence on the electric field through r—despite the measures taken to mitigate this effect, described in

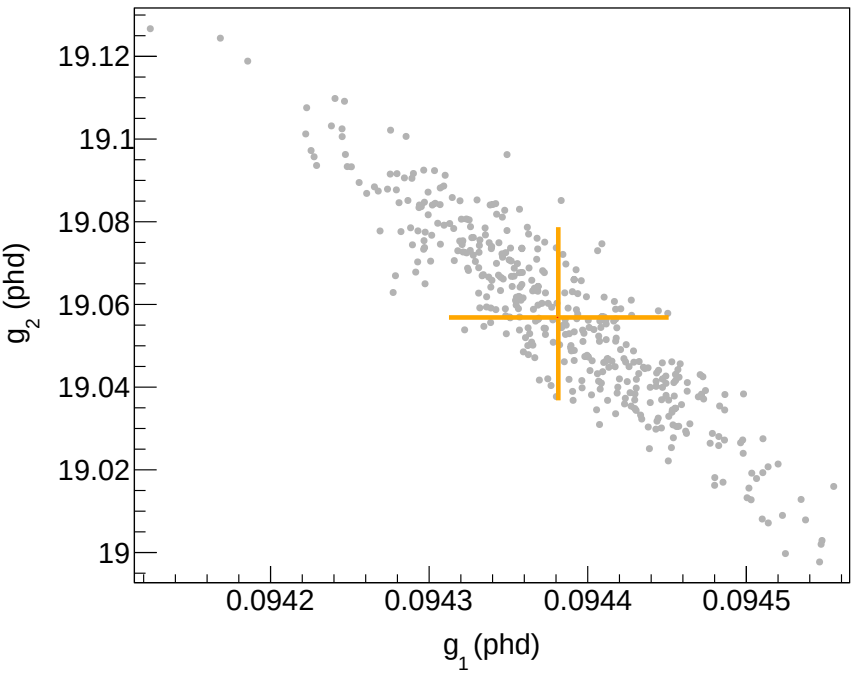

Figure 4.5: Distributions of g_1 and g_2 values calculated for each of the 400 bootstrap trials. In each trial, the Doke plot data (shown in Fig. 4.4) were treated as an empirical probability distribution function. The n datapoints were sampled at random with repetition n times and new g_1 and g_2 values were calculated from the selection. The yellow lines intersect at the 50th percentiles of the distribution and extend from the 14th to the 86th percentiles. The point of intersection is adopted as the final (g_1, g_2) pair and the range of the lines as an estimate of the statistical uncertainty on both these values.

Sec. 2.2 of Chapter 2. The relatively large $S2$s of ^{131m}Xe and ^{129m}Xe events are trailed by large quantities of electrons—discussed in detail in Chapter 3—which the waveform processing software can mistake as part of the primary pulse causing an overestimate of $S2$ size. Finally, there might be unanticipated energy-dependent effects that introduce a similar dependence into the g_1 and g_2 calculation.

Uncertainty introduced by the elliptical cuts was estimated by varying the definition of these cuts based on the error of the elliptical fit. For simplicity, only the parameter defining the angle of the ellipse (θ) was varied as it was considered the most likely to effect the calculation of g_1 and g_2 through their dependence on the covariance of the data. The linear fit was performed three times on data passing an elliptical cut defined at angles θ, $\theta + \sigma_\theta$, and $\theta - \sigma_\theta$, shown in Fig. 4.6. The fractional uncertainty introduced by the elliptical cut was defined as $\pm\frac{|g_{1,2}(\theta) - g_{1,2}(\theta \pm \sigma_\theta)|}{g_{1,2}(\theta)}$. The results are presented in Table 4.1.

The remaining uncertainties were estimated simultaneously by varying relevant param-

Month	g_1	σ_{stat}	$\sigma_{ell,sys}$	σ_{sys}	g_2	σ_{stat}	$\sigma_{ell,sys}$	σ_{sys}
Sep 2014	0.0990	$+0.0001$ -0.0001	$+0.0001$ -0.0001	$+0.0016$ -0.0071	19.74	$+0.03$ -0.03	$+0.02$ -0.03	$+3.67$ -0.57
Mar 2015	0.0973	$+0.0002$ -0.0002	$+0.0006$ -0.0006	$+0.0015$ -0.0070	19.81	$+0.08$ -0.07	$+0.19$ -0.15	$+3.68$ -0.58
Oct 2015	0.0984	$+0.0002$ -0.0002	$+0.0003$ -0.0003	$+0.0016$ -0.0071	18.73	$+0.05$ -0.05	$+0.11$ -0.09	$+3.48$ -0.54
Feb 2016	0.0961	$+0.0001$ -0.0001	$+0.0001$ -0.0001	$+0.0015$ -0.0069	19.01	$+0.03$ -0.03	$+0.03$ -0.03	$+3.54$ -0.55
May 2016	0.0944	$+0.0001$ -0.0001	$+0.0001$ -0.0001	$+0.0015$ -0.0068	19.06	$+0.02$ -0.02	$+0.03$ -0.02	$+3.54$ -0.55

Table 4.1: g_1 and g_2 for each of the five DD calibrations along with estimations of the statistical and systematic errors.

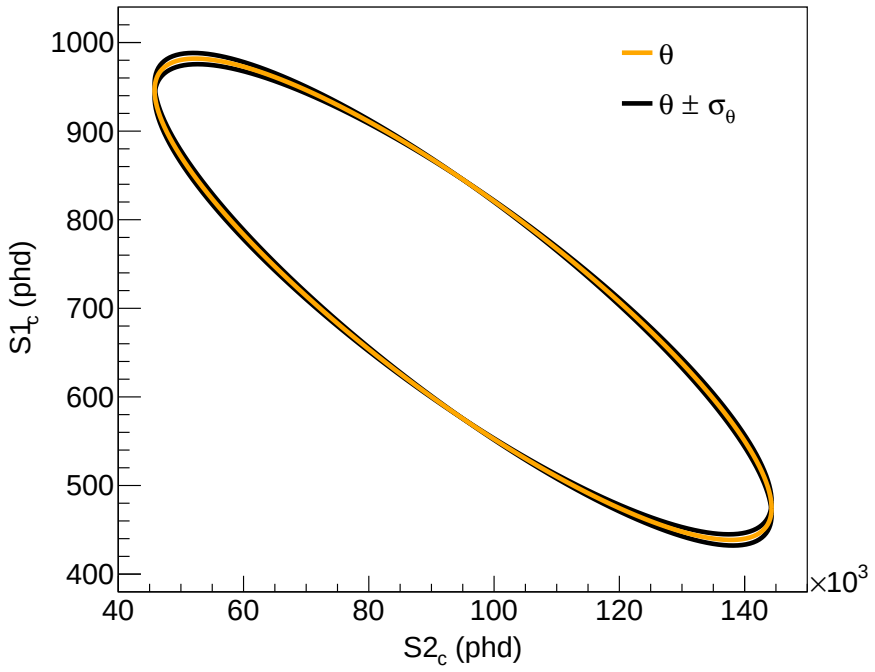

Figure 4.6: The elliptical cut of the May-2016 ^{131m}Xe population drawn at the best fit angle, θ (yellow) and the same elliptical cut drawn at $\theta \pm \sigma_\theta$, where σ_θ is the uncertainty on the fit parameter (black). $g_{1,2}(\theta \pm \sigma_\theta)$ were used to approximate the fractional systematic uncertainty introduced by the elliptical fit, $\pm\frac{|g_{1,2}(\theta)-g_{1,2}(\theta\pm\sigma_\theta)|}{g_{1,2}(\theta)}$.

eters and cuts each time calculating new g_1 and g_2 values. The data were divided into 12 drift-time bins, each containing 8.33% of the data, to capture uncertainty related to electric-field dependence of the corrections. The drift time is the most useful coordinate to use in this pursuit, since the electric field varies more significantly with t_{drift} than (x_{S2}, y_{S2}). The average electric field in each drift bin is shown in Fig. 4.7. The size of $S2$s were measured using two different parameters: the area of the pulse waveform (used in the originally calculation that was presented in the previous section) and the area of a Gaussian fit to the waveform. The latter, reduces the effect of trailing electrons. Finally, ^{131m}Xe and ^{129m}Xe data were separated to look for unanticipated energy dependence visible between 164 and 236 keV.

Fig. 4.8 presents g_1 and g_2 distributions calculated from the 48 variations described above. The corresponding positive and negative fractional systematic uncertainties are defined as $-\frac{|g_{1,2}-g^i_{1,2}(14\%)|)}{g_{1,2}}$ and $+\frac{|g^i_{1,2}(86\%)-g_{1,2}|)}{g_{1,2}}$ where $g_{1,2}$ are the final values calculated from Fig. 4.5.

The final g_1 and g_2 values are offset from the corresponding distributions in the positive and negative directions, respectively. This is understood to be a side effect of the drift time binning. Each bin contains a smaller range of electric fields than is present across the whole drift length. Consequently, selecting data from only one bin reduces the component of the $\left(\frac{S1}{E}, \frac{S1}{E}\right)$ covarience that is generated by the electric field. $g1$ and $g2$ are less tightly constrained under this circumstance causing odd behavior of the fits. (Note that the definition of the systematic uncertainty is conservative; if there was no offset, g_1 and g_2 would lie between the 14th and 86th percentiles and the uncertainty would be smaller.)

As expected, the g_2 values calculated using the Gaussian fit area to measure $S2$ size are smaller than those calculated using the pulse waveform area, due to the former mitigating the effect of trailing electrons. To a lesser extent, g_2 values calculated from ^{131m}Xe (164 keV) data are smaller than those from ^{129m}Xe (236 keV), which is consistent with higher energy events having a large quantity of trailing electrons, a trend observed in Chapter 3.

It was expected that there would be no significant g_1 trends when comparing ^{131m}Xe data with ^{129m}Xe data and $S2$ pulse waveform areas with Gaussian fit areas. ^{131m}Xe pulse-waveform g_1 values are smaller than those from ^{131m}Xe Gaussian fits, while ^{129m}Xe pulse-waveform g_1 values are larger than ^{129m}Xe Gaussian fits. Additionally, the breadth of the ^{129m}Xe g_1 values is greater than that of ^{131m}Xe. These trends are not well understood.

Fig. 4.9 shows the g_2 values increase with drift time suggesting $S2_c$ is overcorrected for the effect of electron lifetime. This fault is a result of the electric field gradient observed in the TPC during WS2014-16. The magnitude of the field decreases with t_{drift} causing r to be greater lower down in the detector. Accordingly, for an event of any particular energy, the average number of electrons, thus the size of the $S2$, would be smaller near the bottom of the detector. The corrections mistakenly attenuate this effect of the electric field gradient in addition to removing that of the electron lifetime.

There are not a significant drift time dependent trend of the g_1 values. This suggests the correction for $S1$s is not greatly affected by the electric field gradient.

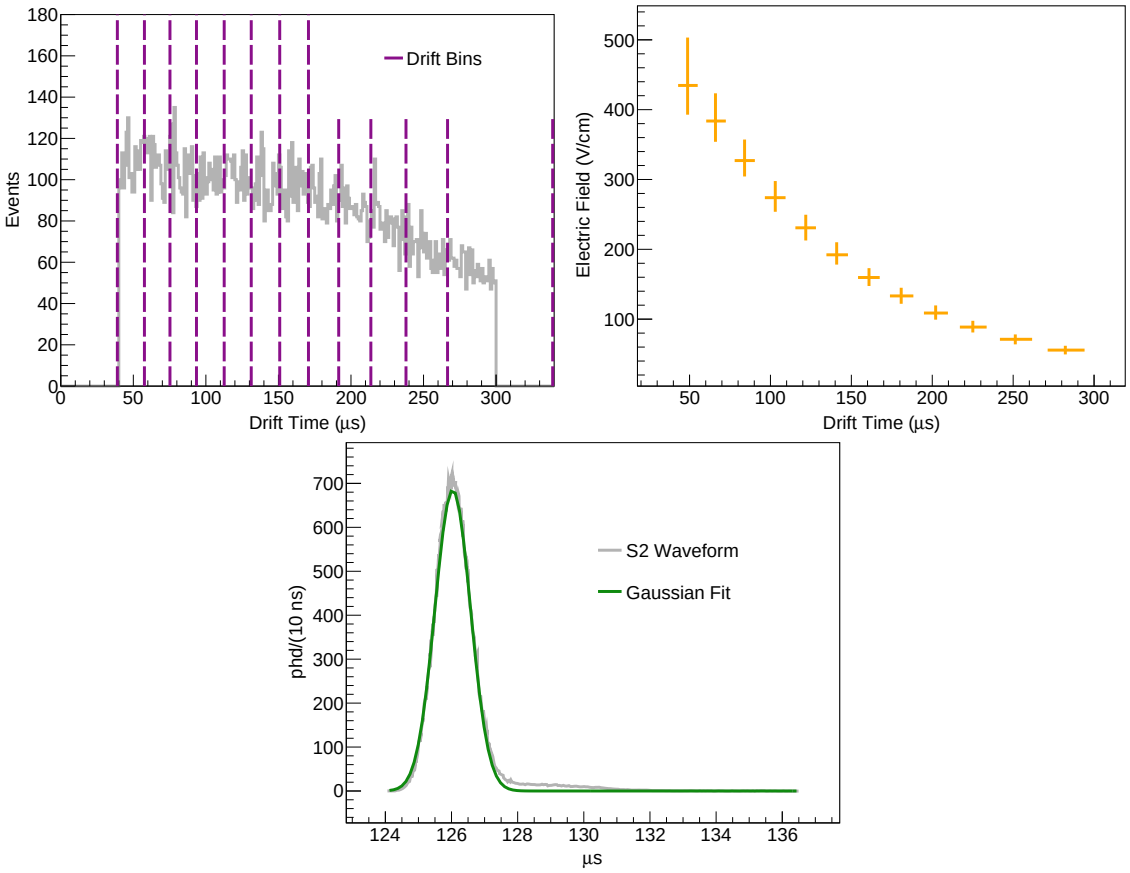

Figure 4.7: On the top left, May-2016 ^{131m}Xe data (solid grey line) and drift bins used to estimate the systematic uncertainty from residual dependence of the $S1/S2$ corrections on the electric field (outlined by dashed purple lines). On the top right, the average electric field in each of the drift bins. In the bottom center, an example of a Gaussian fit (solid green line) to an $S2$ waveform (solid grey line) used to estimate the systematic uncertainty introduced by electrons trailing $S2$s..

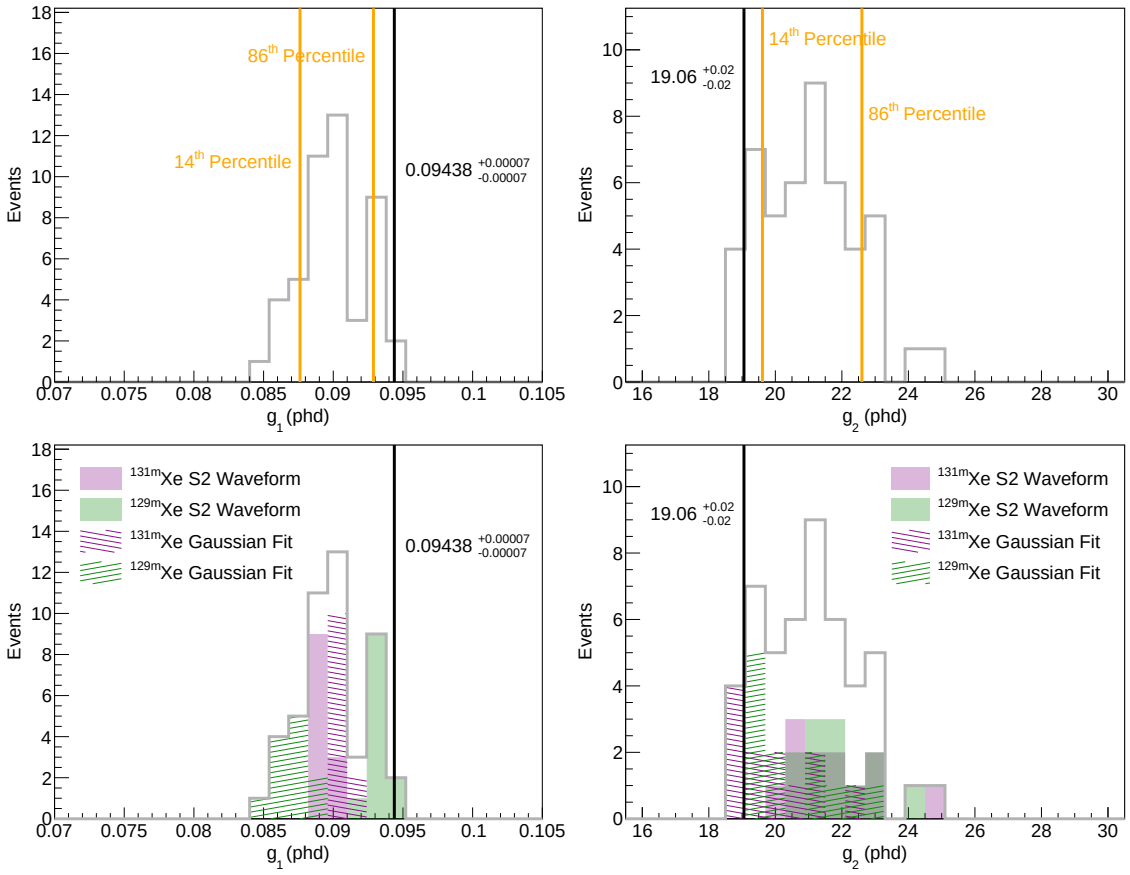

Figure 4.8: Distributions of g_1 and g_2 values calculated by varying relevant parameters and cuts (grey solid lines). The data was broken into subsets of ^{131m}Xe or ^{129m}Xe events, the subsets divided into the drift bins outline in Fig. 4.7, and the $S2$ size was estimated from the pulse waveform area or the Gaussian fit area. In the top plots, the 14th and 86th percentiles of the distributions (yellow) are compared with the final $g1$ and $g2$ values calculated from Fig. 4.5 (black). The positive and negative fractional systematic uncertainties are defined as $-\frac{|g_{1,2}-g^i_{1,2}(14\%)|)}{g_{1,2}}$ and $+\frac{|g^i_{1,2}(86\%)-g_{1,2}|)}{g_{1,2}}$ where $g_{1,2}$ are the final values calculated from Fig. 4.5. In the bottom plot, the distributions are broken into ^{131m}Xe and ^{129m}Xe subsets with $S2$ size calculated from the pulse waveform area or the Gaussian fit area. The g_2 values calculated using the Gaussian fit area are smaller than those calculated using the pulse waveform area, due to the former mitigating the effect of trailing electrons. To a lesser extent, g_2 values calculated from ^{131m}Xe (164 keV) data are smaller than those from ^{129m}Xe (236 keV), due to lower energy events having fewer trailing electrons.

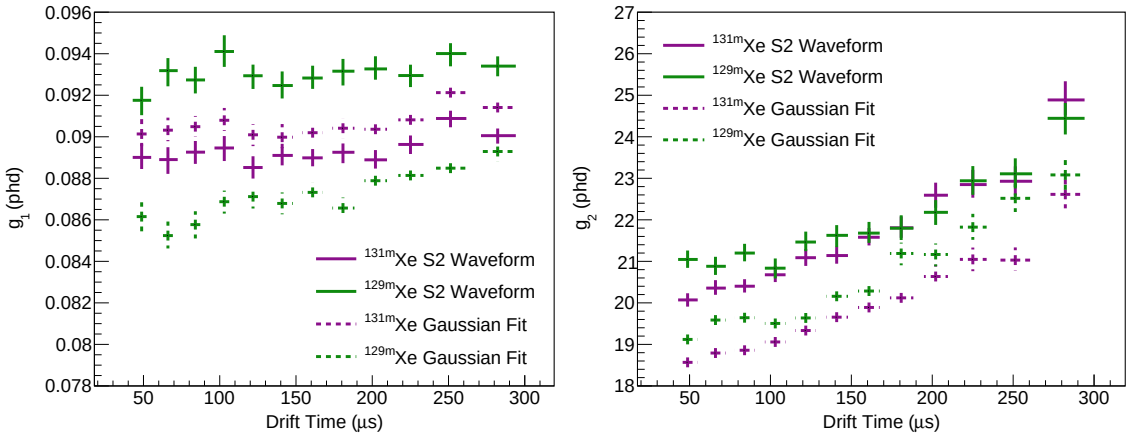

Figure 4.9: Plots of g_1 and g_2 values as a function of drift time. The data is broken into ^{131m}Xe and ^{129m}Xe subsets with $S2$ size calculated from the pulse waveform area or the Gaussian fit area. The g_1 values are relatively stable with drift time while the $g2$ values rise substantially, indicating the $S2$ electron-lifetime correction is overestimated, due to the electric field, thus recombination fraction, gradient. At all drift times, the Gaussian fit areas lead to lower estimates of g_2, as is expected, because this metric reduces the effect of trailing electrons. The variation in g_1 between the ^{131m}Xe/^{129m}Xe subsets and $S2$ size calculations is unanticipated and is not well understood.

4.3 Time Dependence

Fig. 4.10 shows both g_1 and g_2 decrease over the $\sim$ 1.75 year length of WS2014-16. This trend is likely a result of PMT photocathode aging in the form of a slowly diminishing quantum efficiency. Other possible causes are unanticipated effects from the time evolution of the electric field: for example, changing extraction efficiency or single electron size. The former fails to justify the reduction of g_1 in addition to that of g_2, since $S1$s are not affected by the extraction efficiency. Furthermore, independent measurements indicate the single electron size (SE) also decreases with time.

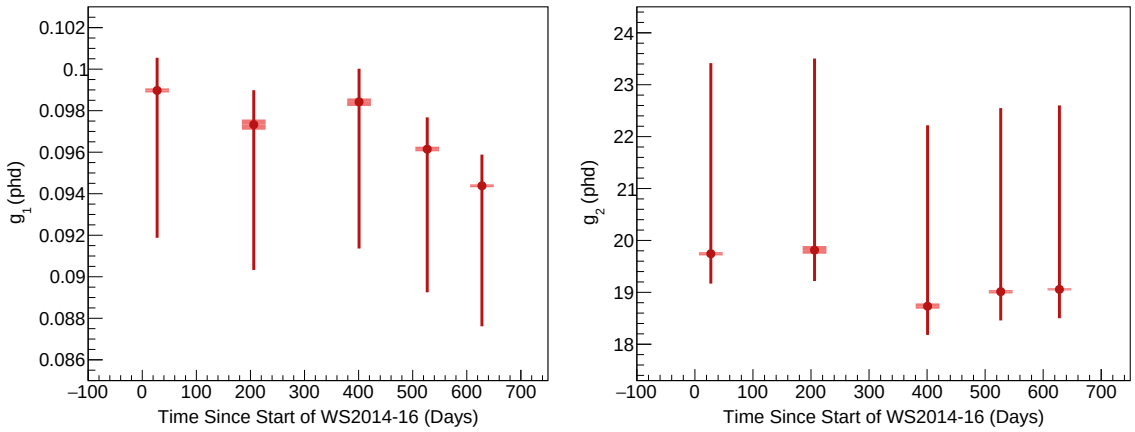

Figure 4.10: g_1 and g_2 as a function of time since the start of the WS2014-16 (red points), their statistical uncertainty (pink bars), and their quadratically-combined systematic uncertainties (red lines). There is a modest decrease in both g_1 and g_2 as a function of time, beyond the size of the statistical uncertainty. This effect is most likely caused by aging of the PMT photocathodes in the form of a slowly diminishing quantum efficiency.

Chapter 5

Radon Backgrounds

One of the highest risk radiocontaminates for dual-phase xenon time projection chambers (TPCs) is radon. This element produces a set of backgrounds over a wide range of energies overlapping the search windows for dark matter (DM), neutrinoless double β decay ($0\nu2\beta$), and many other processes of interest.

Radon is created by three of the four primordial nuclides with half lives short enough to present background challenges on experimental time scales: ^{238}U, ^{232}Th, and ^{235}U (excluding ^{40}K). These isotopes are present in all earthly materials and decay through long chains of daughters of which one is ^{222}Rn, ^{220}Rn, or ^{223}Rn. Only ^{222}Rn and ^{220}Rn are considered in this thesis as the abundance of ^{235}U is not great enough to generate appreciable quantities of ^{223}Rn in most experimental circumstances. The relevant ^{238}U and ^{232}Th decay chains are illustrated in Fig. 6.8.

A factor distinguishing radon as the most pernicious ^{238}U/^{232}Th daughter is its status as a noble gas with very weak intermolecular forces. When a radon parent, ^{226}Ra or ^{224}Ra, happens to be located near a pore space of a material, the atom can α decay at an angle that injects the α particle into the material causing the radon atom to recoil into the pore space. Having very little tendency to bond with the molecules of the pore surface, the radon atom often diffuse out of the pore space and into the surrounding environment.

Liberated radon atoms can introduce radiocontamination into dual-phase xenon TPCs by two paths. First, detector components can inject radon into the xenon through direct contact during operation. Second, radon daughters in the air can plate out on components during construction resulting in long-lived surface contamination from ^{210}Pb, ^{210}Bi, and ^{210}Po. Furthermore, some of these daughters will α decay at an orientation that pushes the recoiling atom below the surface, generating lightly embedded contamination that is less easily washed off. After the detector is closed, some of the surface and embedded contamination remains fixed to the component, and some leaches into the xenon.

This chapter presents a study of radon backgrounds in the Large Underground Xenon (LUX) detector. It begins by detailing a search for α decays from the ^{222}Rn/^{220}Rn chains and uses the results to constrain the interspersed β decays that contaminate searches for new physics. Additionally, it describes how the timing coincidence of ^{214}Bi and ^{214}Po is used to

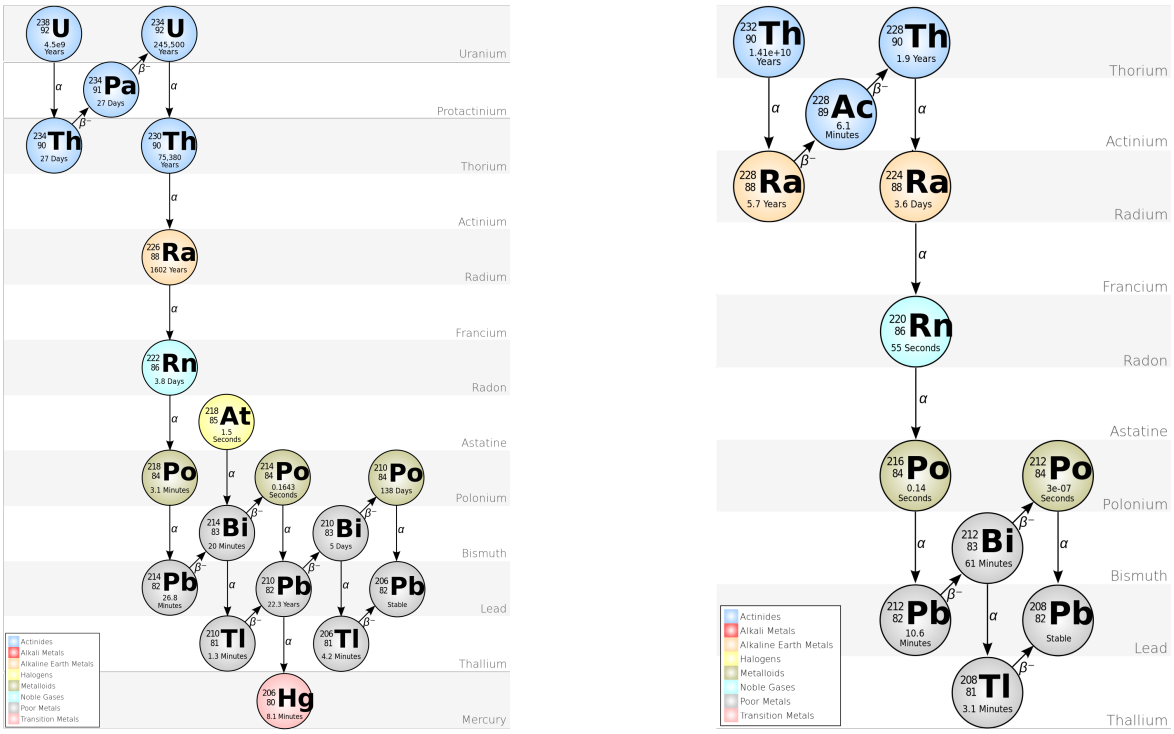

Figure 5.1: ^{238}U or ^{232}Th decay chains containing ^{222}Rn and ^{220}Rn, respectively. Figures from [135].

select these events with high fidelity, to more tightly constrain the ^{214}Pb β decay background. The chapter goes on to present a search for time dependence of surface contamination on the polytetrafluoroethylene (PTFE) walls of the TPC. Finally, it details a search for surface contamination of the wire grid electrodes and outlines systematic differences between the energy calibration of these events and the typical calibration of bulk xenon events.

5.1 Alpha Decays

There are isotopes in the radon chains that α and β decay. The α decays are monoenergetic MeV-scale events that produce very-large quantities of scintillation compared to numbers of free electrons. They are not backgrounds in searches for new physics, because the latter generally occur at lower energies and have charge to light ratios typical of nuclear recoil (NR) or electron recoil (ER) events. However, it is beneficial to study these robust signals, because they can be used to constrain the radon chain β decays which do produce ER events at relevant energies (these are discussed in further detail in Sec. 5.6).

α events in LUX's WS2014-16 dataset were selected by requiring each waveform contain an $S1$ in the range of 20,000–70,000 phd followed by at least one $S2$. A second smaller $S1$

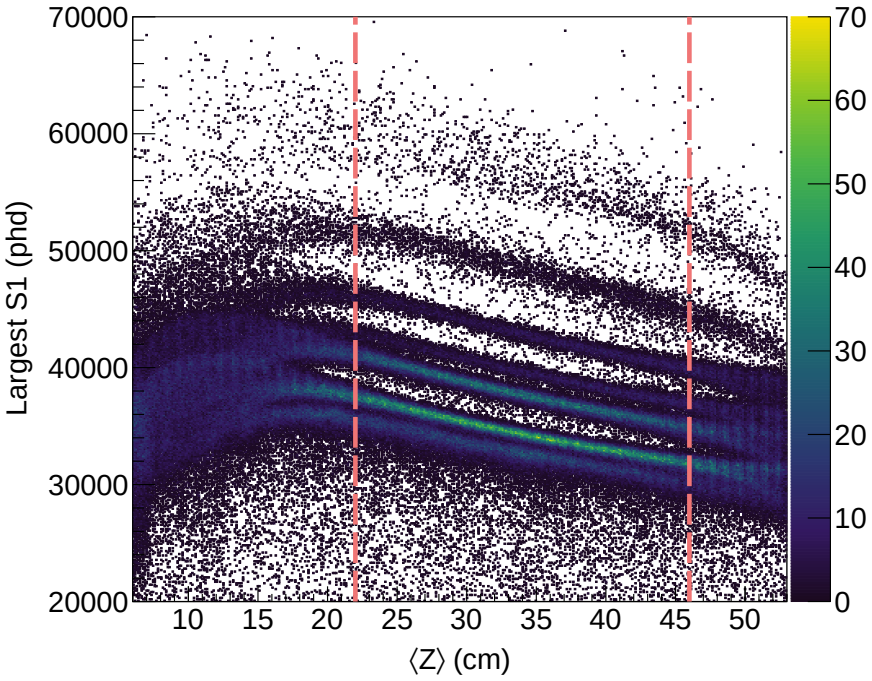

Figure 5.2: $S1$ pulse area as a function of z coordinate for α decays in the ^{222}Rn and ^{220}Rn chains. The pink dashed lines are cuts removing high and low-z events where the scintillation pulse tends to saturate the PMTs reducing $S1$ size and worsening the energy resolution.

was allowed to occur within the same waveform because the short half lives of ^{214}Po and ^{212}Po (162 μs and 0.3 μs, respectively) cause them to usually decay within the same 1 ms event window as their parent, ^{214}Bi or ^{212}Bi. Additional $S2$s were allowed because ^{214}Bi or ^{212}Bi decay through multiple steps emitting both β particles and γ rays often producing several $S2$s.

Because large scintillation signals have a tendency to saturate the photomultiplier tubes (PMTs) by producing signals that exceed the dynamic range of the digitizer—the same effect discussed in Chapter 4 when considering high-energy $S2$s—a second cut on the z coordinate was required to limit the analysis to regions of the detector with $S1$s containing negligible amounts of saturation. This point can be identified in Fig. 5.2 which shows the relationship between the z coordinate and the $S1$ pulse area. It contains 7 stripes each of which correspond to a radon chain α decay. At the very top and bottom of the detector, the fraction of scintillation collected by just a few PMTs nearest to the decay is very large, and the signals observed by these PMTs saturate the digitizer reducing the $S1$ area and worsening the resolution. z limits are placed just below (22 cm) and above (46 cm) these points.

The energy of the selected α decays was reconstructed using only the $S1$, instead of both

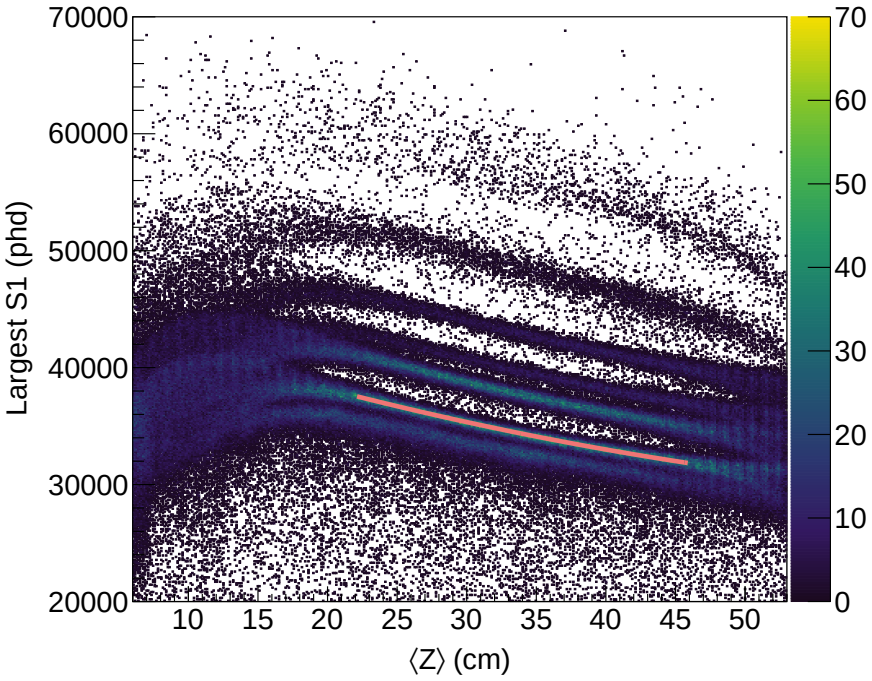

Figure 5.3: Fit of ^{222}Rn events used to correct for z dependence of the photon detection efficiency.

the $S1$ and $S2$, as this method was found to yield sufficiently-low energy resolution due to the vast-majority of energy being channeled into production of scintillation photons [134]. The most prominent streak in the data, from the decay of ^{222}Rn, was fit to a second-degree polynomial to correct for the variation in photon detection efficiency (PDE) with respect to the z coordinate, shown in Fig. 5.3. The corrected data were scaled so that the ^{222}Rn peak was centered at 5.59 MeV. The entire corrected spectrum is shown in Fig. 5.4.

The activity of each isotope was extracted by fitting every peak in the spectrum with an analytical function that best matched its shape, shown in Fig. 5.4. For most peaks this was a Gaussian with small symmetric exponential tails. For ^{210}Po it was a Crystal Ball function generally used to model processes in which a variable fraction of energy is lost to some known or unknown mechanism [136]. In LUX, the process is loss of scintillation to the PTFE walls that occurs because ^{210}Po, unlike the other isotopes, is located at the wall. This fact is demonstrated by the second spectrum in Fig. 5.4, which contains the same data but with a cut removing events within 3 cm of the wall. The ^{210}Po peak is no-longer present after applying the cut indicating all ^{210}Po in the TPC is leftover from radon plate out that occurred prior to the start of WS2014-16. Furthermore, the spectrum indicates these surface contaminates are fixed to the wall, not washing off into the xenon.

There is no difference in the activities of most other isotopes after applying the radial cut,

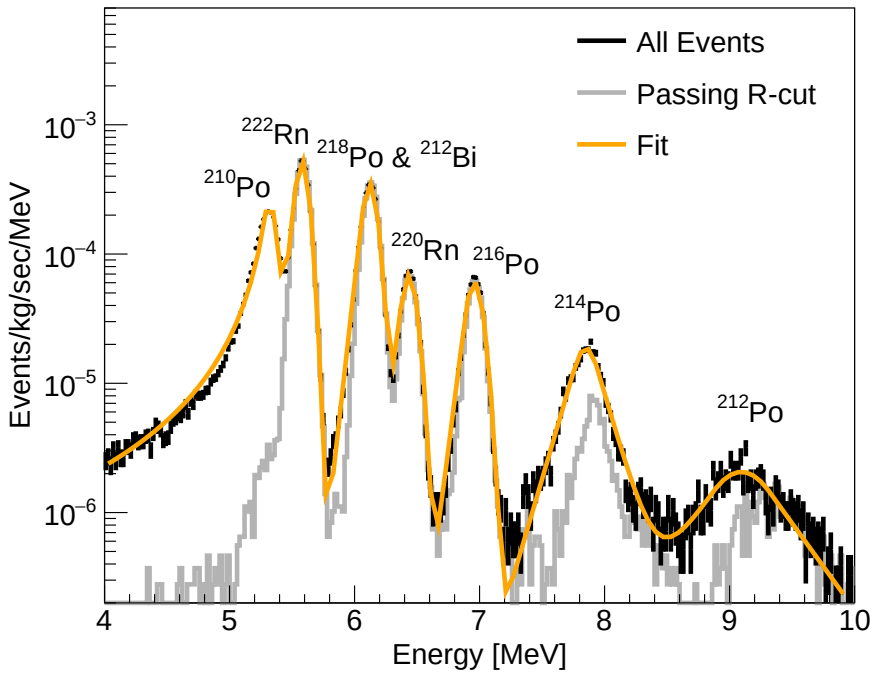

Figure 5.4: Spectrum of α decay events from the ^{222}Rn and ^{220}Rn chains before and after applying a radial cut to reject events within 3 cm of the detector wall. The cut removes essentially all ^{210}Po surface contamination. It also reduces the numbers of ^{214}Po and ^{212}Po events which is a side-effect of inefficiencies in the way data were selected.

because they are distributed mostly-uniformly throughout the liquid xenon. However, ^{214}Po and ^{212}Po have a moderate decrease in event rate that superficially indicates the existence of wall populations. For these isotopes the coincident ^{214}Bi or ^{212}Bi β decay is the culprit. Both are high-energy decays that produce many free electrons and correspondingly huge $S2$s. The electroluminesence light of the $S2$s photoionizes impurities in the xenon producing thick trails of electrons following the primary pulse. Additionally, some of the electrons are trapped at the liquid surface or are captured by impurities and released again with delays of up to seconds (see Chapter 3 for more detail). The trails of electrons sometimes overlap with the ^{214}Po or ^{212}Po $S1$ causing the pulse to be misclassified; however, this happens less frequently near the wall where the ^{214}Bi or ^{212}Bi γ rays have a higher probability of escaping the TPC, in which case they do not produce $S2$s or contribute to the electron trail density. The overall frequency at which misclassification occurs is not known and would require a great deal of effort to measure accurately; therefore, in this work, ^{214}Po or ^{212}Po event rates are always treated as lower limits on their activity.

Table 5.1 summarises the activities and limits extracted from the fit in Fig. 5.4. Isotopes whose decays do not overlap with that of another isotope [^{222}Rn, ^{220}Rn, ^{218}Po, ^{216}Po, and

Decay Chain	Isotope	Q-value (MeV)	Half-life	Event Rate (μBq/kg)
^{238}U	^{222}Rn	5.6	3.8 d	75 ± 1
	^{218}Po	6.2	3.1 m	< 56
	^{214}Po	7.8	164 μs	> 6.0
	^{210}Po	5.3	138 2	> 0.3
^{232}Th	^{220}Rn	6.4	55 s	10.3 ± 0.3
	^{216}Po	6.4	0.14 s	9.9 ± 0.3
	^{212}Bi	6.9	61 m	< 56
	^{212}Po	8.8	0.3 μs	> 1.8

Table 5.1: Activities of ^{222}Rn and ^{220}Rn chain α decaying isotopes.

^{212}Bi (with branching ratio = 35.93)] pass all analysis cuts with negligible efficiency loss. In these cases, the integral of their fit is interpreted as a measurement. Isotopes that occur in an event window with another decay (^{214}Po and ^{212}Po) will sometimes be misclassified via the mechanism mentioned in the previous paragraph, thus the integral of their fit is considered to be a lower limit. The same is true for ^{210}Po. Since this isotope is located on or just-beneath the surface of the PTFE wall, not all of the α particles make it far enough into the xenon to produce $S1$s or $S2$s.

5.2 Coincident Bismuth and Polonium Decays

Because ^{214}Po and ^{212}Po have short half lives, there is potential to select these events by searching for their coincidence with a parent decay of ^{214}Bi or ^{212}Bi. The pairings could be used to produce a spectrum of polonium $S1$ time delays—at least for the particular range in which the delay is long enough to prevent the two $S1$s from overlapping but short enough to pair the $S1$s with high fidelity. Assuming the known half lives of the polonium isotopes, the spectra can be extrapolated to estimate the total ^{214}Po and ^{212}Po rate.

The time delay method is successful when both scintillation signals are efficiently detected as separate $S1$s and neither is in danger of overlapping with an $S2$. ^{212}Po-^{212}Bi pair fails the first criteria because the polonium half life is short enough (0.3 μs) to prevent the pulse finder from adequately separating the $S1$s—although this could be rectified by building a new more-precise $S1$ separation algorithm. The longer half life of ^{214}Po (162.3 μs) ensures the ^{214}Po-^{214}Bi pair will usually pass the first criteria. However, the half life is within the range of drift times for $S2$s, $7 - 321\mu$s, causing ^{214}Po-^{214}Bi to frequently fail the second criteria. Both criteria are met, when the ^{214}Po decay occurs at a delay greater than the drift length of the detector, i.e. when the ^{214}Po decay is generated in an event window separate from the ^{214}Bi decay.

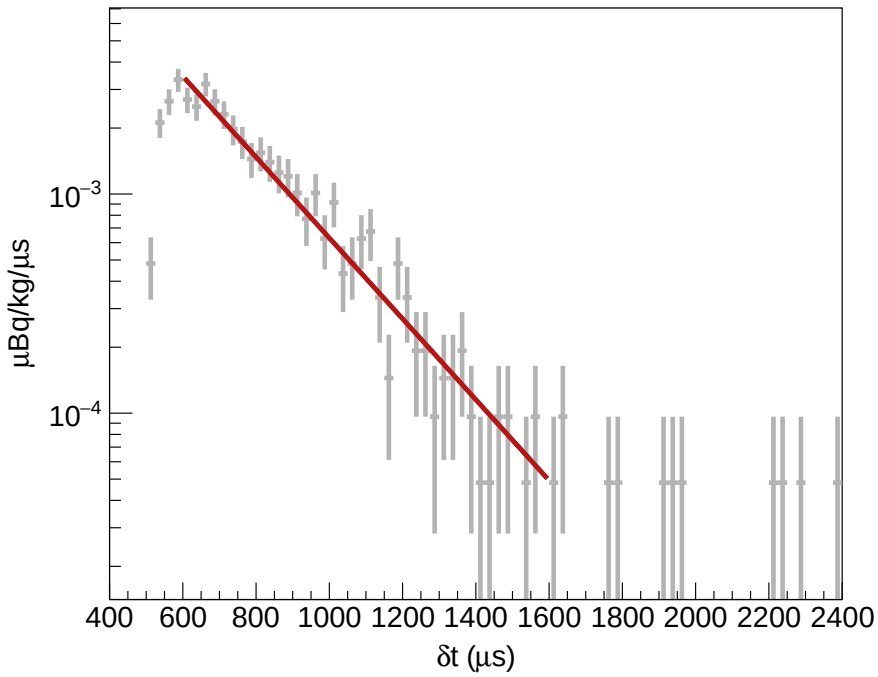

Figure 5.5: Spectrum of time delays between ^{214}Bi and ^{214}Po $S1$s for decays that occur in separate time windows. The red line is an exponential fit to the data with the half life constrained to 164 μs.

Fig. 5.5 shows the spectrum of ^{214}Po-^{214}Bi $S1$ time delays for decays occurring in separate event windows. The pairs were selected by requiring a ^{214}Po event with one $S1$ in the range 7.3–8.5 MeV and one $S2$. No further cuts were applied to the ^{214}Bi events. The spectrum was fit with an exponential decay fixed at the ^{214}Po half life to extract the rate of detectable ^{214}Po events in the xenon, 10.4 ± 0.8 μBq/kg.

Note this measurement is still subject to the efficiency loss from $S1$ misclassification due to ^{214}Bi electron trails; therefore, it is still considered a lower limit. Although it appears there is little dependence of the misclassification rate on the length of the ^{214}Po-^{214}Bi time delay—at least in the few-hundreds of microseconds range considered here—since the spectrum had a decay constant apparently very-near the ^{214}Po half life.

5.3 Drift dependence

The daughters of α and β decays have either neutral or positive charge. As for the ^{222}Rn chain in liquid xenon, the daughter ion fractions of ^{218}Po$^+$ and ^{218}Bi$^+$ have been measured as $50.3 \pm 3.0\%$ and $76.4 \pm 5.7\%$ by [137].

Charged radon daughters in the active volume would be drifted downward by the electric

field towards the cathode at the bottom of the TPC. When the mobility of a daughter ion is great enough for it to travel ∼cm long distances within a half life, the effect can create concentration gradients for the daughter and all isotopes following it in the chain. [137] has measured an initial ion mobility for $^{218}Po^{+}$ of 0.390 ± 0.006 cm^2/(kV·s). Assuming a typical electric field of 177 V/cm, the distance travelled by a $^{218}Po^{+}$ ions over the length of this isotope's half life (3.05 m) is 12.6 cm. Other radon chain isotopes have longer half lives that would cause their ions to drift even greater distances, if they have similar mobility to that of $^{218}Po^{+}$.

However, thermally conductive currents in the xenon wash out the activity gradients put in place by drifting ions. Having no definitive study of thermal conduction in the LUX TPC, it is to be determined whether there are are significant gradients of the ^{222}Rn and ^{220}Rn backgrounds.

^{222}Rn and ^{220}Rn should have neutral charge and be evenly distributed throughout the xenon: positively charged radon isotopes would be much less likely to escape the material from which they originate, because they would adhere to the surface of pore spaces. Considering their daughters, if thermal conduction is not significant, each successive daughter should have a gradient steeper than the isotope preceding it.

Scatter plots of ^{222}Rn and ^{220}Rn α decay positions are shown in Fig. 5.6 and 5.7.

^{222}Rn is distributed uniformly throughout the xenon and so is its daughter ^{218}Po, suggesting thermal conduction is a significant source of ion dispersal in the LUX TPC. The next α in the chain, ^{214}Po, is also somewhat evenly distributed, although it is subject to the $S1$ misclassification effect that increases selection efficiency near the wall compared to the bulk. The ^{210}Po population is heavily concentrated about the position of the wall, but there is some bleeding into the central xenon. This is likely due to imperfect separation of these events from those of ^{222}Rn, done using an energy cut that lies at the minimum point between the two populations of events in Fig. 5.4 (similar cuts were used to separate all of the α populations). In general, there is not expected to be much correlation between the first three isotopes in the ^{222}Rn chain and ^{210}Po, since this isotope was deposited on the wall before the experiment began thus is unrelated to the activity in the xenon.

^{220}Rn and its daughter ^{216}Po are more heavily concentrated at the top and center of the TPC; this is especially apparent in the histograms of α-decay z position shown in Fig. 5.8. ^{216}Po has a short 0.148 s half life that would not allow its ions to drift significant lengths before decaying, assuming it has a mobility similar to that of ^{218}Po. Therefore, it is expected that ^{220}Rn and ^{216}Po would have the same position distribution, as is apparent in the figures. However, the ^{220}Rn and ^{216}Po gradient is unexpected and the author has no valid explanation for this behavior.

5.4 Surface backgrounds on PTFE

The LUX data contains large numbers of events located at the surfaces of components surrounding the active volume. Much of the radiocontamination producing these events

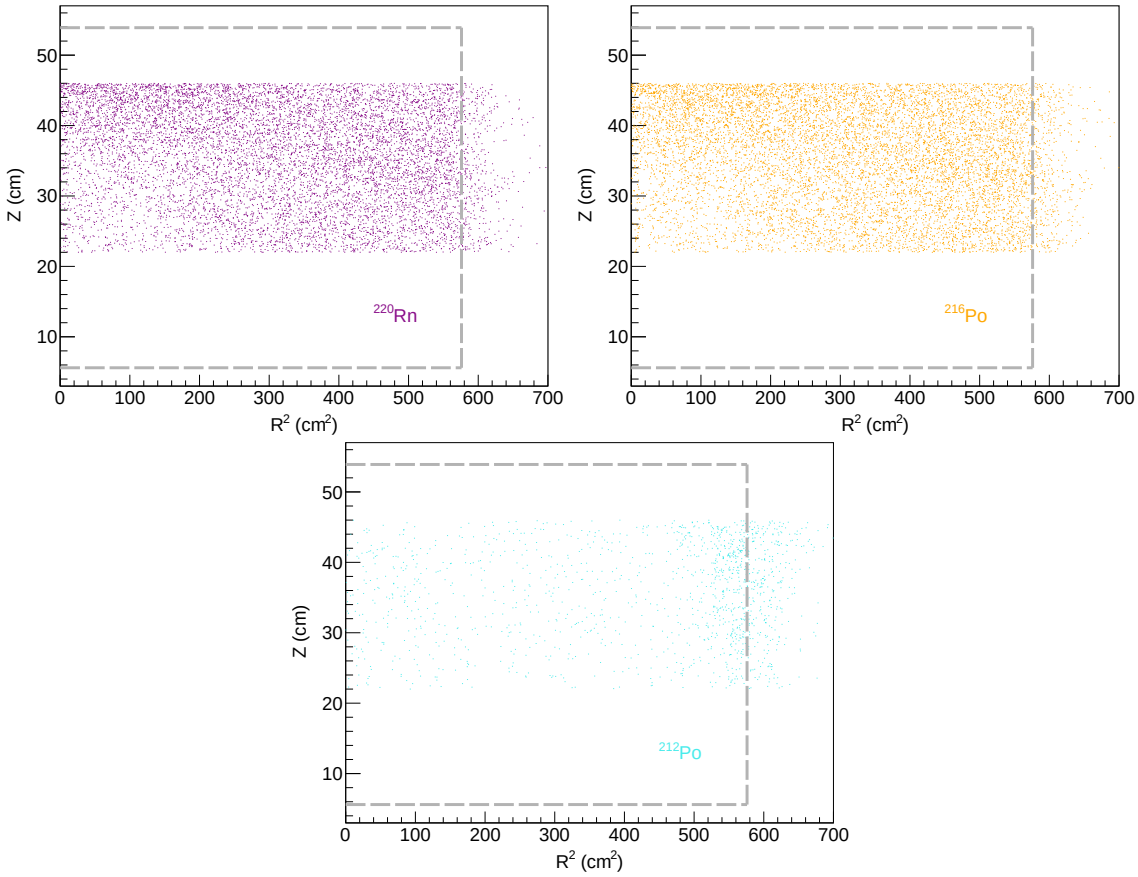

Figure 5.6: Positions of α decays from isotopes in the ^{222}Rn chain. ^{214}Po events were selected by two methods: requiring events contain up to two $S1$s and any number of $S2$s, and requiring events contain one $S1/S2$ pair and be in coincidence with a previous ^{214}Bi event.

is introduced during detector construction when all of the components are exposed to air with typical quantities of radon. As this isotope decays, it produces nongaseous daughters that can plate out on the exposed component surfaces. The same process also occurs during detector operation when radon daughters absorbed in the xenon plate out on surfaces directly contacting the active volume. After plate out, most of the daughters quickly decay away due to their short half lives; but, ^{210}Pb with a 22 year half life and its two daughters, ^{210}Bi and ^{210}Po, remain on the surfaces long after the detector has been closed.

During operation, ^{210}Pb and its daughters can remain on the component surfaces, wash off the surfaces, or recoil into the xenon during a decay. When the isotopes remain surface bound, they produce benign background events that can easily be removed with a position cut. However, if the isotopes become absorbed in the xenon, they produce background events in searches for new physics. The latter is a worrisome scenario, because noble element

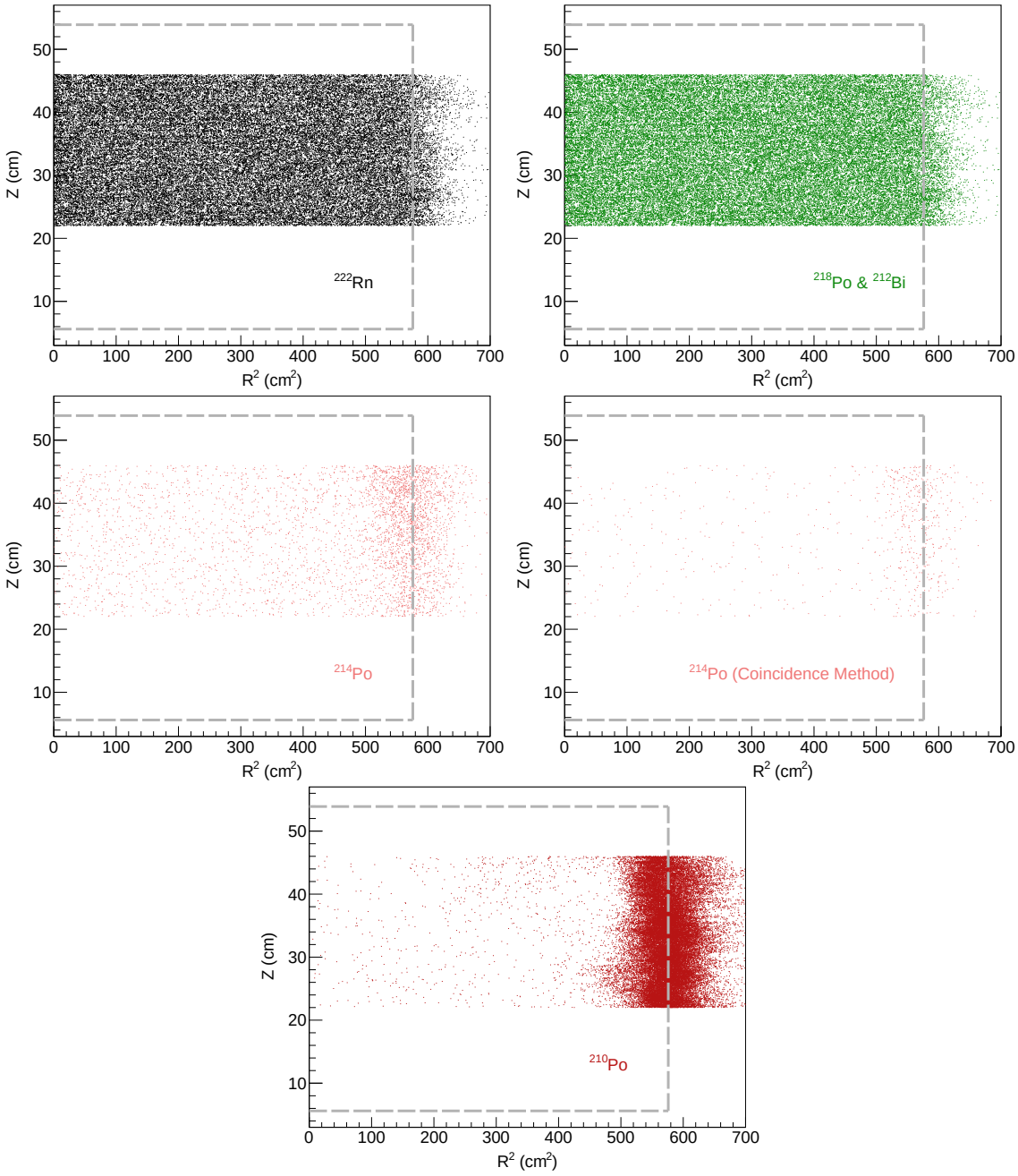

Figure 5.7: Positions of α decays from isotopes in the ^{220}Rn chain.

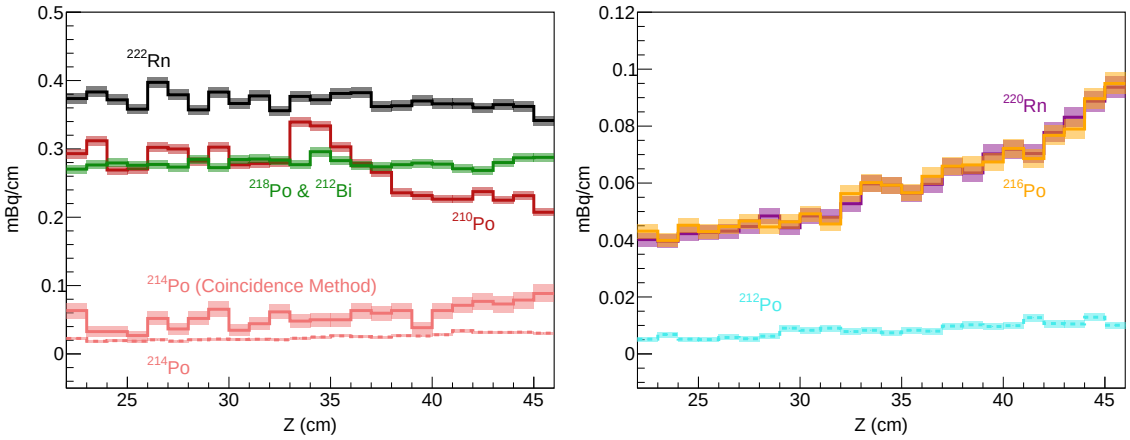

Figure 5.8: Histograms of ^{222}Rn and ^{220}Rn α-decay z coordinates. ^{214}Po events were selected by two methods: requiring events contain up to two $S1$s and any number of $S2$s (solid pink line), and requiring events contain one $S1/S2$ pair and be in coincidence with a previous ^{214}Bi event (dashed pink line).

experiments have observed quantities of surface contamination a factor of $\sim 10^2$ greater than contamination of detection mediums. If ^{210}Pb/^{210}Bi/^{210}Po were to leave component surfaces at significant rates, events from these isotope's could overwhelm searches for new physics.

This section concerns itself with the β decays, ^{210}Pb and ^{210}Bi. The decays emit electrons and photons over a wide range of energies ending at their Q-values of 63.5 and 1162 keV. Of these two isotopes ^{210}Pb is of greater interest, because its decay to the 46.5 keV excited state of ^{210}Bi (branching ratio = 80%) which can generate prominent monoenergetic or near-monoenergetic signals. They occur when ^{210}Bi nucleus deexcites via one of a set of a conversion electrons (CEs) or a γ ray. Following emission of the conversion electron, there is a hole in the atom which becomes filled during an atomic cascade emitting x rays and Auger electrons (AEs). If the decay occurs on a component surface, each of the decay products can burrow into the component or travel into the xenon. Prominent monoenergetic signals are generated when only a CE, x-ray, AE, or γ ray travels into the xenon. Conversely, if the decay occurs in the xenon, all of the decay products will contribute to the event energy generating a distinguishable, 46.5–63.5 keV β spectrum. Table 5.2 summarizes the individual ^{210}Pb decay products.

A subset of the WS2014-16 dataset with insignificant ^{83m}Kr content was used to search for evidence of ^{210}Pb absorbed in the liquid xenon. This calibration source was periodically injected into the detector with an activity far greater than that of the absorbed radon daughters. Having a 41.5 keV decay energy, its presence would obscure some of the prominent signals of the excited state β spectrum described in the previous paragraph.

The energy of the remaining WS2014-16 events was reconstructed using $E = W(\frac{S1_c}{g_1} + \frac{S2_c}{g_2})$ with values of g_1 and g_2 calculated in Chapter 4. Fig. 5.9 shows events within a central xenon

Decay Product	Energy (keV) Energy (keV)	Number per 100 Parent Decays
γ ray	46.5	4
M,N-shell CE	$42.5 - 46.4$	17
L-shell CE	$30.1 - 33.1$	58
X rays	$9.4 - 15.7$	22
AE	$5.3 - 10.7$	36

Table 5.2: Summary of decay products emitted after ^{210}Pb decays to the excited state of ^{210}Bi. Only the x rays and Auger electrons produced when there is a hole in the K- or L-shell of the atom are included for brevity. Conversion electrons and Auger electrons are abbreviated as CE and AE, respectively.

volume defined by the cuts $40 < t_{drift} < 300$ μs and $|r_{S2} - r_{wall}| > 4$ cm where t_{drift} is the drift time, r_{S2} the radial coordinate of the event, and r_{wall} the radial coordinate of the wall. In the range of ^{210}Pb's excited state β decay, the data produce a flat energy spectrum. 41–64 keV was identified as a signal region since it should contain 99% of all excited state β decays assuming the energy resolution of 5% from [103]. Two side band regions, 18–41 and 64–87 keV, were used to estimate the background rate in the signal region. A 90% confidence limit on the activity of ^{210}Pb absorbed in the xenon was placed at < 0.025 mBq.

The same WS2014-16 subset was also used to search for evidence of ^{210}Pb contamination in events reconstructed within 4 cm of the PTFE walls. Fig. 5.10 shows the energy spectrum of events in this location. There are visible populations corresponding the ^{210}Pb γ ray, CEs, x rays, and AEs with energies 46.5, 42.5–46.4, 30.1–33.1, 9.4–15.7, and 5.3–10.7 keV.

As with ^{210}Po, the ^{210}Pb features can only be used to place a lower limit on the activity on the wall, since many of these decays may not produce detectable signals. Exponential Gaussian functions—where the exponential is used to estimate energy loss—were used to model the ^{210}Pb γ ray and the seven most-probable CEs. To minimise the number of parameters of the fit, all of the CEs and γ ray were given the same three energy reconstruction parameters (resolution, a scaling factor with respect to the true energy, and the relative size of the exponential tail) and only two amplitude parameters that separately scale the L-shell CEs and the NOP-shell CEs + γ ray with relative intensities of each group constrained to their literature values. Other features in the spectrum were treated as background and modeled with a constant, exponential, and two Gaussians. An additional component was added to model a set of x rays produced when an outer-shell electron drops to fill an empty k shell of a xenon atom. These events are produced when incident radiation interacts with xenon atoms in the pore spaces of the PTFE or cracks in the panels. If the radiation ionizes the k shell, the subsequent x ray can travel into the active volume while the incident particle remains in the pore space or crack. The x rays were modelled with a Gaussian functions constrained to have the same energy resolution as the ^{210}Pb fit components. The relative

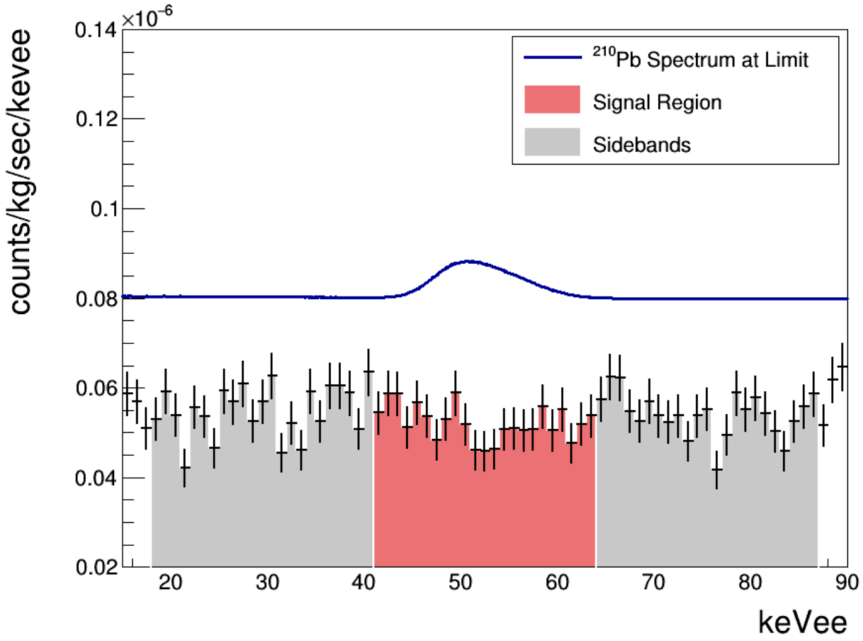

Figure 5.9: Spectrum of events in the energy range of the ^{210}Pb excited-state β decay. The pink and grey are signal and background region use to calculate an upper limit on the activity which is shown by the blue solid line.

amplitudes of the x rays were constrained to their literature values.

Taking into account relevant branching ratios, the L-shell-CE and NOP-shell-CE + γ-ray fits were used to calculate two lower limits on ^{210}Pb activity on the walls of the detector, $> 1.6 \pm 0.1$ and $> 0.96 \pm 0.6$ mBq, respectively. The L-shell CE feature significantly overlaps with the other background features that are modelled only approximately by the components of the fit. This introduces an additional systematic error that was estimated by repeating the fit with the background features fixed at $\pm 1 \cdot \sigma_i$ their original best fit values, where σ_i is the error on any of the original fit parameters. This resulted in an additional $\pm 20\%$ systematic uncertainty on the L-shell-CE limit. Considering both the statistical and systematic uncertainties, the two limits agree with one another.

The limit calculations conservatively assume every CE or γ ray will travel into the active volume although every decay product has some probability of burrowing into the wall or a crevasse where no signal can be detected. Fig. 5.10 actually reveals the probability for decay products to travel into the active volume must actually be quite low, because it shows distinct peak-like features. The γ ray and CEs are being detected individually, not accompanied by a β particle or x rays/AEs that would smear the γ ray/CE spectral features toward higher energies. Consider a toy model where every decay product has a probability P of traveling into the active volume. If $P \ll 1$, detection of a single decay product is much greater

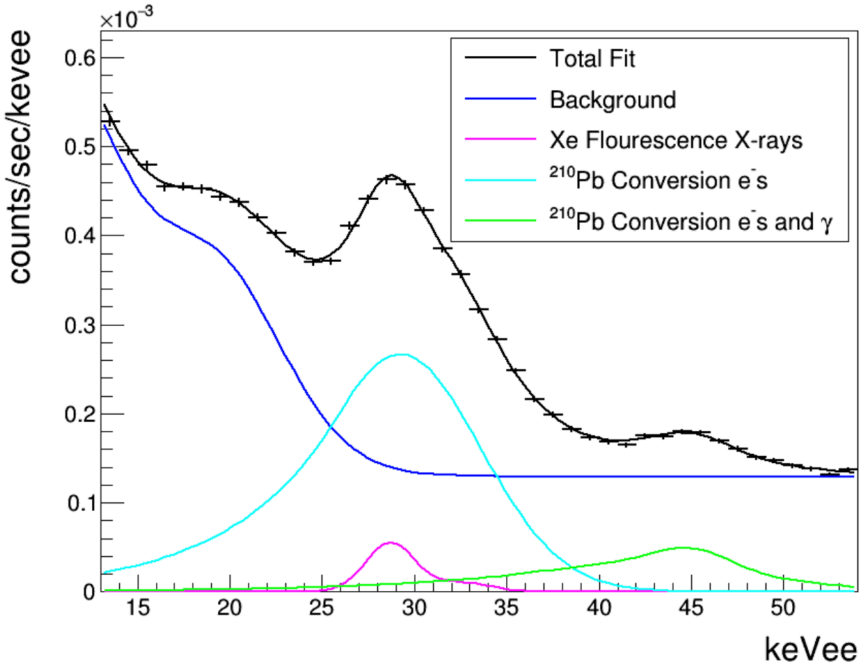

Figure 5.10: Spectrum of events within 4 cm of the PTFE walls in the energy range of the ^{210}Pb excited-state β decay.

than detection of multiple decay products, $P \gg P^{n\geq 2}$, indicating prominent features of the spectrum will be produced by individual decay products.

To look for time dependence of ^{210}Pb wall contamination, the same fit was applied to data broken into five date bins: 11 Sep 2014–1 Jan 2015, 1 Jan 2015–1 Apr 2015, 1 Apr 2015–1 Oct 2015, and 1 Oct 2015–2 May 2016. A decrease in wall activity beyond what is predicted by the 22 year half-life of ^{210}Pb, is evidence of this isotope washing off of the wall and into the xenon. Fig. 5.11 shows the integrals of the NOP-shell CE + γ-ray fit for each date bin are consistent with ^{210}Pb remaining affixed to the wall. A limit on the rate of ^{210}Pb leaving the wall was calculated to be > 4.4 years.

5.5 Surface backgrounds on electrodes

As described in Chapter 2, the WS2014-16 data is affected by gross field distortion that pushed electrons near the PTFE walls inward as they drift. The distortion most greatly effected events near the bottom of the TPC causing them to exit the liquid near the radial center of the detector. In the WS2014-16 dataset, these events are spatially mixed with backgrounds from the cathode making it difficult to study the latter. For this reason, data from WS2013, having been taken at a time with much less significant distortion, was used

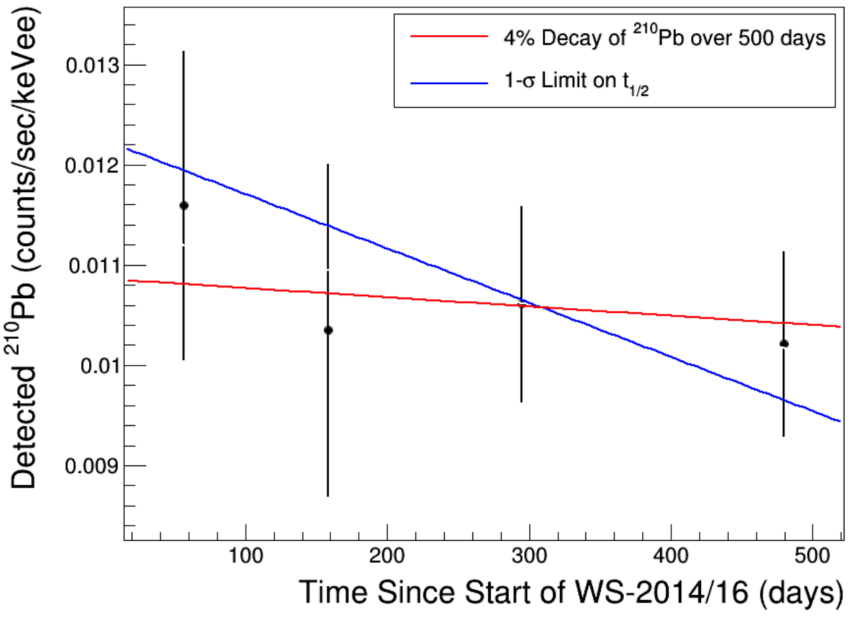

Figure 5.11: Time dependence of ^{210}Pb NOP-shell CE + γ-ray events on the PTFE wall.

to study radiocontamination on the gate and cathode wire grid electrodes that bound the active volume.

The same isotopes found on the PTFE walls are expected to be present on the electrodes: ^{210}Pb and its daughters ^{210}Bi and ^{210}Po. Several cuts and vetoes were applied to search for evidence of their existence. As in the previous section, acquisitions containing ^{83m}Kr were removed so that events from this calibration source would not hide those of ^{210}Pb in the same energy range. Several additional vetoes were used to remove all April 2013 data, livetime following large events that produce substantial electron trails, and livetime occurring during a grid hotspot flare. A cut on the parameter "badarea" was used to remove backgrounds from events occur in the vapor. The vetoes and the badarea cut are used to remove few-electron $S2$ backgrounds from the very-low-energy data and are discussed in more detail in this context in Chapter 7. A radial cut in combination with a second cut on the χ-squared output of the position reconstruction algorithm was use to remove backgrounds occurring on the walls and any events in which the position reconstruction had failed. Finally, drift time cuts were used to select events occurring at either the gate or cathode, $t_{drift} < 7\mu$s or $321\mu\text{s} < t_{drift}$, respectively.

Fig. 5.12 (left) shows the energy of gate and cathode events reconstructed using $E = W(\frac{S1_c}{g_1} + \frac{S2_c}{g_2})$ with $g_1 = 0.117 \pm 0.003$ phd/photon and $g_2 = 12.1 \pm 0.8$ phd/electron from [64]. The gate spectrum contains prominent features at ~ 8, ~ 28, and $\sim$ 40 keV which are just a few-keV lower than the AEs/x-rays, L-shell CEs, and NOP-shell CEs/γ-ray of ^{210}Pb.

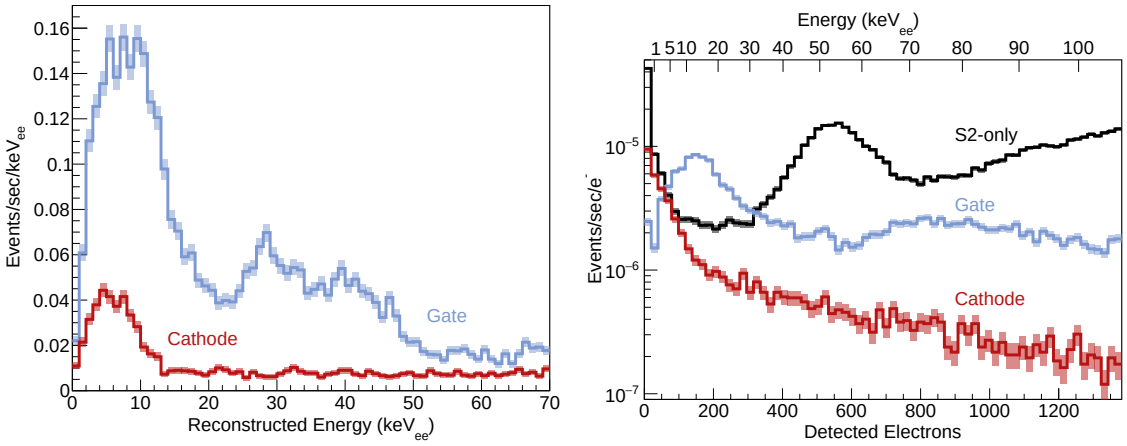

Figure 5.12: (a) Energy spectra of events originating on the gate and cathode show evidence of ^{210}Pb contamination. The gate has three peaks corresponding relevant decay products. Only the most prominent feature is visible at the cathode, because electric fields prevent events near the wires from producing S2s. (b) Gate, cathode, and $S2$-only spectra in units detected electrons. The $S2$-only spectrum contains a peak from Xe K-shell x-rays produced by scatters in the vapor. The top axis is the energy predicted by averaging geometric detector effects over the fiducial volume using NESTv2.0.1.

This energy shift is expected, because so near the wire surface a significant fraction of the scinillation photons would be absorbed by the wire.

The area of the $\sim$ 8 keV feature, relative to that of the $\sim$ 28 or $\sim$ 40 keV features, is much greater than would be predicted by the intensities of AEs/x rays listed in the decay summary presented in Table 5.2. This oddity can be explained by an additional contribution from the 103 keV ^{206}Pb recoils. Unlike the ^{210}Pb deexcitation products, a recoiling ^{206}Pb atom would interact with xenon nuclei through processes that deposit a significant fraction of their energy in thermal excitations. As a result, this decay will be reconstructed at 13.5 keV, according to NEST v2.0.1, a value subsumed by the $\sim$ 8 keV peak.

The cathode spectrum in Fig. 5.12 (left) contains only one feature that likely contains events from all of the ^{210}Pb decay products regardless of their energy. This is a consequence of the electric field profile around cathode wires. Only 16% of field lines near the wires point upward drifting electrons toward the liquid surface where they can produce detectable electroluminesence. As electrons drift and diffuse away from the wire, many follow the 84% of field lines that travel downward, thus are not detected. The result is that all of the features of ^{210}Pb decay products have greatly-degraded energy and poor energy resolution.

Gate and cathode backgrounds are a problem for physics searches that include very-low-energy events which have $S2$s but no $S1$s (see Chapter 7). For comparison with these data, Fig. 5.12 (right) calculates the gate and cathode event energies using only the number of detected electrons. The gate spectrum contains the same three features visible in Fig. 5.12 (left)

with a couple of key differences. First, the energy resolution is degraded, spreading the peaks over a wide range of detected electrons and causing overlap of the ~ 28 and ~ 40 keV peaks. Second, the energy of the peaks, as estimated from the top axis of the plot, is a factor of 1–3 greater than the real energies of the decays. This is partially because the energy scale was calculated using NEST to average the deteriorating effect of electron lifetime over the fiducial volume; $S2$s from events at the top of the detector (e.g. gate) are $\sim 30\%$ larger than those at the bottom (e.g. cathode). A larger effect is electric field enhancement of Q_y. NEST predicts Q_ys of gate events are enlarged by a factor of 1.6–2.5 for the ^{210}Pb decay products and ~ 3 for the ^{206}Pb recoils. Considering the large systematic uncertainties in detector parameters near the electrode wires and NEST models at high electric fields, the electron lifetime and Q_y estimates adequately predict the placement of the gate features.

In Fig. 5.12 (right), a third spectrum containing $S2$-only events is presented for comparison with the gate and cathode data. At high energies, the event rate gradually rises because γ-ray backgrounds from radioactivity in the detector components are significant in this region. At very low energies the rate of $S2$-only events skyrockets. This feature can be partially attributed to electrode electron emission processes that become significant in this region. Somewhat similarly, the gate spectrum shows minor increase in events in its very lowest-energy bin. These could be gate electron emission events with corresponding light emission, a phenomenon observed at small rates in [114].

Table 5.3: X-rays and Auger electrons (AE) produced when outer shell electrons fill a hole in the K-/L-shells of a Xe atom. Outer shell de-excitations are not included for brevity. "K-shell x-rays" have long ranges in the vapor and short ranges in the liquid suggesting they produce the peak in Fig. 5.12 (right) $S2$-only spectrum. The range column contains mean free paths (MFP) for photons and continuous-slowing-down approximation (CSDA) ranges for electrons.

Shell	Fluor. yield	Type	Energy (keV)	Range (mm) Vapor	Range (mm) Liquid
K	0.89	X-ray	$29-34$	$108-164$	$0.4-0.6$
		AE	$23-34$	$2.3-4.5$	$0.008-0.02$
L	0.08	X-ray	$3.6-5.0$	$1.6-4.1$	$0.006-0.01$
		AE	$2.4-5.4$	–	–

At intermediate energies, there is a peak in the range 300–800 detected electrons that requires further explanation. The shape of the $S2$ waveforms reveal these events must have occurred at the very top of the detector. They have short, square shapes and many are, in reality, combined $S1/S2$ pairs that have been mistakenly categorized as a single pulse due to their short time separation. This peak is created by several 29–34 keV x rays produced when radioactive decay products scatter on the K-shell of xenon atoms in the vapor. The mean free path (MFP) calculations presented in Table 5.3 show these x rays travel 10^2 mm long distances through the vapor, but scatter within 10^{-1} mm after

Decay Chain	Isotope	Q-value (keV)	Constraints (μBq/kg)
^{238}U	^{214}Pb	1019	5.4–56
	^{214}Bi	3270	5.4–56
	^{210}Pb	63.5	< 0.099
	^{210}Bi	1162	< 0.099
^{232}Th	^{212}Pb	570	2–10.2
	^{212}Bi	8954	2–10.2
	^{208}Tl	4999	< 0.96

Table 5.4: Constraints on activities of β-decay isotopes in the ^{222}Rn and ^{220}Rn chains from measurements of the α decays and ^{210}Pb.

passing the liquid surface. Other xenon atomic deexcitation products are created by the same process, but all travel short distance in the vapor making them less likely to produce liquid surface events. Importantly, the energy scale at the top of the plot places the "K-shell x-ray peak" a factor of ~ 1.7 above the expected energy range. NEST predicts the electric field at the liquid surface, 3500 kV/cm, will enlarge the Q_y by a factor of ~ 2, reasonably consistent with placement of the peak.

5.6 Constraints on β Decays for PLR

This section consolidates and interprets the results of the previous sections, to extract the best measurements and limits on the activity of each radon chain isotope in the xenon during WS2014-16.

A basic assumption about the LUX detector is used to achieve this end. While running, the xenon is constantly travelling through a circulation system that includes a zirconium getter purifier. During each pass through the system, a fraction of the non-noble radon daughters bind with the material inside the getter and are removed from the xenon—they also plate out on the inner surfaces of the pipes. Equilibrium concentrations of each isotope depend on the rate at which radon is absorbed into the xenon and the rates at which each daughter is removed, a scenario that causes every successive daughter to have an activity lower than its parent.

This trend can be used to place constrains on activities of the β decays, since they would lie somewhere between the activities of the previous and subsequent α decays. An additional constraint comes from the limit on ^{210}Pb absorbed in the xenon. All constraints are presented in Table 5.4.

Chapter 6

Radiological Assays of Materials for LUX-ZEPLIN

The materials from which components are built inevitably contain some level of radiocontamination; thus, background rates (b) from these sources grow with detector size unless specific effort is made to select more radiopure materials. This trend can have a significant impact on the success of future experiments since dark matter (DM) sensitivity scales with $\sim \frac{V}{\sqrt{b}}$.

In preparation for LUX-ZEPLIN (LZ), extensive effort was made to reduce detector component backgrounds to the lowest possible levels. A material screening campaign was carried out by collaborators at Black Hills State University (BHSU), Boulby Underground Germanium Suite (BUGS), Berkeley Low Background Counting Facility (BLBF), Sanford Underground Research Facility (SURF), and University of Alabama. Most notably, individuals at BHSU and BLBF—including the author—constructed a new low-background counting facility on the 4850 ft level of SURF named the Black Hills Underground Campus (BHUC).

This chapter summarises construction of the BHUC and other work carried out at this location as part of the LZ material screening campaign. When describing the BHUC's infrastructure, it goes into depth about the automated liquid nitrogen system used to cool the array of high-purity germanium (HPGe) detectors installed within the facility. Programming and maintenance of the software controlling this system is the primary contribution made by the author to the BHUC infrastructure. It continues by describing the function of HPGe detectors, and the standard methods used by members of the BLBF to analyse data from detectors of this type. In doing so it presents the results of several assays that are of interest to LUX and LZ (assays performed by the author). Additionally, the chapter details the design of a powerful dual-crystal detector named Morvydd & Owain which was installed at the BHUC just prior to composition of this dissertation. The author lead this effort, specifically working with an engineer to design the moving components of the shield and install the detector underground. The chapter concludes with a description of how the material screening campaign affected the LZ projected sensitivity to spin-independent DM-nucleus scattering.

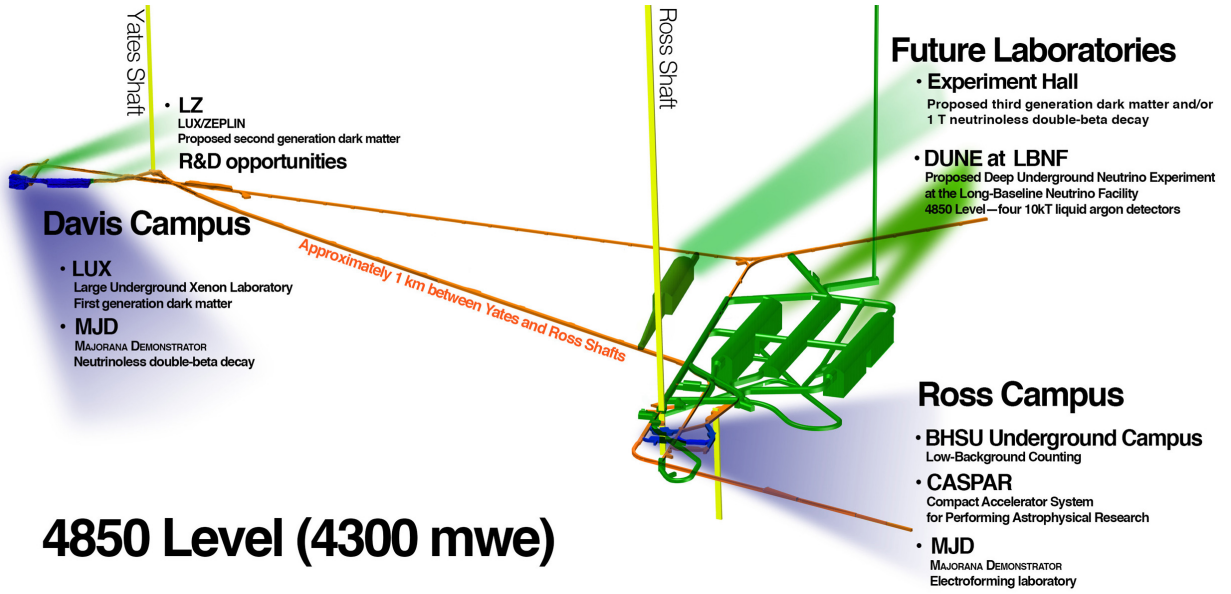

Figure 6.1: Map of 4850 ft level of the Sanford Underground Research Facility (SURF). Figure from [138].

6.1 Black Hills Underground Campus

The BHUC cavern was located on the 4850 ft level of SURF at the Ross campus, ~ 1 km away from the Davis cavern, as shown in Fig. 6.1. Renovation of the cavern began in 2015 with application of shotcrete to the cavern walls, construction of concrete floors, installation of electrical and ventilation infrastructure, and assembly of class $1,000$ and $10,000$ cleanrooms. The larger 55 m^2 class $1,000$ cleanroom was dedicated solely to ultra-low background material screening for rare event searches. The facility was open to all experimental collaborations, although from 2016 to 2019 it was used primarily for assaying the materials and components used to build LZ.[1]

The class $1,000$ cleanroom was spacious enough to house approximately ten background counting stations. As of 2019, five HPGe detectors with copper and lead shields had been installed in the cleanroom by BLBF and BHUC personal, including the author: Morgan, Maeve, Mordred, SOLO, and Morvydd & Owain. An additional germanium detector, Ge-IV, was installed in the staging area outside of the cleanroom by individuals at South Dakota State University. Fig. 6.2 contains diagrams of the cleanrooms in the BHUC cavern and an illustration of detectors installed in the class $1,000$ cleanroom as of 2019, along with

[1]In the fall of 2019, the BHUC was disassembled in preparation for blasting of new Ross campus caverns in which the future Deep Underground Neutrino Experiment (DUNE) will be installed. It has been reconstructed within the Davis Campus where the facility can operate without interference from nearby explosions.

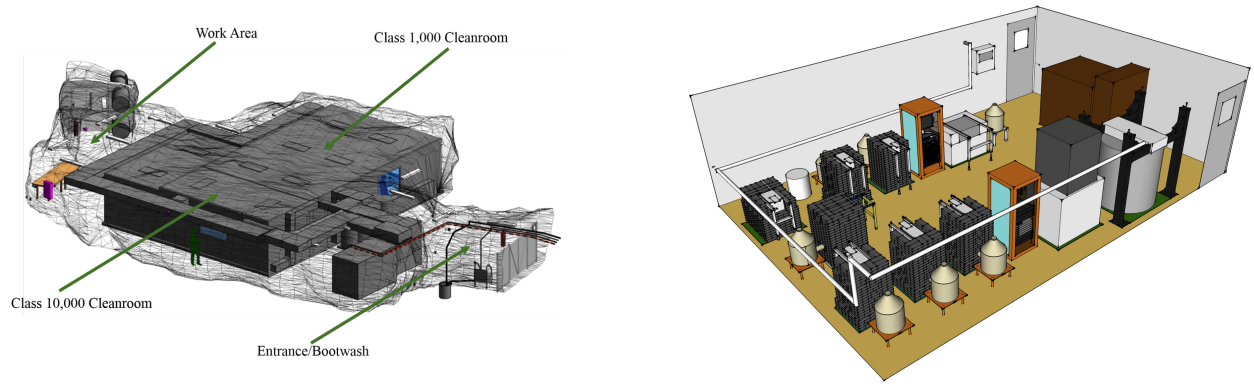

Figure 6.2: Diagrams of the Black Hills Underground Campus (BHUC) cleanrooms. On the left, both class 1,000 and 10,000 cleanrooms are shown as constructed within the BHUC cavern. On the right is an illustration of the high purity germanium (HPGe) detectors installed in the class 1,000 cleanroom as of 2019, along with anticipated future detectors of the same type. Left and right figures are from [139] and [138], respectively.

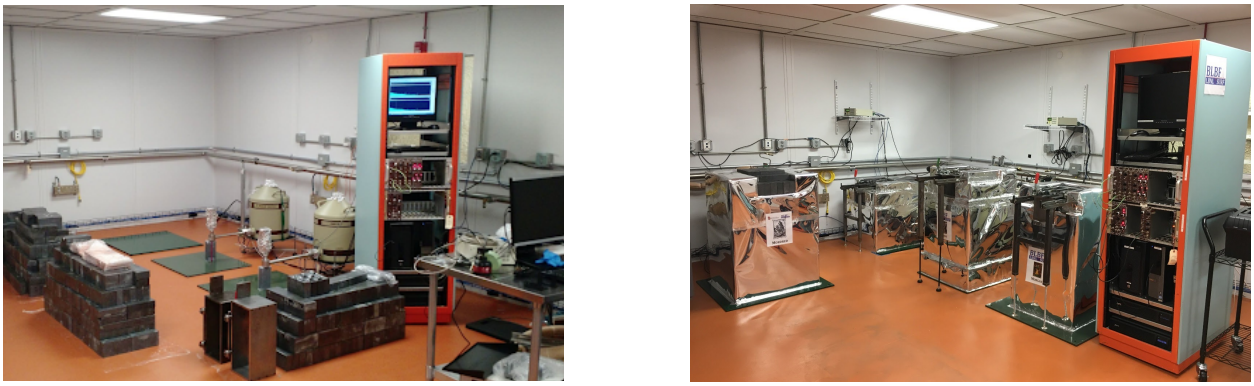

Figure 6.3: The BHUC class 1,000 cleanroom before and after installing four of the high purity germanium (HPGe) detectors: Morgan, Maeve, Mordred, and SOLO. The photo on the right shows the status of the cleanroom at the beginning of 2017.

anticipated future detectors of the same type. Fig. 6.3 shows photographs of the class 1,000 cleanroom before and after installing the four of the detectors.

Liquid Nitrogen System

An automated liquid nitrogen (LN) system was built to provide dependable cooling power to all detectors installed at the BHUC. It transferred LN from four 180 L storage dewars located outside the cleanroom on Arlyn platform scales, through a vacuum jacketed pipe

running along the inner cleanroom wall, to the small dewars that are integrated components of each germanium detector. It used a National Control Devices (NCD) FLL_FXSSR16X 16-channel relay controller to power four solenoid valves connected to each of the storage dewars and two additional solenoid valves opened when "pre-cooling" the pipe prior to filling one or more of the detectors. It also used American Magnetics Inc. (AMI) 286 multi-channel liquid level controllers to measure the height of the liquid in each of the small detector dewars and power solenoid valves located at the mouth of these dewars.

Gaseous nitrogen, boiled from the LN contained in the four storage dewars, was piped into the cavity of each detector to displace radon laden underground air that would otherwise bias assay results. It was supplied from a pressure manifold connected to the gas outlet of each dewar, through a stainless steel tube running along the inner wall of the cleanroom. Manually operated mass flow controllers (MFCs) connected this line to high-density polyethylene tubes that transferred gas to the inner cavities of each detector. The pressure at the outlet of each MFC was raised just above the local atmospheric pressure so that the gaseous nitrogen would continually flow into the detector cavities pushing out radon laden underground air.

The LN system incorporated two additional measurement devices used to ensure the system operated only under safe physical conditions. The first was a transducer on the pressure manifold that would open a solenoid valve allowing nitrogen gas to flow into the cavern whenever it measured a pressure above 30 psig. The transducer was connected to a dedicate LN system computer through a digital readout instrument to track the evolution of the pressure in the gas line. The second device was a Ross campus oxygen meter which was connected to the relay board to monitor its alarm status.

Labview Liquid Nitrogen Program

All physical elements of the LN system were controlled with a custom LabVIEW program installed on the system computer [140]. The components operated by this program—dewars, pipes, solenoid valves, and measurement devices—as well as connections to the computer are outlined in Fig. 6.4. The program performed three primary operations: hourly system checks, bi-weekly transfers of LN to every detector dewar, and continual monitoring of alarm statuses. These operations are outlined in the bullet points below.

- The program completed *hourly system checks* of the LN mass contained in every storage dewar, the LN height in every detector dewar, and the nitrogen gas pressure in the pressure manifold. It would send RS-232 queries to each measurement device (scales, level controllers, and pressure transducer) in turn, wait for a response, and iterate up to 15 times if no response was received. After the 15th failure, the program would deliver an e-mail describing the error to the list of BHUC collaborators. During this procedure, if any device measured an unsafe condition (for example, the pressure was too high), an alert e-mail was sent to the collaborators. The results of each hourly system check were written to a form which, upon submission, would populate a spreadsheet located in the LN systems google drive. The spreadsheet acted as a record of LN usage

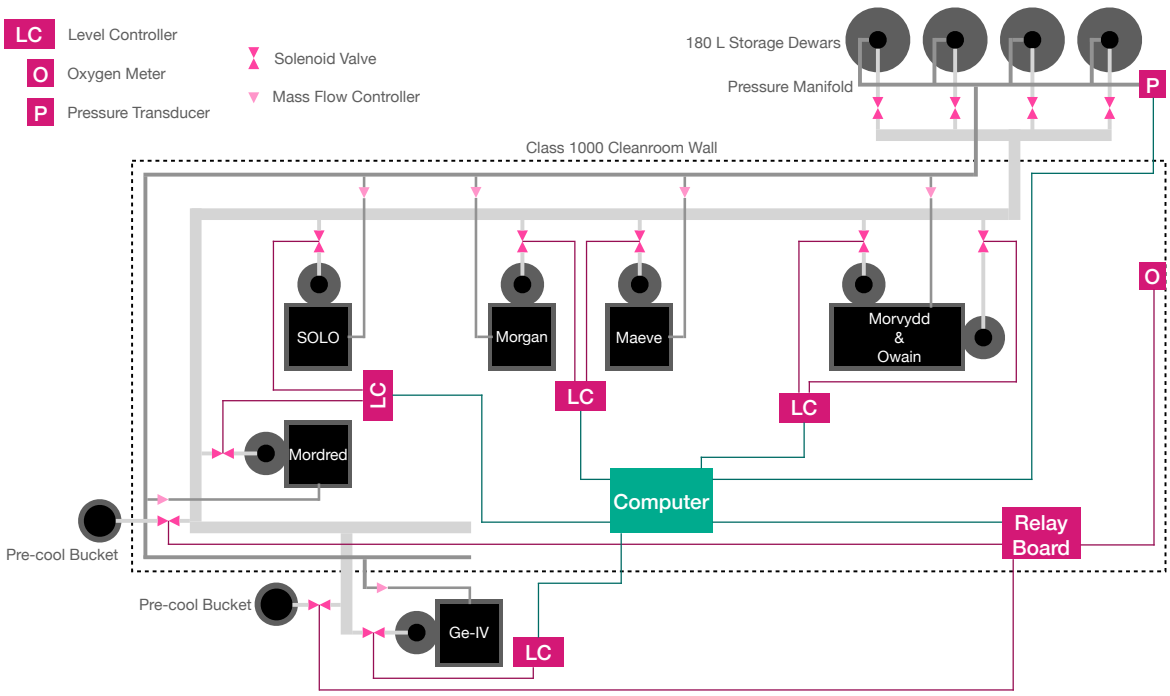

Figure 6.4: All physical elements of the BHUC liquid nitrogen (LN) system automated with a custom LabVIEW program installed on the computer [140].

by all parts of the system so that inefficiencies could be identified and mitigated. Additionally, at a specified hour of the day, the results of the system check were e-mailed to the collaborators allowing them to monitor the status of the equipment so that any problems arising while the program operated could be solved expeditiously.

- The program performed *bi-weekly LN transfers* from the storage dewars to the detector dewars. The procedure began by cooling down the vacuum jacketed pipe with a "pre-cool" in which a solenoid valve leading to one storage dewar was opened allowing LN to enter the warm pipe, evaporate, then escape through a second open solenoid valve leading to an external bucket. When the pipe cooled to a temperature that would allow the flow of liquid, the solenoid valves were shut so the "fill" could start. Solenoid valves leading to one storage dewar and one detector dewar—whose liquid level had dropped below 80% its height—were opened to allow the flow of LN. Once the liquid level of the detector dewar had exceeded 93%, the solenoid valves were closed and the program moved on to the next detector dewar with liquid level below 80%. After the last detector dewar, the weight of LN consumed be each detector was recorded in a google drive spreadsheet and, at a specified hour of the day, the results were e-mailed to the collaborators. Several measures were implemented to ensure the system operated

safely throughout the full length of LN transfer. First, the status of all relevant valves was continuously monitored and all open/shut commands were repeated up to 15 times as needed to receive the desired response. If the liquid level in a detector dewar ever rose above 95%, the manifold pressure ever exceeded 30 psig, or a valve was ever found in an incorrect open/shut position; the transfer was terminated and all valves were shut. In the event that a connection on the pipe was compromised, to prevent LN from spilling into the lab for long periods of time , each detecter dewar was required to fill in no more than 15 minutes. If this time constraint was not met, all valves were shut and an e-mail sent to the collaborators. In case the connection between the computer and equipment was lost, procedures for shutting valves were programmed into the relevant pieces of equipment themselves: all valves operated by the relay board were opened on 16 minute timers and the level controllers were setup to shut the valves to each detector dewar if the the liquid level exceed 95%.

- The program performed liquid level and oxygen *alarm monitoring* using the relay board. If a level controller or the oxygen meter entered an alarm status, a relay within the device would close grounding terminals on the relay board to which the relay was connected. In response, the relay board would send a push notification to the computer. The LN program would receive the notification, immediately shut all valves, and send an alert e-mail to the collaborators.

6.2 High-purity Germanium Semiconductor Detectors

Fig. 6.5 illustrates the primary components of a HPGe semiconductor detector, like those installed at the BHUC. When a particle interacts in the germanium crystal, it generates charge carriers in the form of electrons excited into the conduction band and holes left in the valence band. An electric field drifts the electrons and holes through the crystal to opposing contacts and a pre-amplifier converts the resulting small charge signal into an output voltage large enough for further processing. The gap between conduction and valence band is small enough (0.67 eV [141]) that typical room temperatures will generate leakage currents capable of damaging the crystal and leakage-current-induced noise will destroy the energy resolution of the detector. Consequently, a liquid nitrogen dewar, attached via a coldfinger, is used to cool the crystal to cryogenic temperatures.

A graded shield of $\sim$ 20 cm of lead surrounding $\sim$ 2 cm copper is built around the crystal to mitigate backgrounds. The lead, being very dense, efficiently absorbs γ rays emitted by radiocontaminates in the surrounding environment; however, it emits 70–85 keV x rays produced when the γ rays eject electrons from the K-shell of lead atoms. The layer of copper absorbs these x rays and emits lower-energy x rays (8–9 keV) with shorter attenuation lengths that make them less likely to travel out of the copper into the crystal. In addition, lead shielding can be contaminated by ^{210}Pb that is present in the ore from which the lead

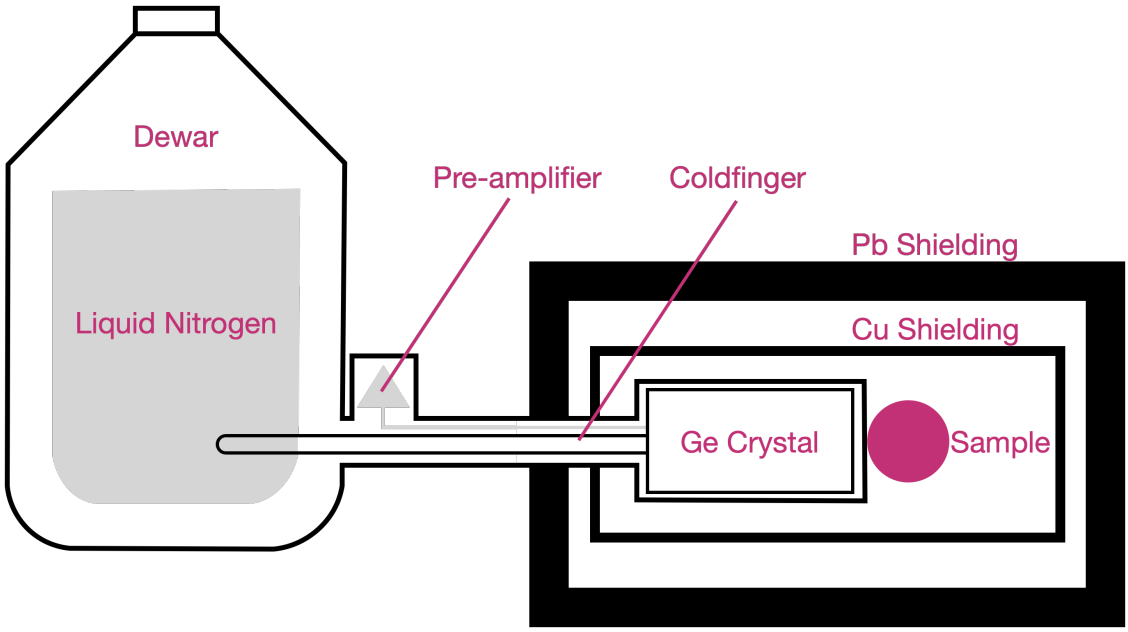

Figure 6.5: Primary components of a HPGe detector.

is smelted—unless special precaution is taken to select lead smelted centuries ago since it's ^{210}Pb contamination will have decayed away ($t_{1/2}$ = 22 years). When ^{210}Pb β decays to an excited state of ^{210}Bi, the nucleus sometimes deexcites by emission of a 46.5 keV γ ray. Its daughter, ^{210}Bi, also β decays emitting higher-energy electrons (Q-value = 1162 keV) that produce a Bremmsstrahlung spectrum extending up to few hundred keV. The copper absorbs the photons from these radiocontaminates and introduces little additional long-lived contamination, other than ^{60}Co from cosmognic activation which emits 1173 and 1332 keV γ rays ($t_{1/2}$ = 1925 days).

In addition to radiocontaminates in the environment, HPGe detectors are affected by backgrounds from cosmic-ray muons, protons, and neutrons. These detectors are often surrounded by scintillating-plastic muon-veto detectors, or are installed at underground locations to reduce the rate at which cosmic rays travel through the crystal.

HPGe detectors are most often used for spectroscopy of γ rays in the 10–10,000 keV range, which have attenuation lengths of 0.005–6 cm in germanium [142]. Crystals volumes of at least several cm^3 are required to achieve high detection efficiency for these photons; much larger crystals of several hundred cm^3 are used in the detectors at the BHUC. Low impurity concentrations of 1 part per trillion are necessary to fully deplete the crystal volume of charge carriers under an applied voltage and to establish high electric fields for fast and complete charge collection. These parameters can be met using a zone refining technique and in some detectors subsequent doping [143].

Large crystals are produced by dipping a smaller seed crystal into molten germanium then

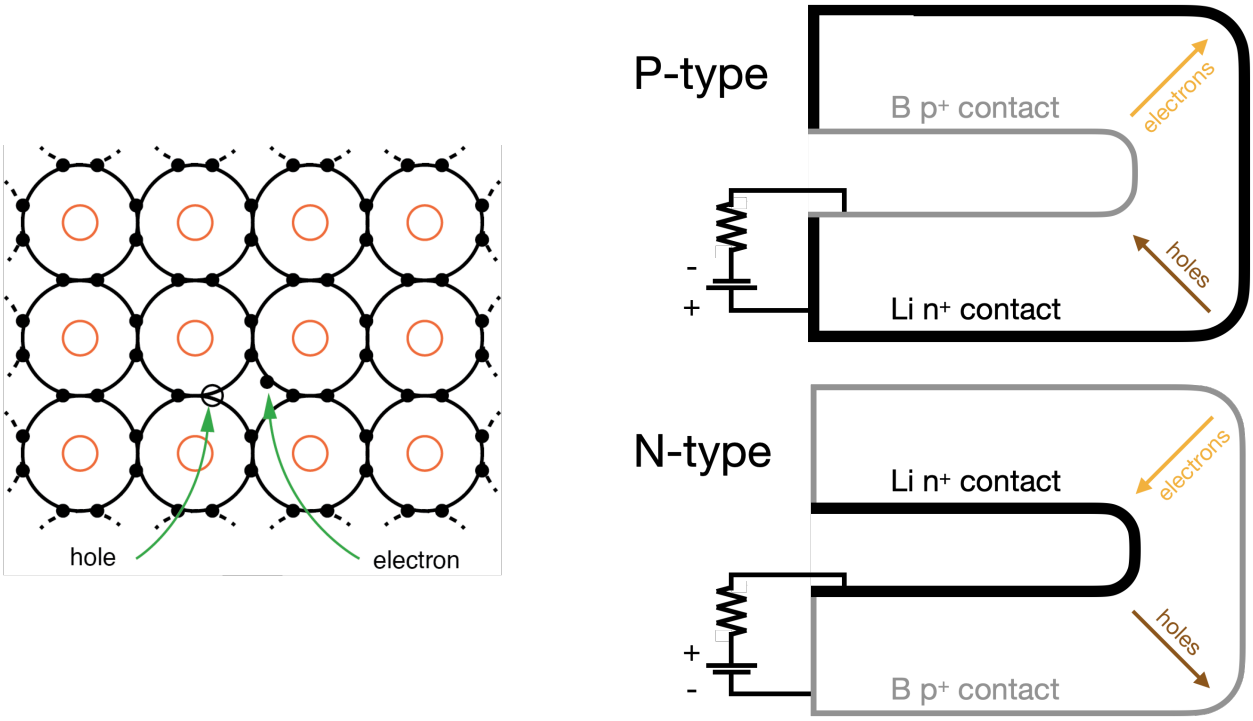

Figure 6.6: Left, depiction of p- and n-type impurities which insert hole and electron charge carriers into germanium crystal lattice (from [144]). Right, illustration of p- and n-type coaxial germanium crystals.

slowly pulling upward using the Czochralski method. The crystals are then cut into a closed-end coaxial shapes and put through several steps of mechanical and chemical polishing before electrical contacts are added to their inner and outer surfaces, as illustrated in Fig. 6.6 (right). There are two types of crystals named for the net type of residual impurities remaining post factum; n-type crystals have an excess of electron donors and p-type crystals have an excess of electron acceptors. The former have a ~ 0.5 mm layer of lithium diffused into the surface of their inner cavity, while the latter have this layer on the exterior. A 0.1–1 μm layer of ion implanted boron is present on the opposing surfaces of both types of crystals. For n-type, the outer boron contact is negatively biased causing unbound electrons in the crystal to migrate toward the inner lithium layer, in this way creating a depletion region without mobile charge carriers. Because boron is trivalent, thus p-type, it does not inject charge carriers into the crystal when biased in this manner. In a p-type detector, the outer lithium layer (n-type) is positively biased causing holes in the crystal to migrate toward the inner boron layer [145].

Detector	Type	Size (kg)	Owner	Sensitivity (mBq/kg) ^{238}U	^{232}Th
Maeve	p	2.1	BLBF	0.1	0.1
Morgan	p	1.7	BLBF	0.2	0.2
Mordred	n	1.4	USD/BLBF	0.7	0.7
SOLO	p	0.6	LZ	0.6	0.3
Morvydd & Owain	p	2×2.1	BLBF	0.05	0.05

Table 6.1: Summary of HPGe detectors located at the BHUC and operated by Berkeley Low Background Facility collaborators during the LZ material screening campaign. Sensitivity estimates assume ^{238}U and ^{232}Th at quasi-static equilibrium in 1 kg of sample material after accumulation of 2 weeks of live-time.

BHUC Detectors

BLBF collaborators used the more-commonly-produced p-type detectors as well as an n-type detector (summarised in Table 6.1) for the LZ material screening campaign. The greater crystal mass of the largest p-type detectors provided increased detection efficiency for photons emitted from material samples (s), but also particles emitted by radiocontamination in the surrounding environment (b). Because limits on activity are proportional to $\sim \frac{s}{\sqrt{b}}$, the greater mass leads to an overall increase in sensitivity that is beneficial when assaying low-activity samples. The n-type detector has the thinner boron layer on the outer surface of the crystal thus has greater efficiency for detecting photons of 10–100 keV, which have attenuation lengths short enough to hinder them penetrating the thicker lithium layer. It is effective at obtaining measurements of contamination by the "early" part of the ^{238}U chain (whose isotopes emit just a few prominent γ rays of ≤ 92 keV) and ^{210}Pb (with a 46.5 keV γ ray), discussed further in the following subsection.

BLBF Analysis

When a γ ray travels through a HPGe detector it can undergo photoabsorption transforming its total energy ($h\nu$) into kinetic energy of an electron in the germanium crystal. This "primary" electron will rapidly thermalize through a variety of secondary processes, including production of energetic electrons and holes which themselves produce further ionisation. Consecutive photoabsorptions of a given energy will produce a spectral feature named the "photopeak", illustrated in Fig. 6.7 (bottom). Its mean is proportional to $n\epsilon$, where n is the average number of electron-hole pairs and ϵ is the average energy used to produce a single pair (~ 3 eV in a germanium crystal [145]), and its width is finite due to variation of the total number of pairs caused by random division of energy between ionization and competing processes. The latter behavior is expressed by F a Fano factor which modifies the Poisson expression for the energy resolution, $\frac{\Delta E}{E} = 2.35 \times \sqrt{\frac{F\epsilon}{E}}$. F is typically ~ 0.1 in

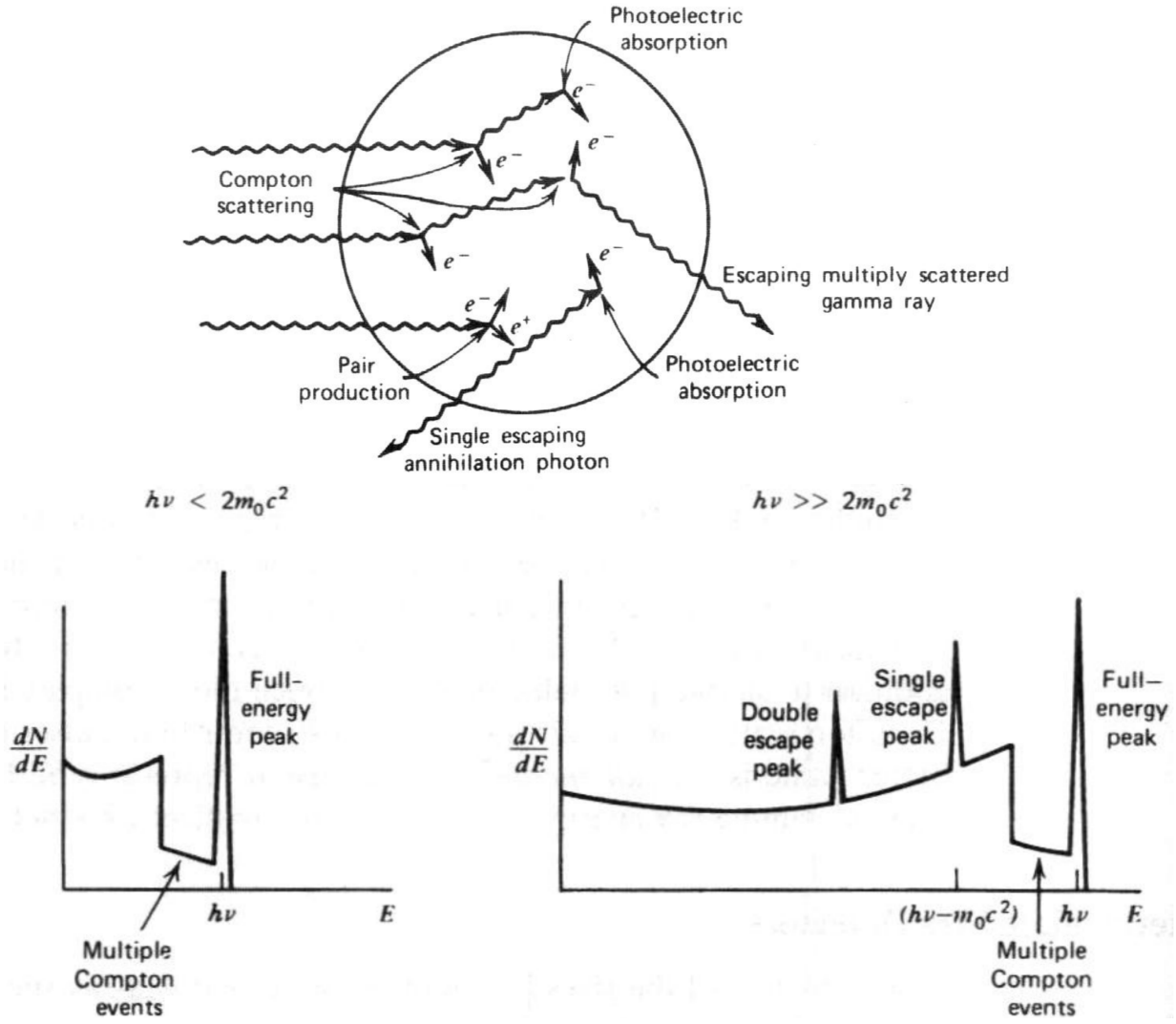

Figure 6.7: γ-ray interactions and corresponding spectral features. $h\nu$ is the γ-ray energy, E is the energy deposited during interactions within the crystal, $\frac{dN}{dE}$ is the differential rate of interactions of energy E, and m_0 is the mass of an electron (511 keV). When $h\nu$ exceeds $2m_0c^2$, the γ-ray can undergo pair production interactions producing single and double escape peaks as shown in the energy spectrum on the right. Illustrations are reproduced from [145].

HPGe detectors used for γ-ray spectroscopy [145].

Compton collision and pair production are additional interactions that produce significant features in a HPGe spectrum. In a Compton collision, only part of the γ rays energy is transferred to the electron. The scattered γ ray can travel out of the crystal carrying with it the remaining energy producing a signal that will contribute to spectral feature named

the "Compton continuum". It can also undergo additional interactions of which one is a photoelectric absorption, producing a signal that will contribute to the photopeak. In pair production, a γ ray of $\geq 2 \times 511$ keV expends its energy producing an electron and positron pair. The mass energy of the pair reappears when the positron annihilates with a nearby electron producing two 511 keV photons. The two photons can undergo any of the previously mentioned interactions depositing all or part of the original γ rays energy in the crystal. Most notably, if one or both of the photons escape, the resulting signal will contribute to the single or double "escape peak" spectral features.

BLBFs standard material screening analysis calculates the activity of several common radiocontaminates by measuring the number of photopeak events from prominent γ rays associated with those isotopes. There is ^{60}Co from activation of copper and steel and ^{46}Sc from activation of titanium. The analysis also looks for three primordial nuclides with half lives short-enough to produce backgrounds on experimental time scales: ^{40}K, and the ^{238}U and ^{232}Th decay chains. The activated isotopes and ^{40}K all undergo a single electron capture (ε) or β decay to a nuclear state that deexcites through emission of γ rays. The remaining two primordial isotopes decay through long chains of daughters some of which β decay to excited nuclear states that emit γ rays (illustrated in Fig. 6.8). In this latter case, the γ rays are used not only to measure the activity of the daughter, but also to infer the activity of the parent assuming a condition of "quasistatic equilibrium". The condition occurs when ^{238}U or ^{232}Th have remained in a material undisturbed for lengths of time much greater than the half life of these isotopes. Because the daughter half lives are much shorter than that of the parent, the daughter concentrations will decrease until their decay rate is equal to that of their parent. Some manufacturing processes can disturb the equilibrium by removing several of the daughter isotopes, including ^{226}Ra and ^{228}Ra, which are present in the ^{238}U and ^{232}Th chains and have a long half lives compared to other daughters. If one of these processes occurs, the chains become broken into early and late sections with the late section reaching a separate quasistatic equilibrium with the radium isotope. Equilibrium can also be broken by elevated ^{210}Pb contamination, usually introduced when ^{222}Rn daughters in the air plate out on exposed surfaces. The radiocontaminates discussed in this paragraph are summarised in Table 6.2.

The number of photopeak events is translated into a samples activity using a calibration factor that takes into account geometry dependent effects that determine the detection efficiency. For example, γ rays emitted by radiocontaminates within a sample sometimes travel in a direction that does not intersect with the crystal. They can also travel toward the crystal, but interact with the material of the sample before reaching the crystal, undergo interactions in the crystal which deposit only a portion of the γ rays energy, or travel entirely through the crystal without interacting. The efficiency can be calculated with a Monte Carlo simulations of the passage of particles through matter, such as GEANT4 [116], or a calibration source of similar shape and density to the sample. BLBF collaborators frequently used a Table Mountain Latite silicate rock standard with consistent concentrations of ^{238}U and ^{232}Th both in quasistatic equilibrium [146].

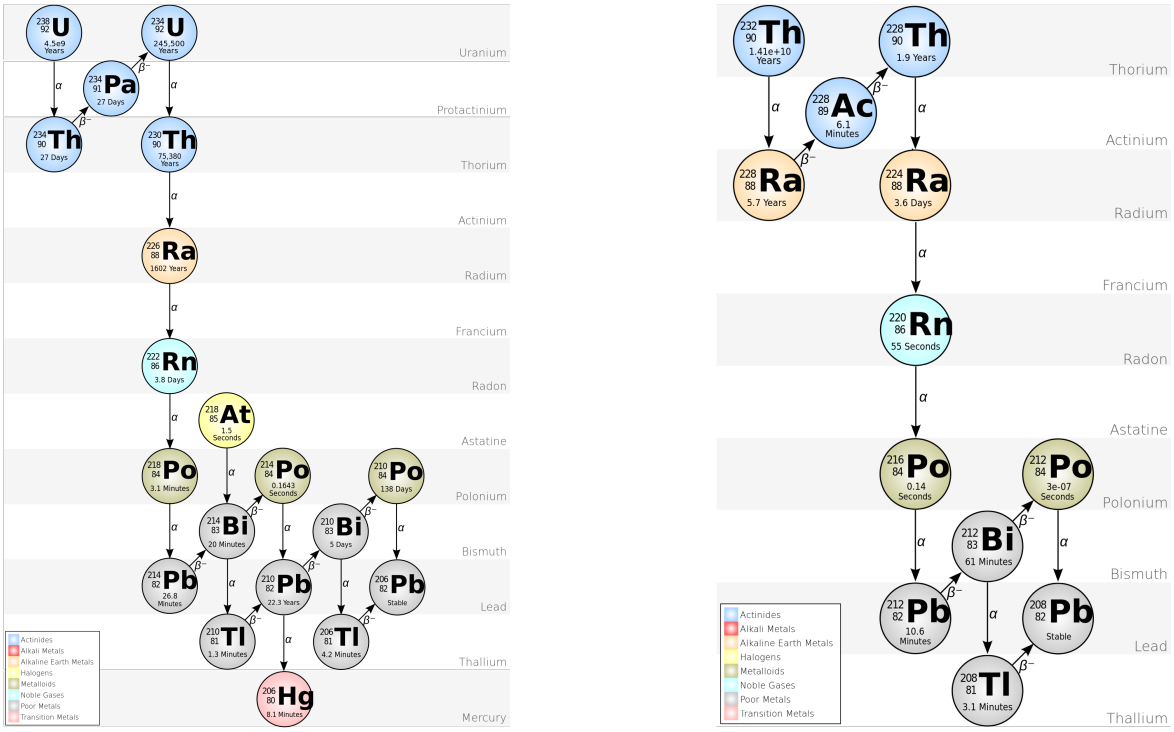

Figure 6.8: ^{238}U or ^{232}Th decay chains from [135].

Type	Radiocontaminate	Decay(s)	Half-life (yr)	Prominent γ rays (keV)
Single Decay	^{60}Co	β	5.3	1173, 1332
	^{46}Sr	β	0.23	889, 1120
	^{40}K	ε	1.25×10^9	1461
Decay Chain	^{238}U (U-early)	β, α	4.47×10^9	92.4, 92.8, 1001
	^{226}Ra (U-late)	β, α	1600	295, 352, 609, 1764
	^{210}Pb	β, α	22.3	46.5
	^{232}Th (Th-early)	β, α	1.4×10^{10}	911, 965, 969
	^{228}Ra (Th-late)	β, α	5.75	511, 583, 2614

Table 6.2: Prominent γ rays of radiocontaminates measured in BLBFs standard material screening analysis.

6.3 Material Screening Results

LZ collaborators carried out an extensive campaign of screening all raw materials proposed for building the detector. Those candidate materials producing the lowest number of backgrounds events in the nominal LZ WIMP search analysis were selected for manufacturing all detector components. Furthermore, many fully assembled components were assayed to look for any evidence of radiocontamination introduced by the manufacturing process. The results of this campaign are summarised in publications [131] and [115]. This section presents the assay results for two samples not discussed in these publications: components removed from the bottom of LUX and the gadolinium loaded liquid scintillator for use in the LZ outer detector.

Components in the Bottom of LUX

While LUX was taking data, the rate of 0–2 MeV γ-ray events occurring near the bottom of the active xenon volume was observed to be greater than what had been predicted by the simulation. Moreover, these extra events blurred the energy resolution as if they had been produced by γ rays that had lost part of their energy through interactions occurring prior to entering the active volume. It was hypothesised a high activity source several centimeters away from the bottom of the TPC was emitting γ rays that were scattering in other components as they travelled toward the xenon. Specifically, there were several components in this region which had not been assayed prior to assembly of the detector as they were far from the active volume thus unlikely to be a major source of backgrounds.

Several simulations were performed to explore the hypothesis that an unanticipated background source existed inside the cryostat below the TPC. ^{238}U, ^{232}Th, and ^{60}Co were simulated uniformly throughout the two copper γ-ray shields that filled the majority of this space. Additionally, these isotopes were simulated in a cylindrical plane at varying depths within the shields. It was found that a 102 Bq ^{60}Co, 173 Bq ^{238}U, and 10.4 Bq ^{232}Th source distributed in a plane 23.5 cm below the TPCs bottom grid electrode best reproduced the energy spectrum of the LUX data [147].

While LUX was being deconstructed, components from the bottom of the TPC were removed so their activity could be measured and compared to what was predicted by the simulation. There were pieces of the two copper γ-ray shields as well as components distributed around the shields: thermally insulating foam; aluminum grating that provided support for the foam; part of the thermosiphon used to cool the liquid xenon; the filler chiller shield (FCS) level sensor; and a miscellaneous collection of nuts, bolts and copper pieces. All of the components were brought to the BHUC where they were assayed. The results are summarised in Table 6.3.

All of the new assays measured activities orders of magnitude below what was predicted by the LUX simulation. The results utterly contradict the presence of an unanticipated background source inside the cryostat just below the TPC.

Component	Mass (kg)	Activity (mBq) ^{238}U	^{226}Ra	^{232}Th	^{228}Ra	^{40}K	^{60}Co
Cu Shield 1	150	200 ± 100	< 21	27 ± 4	< 28	< 16	< 3.4
Cu Shield 2	300	480 ± 200	< 31	37 ± 6	< 33	120 ± 8	< 4
Foam	0.5	< 330	< 22	< 15	< 20	17 ± 2	-
Al Grating	1.5	$(12 \pm 2) \times 10^3$	< 11	140 ± 30	160 ± 21	< 58	-
Thermo.	0.14	160 ± 40	26 ± 5	12 ± 2	19 ± 4	100 ± 6	< 0.52
Level Sensor	0.11	11 ± 9	< 1.3	< 1.7	< 1.7	< 4.8	< 0.25
Misc.	2.9	1600 ± 200	< 4.6	< 28	< 67	< 16	< 6.8
Sum	455	$< 16,500$	< 70	< 260	< 260	< 300	< 15

Table 6.3: Assay results for components pulled from the bottom of the LUX TPC: pieces of the two copper γ-ray shields; thermally insulating foam; aluminum grating that provided support for the foam; part of the thermosiphon used to cool the liquid xenon; the filler chiller shield (FCS) level sensor; and a miscellaneous collection of nuts, bolts and copper pieces. All limits are placed at $1 \cdot \sigma$ significance. The row labelled "Sum" contains the sum of all measurements added to the quadratic sum of all limits and uncertainties.

An alternate explanation is the background excess was composed of events in which a γ ray had interacted in the "reverse field region" at least once before or after interacting in the active volume—nicknamed (γ, X) events. This region was a 3.6 cm layer of xenon located between the cathode and bottom grid electrodes [90]. In the active volume, the electric field caused electrons to drift upward toward the vapor where they would produce detectable electroluminesence; in the reverse field region, the electrons drifted downward and were not detected. On the other hand, scintillation was detected with similar efficiency in both regions.

(γ, X) events were handled incorrectly in the simulation in two ways. First, the total energy of a simulated event was calculated by summing up the energy deposited at every interaction point in the xenon. In the real detector, the fraction of energy used to produce electrons in the reverse field region would be lost causing these events to have degraded energy resolution. Second the positions of a simulated event was calculated from the energy-weighted average position of every interaction in the xenon, and a cut was applied to remove events occurring near the edges of the volume. In the real detector, the energy-weighted average position would only include interactions in the forward field region which produced detectable electrons required to calculate a position. Consequently, the position of real (γ, X) events would be reconstructed higher in the xenon and they would not be removed by the position cut. Overall, many more simulated (γ, X) events would be cut than real (γ, X) events.

Gadolinium Loaded Liquid Scintillator for LZ

The LZ outer detector (OD) is composed of gadolinium loaded liquid scintillator (GDLS). When neutrons travel through the OD, they can be captured by a gadolinium nucleus that subsequently emits γ rays with energies that add up to ~ 8 MeV [130]. Some of the γ rays will interact within the OD depositing MeV quantities of energy that are transformed into scintillation photons detected by surrounding PMTs.

Backgrounds of the neutron capture signal come from the primordial nuclides, and several radioactive isotopes that accompany the gadolinium. Some of the contaminates are introduced when ^{222}Rn in the air, or its daughters, becomes absorbed in the liquid scintillator. Most isotopes in the chain have half lives less than a few tens of minutes, thus are in quasistatic equilibrium with ^{222}Rn which has a 3.8 day half life. These isotopes will decay away within days of closing the OD, so will not produce backgrounds throughout the majority of LZs runtime. However, the daughter ^{210}Pb, with a 22 year half life, and its progeny ^{210}Bi and ^{210}Po, will remain in the liquid scintillator for the duration of LZ.

To minimise ^{210}Pb backgrounds, it is necessary to limit the exposure of the GdLS to air. This is especially true of air at the 4850 foot level of SURF which can contain concentrations of ^{222}Rn of 150–1000 Bq/m^3 [148], a factor 15–100 greater than the average atmospheric concentration [149].

In 2016, a batch of GdLS that had been recently shipped to the 4850 foot level was suspected of being exposed to underground air. A sample of the liquid was loaded into Maeve and screened for evidence of contamination. Fig. 6.9 plots the time-dependent activity of two ^{222}Rn daughters, ^{214}Pb and ^{214}Bi, using signals from 352and 609 keV γ rays. The activities dissipated with 2.2 ± 0.2 day half lives much longer than the 20 and 27 min half lives of ^{214}Pb and ^{214}Bi, but similar to the 3.8 day half life of ^{222}Rn. If the GdLS had recently absorbed significant quantities of these three isotopes, and it had absorbed greater amounts of ^{214}Pb and ^{214}Bi than ^{222}Rn, then the daughter activities would dissipate until they decay at a rate equal to the half life of the parent. The result is strong evidence the GdLS had recently absorbed a significant quantity of ^{222}Rn and its daughters.

6.4 Morvydd & Owain

Throughout 2017 and 2018 a state-of-the-art HPGe detector named Morvydd & Owain (nicknamed "The Twins") was designed then installed at the BHUC. The detector housed two p-type crystals inside of a shield composed of a 1" thick, radiopure copper box surrounded on all sides by ≥ 8" of lead bricks. A copper lid holding an additional 1560 lbs of lead bricks was slid on/off the top of the shield on two steel tracks. Ledges hung over the sides of the lid to block external γ rays from traveling through the crevice between lid and shield unimpeded. Fig. 6.10 shows the computer aided design (CAD) of the detector and a photograph after it was fully installed.

Morvydd & Owain was designed to achieve sensitivity to very low levels of radiocon-

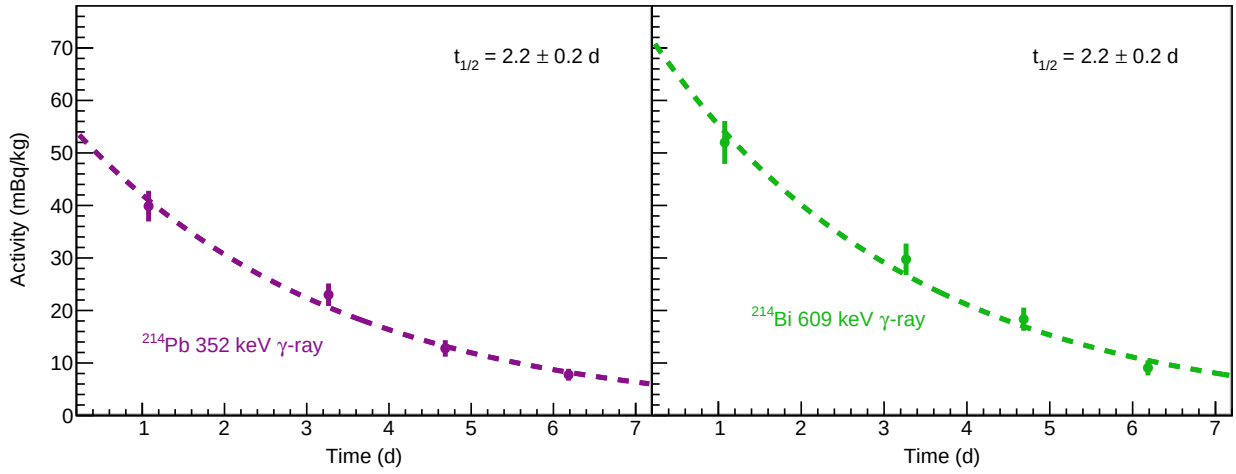

Figure 6.9: Time dependent activity of two ^{222}Rn daughters in a batch of gadolinium loaded liquid scintillator expected to have been exposed to underground air.

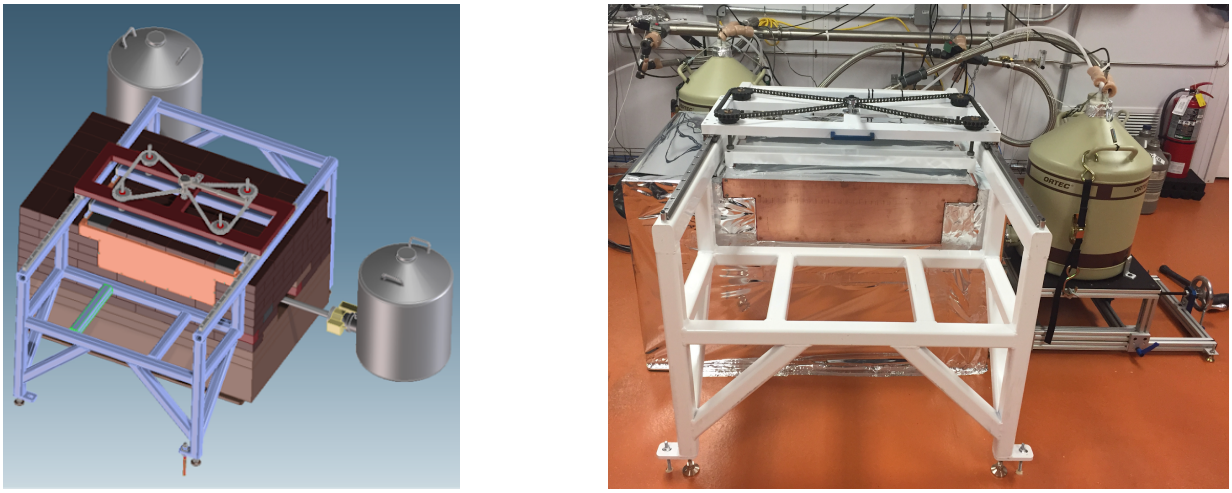

Figure 6.10: State of the art HPGe detector Morvydd & Owain.

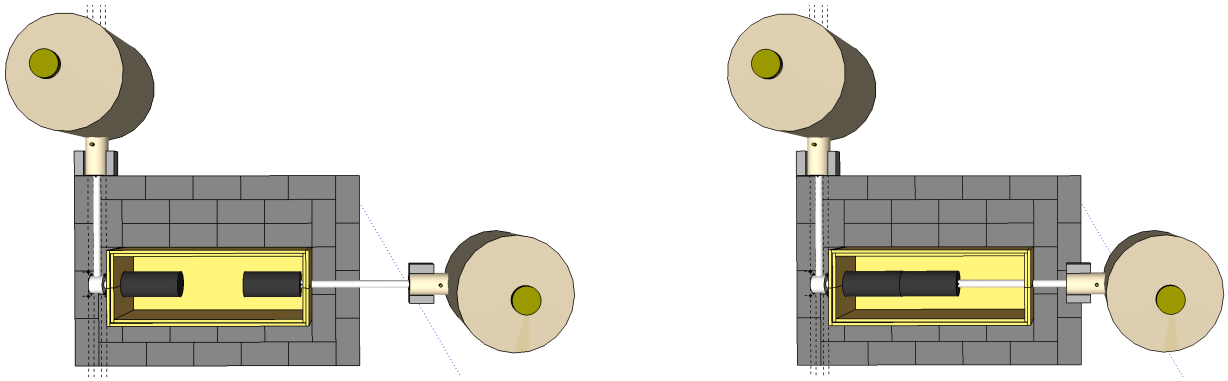

Figure 6.11: Morvydd & Owain with crystals in fully separated and united orientations.

tamination. The two crystals were selected for their large mass, 2.1 kg, to maximise the γ ray detection efficiency[2]. Furthermore, the copper box was made to fit sample material in two Marinelli beakers of the largest standard size, 4 L. A special feature of the detector is the sliding plateform that holds one of the dewars allowing the corresponding crystal to be moved forward to meet its counterpart. Small samples could then be placed between the faces of the two crystals to nearly surround them with detection medium (i.e. to obtain almost 4π solid-angle coverage of the sample). Fig. 6.10 (right) shows the sliding platform while Fig. 6.11 contains illustrations of the crystals in fully separated and united orientations.

The sensitivity of Morvydd & Owain was estimated to be 0.05 mBq/kg for both ^{238}U and ^{232}Th at quasistatic equilibrium in 1 kg of sample material after accumulation of 2 weeks of livetime. Table 6.1 compares this number to sensitivities of other detectors that are operated by BLBF collaborators. The sensitivity of Morvydd & Owain will be a factor of 2 greater than Maeve, the next-most sensitive detector installed at the BHUC.

6.5 LZ WIMP Sensitivity

Throughout the LZ material screening campaign, over 1000 samples were assayed at the BHUC and BUGS underground facilities, as well as the LBNL and UA surface level facilities [131, 115]. The results were used to select detector construction materials that would contribute the lowest numbers of background events to the search for WIMP dark matter. Fig. 6.12 demonstrates the selection procedure with samples of titanium considered for construction of the cryostats. It plots the expected number of nuclear recoil (NR) and electron recoil (ER) events within the LZ fiducial volume after applying all WIMP search cuts and vetoes including a 50% NR acceptance cut which rejects 99.5% of ER backgrounds. To guide the eye, several lines of constant background are drawn at 10% of the pp solar neutrino ER

[2]These crystals were obtained from Kai Vetter, Nuclear Engineering Department, University of California Berkeley.

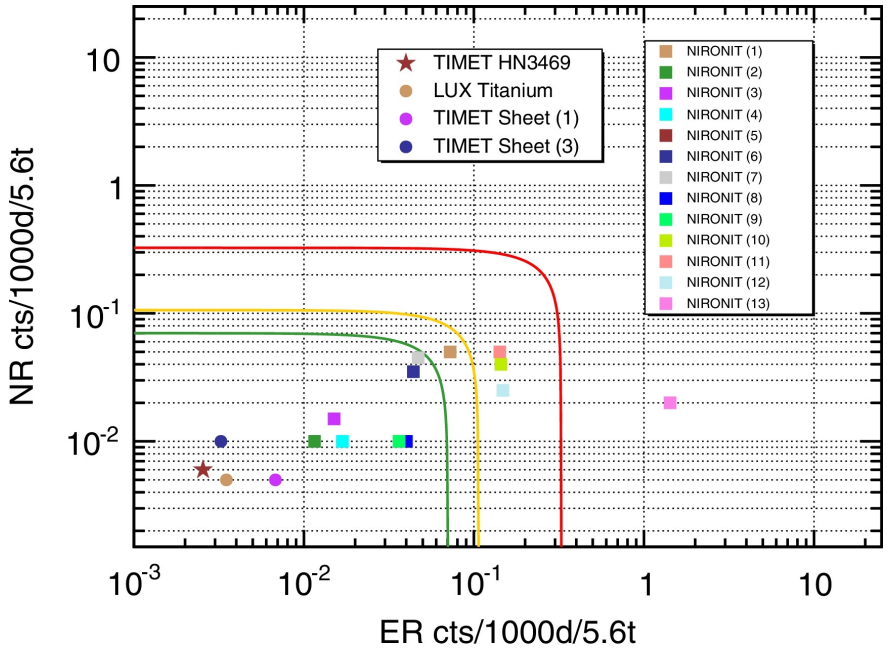

Figure 6.12: Expected number of nuclear recoil (NR) and electron recoil (ER) events within LZ's fiducial volume after applying all WIMP search cuts and vetoes including a 50% NR acceptance cut which rejects 99.5% of ER backgrounds. Lines of constant background are drawn at 10% of the pp solar neutrino ER background and 0.2 NR events, 5% of the pp solar neutrino ER background and 0.05 NR events, and 3.3% of the pp solar neutrino ER background and 0.03 NR events. The titanium sample selected for construction of the cryostat is TIMET HN3469. Figure from [131].

background and 0.2 NR events, 5% of the pp solar neutrino ER background and 0.05 NR events, and 3.3% of the pp solar neutrino ER background and 0.03 NR events. The titanium sample selected for construction of the cryostat, TIMET HN3469, is expected to produce fewer background events than that of the most stringent constant background line.

Fig. 6.13 illustrates the relative number of ER events in LZs WIMP search region produced by five significant classes of background sources: xenon contaminates, neutrinos, surface contamination, detector components, and laboratory/cosmogenics. The percentage of events from detector components was reduced to just 0.8% of the total background load by the material screening campaign.

For comparison, a pre-campaign simulation predicted 11.85 ER and 0.33 NR events in a 1000-liveday 5.6-tonne exposure. It assumed the LZ detector would be constructed from materials with the worlds lowest measured activities to date [150]. The campaign identified even-lower activity materials which were inserted into the simulation to calculate a new prediction of 9 ER and 0.12 NR events [53]. To restate, the material screening campaign

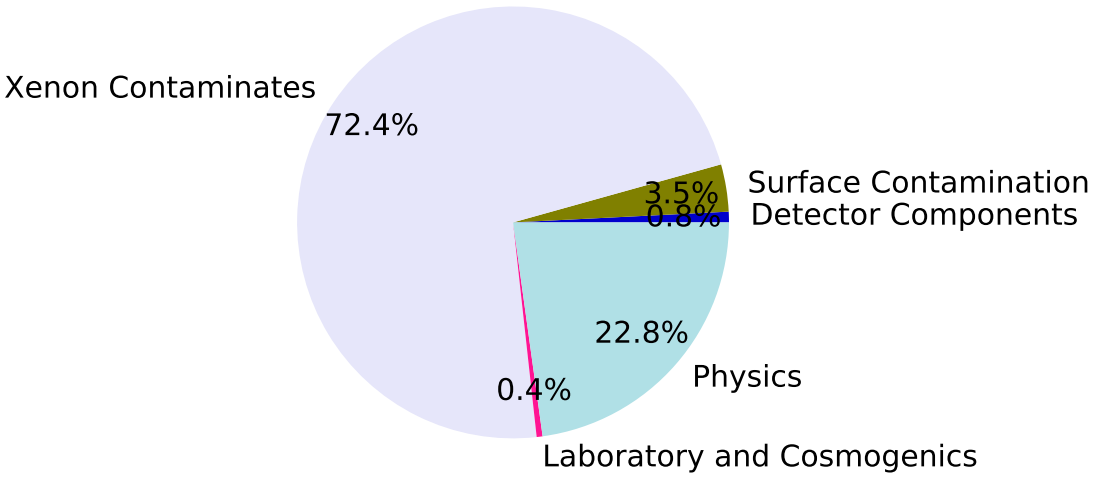

Figure 6.13: Predicted percentages of ER events in LZs WIMP search region produced by five significant classes of background sources: xenon contaminates, neutrinos, surface contamination, detector components, and laboratory/cosmogenics. Data is reproduced from [53].

resulted in the rate of radioactivity-induced NRs—the backgrounds most similar WIMPs—being reduced of a factor of 3.

Chapter 7

Improving Sensitivity to Low-mass Dark Matter in LUX Using a Novel Electrode Background Mitigation Technique

The dark matter (DM) community has long pursued a class of hypothetical particles predicted by freeze out to have scattering cross sections of approximately the weak scale, $\langle\sigma\nu\rangle \sim 3 \cdot 10^{-25}$ cm^3/s, and heavy masses of $m_\chi \in$ 10–10,000 GeV [151]. Coincidentally, the characteristics of these Weakly Interacting Massive Particles (WIMPs) align with those of particles predicted by R-parity-conserving supersymmetry, a popular extension to the Standard Model [56]. Because of the WIMP's robust theoretical motivation, experimentalists have been driven to develop the competitive field of direct dark matter detection via dual-phase xenon time projection chambers (TPCs). By nature, these detectors specialise in observation of WIMPs due to xenon's similar heavy mass, $\sim$ 131 GeV, which would promote large transfers of energy in elastic DM-nucleus collisions according to Equation 1.11. They have $\sim$ 5 GeV mass thresholds determined by the $\sim \left(\frac{m_\chi}{m_{Xe}}\right)^2$ scaling of energy transferred to the xenon nucleus when $m_\chi \ll m_{Xe}$.

As successive direct DM detection experiments have produced ever more powerful null results and the LHC has thus far failed to find evidence of supersymmetry, the DM community has begun to more seriously consider well motivated low-mass alternatives to WIMPs [38]. Chapter **??** summarises several of these models: there is dark sector, freeze-in, and asymmetric DM. The last category contains particles with predicted masses of $\sim$ 1–15 GeV [152], a range that straddles the dual-phase xenon TPC lower mass threshold. The situation offers a challenge to experimentalists working with dual-phase xenon TPCs. This type of detector is a mature technology that has been highly successful at searching for WIMPs. Are there analysis techniques that can lower mass thresholds so that these detectors can better search for low-mass DM?

The end of Chapter 2 summarises three such techniques, while the current chapter goes into depth about the most powerful of these: an "$S1$-agnostic" analysis. Unlike the standard WIMP search, which requires all events contain exactly one $S1/S2$ pair, an $S1$-agnostic analysis includes events with both zero or one $S1$ and one $S2$. This choice takes advantage of the much higher electron detection efficiencies (~ 1) observed in dual-phase xenon TPCs compared to photon detection efficiencies (~ 0.1). Scatters of < 5 GeV DM would produce xenon atom recoils of only a few keV which would subsequently drive production of only a handful of scintillation photons and freed electrons. The asymmetry in detection efficiencies for the two types of quanta would prevent many of these events from generating $S1$s while still allowing them to produce $S2$s. Alone, $S1$-agnostic analyses have been used to lower mass thresholds to ~ 2 GeV [122, 123, 125]; however, when used in combination with predictions of the Migdal effect, they have pushed thresholds all the way down to ~ 0.1 GeV [125].

The impact of performing an "$S1$-agnostic" analysis with the LUX WS2013 dataset is illustrated in Fig. **??**, which compares the low $S1 + S2$ and the high $S2$ detection efficiencies in the energy range of xenon nuclear recoils (NRs) induced by low-mass DM. These curves are calculated using the Noble Element Simulation Technique (NEST) version 2.0.1 [134] to simulate the liquid xenon microphysics of signal production and detector physics of signal collection. Below 6 keV_{nr}, the $S1 + S2$ detection efficiency diminishes because low photon detection efficiency prevents the small scintillation signals of nuclear recoils in this energy regime from producing $S1$s that pass the two PMT coincidence criterion (described in Sec. 7.1). When the requirement that events contain an $S1$ is dropped, efficiency remains high down to 1 keV_{nr}. Below this point, the small number of electrons produced by NRs are sometimes lost due to capture by impurities while drifting (a 0–30% effect) or remain trapped at the liquid surface due to the 49% extraction efficiency observed in WS2013. (Further details on the additional efficiency curves presented in Fig. **??** are discussed in Sec. 7.1.)

An important side effect of incorporating events with only an $S2$ is that background rejection based on $S2/S1$ ratio and z-coordinate becomes impossible. As a consequence, "$S1$-agnostic" analyses have elevated rates of low-energy background events from multiple sources.

In WS2013, there are three categories of electron emission trailing preceding $S1$s and $S2$s (outlined previously in Chapter 3 and detailed in publication [111]). There was photoionization and the photoelectric effect induced by xenon luminescence, delayed emission of electrons trapped under the liquid surface, and capture and release of drifting electrons by impurities. The first category of emission is dominant up to 325 μs following $S1$s or $S2$s (the length of time for an electron to drift the full length of the TPC), but disappears after this point. These emissions are not a major source of $S2$-only backgrounds because their short time delays allow them to be easily associated with preceding pulses—however they do complicate event selection, discussed in Sec. 7.1. The last two categories of emission decay over long timescales and generate significant $S2$-only backgrounds within second-wide time windows following high energy events that produce many electrons.

In addition to emissions that trailed preceding pulses, there are two, particularly prevalent categories of events originating on the gate and cathode grids (discussed previously in

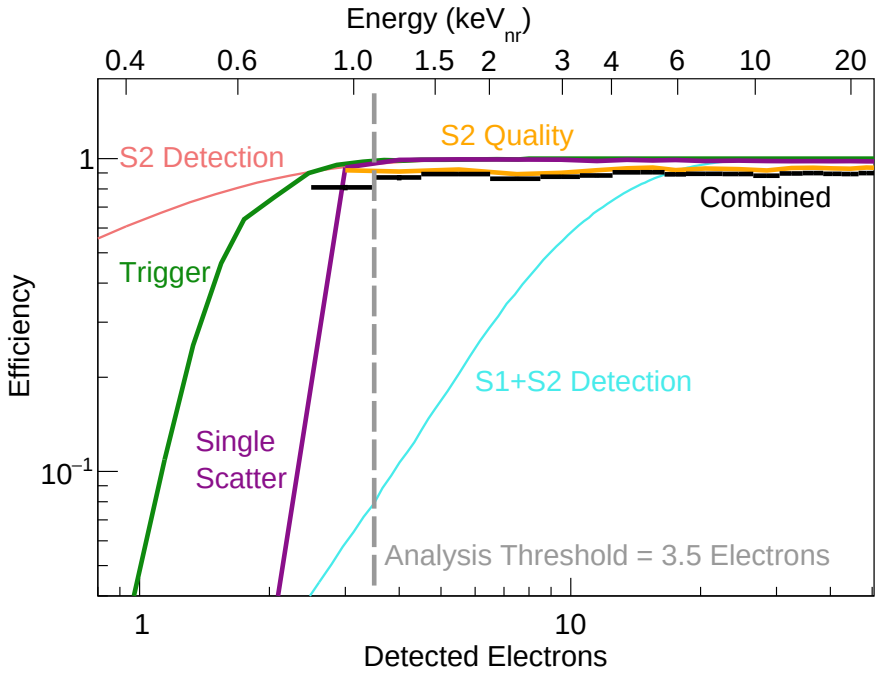

Figure 7.1: Trigger [93], single scatter, and $S2$-quality cut efficiencies, as well as their combined efficiency (including the 1.6% acceptance loss from the single photon $S1$ cut). The curves labeled "$S2$ Detection" and "$S1$+$S2$ Detection" encompass the liquid xenon microphysics of signal production and detector physics of signal collection as modeled with NEST v2.0.1 [134]. The latter diminishes more rapidly at low energy due to the requirement that $S1$s be composed of photon signals in two or more PMT channels. It is not used as part of this analysis, but is shown to illustrate the extra low-mass dark matter sensitivity gained in this search.

Chapter 3). There was grid electron emission and radiogenic events occurring on/in the grid wires. The former is a process that produces single or multiple electron $S2$s whose intensities correlate with the electric field magnitude near grid wires [113, 114]. These events were observed to occur at hotspots on the grids that intermittently emit electrons for periods of time up to a few tens of seconds, and are also expected to occur in less conspicuous patterns continuously throughout the run. The latter are backgrounds from ^{238}U/^{232}Th contamination inherent to grid wires and plate-out of ^{222}Rn daughters on wire surfaces. Plate-out occurs primarily during construction when components are exposed to air with typical quantities of ^{222}Rn. However, it also occurs during operation when charged ^{222}Rn daughters in the xenon drift along electric field lines that terminate on wire surfaces. Small amounts of these isotopes are continuously absorbed in the xenon during normal operation conditions. Specifically in LUX, they were introduced during a 150 Bq ^{222}Rn injection [153]. After an initial plate-out event, the short-lived daughters quickly decay away leaving only ^{210}Pb, with

a 22-year half-life, and its two daughters ^{210}Bi and ^{210}Po. The most harmful decay products are emitted at low energies. They include ^{210}Pb and ^{210}Bi β-decay products, and recoils of ^{206}Pb nuclei following ^{210}Po α decays in which the α particle travels into the wire.

This chapter presents a search for low-mass dark matter via an $S1$-agnostic analysis of the WS2013 dataset, the results of which have been published in Physical Review D [106]. A major component of the work was mitigation of "$S2$-only" backgrounds. Where possible, strong selection criteria were developed to remove suspicious events while maintaining high signal detection efficiency. After applying a set of data selection criteria to minimise most backgrounds, there was a remaining excess of electrode events. To address this finding, a machine learning technique was developed to identify and reject events based on $S2$ pulse shape, which was observed to differ between $S2$s originating on the electrodes and those originating in the bulk xenon. The technique is shown to significantly improve limits in an $S1$-agnostic analysis. The chapter ends with a brief discussion of how the technique might be refined for near future experiments, such as LZ and XENONnT.

7.1 Event Selection Criteria

To achieve maximum DM sensitivity in an $S1$-agnostic analysis, new event selection criteria were introduced to address background challenges not present in previous analyses requiring both an $S1$ and $S2$ [64, 154, 155, 121]. There are extensive modification to the definition of a candidate DM event, software threshold, exposure, and event quality cuts. These are detailed in the subsections below.

Definition of a Candidate DM Event

Candidate DM events are interactions in the active xenon volume that generate one burst of scintillation and one localized cloud of ionization, as would a single scatter of a DM particle on a xenon nucleus. The corresponding $S1$ and $S2$ pulses are grouped in 1 ms event windows by the data processing framework (DPF). Within each window there may be small secondary pulses from a variety of sources. The most significant contributors are single electron $S2$s from photoionization and the photoelectric effect of the interactions luminescence, and single photon $S1$s from thermionic dark counts of the PMTs and PTFE fluorescence induced when xenon luminescence photons are absorbed by the reflective PTFE walls surrounding the TPC [96, 111]. [In addition, to secondary $S2$s induced by the interaction itself, there can be significant rates of secondary $S2$s induced by previous large events; however, these pulses are mitigated with a veto detailed in the subsection titled "Exposure".]

Several criteria, similar to those described in [63, 64, 52], were applied to efficiently select single scatter events containing the secondary pulses. $S1$s were required to have a two PMT coincidence to distinguish them from a single photon; $S2$s were required to have greater than 55 spikes in their pulse waveform; and event windows were required to contain exactly one $S2$ preceded by one or zero $S1$s which pass the second and first conditions, respectively.

The $S2$ condition utilizes a variable called "spike count", an alternative measure of pulse size sometimes used in place of area in sparse pulses. It corresponds to approximately 2.2 detected electrons as measured using pulse area, $5 \cdot \sigma$ greater than the mean pulse area of a single electron.

The single scatter detection efficiency, shown in Fig. 7.1, was measured using tritium β-decay calibration data as a robust sample of low-energy events in the liquid xenon bulk [74]. The efficiency is ~ 1 for events with $S2$s above the software threshold discussed in the next point.

Software Threshold

An $S2$ software threshold of 3.5 detected electrons ($S2 = 85.75$ phd) was selected because efficiency measurements that use tritium calibration data are robust for events with $S2$s larger than this size. Below 3.5 detected electrons, the calibration data were found to contain non-negligible quantities of background events from delayed emission of electrons trapped under the liquid surface, and capture and release of drifting electrons by impurities. This is demonstrated in Fig. 7.2 which shows the low-energy region of the tritium spectrum where the event rate rises due to these secondary electron emissions. The data are fit with linear and exponential functions that estimate the relative contributions from tritium and secondary emission events. The exponential comprises only 0.3% of the integral between 3.5–4.5 detected electrons (the lowest energy bin used in subsequent parts of the analysis).

Exposure

Target Volume

Backgrounds from radioactive contamination on the electrodes and detector walls were mitigated with cuts on event position.

- Electrode events with $S1$s were removed with a drift time cut at $7 < t_{drift} < 321$ μs, whose boundaries correspond to 5 mm below the gate and 2 mm above the cathode.
- Due to the geometry of the detector, $S2$s produced at the junction of the wall and cathode, a starting radius of ~ 24 cm, drift upward with a slight radial bias exiting the liquid at a reconstructed radial coordinate of $r_{S2} \sim 20$ cm [90]. At this exit radius, $S2$s just above the software threshold have an uncertainty of $\sigma_{r_{S2}} \sim 1.5$ cm [94]. A cut of $r_{S2} < 16$ cm, greater than $2 \cdot \sigma_{r_{S2}}$ in from the exit radius, was selected to remove the vast majority of these events.

The 124 kg of xenon mass delimited by the two cuts was calculated from the fraction of accepted ^{83m}Kr events. The uncertainty on the calculation has two major contributors. The first is a $\pm 0.8\%$ contribution from estimates of xenon volume and density used in the active mass calculation from [88]. The second is introduced by the drift cut which can only

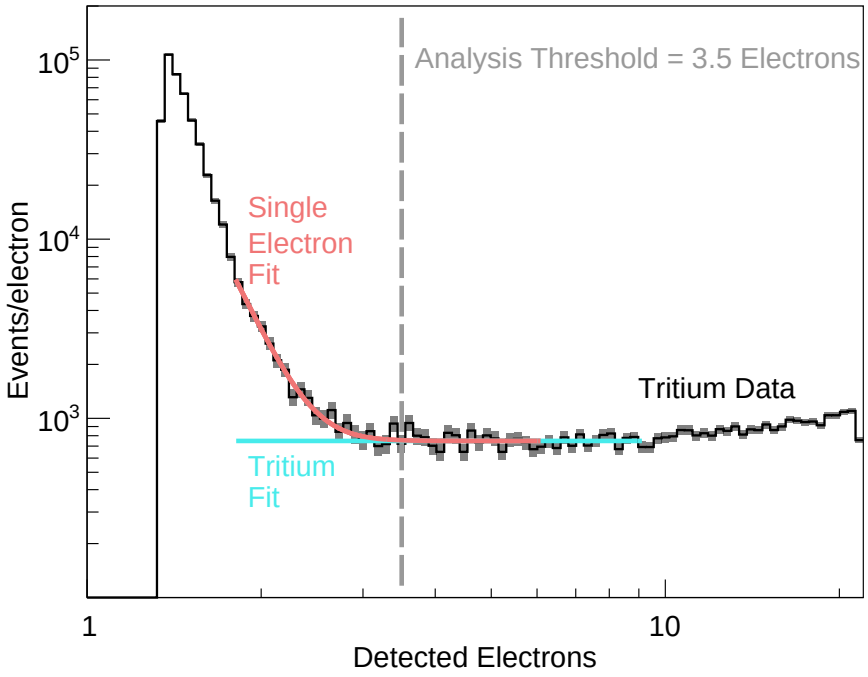

Figure 7.2: Low-energy region of the tritium spectrum where the event rate rises due to delayed emission of electrons trapped under the liquid surface, and capture and release of drifting electrons by impurities. The data are fit with linear and exponential functions that estimate the relative contributions from tritium and secondary emission events. The exponential comprises only 0.3% of the integral between 3.5–4.5 detected electrons, thus the analysis threshold was chosen to be 3.5 detected electrons.

be applied to events that do have an $S1$ and, therefore, a determinate t_{drift}. There is an additional 2% contribution to the uncertainty from the mass increase that would occur if the drift cut were to be removed.

Exposure

Three data quality vetoes were used to remove WS2013 data taken under unstable detector conditions or during periods of time with high rates of $S2$-only backgrounds.

- Data taken during April 2013, the beginning of the WS2013 dataset, was removed from the analysis because of unstable electron lifetime during this period of time.
- A 50 ms veto following large events with a full waveform area greater than 10^5 phd was implemented to reduce backgrounds from delayed emission of electrons trapped under the liquid surface, and capture and release of drifting electrons by impurities; two backgrounds whose intensities directly correlate with the size of preceding $S2$s

and decay with exponential and power law-like time dependencies, respectively [111]. This "large event veto" maximally reduced the event rate above the software threshold while preserving 93% of the live-time as is demonstrated in Fig. 7.3 by comparing the WS2013 spectrum after applying the selected veto with that after applying a more aggressive veto preserving only 10% of the live-time. Below the software threshold, the aggressive veto was able reduce the event rate by an additional factor of ~ 10 suggesting one or both of the emission sources contribute significantly to the rate in this region of the spectrum—even after application of the selected veto. It had no effect on the above-threshold event rate indicating backgrounds that are independent of previous events dominate the rate in this region of the spectrum, namely those originating on the electrodes.

- Periods of a few tens of seconds with an unusually high rate of $S2$s below the analysis threshold were removed because they correlated with high rates of $S2$s just above the threshold originating from hotspots on the electrodes [113, 114]. The below threshold $S2$s were required to appear in events with a full waveform area less than 2000 phd, to mitigate backgrounds from photoionization and the photoelectric effect induced by xenon luminescence, which are significant in large events. Primarily, this cut eliminated a periodic rise and exponential decay in the rate of few electron $S2$s induced by $83m$Kr calibrations. The remaining $S2$s were required to be composed of greater than 1.2 detected electrons, because a large fraction of $S2$s failing this cut were observed to be delayed emissions of electrons trapped under the liquid surface, and captures and releases of drifting electrons by impurities. After applying these cuts, the average below threshold $S2$ rate was just a few Hz making spikes in $S2$ rate apparent. As plotted in Fig. 7.4(top), the data were grouped in 1 hr long bins and 6% of bins with the highest $S2$ rates were rejected. Fig. 7.4 (bottom) shows the x, y coordinates of events before and after applying this "electrode hotspot veto".

The three vetoes have the combined effect of reducing the livetime from the original 95-day exposure to 81 days. [1]

$S2$ Quality Cuts

The April 2013 data were scrutinized to identify several categories of pathological events. This task was accomplished by comparing the April data with tritium calibration data using plots of parameters quantifying characteristics of the event waveforms. When outlying populations were visible in the April data, but absent in the tritium data, cuts were defined at the 1% and 99% contours of the tritium distribution to maintain high acceptance of

[1] Note the size, time, and horizontal position of previous large $S2$s could be utilized in the definition of the large event veto to minimise loss of livetime, since the backgrounds targeted by this veto correlate highly with the location of these $S2$s. Furthermore, differences in time and position of consecutive $S2$s could be used to optimize the electrode hotspot veto. Preliminary tests incorporating this information showed potential for reducing loss of livetime, but were not finalized for this work.

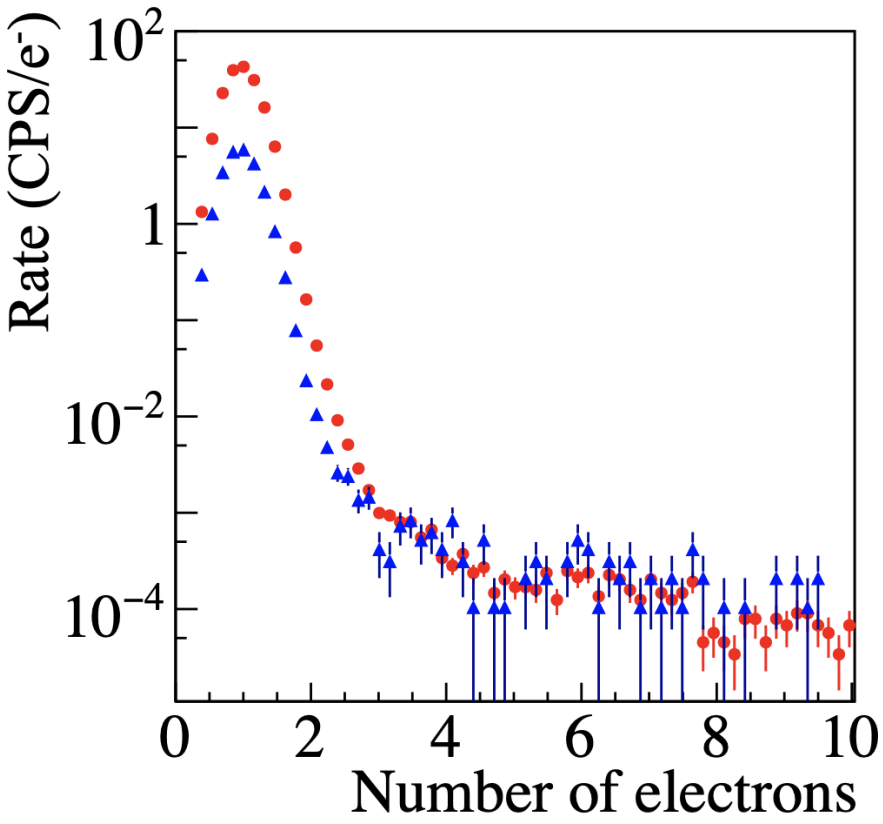

Figure 7.3: The WS2013 $S2$ spectrum after applying the selected "large event veto" preserving 93% of the live-time (red) and a more aggressive veto preserving only 10% of the live-time (blue). The above-threshold event rate is unaffected by the more aggressive veto indicating backgrounds from delayed emission of electrons trapped under the liquid surface, and capture and release of drifting electrons by impurities are reduced to insignificant rates by the selected veto. The remaining event rate is dominated by backgrounds that are independent of previous events, for example those originating on the electrodes. Figure from [111].

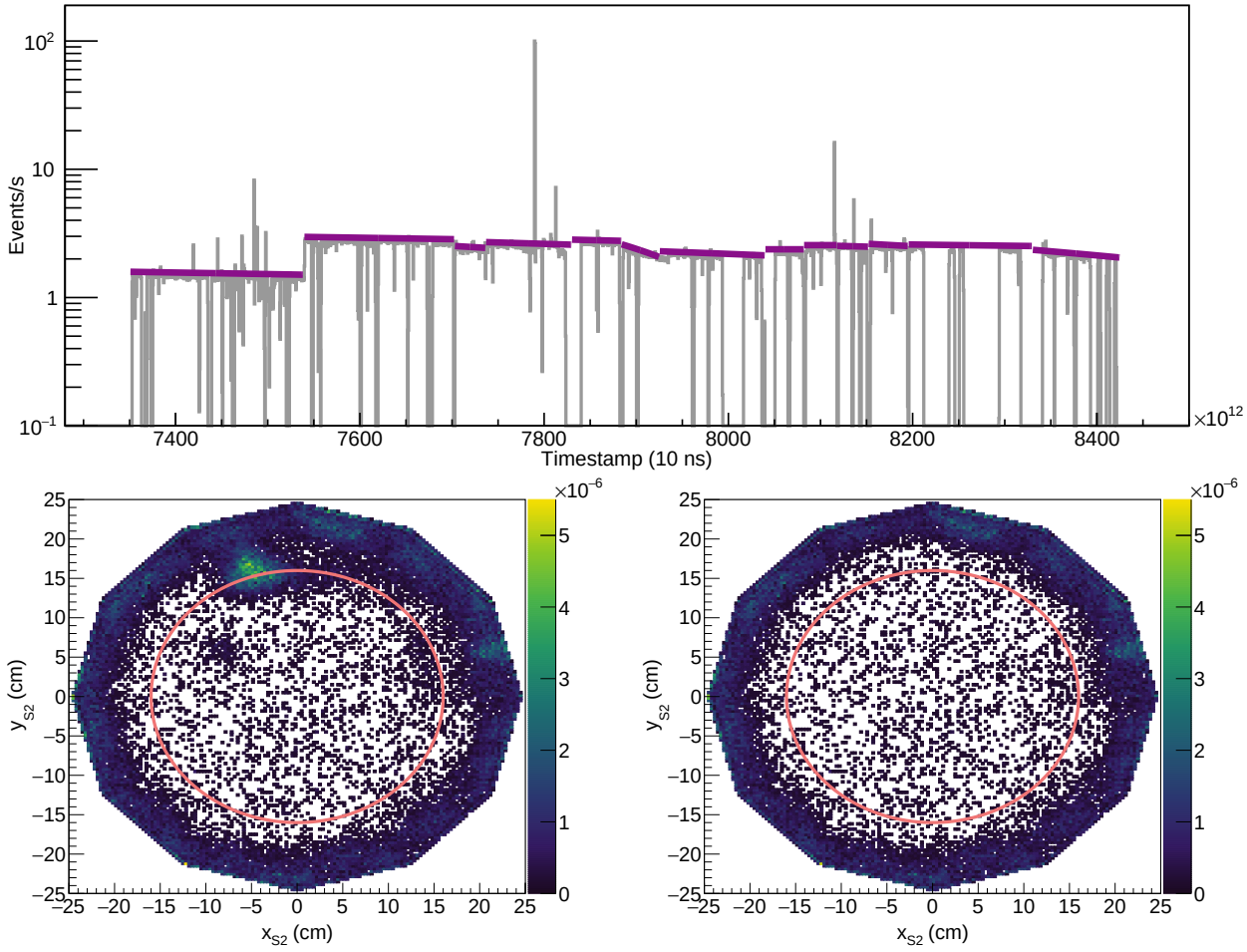

Figure 7.4: Rate of $S2$s of 1.2–3.5 detected electrons occurring in events with a full waveform area less than 2000 phd (top). There are visible spikes in $S2$ rate from hot spots on the gate and cathode which were removed with the "electrode hot spot veto". x, y coordinates of events with $S2$s in range $3.5 < n_e < 50.5$ passing the "large event veto" and $S2$ quality cuts (bottom left). The subset of these events remaining after the electrode hot spot veto (bottom right).

signal-like events in the liquid xenon bulk. All cuts were defined as functions of the $S2$ size to ensure the signal acceptance remained high throughout the entire energy range used in the DM search.

Eight cuts (drawn in Fig. 7.6–7.13) were defined in two iterations. The first round lead to development of the four cuts itemised below.

- Many vapor events have wide, degraded $S2$s due to their electrons traveling through atypical, electroluminescence paths—not simply from liquid surface to anode—and extended scintillation pulses because of the long ~ 100 ns lifetime of the scintillation-producing triplet xenon dimer state in the gas phase [156, 157, 158, 159]. The DPF software tends to divide the waveforms of these events into many pulses labeling just one an $S2$, as shown in Fig. 7.5(a). They were removed with a cut on "badarea," a parameter defined as the integrated area of the waveform trace minus the area of the $S1$ and $S2$ pulses. To a smaller extent, the badarea cut removes backgrounds from delayed emission of electrons captured by impurities; however, the large event veto removes most of these backgrounds prior to application of this cut.

- A small fraction of events from radiocontamination on the detector walls have poor x_{S2}, y_{S2} position reconstruction causing them to pass the radial cut. Because wall activities are $\sim 10^2$ greater than the bulk, this pathology can be significant. These events were removed using a cut on the χ^2 value of the Mercury position reconstruction algorithm. Multiple scatters with interaction vertices at the same vertical position, but differing horizontal positions, are also removed via this cut.

- Another fraction of the vapor events occurs just above or below an anode grid wire causing an unusually large fraction of electroluminesence to reach the top or bottom PMTs. These events were mitigated with cut on the asymmetry of $S2$ light collected by top and bottom PMTs.

- Events occurring very near the top and bottom of the detector were mitigated with a cut on $S2$ half width. This parameter was defined as the difference between the times at which the $S2$ waveform reaches 5% and 50% of its total area. It avoids asymmetric tails occurring on the trailing edge of some pulses due to electron emissions and instrumental effects.

All April data passing the first iteration cuts were visually scanned to identify any remaining pathological events. There were seven events appearing to have occurred in the vapor which had a combined scintillation+electroluminesence trace that had been identified by the DPF as a single $S2$. The four cuts listed below were defined to target these events.

- $S2$s from combined traces have bimodal shapes that differ from the Gaussian-like $S2$s of events originating in the center of the liquid xenon. This characteristic can be targeted with a cut on the difference between the times at which the $S2$ waveform reaches 25%

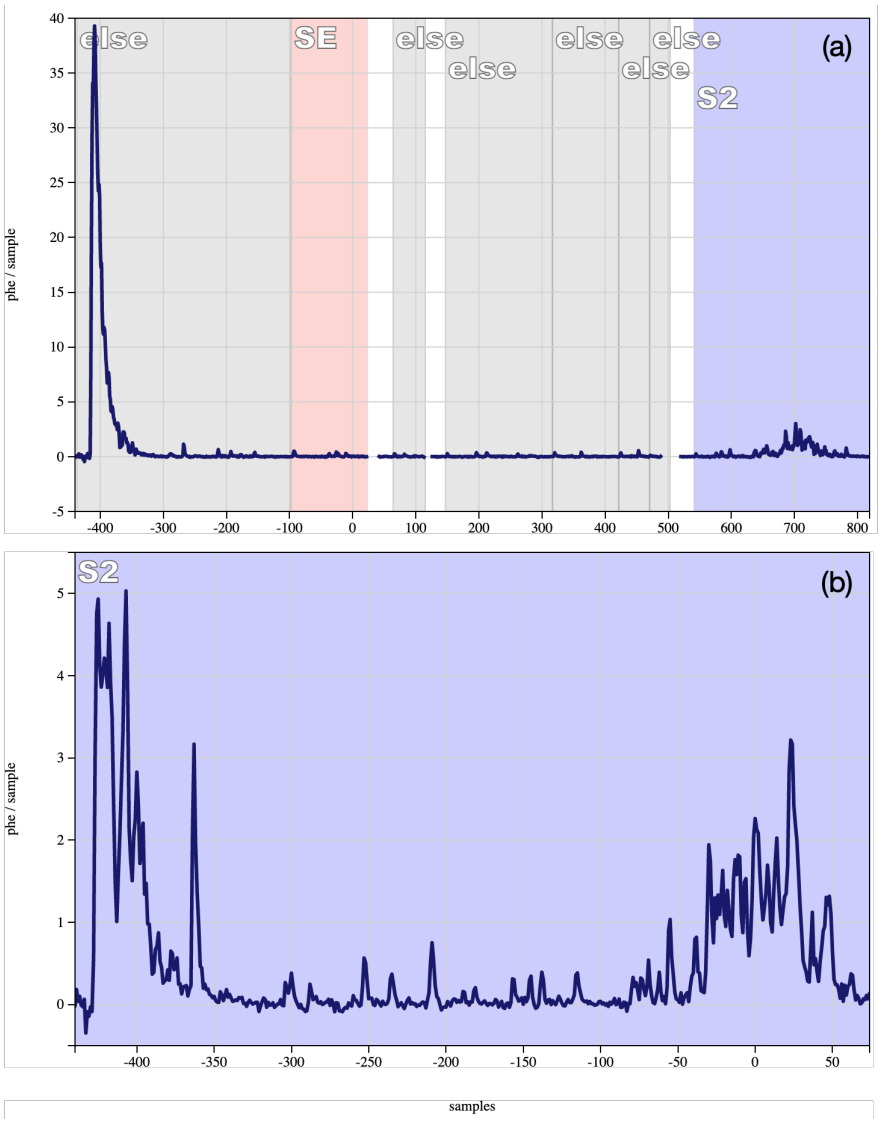

Figure 7.5: Events occurring in the vapor with degraded $S2$s and extended scintillation pulses. (a) shows an instance where the DPF has divided the event waveform into many pulses labeling just one an $S2$. (b) shows an instance where the DPR has identified the combined scintillation+electroluminesence trace as an $S2$.

and 75% of its total area. This difference is sometimes unusually long for $S2$s with bimodal shapes.

- $S2$s from combined traces often reach their maximum height very close to their leading edge. This characteristic can be targeted with a variety of cuts based on timing parameters that outline the leading edge of the pulse. One is the difference in times at which the $S2$ waveform reaches 0% and 50% of its total area.

- $S2$s which reach their max near their leading edge were also mitigated with a cut on the difference in times at which the $S2$ waveform reaches 0% and 5% of its total area.

- $S2$s which reach their max near their leading edge were also mitigated with a cut on the difference in times at which the $S2$ waveform reaches 5% and 25% of its total area.

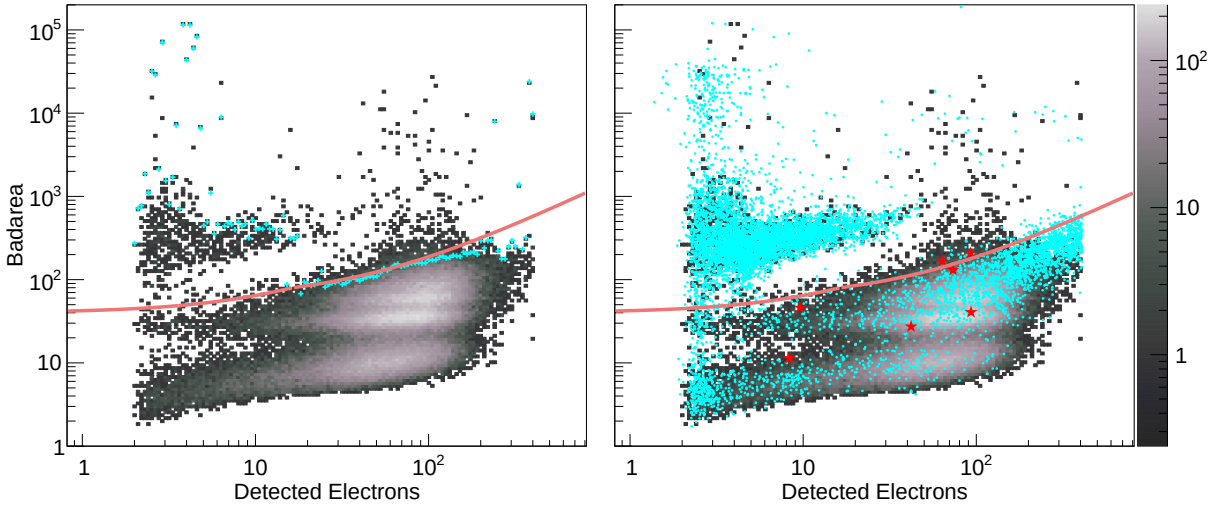

Figure 7.6: "badarea", defined as the integrated area of the waveform trace less the area of the $S1$ and $S2$ pulses, as a function of $S2$ size. On the left, tritium calibration data is plotted as a grey heat map overlaid with teal + markers at the 99th percentile of the distribution. On the right, the same data is overlaid with April 2013 background events plotted as teal points; the red stars indicate the seven events occurring in the vapor which had a combined scintillation+electroluminesence. The solid pink line is drawn at the location of the badarea cut. The same data is drawn in the subsequent plots which illustrate the seven additional $S2$ quality cuts. The teal + markers are drawn at either the 1st or 99th percentiles of the distributions.

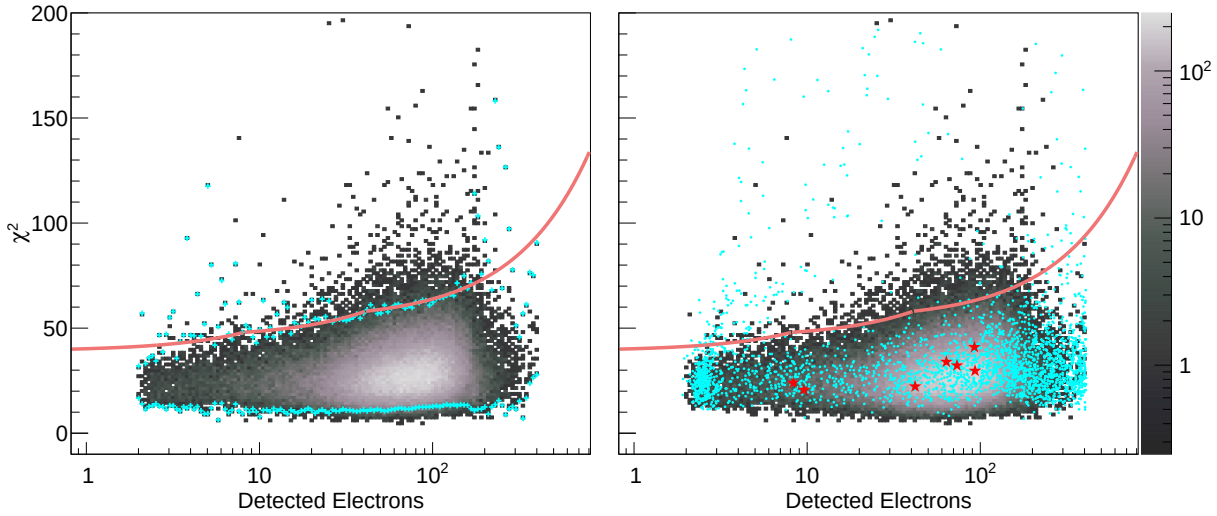

Figure 7.7: χ^2 value of the Mercury position reconstruction algorithm as a function of $S2$ size.

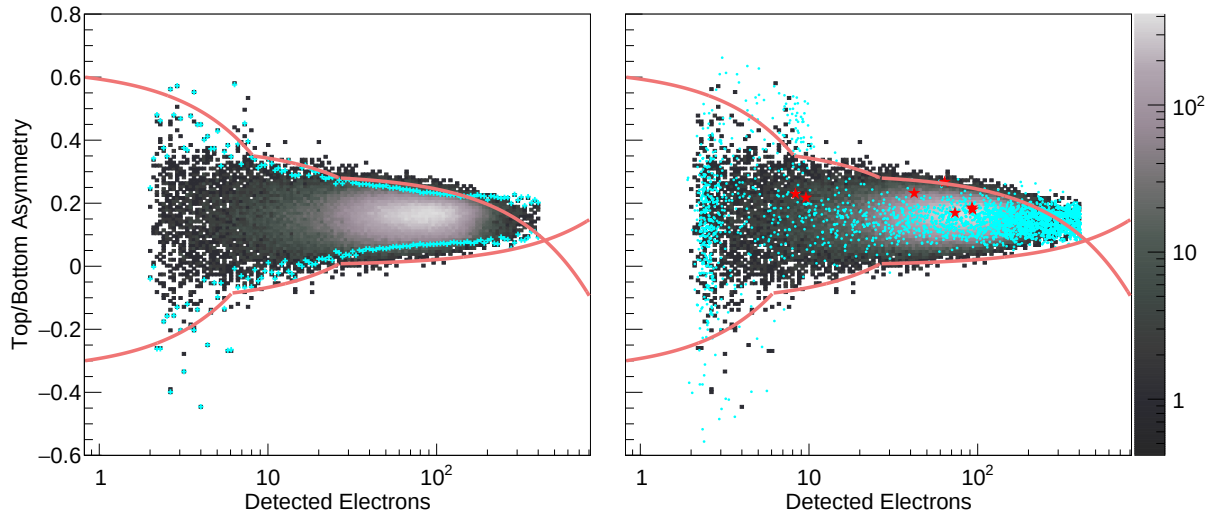

Figure 7.8: Asymmetry of $S2$ light collected by the top and bottom PMTs as a function of $S2$ size.

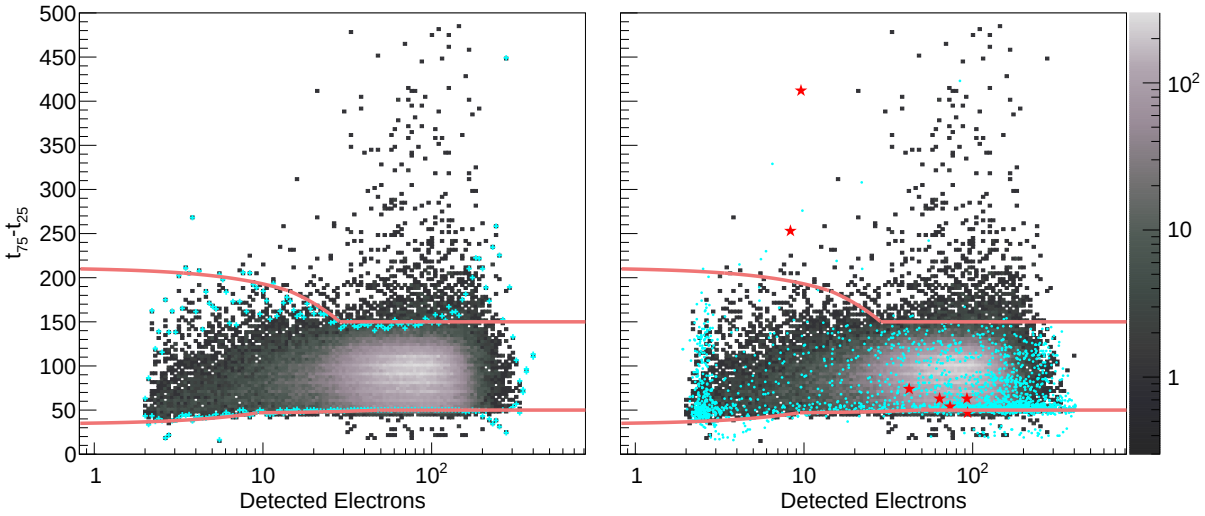

Figure 7.9: Difference between the times at which the $S2$ waveform reaches 25% and 75% of its total area as a function of $S2$ size.

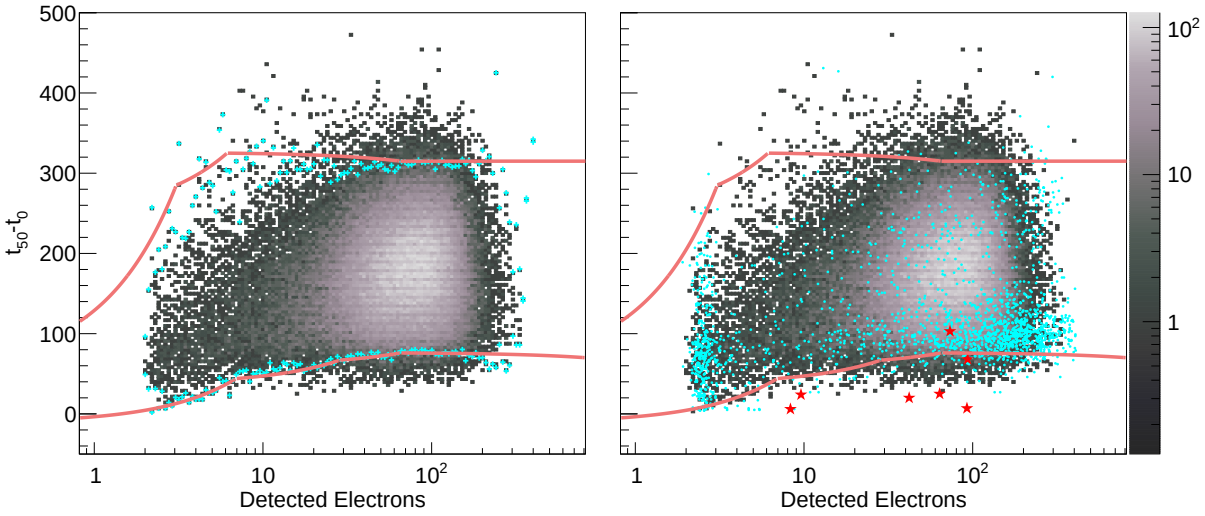

Figure 7.10: Difference between the times at which the $S2$ waveform reaches 0% and 50% of its total area as a function of $S2$ size.

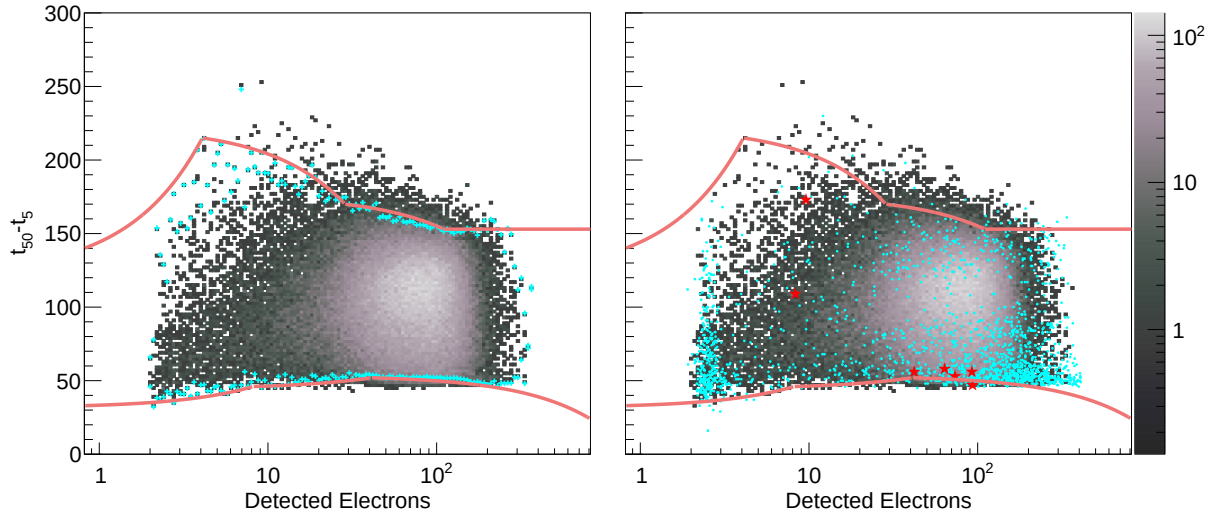

Figure 7.11: Difference between the times at which the $S2$ waveform reaches 5% and 50% of its total area as a function of $S2$ size.

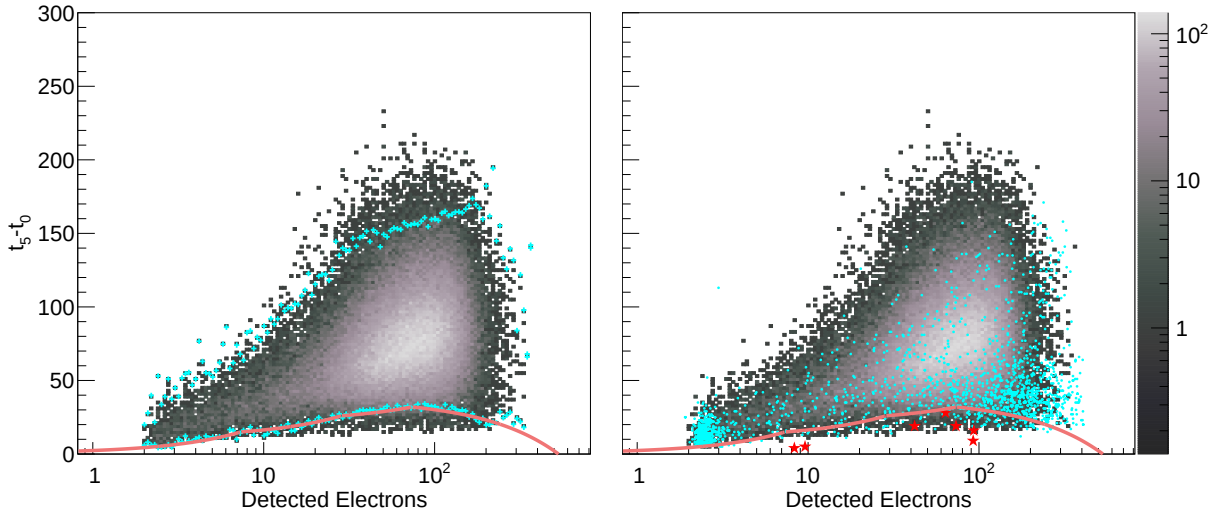

Figure 7.12: Difference between the times at which the $S2$ waveform reaches 0% and 5% of its total area as a function of $S2$ size.

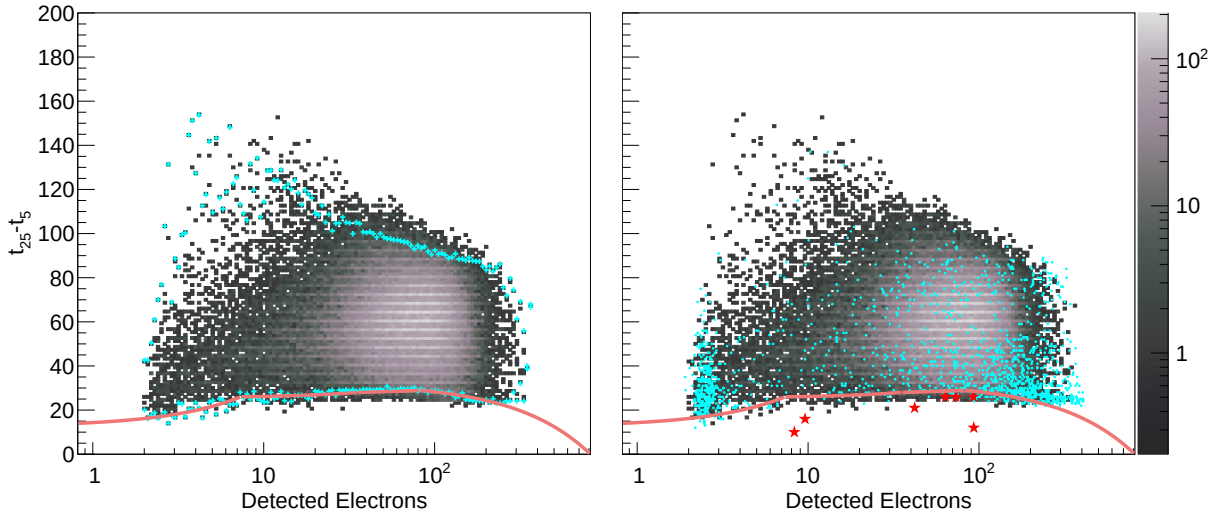

Figure 7.13: Difference between the times at which the $S2$ waveform reaches 5% and 25% of its total area as a function of $S2$ size.

In addition to the $S2$ quality cuts, events were required to meet two requirements related to the $S1$. These are described below.

- Events with $S2/S1$ ratios outside the 1 % and 99 % contours of the NR band were rejected for having the wrong recoil type.

- Populations of $S2$-only events with a single photon pulse preceding the $S2$ by $0-7$ μs or 321–326 μs are almost entirely composed of gate and cathode backgrounds that have $S1$s with too few photons to pass the two PMT coincidence requirement. Because the LUX DPF only records information about 10 pulses in each event some of the single photons are not recorded in the final dataset forcing us to identify and reject these backgrounds by eye.

  Occasionally, the waveform of a genuine bulk event will contain a thermionic PMT dark count or PTFE fluorescence photon preceding the $S2$ by the aforementioned time windows, thus causing the event to be falsely identified as an electrode background. A 1.6 ± 0.1% efficiency loss due to this random coincidence was calculated from WS2013 average single photon rate measurements for top and bottom PMTs from [96]—a LUX publication describing a detailed study of single photon $S1$ pulses.

Effectiveness of Event Selection Criteria

The effectiveness of the large event veto, $S2$ quality cuts, and electrode hotspot veto are quantified in Table 7.1 which compares the combined acceptance of these vetoes/cuts with the event rate in the region just above the software threshold that most greatly determines

Table 7.1: Combined signal acceptance of relevant vetoes/cuts (calculated from loss of livetime or using tritium data) compared with the percentage of events remaining just above the software threshold.

Description of Cut/Veto	Signal Acceptance	Events $3.5 < n_e < 4.5$
Starting Events	100%	100%
Large Event Veto	93%	28%
$S2$ Quality	85%	3.5%
Electrode Hotspot Veto	79%	0.3%

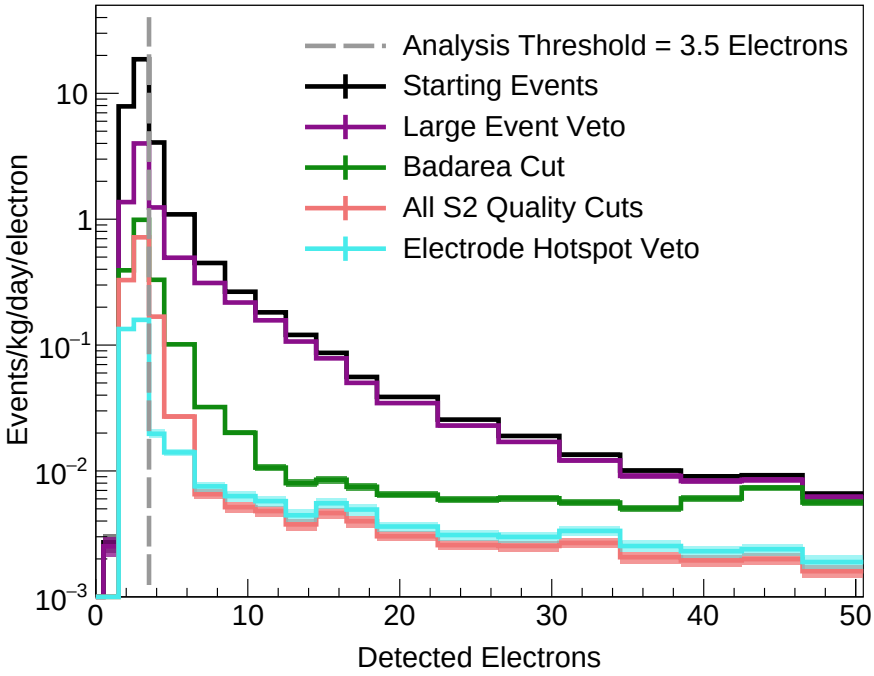

Figure 7.14: Background spectrum after large event veto, $S2$ quality cuts, and electrode hotspot veto. The badarea cut is segregated from the other $S2$ quality cuts to show its dramatic reduction of the event rate caused by removal of events occurring in the vapor.

sensitivity to low-mass DM. Each successive cut/veto reduces the event rate by an additional factor of 3–12 while reducing the acceptance by $\sim$ 10%. Corresponding changes in the magnitude and shape of the background spectrum are shown in Fig. 7.14.

7.2 Machine Learning Technique for Removing Electrode Backgrounds

The event selection criteria described in the previous section greatly reduce the background rate, but leave significant populations of events originating on the gate and cathode. This is evident in Fig. 7.15 (top), which shows events in the dark matter search region that do have an $S1$ and, therefore, a determinate z position.

Fig. 7.15 (bottom) shows the $S2$ pulse half-width[2] distributions of the gate, bulk xenon, and cathode events defined by the drift time cuts $t_d < 7$ μs, 7 μs $< t_d <$ 321 μs, and 321 μs $< t_d$. The bulk distribution shows a $\sqrt{t_d}$ trend that is consistent with expectations from diffusion of drifting electrons. If $S2$-only background events from interactions on the gate and cathode followed this trend, they could be removed using a pulse width cut. However, the gate and cathode distributions have a significantly broader spread than what is observed in the bulk, indicating that efficient removal of electrode backgrounds requires a more sophisticated cut.

The discrepancy between electrode and bulk xenon $S2$ half-width distributions can be explained by the differences in pulse shape summarized in Fig. 7.16. Panels (a–e) contain skew-Gaussian fits of $S2$ pulses typically found in the WS2013 data. The top panels are fits to bulk xenon $S2$s from the top, middle, and bottom of the TPC (drift times of ~ 10 μs, ~ 150 μs, and ~ 300 μs). The $S2$s are symmetric and have widths that grow predictably with $\sqrt{t_d}$. Some electrode $S2$s are indistinguishable from those in the bulk xenon, but others are asymmetric and/or sharply peaked like the fits shown in panels (d–e). This variety of electrode $S2$ pulse shapes impairs the accuracy of typical pulse width metrics resulting in broader width distributions.

The phenomenon generating the odd $S2$ pulse shapes is electric field fringing around grid wires. Fig. 7.16 (f) shows a typical electric field profile around a single gate wire (reproduced from [160]). The field lines do not point uniformly in the z direction; instead, they stretch away from the wire surface in arcuate patterns. Furthermore, very near the wire surface, the electric field magnitude is proportional to $\sim 1/r_w$, where r_w is the wire's radial coordinate. A 2-dimensional COMSOL model was used to calculate the electric field magnitude near gate and cathode wires in WS2013. They are a factor of $\sim 10^2$ greater than in the bulk xenon.

When an interaction occurs in a region with electric field fringing, it creates a cloud of electrons that is contorted such that it produces an odd $S2$ pulse shape. As the electrons drift they experience drastic changes in electric field that cause their velocity to vary and, thus, the distance between adjacent electrons to stretch or contract. Additionally, sufficiently far apart electrons can experience differences in path length that significantly alter their proximity. The latter effect is most significant near the bottom of gate wires where the curvature of field

[2]In this analysis, half-width is defined as the difference between the times at which the pulse integrates to 50% and 5% of it of its total area. This width metric was selected to avoid asymmetric tails occurring on the trailing edge of some pulses due to delayed emission of $S2$ electrons by mechanisms summarised in [111].

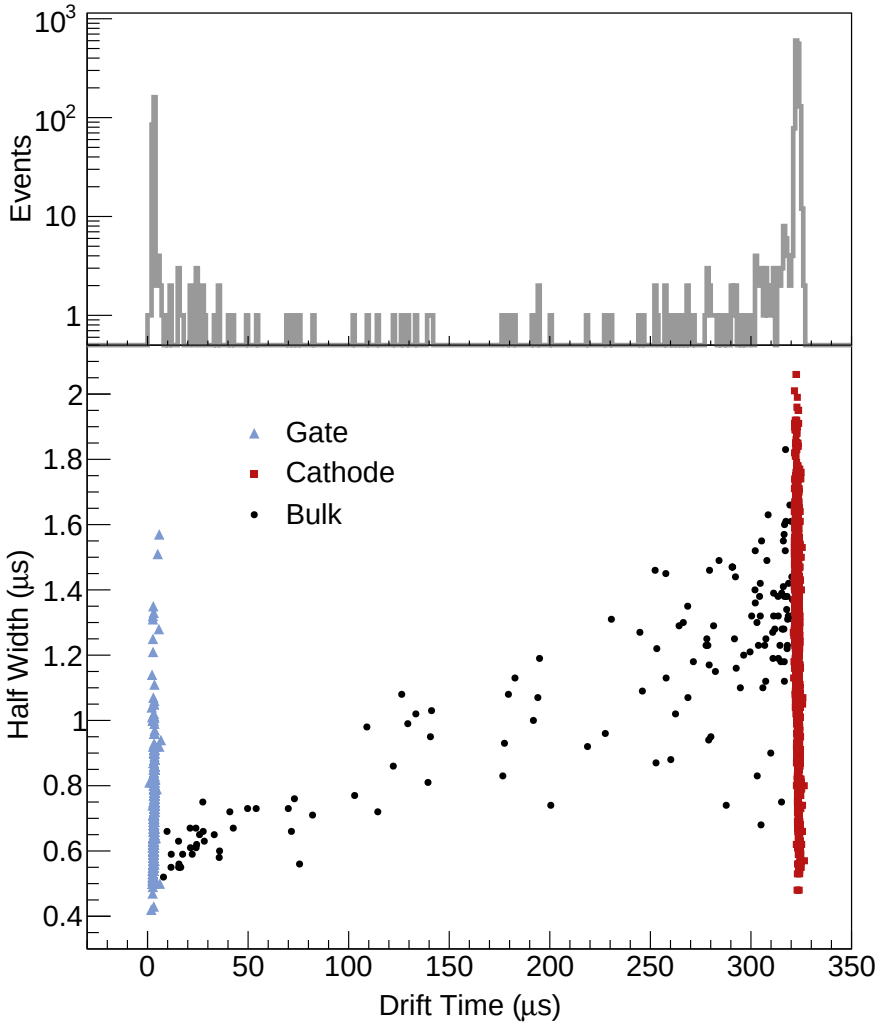

Figure 7.15: All WS2013 events in range $3.5 < n_e < 50.5$ containing both an $S1$ (passing the two PMT coincidence requirement) and $S2$ pulse, and passing all vetoes/quality cuts applied to $S2$-only events. Gate, bulk, and cathode events are defined by drift time cuts: $t_d < 7$ μs, 7 μs $< t_d <$ 321 μs, and 321 μs $< t_d$. The event rate is vastly higher at the gate and cathode drift times suggesting electrode events are the dominant source of backgrounds.

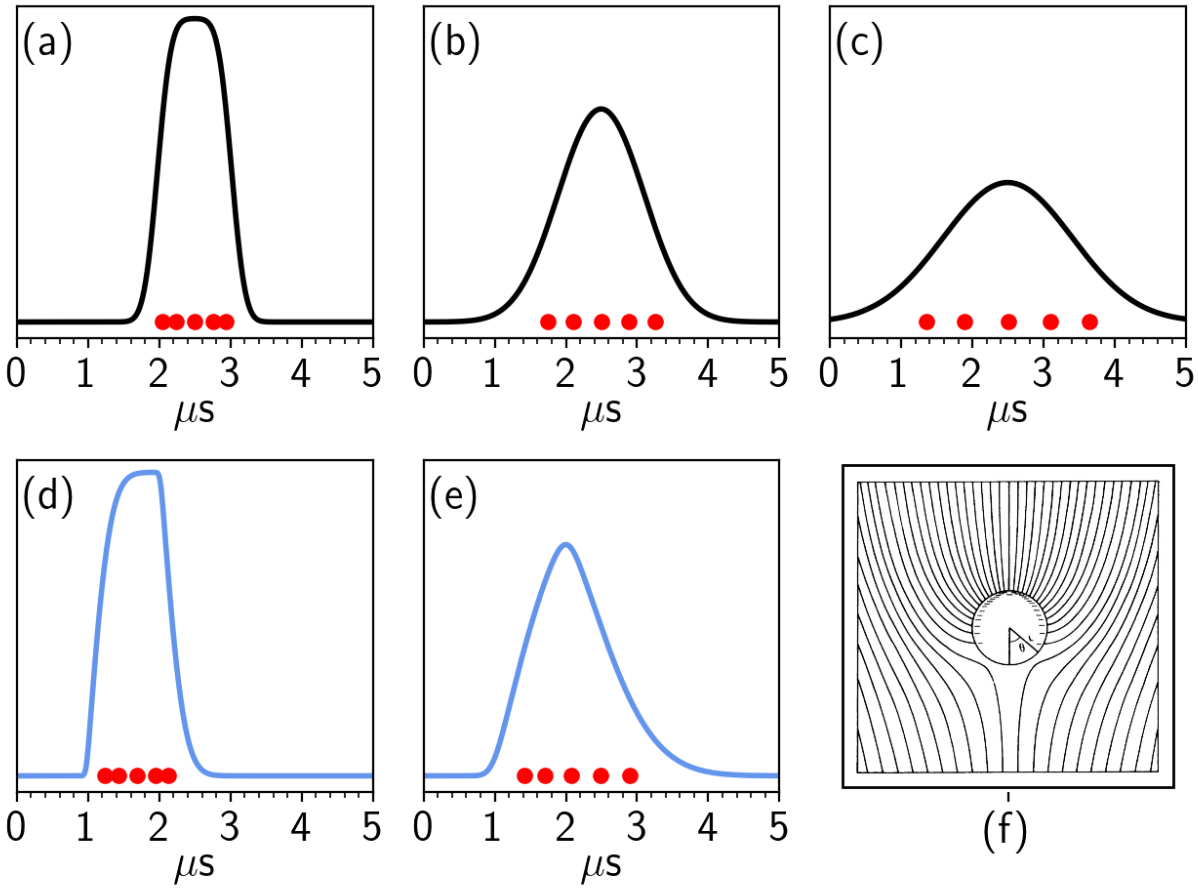

Figure 7.16: Panels (a–e) show typical $S2$ pulse shapes obtained from skew-Gaussian fits to LUX data. The top panels have symmetric shapes that are characteristic of bulk events near the top, middle, and bottom of the TPC (drift times $\sim$ 10 μs, $\sim$ 150 μs, and $\sim$ 300 μs). Panels (d–e) show asymmetry characteristic of gate $S2$s whose electrons travel through a range of electric fields. Panel (f) shows a typical electric field profile around a single gate wire (reproduced from [160]). Electric field profiles of cathode wires have a similarly wide range of magnitudes although most field lines, except those at the very top of the wire, point downward. The five red circles in panels (a-e) are parameters (t_{10}, t_{25}, t_{50}, t_{75}, and t_{90}) that mark the times at which the pulse attains 10%, 25%, 50%, 75%, and 90% of its total area. These parameters were used as input to the machine learning algorithm along with maximum pulse height, the time at which the pulse attains its maximum height, and the times at which the rising and falling edges of the pulse reach 0 phd/sample. Note the bulk event profiles on the top panels can also occur for gate and cathode $S2$s originating on the top of a wire where field curvature is less dramatic.

lines is most dramatic. Events near the cathode wires usually do not produce $S2$s, because their electrons drift downward along field lines that terminate on the electrode that shields the bottom PMTs. Only 16% of field lines near cathode wires extend upward and those that do stem from the top of the wire where field curvature is less dramatic. Despite this, some $S2$s originating on the cathode, as well as those on the gate, were observed to have visibly asymmetric shapes.

Fortunately, the odd $S2$ shapes created by field fringing can be successfully tagged by holistically quantifying pulse shape. For this reason, a machine learning algorithm was used to design a cut on the full set of parameters that quantify pulse shape. Some examples of these parameters are provided in Fig. 7.16 (a–e). The five red circles along the horizontal axis are the points at which the pulse attains 10, 25, 50, 75 and 90% of its total area. The varying distances between red circles in panels (a–e) is evidence that pulse shape asymmetry is encoded in these quantities. Other shape quantifying parameters are the maximum pulse height, the time at which the pulse attains its maximum height, and the times at which the rising and falling edges of the pulse reach 0 phd/sample. The following subsections provide details of the algorithm, training data, and results of this work.

Adaptively Boosted Decision Tree

Out of the many available machine learning methods, an adaptively boosted decision tree (BDT) was chosen for ease in understanding how the algorithm uses and values input parameters. This algorithm is implemented in Python through the *scikit-learn* library's AdaBoost (Adaptive Boosting [161]) classifier.

AdaBoost builds a sequence of weak classifiers that focus on different subsets of the training data. In this work, the weak classifiers are decision trees that perform cuts on input parameters to decide whether each datapoint should be assigned a value of $+1$ (bulk-like) or -1 (electrode-like). When the nth tree has been trained, the datapoints are re-weighted so that misclassified points are given higher importance during training of the $(n+1)$th tree. This iterative procedure is repeated until the desired number of trees have been trained. Although the prediction of each tree is binary, the final discrimination score may take on continuous values from -1 to $+1$. It is calculated by averaging the predictions of the decision trees with weights that vary depending on the classification accuracy of the tree [162]. The steps of this procedure are detailed below.

- Given a dataset with n points, initialise the weight of each point as $\frac{1}{n}$. Below, x_i are the datapoints, y_i the class labels, and w_i the weights.

$$x_i \in \mathbb{R}^d, \tag{7.1}$$

$$y_i \in \{-1, 1\}, \tag{7.2}$$

$$w_i(x_i, y_i) = \frac{1}{n} \qquad i = 1, ..., n. \tag{7.3}$$

- Train a weak classifier on the parameters of the data to best separate the points into two classes of lowest impurity. Calculate the weight of the weak classifier (θ_m, for the mth weak classifier) using the classification error (ϵ_m) as written below.

$$\epsilon_m = E_{w_m}[1_{y \neq f(x)}] \tag{7.4}$$

$$\theta_m = \frac{1}{2} \ln \left(\frac{1 - \epsilon_m}{\epsilon_m} \right) \tag{7.5}$$

  Above, $f_m(x_i)$ is the mth weak classifiers result when applied to datapoint x_i.

- Update the weights of each datapoint to be

$$w_{m+1}(x_i, y_i) = \frac{w_m(x_i, y_i) e^{-\theta_m * y_i * f_m(x_i)}}{Z_m}, \tag{7.6}$$

  where Z_m is a normalisation constant that ensures the sum of the weights is 1.

- Repeat this process M times to produce the final classification result (F).

$$F(x) = sign \left(\sum_{m=1}^{M} \theta_m f_m(x) \right) \tag{7.7}$$

  For every datapoint, F is a number in range -1 to 1. Negative values of F indicate the datapoint is more similar to the class labelled -1, while positive values indicate the datapoint is more similar to the class labelled 1.

The BDT hyperparameters, such as maximum decision tree depth and number of trees, were optimised with cross-validation on multiple subsets of the training data. The optimal maximum depth of was 2 and the optimal number of trees was 100, though performance was robust across a wide range of hyperparameter values.

Training Data

The training and testing data were selected to include $S2$s of all sizes in the dark matter search range of $3.5 - 50.5$ detected electrons (Fig. 7.17). Bulk-like events were sourced from the tritium calibration dataset. They were required to pass the event selection criteria outlined in Sec. **??**. Gate- and cathode-like events were sourced from WS2013. They were required to have both an $S1$ and $S2$, pass all vetoes/quality cuts applied to $S2$-only events, and pass gate or cathode drift time cuts of $t_d < 7$ μs or 321 μs $< t_d$. Because these criteria produced many more cathode than gate events, the radial cut was relaxed for the latter, to generate a sufficiently large training sample. This choice could potentially make the training data less representative of the backgrounds in WS2013 by affecting how optimally the BDT removes grid events. It would not affect the BDT efficiency for selecting signal-like events, thus the conservative nature of the final limit.

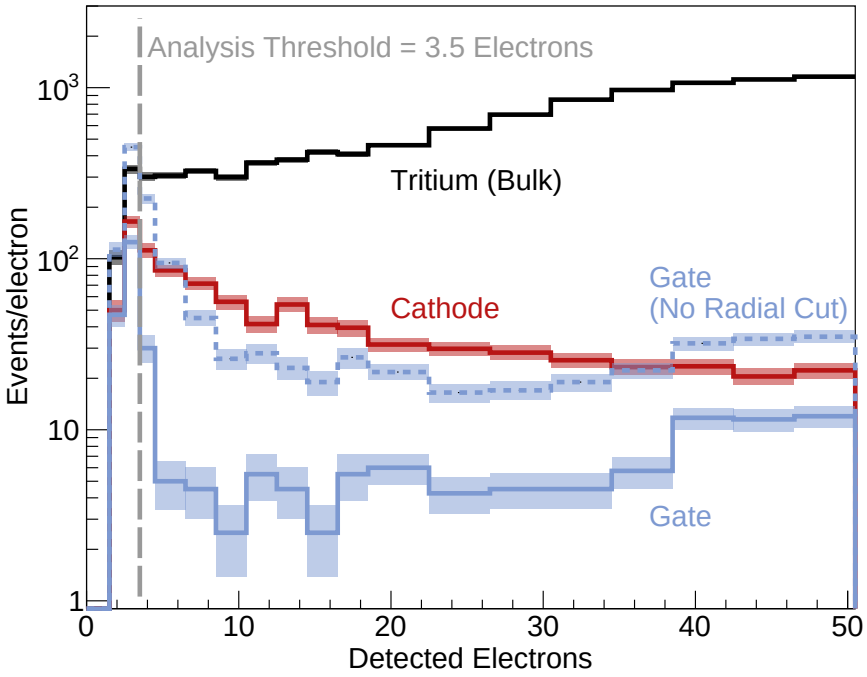

Figure 7.17: WS2013 gate, cathode, and tritium calibration data used to train a boosted decision tree to recognize electrode backgrounds. All events pass the $S2$-only quality cuts, except some gate events that fail the radial cut. This cut was removed to increase the number of gate training events. Before training, this data was re-weighted to give identical spectra for the three sources, as well as a 1:1 ratio of gate/cathode events.

Despite the electric field profile around cathode wires preventing most events from producing $S2$s, there are many more cathode than gate training events. This is not reliable evidence of greater ^{222}Rn daughter contamination or a higher electron emission rate on the cathode. Instead, it is primarily a result of detector conditions that tend to enlarge $S2$s originating on the gate to sizes greater than the 50.5 detected electron upper threshold used in this analysis (described in detail in Chapter 5, Sec. 5.5). Primarily, the larger average electric field near gate wires (52 kV/cm compared to 18 kV/cm on the cathode) enhances the charge yield. Additionally, electrons originating on the cathode drift through the full length of the detector during which they have a 30% chance of being captured by a xenon impurity, while those originating on the gate drift a very short distance and have a very low capture probability. This causes more cathode events to appear in the signal region below 50.5 detected electrons.

The gate, cathode, and tritium training data were weighted to share the same flat $S2$ area spectrum with a single step at 12.5 detected electrons. Below the step, where both the DM signal spectrum and the April 2013 background spectrum are strongest, the training

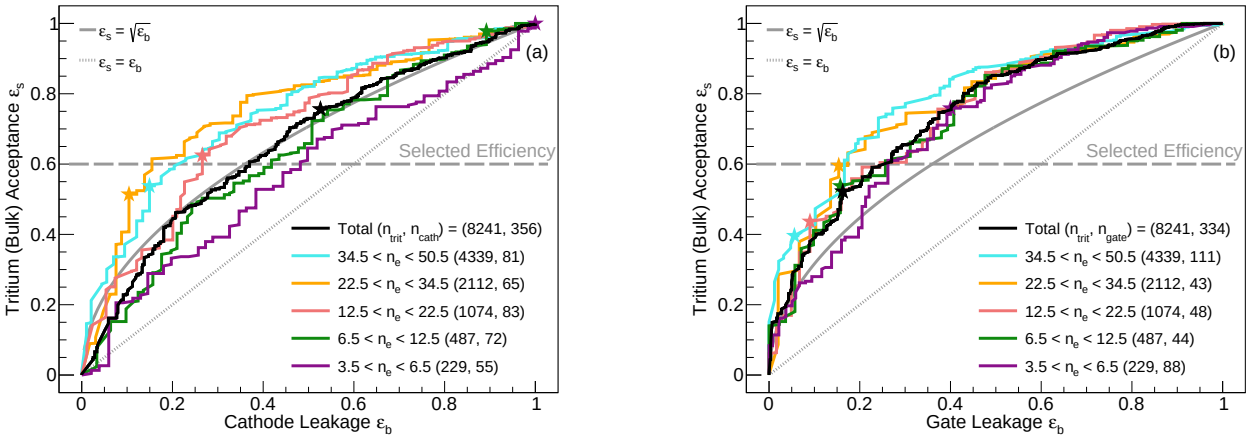

Figure 7.18: ROC curves for (a) bulk tritium vs cathode and (b) bulk tritium vs gate test data. The curves can be used to estimate a BDT discriminator threshold that maximizes sensitivity to dark matter signals in an extreme scenario where only gate or cathode backgrounds are present. Two additional curves are plotted to guide the eye: $\epsilon_s = \epsilon_b$ and $\epsilon_s = \sqrt{\epsilon_b}$, the thresholds that must be exceeded by the ROC curves for a BDT discriminator threshold to improve sensitivity in a Poisson or background subtracted DM analysis. Stars indicate the points of optimal $\epsilon_s/\sqrt{\epsilon_b}$.

data were weighted more heavily. Keeping the same spectrum for bulk- and electrode-like classes ensures the algorithm does not rely on $S2$ area as a means of discrimination through residual correlation with input parameters. It is necessary because the shapes of the gate and cathode background spectra are unknown, due to the lack of $S1$s for most events.

Receiver Operating Characteristic

The BDT training performance is best summarized with receiver operating characteristic (ROC) curves. These are plots of signal [tritium (bulk)] acceptance (ϵ_s) vs electrode background leakage (ϵ_b) calculated by placing a threshold cut on the discriminator scores ($F(x_i)$) of the testing datapoints (x_i) at successive values spanning the range -1–1. In this space, the diagonal $\epsilon_s = \epsilon_b$ corresponds to no discrimination (random guessing) and $\epsilon_s = 1$ to perfect discrimination. The greater the area under the curve, the greater the discrimination power.

Families of ROC curves generated from gate and cathode training data with differing cuts on $S2$ size are shown in Fig. 7.18. It is immediately clear the BDT is more adept at removing gate events compared to cathode events. This outcome was expected, as electron clouds from the cathode experience additional diffusion that erases initial $S2$ shape information. Discrimination power also increases with $S2$ size, because larger numbers of electrons form more recognizable pulse shape patterns. This trend is weaker for gate events, which can be efficiently identified and rejected even with few detected electrons.

The ROC curves can be used to estimate an BDT $F(x)$ threshold that maximizes sensitivity to dark matter signals. To aid understanding of these curves, consider two benchmark scenarios where the sensitivity of the analysis is a simple analytic function of the signal and background efficiencies, the quantities plotted in the curves. The background-subtracted scenario models a rare event search analysis with both an assumed signal and background model (e.g. a profile likelihood ratio). In this case, the sensitivity scales as $\epsilon_s/\sqrt{\epsilon_b}$, because the mean of the background spectrum can be subtracted, leaving only statistical fluctuations. The second scenario is a naive Poisson limit with no background subtraction, in which case the sensitivity scales as ϵ_s/ϵ_b. In order to improve the sensitivity relative to an analysis with no grid background cut, the ROC curves must exceed thresholds of $\epsilon_s = \sqrt{\epsilon_b}$ (background subtracted) or $\epsilon_s = \epsilon_b$ (Poisson).

The present analysis uses Yellin's $p_{\max}$ test statistic [163] to calculate sensitivity, as described further in Sec. **??**. This approach is expected to scale somewhere between the Poisson and background subtracted extremes, because it takes into account the difference in shape of the data and signal energy distributions, but makes no assumptions about the shape of the background distribution. Given this, both $\epsilon_s = \sqrt{\epsilon_b}$ and $\epsilon_s = \epsilon_b$ thresholds are drawn in Fig. 7.18 for comparison with the gate and cathode ROC curves of each $S2$ size bin. All of the gate curves pass the more stringent $\epsilon_s = \sqrt{\epsilon_b}$ requirement for most values of the $F(x)$ threshold while the cathode curves pass the requirement only in bins with $S2$s of $n_e > 12.5$. This behavior shows the BDT cut can be used to improve sensitivity in extreme scenarios where only gate backgrounds are present, or cathode backgrounds with $n_e > 12.5$.

In this analysis, the discriminator cut was designed to be signal model agnostic by requiring signal acceptance be constant with respect to event energy. It was chosen considering the points of maximum $\epsilon_s/\sqrt{\epsilon_b}$, indicated as stars on the ROC curves. Based on the clustering of these points, a flat 60% signal acceptance was imposed by selecting a different $F(x)$ threshold for each of the $S2$ size bins. At this signal acceptance, all ROC curves pass the $\epsilon_s/\sqrt{\epsilon_b}$ requirement except those from the cathode with $S2$s of $n_e < 12.5$.

The signal acceptance and background rejection of the discriminator cut (calculated from the training data) are plotted in Fig. 7.19. By design, the signal acceptance remains near 60% at all $S2$ sizes. The background rejection slightly improves with $S2$ size as is expected from the trends observed in the ROC curves. Additionally, gate and cathode rejection is similar for $S2$s with $n_e > 12.5$, but cathode rejection falls short of gate rejection by $\sim 15\%$ for $n_e < 12.5$.

7.3 Effectiveness of Electrode Background Removal

An understanding of the parameters most useful to the BDT can be gained by looking at "importance". For a single decision tree, a parameter's importance (p) is the fraction of training events separated by each branching node using the parameter, weighted by the reduction of impurity at each node (n_j). Mathematically, parameter importance can be

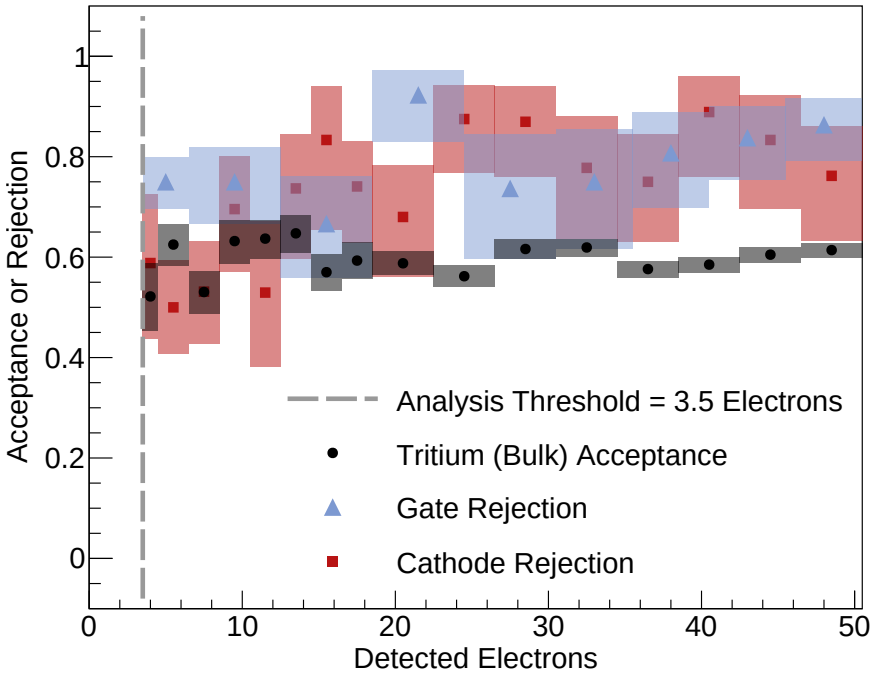

Figure 7.19: Signal acceptance and background rejection capability of the boosted decision tree used to tag and remove gate- and cathode-like events. The cut is not applied below the software threshold.

written as

$$n_j = w_j C_j - w_{left(j)} C_{left(j)} - w_{right(j)} C_{right(j)} \tag{7.8}$$

$$p_i = \frac{\sum_{j:node\ j\ splits\ on\ parameter\ i} n_j}{\sum_{k\in\ all\ nodes} n_k}, \tag{7.9}$$

where C_j is the impurity at node j, and $left(j)/right(j)$ are the daughter nodes from the split on node j.

The BDT parameter importances presented in Tab. 7.3 are an average of the individual decision tree importances with weights that vary depending on the classification accuracy of the tree, the same weights used in the calculation of the discriminator score. For the training data, the time differences outlining the middle of the pulse (e.g. $t_{75} - t_{50}$), as well as the pulse height, are more important than the time differences outlining the tails (not shown in Tab. 7.3). This inclination of the BDT could be a result of $S2$ waveform noise from photoionization and ionization phenomena that more readily appears at the edges of $S2$ pulses. For example, the trailing edge of $S2$s can overlap with electron signals produced by photoelectron emission of the gate cause by incident electroluminesence. These additional electrons will obscure the original shape of the $S2$'s trailing edge.

Table 7.2: Importance of parameters in the BDT. For brevity, only the top five (of twelve) are tabulated. Here, t_x corresponds to the time at which the pulse attains x% of its total area, as illustrated in Fig. 7.16, while V_{max} is the maximum pulse height.

Variable	Importance
$t_{75} - t_{50}$	0.212
V_{max}	0.153
$t_{25} - t_{10}$	0.148
$t_{90} - t_{75}$	0.131
$t_{50} - t_{25}$	0.083

Fig. 7.20 shows the half width distributions of training data before and after applying the selected discriminator cut. As designed, the cut greatly reduces the gate and cathode distributions while mostly preserving the tritium (bulk) distribution. While the averages of all three distributions shift towards central (bulk-like) values, there are tails remaining at small and large half widths. These tails are evidence the BDT is finding new features, more subtle than half width, that are useful for discriminating between electrode and bulk events.

Fig. 7.21 shows $S2$s at three different sizes that were tagged as signal- and electrode-like. Although antisymmetric patterns become less obvious in small pulses, there are still visible differences between electrode- and signal-like S2s of the smallest size considered in this analysis.

To characterize improvement of limits from using the full set of shape quantifying parameters compared to just half width, a second BDT was run using half width as the only input parameter. Fig. 7.22 compares the ROC curves of the "total" and "half width" BDTs for the smallest and largest $S2$ size bins using the combined training+testing dataset. For the cathode, both bins have similarly shaped total and half width ROC curves suggesting diffusion experienced by cathode $S2$s has the effect of washing away pulse shape information other than pulse width. For the gate, the ROC curves of the smallest bin show the same lack of improvement. However, in the largest bin, the total ROC curve sits far above the half width ROC curve indicating a large improvement from the addition of extra shape parameters.

The points of maximum improvement for background subtracted and Poisson limits are indicated as stars and circles in Fig. 7.22. Poisson limits are maximized at equal or lower ϵ_s than background subtracted limits. Because they have a greater dependence on ϵ_b than background subtracted limits, Poisson limits favor lower values of ϵ_b despite the accompanying decrease in ϵ_s.

Figure 7.23 uses the combined training+testing data set to show the effectiveness of the BDT as it depends on $S2$ size. It shows the maximum expected limit improvement for each $S2$ size bin considering extreme cases of only gate backgrounds or only cathode backgrounds. Poisson limit improvement factors are in the range 1.7–3 demonstrating our machine learning technique is effective at improving limits based solely on comparing signal

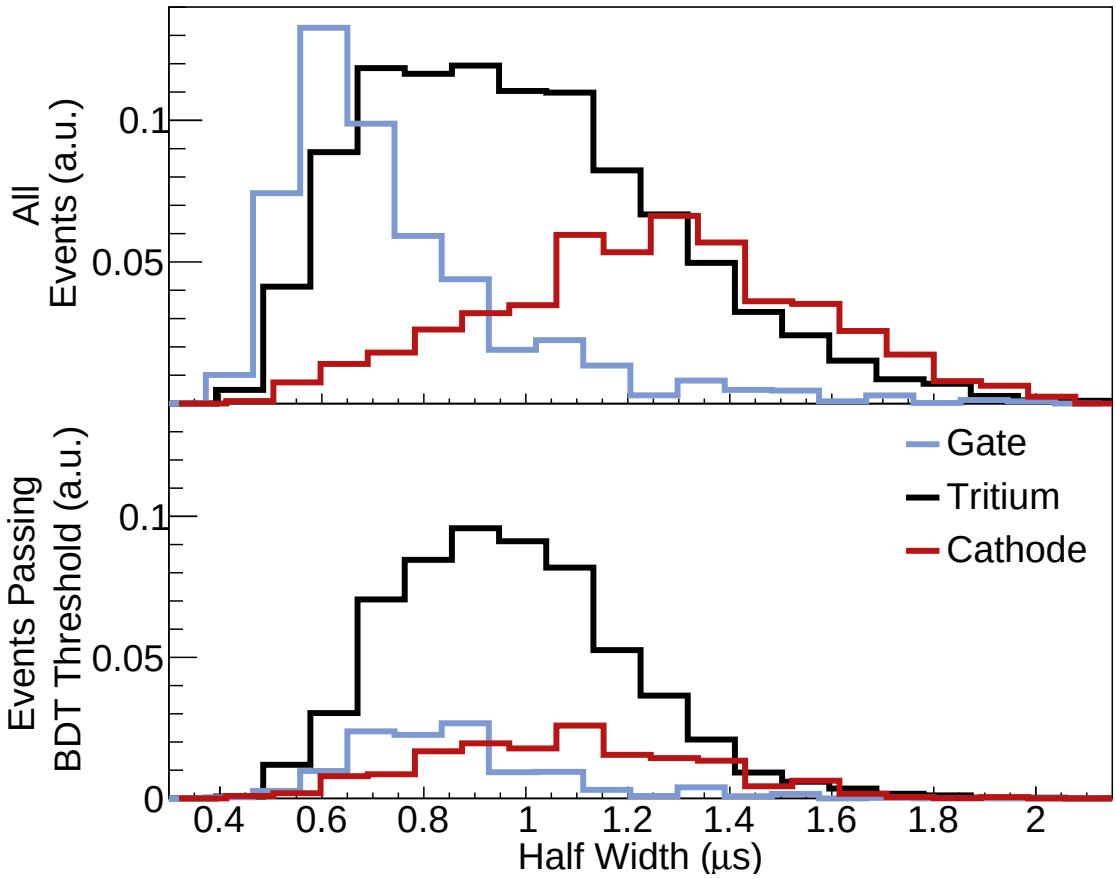

Figure 7.20: Half width distributions of training data before and after applying a discriminator cut tuned to 60% signal efficiency.

and observed event spectra. Poisson limit improvement is a factor of 1.3–2 greater than that calculated for background subtracted limits, which can be explained by the Poisson limits' greater dependence on ϵ_b. For all gate background scenarios, the limit improvement increases by a factor of 1.5–2 from smallest to largest bin. An increase is expected due to the greater amount of pulse shape information encoded in larger pulses.

7.4 Dark Matter Limits

The final WS2013 data, after applying all cuts described in Sec. 7.1 and the BDT discriminator cut in Sec. 7.2, are plotted in Fig. . The spectrum rises near the analysis threshold, though this is significantly mitigated by the BDT cut, which reduces the observed event rate by a factor of ~ 4 while retaining approximately 60% signal efficiency independent of $S2$ size. This outcome demonstrates a substantial and efficient removal of electrode backgrounds us-

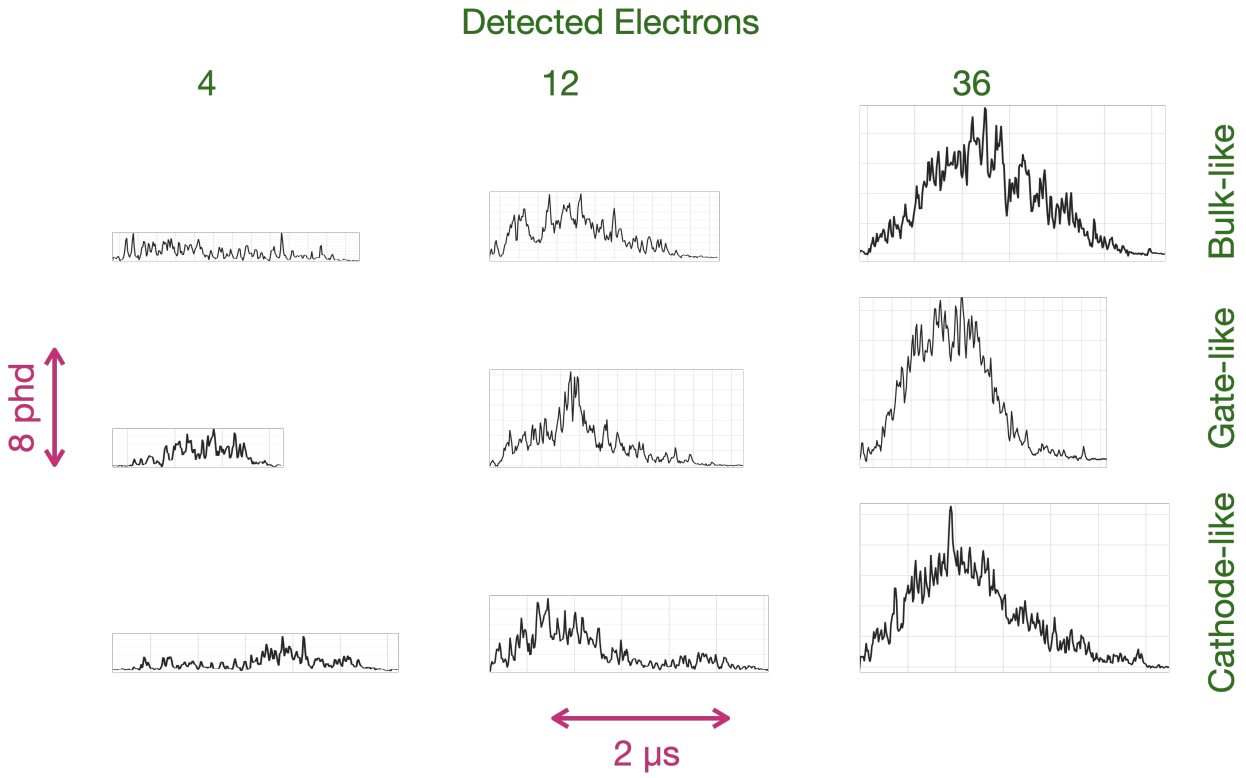

Figure 7.21: $S2$s composed of approximately 4, 12, and 36 detected electrons that were tagged as signal- and electrode-like. The electrode-like pulses were separated into gate and cathode categories based on their visual appearance: tall, thin pulses were identified as gate-like and wide, flat pulses as cathode-like.

ing only $S2$ pulse shape information, which is useful even for small $S2$s of only a few detected electrons. The residual rate of events just above the 3.5 detected electron software threshold is approximately 7 events/tonne/day/electron, after correcting for cut efficiencies.

Signal Model

Two DM signal hypotheses were tested against the data presented in Fig. 7.25. First was occurrence of traditional spin-independent (SI) elastic scattering of DM particles on a xenon nuclei whereafter the nuclei recoil, ionizing and exciting neighboring xenon atoms within the recoil path (detailed throughout Chapter 2). Detection through this NR channel is limited to dark matter particles with mass $m_\chi \gtrsim 2$ GeV which are able to transfer enough momentum to a heavy xenon nucleus to produce $S2$s above the analysis threshold. The second hypothesis was occurrence of a rare process by which DM scatters on a xenon nuclei result in emission of ∼keV electrons via the "Migdal effect" [120, 164] (summarised in Chapter 2, Sec. 2.3). A

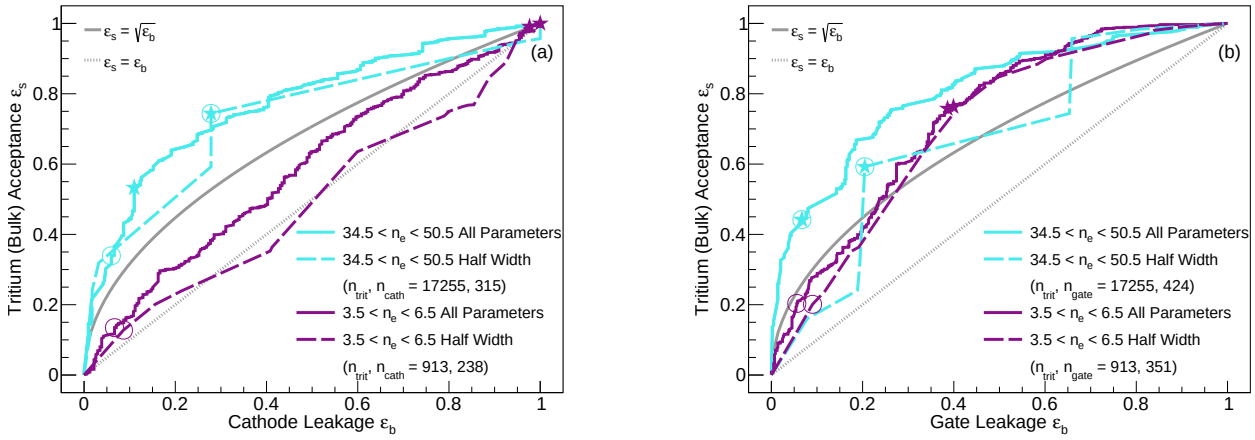

Figure 7.22: ROC curves of of training+testing data for a BDT using all shape quantifying parameters compared to a BDT using only half width. Points of maximum limit improvement are shown by stars and circles for background subtracted and Poisson cases, respectively.

detailed description of how this ER channel was modeled is published in [121], which outlines a search for DM via the Migdal effect using WS2013 data with both an $S1$ and $S2$.

The detectors response to these two signal types was modeled with NEST v2.0.1—assuming a DM velocity distribution calculated from the Standard Halo Model as in [169]. NESTs NR and ER charge field models, and some of the empirical data to which NEST fit the models, are shown in Fig. 2.19 of Chapter 2. Below the lowest experimental datapoints at 0.3 keV$_{nr}$ and 0.186 keV$_{ee}$, the charge yields were conservatively assumed to be zero.

The overall signal efficiency was modeled according to Fig. 7.1, with an additional $\sim 60\%$ reduction from the BDT cut.

Limit

The SI WIMP-nucleon (NR) and Migdal (ER) upper limits presented in Fig. 7.25 were calculated using Yellin's $p_{\max}$ test statistic, described in [163]. This method considers the intervals between pairs of events in a distribution of some parameter. For this analysis, the selected parameter was energy as measured by the $S2$ area. The method uses a signal model to calculate the Poisson probability of there existing more events within each interval than were actually observed. For a given set of cross-sections, it finds the interval that excludes each cross-section most strongly: in other words, the interval that has the greatest probability of containing more events than were observed. A cross-section is excluded with a 90% confidence level if a random experiment would give a smaller maximum probability ($p_{\max}$) 90% of the time.

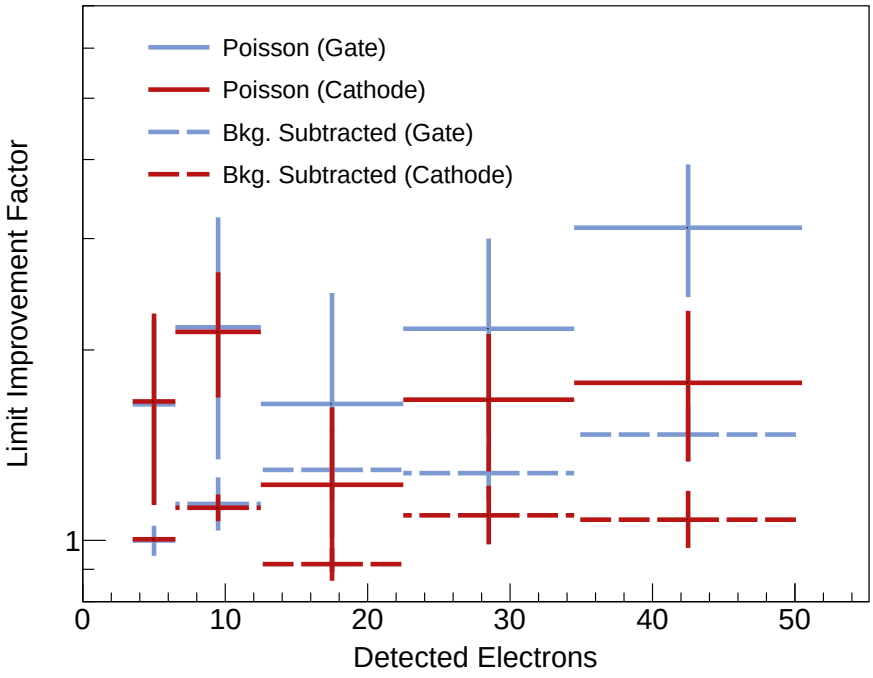

Figure 7.23: Predicted maximum improvement in exclusion limits for background subtracted ($\epsilon_s/\sqrt{\epsilon_b}$) and Poisson ($\epsilon_s/\epsilon_b$) scenarios, calculated separately for extreme cases of only gate backgrounds or only cathode backgrounds. Points of maximum improvement correspond to the stars and circles from Fig. 7.22 for the BDT using all parameters. Because the shape of the background energy spectrum is unknown, distinct values are given for each $S2$ size bin; the final improvement would be a weighted average of the values shown.

Discussion of Results

The $S1$-agnostic analysis described in this chapter provides increased sensitivity to low-mass DM compared to the standard, $S1 + S2$ analyses of NR and Migdal signals [52, 121]. The improvement is primarily due to inclusion of events with $S2$s of 4–10 detected electrons and no $S1$s.

Through a combination of lower threshold and careful reduction of backgrounds, especially electrode events; this analysis improves on a previous DM-nucleon scattering cross section limit from XENON100 [123], an experiment with an active xenon mass of 62 kg [170]. The present sensitivity is comparable to that obtained by DarkSide-50 [124], an experiment utilizing a dual-phase argon TPC of 46 kg [171]. The lower mass target nuclei used in that experiment promote greater transfers of energy of $\sim \left(\frac{m_{Xe}}{m_{Ar}}\right)^2 = 11$ in collisions with DM of $m_\chi \ll m_{Ar}, m_{Xe}$ resulting in improved sensitivity to the lowest mass particles. Finally, note that the present results are not as stringent as those obtained by XENON1T, an experiment

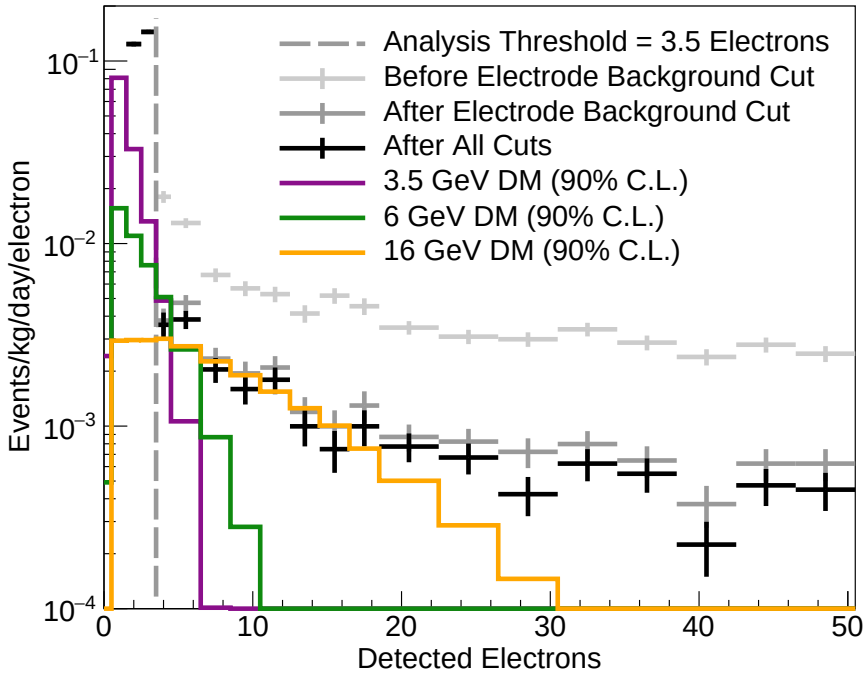

Figure 7.24: Dark matter (DM) search data from May through Sept 2013 before and after applying the BDT cut and hand-scanning to remove events that originated on the electrodes. The BDT cut reduces the observed event rate by a factor of ~ 4 while retaining approximately 60% signal efficiency independent of $S2$ size. DM spectra at the 90% confidence interval cross-section limit are overlaid for comparison.

with a 2 tonne active mass and an exposure approximately a factor of 4 greater than that of LUX [125].

Electrode events are likely to remain a challenge for LZ and other xenon experiments searching for low-mass DM, as well as coherent neutrino-nucleus scattering of solar ^{8}B neutrinos. Because the machine learning technique described in this chapter is highly dependent on $S2$ size, it is expected to be of equal or greater success in LZ due to low-energy signals containing greater numbers of electrons (primarily a result of a greater extraction efficiency, predicted to be 95% in LZ compared to 49% in LUX WS2013). The technique works in concert with treatments used to reduce electron emission rates from LZ grid wires. In particular, acid passivation was demonstrated by [114] to bring about order-of-magnitude reductions of emission rate by improving the quality of the oxide layer on wire surfaces.

Although LZ is predicted to have a higher event rate than that measured in LUX, thus a greater intensity of electron emissions trailing previous events, these backgrounds are expected to remain manageable in the region of the spectrum above a few electrons. The larger size of the LZ TPC will allow selection of a low background region near the center of

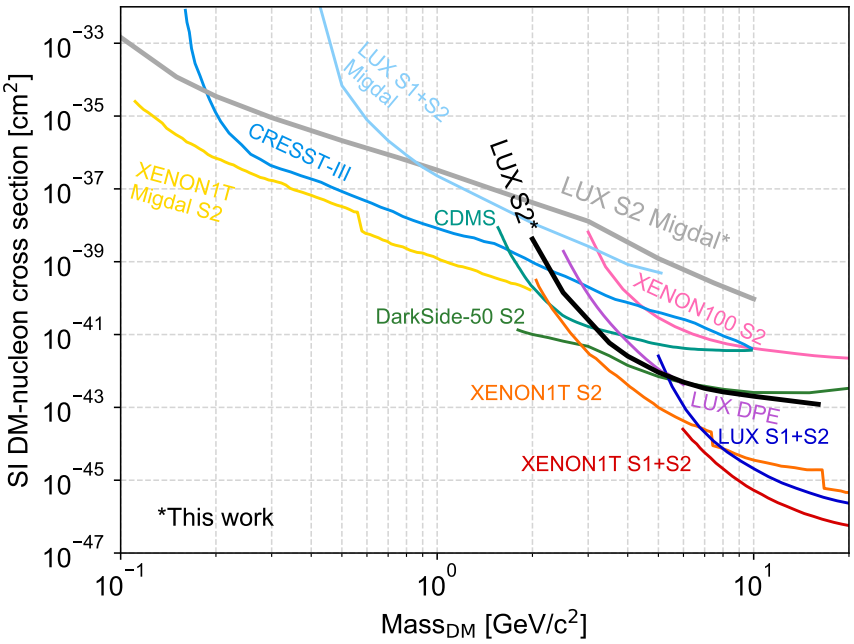

Figure 7.25: Upper limits on the spin-independent DM-nucleon cross section at 90% C.L. The result of the $S2$-only analysis with an NR signal model is shown in black, and the result of the $S2$-only analysis with a signal model based on the Migdal effect is shown in grey. Also shown are limits from DarkSide-50 [165] ($S2$-only, binomial fluctuation assumption), CDMSlite [166], CRESST-III [167], XENON100 $S2$-only [123], XENON1T $S1 + S2$ [51], XENON1T $S2$-only [125] (NEST 2.0.1 yields), XENON1T $S2$-only with Migdal effect [168], and past LUX searches using $S1 + S2$ events [**LUX2016**], including S1s with single photons using double photoelectron emission (DPE) [96], and the Migdal effect [121].

the active mass with a significantly attenuated γ-ray intensity, the greatest source of high energy backgrounds in this type of detector. Furthermore, previous $S2$ size, position, and time delay information can be used to design a more advanced veto than what was used in this LUX analysis. Also note the improved extraction efficiency will mitigate backgrounds from delayed emission of electrons trapped at the liquid surface, the only source of multiple electron $S2$s identified in [111] apart from those originating at the electrodes or radiogenic events within the xenon.

Chapter 8

Closing Remarks

The properties and behavior of the cosmos cannot be fully explained through the Standard Model (SM) of particle physics. The observed phenomena strongly indicate the existence of an additional class of particles that exert gravitational force but are blind to electromagnetism.

The LUX and LZ detectors are dual-phase xenon time projection chambers (TPCs) designed to directly detect the scatters of Weakly Interacting Massive Particles (WIMPs), a strong set of dark matter (DM) candidates with masses of $m_\chi \in 10\text{–}10,000$ GeV. The Large Underground Xenon (LUX) experiment utilized this type of detector to set multiple world leading limits on the spin-independent dark matter (DM)-nucleon scattering cross section for $m_\chi \gtrsim 5$ GeV. It's successor, LUX-ZEPLIN (LZ), is currently being commissioned in its former position one mile underground at Sanford Underground Research Facility (SURF), and will begin taking data in 2021.

As consecutive experiments have ever-more tightly constrained the parameters of WIMPs, the physics community has begun to more-seriously consider lower-mass alternatives to these particles. Some well-motivated extensions of the SM suggest dark candidates with masses just below the threshold of dual-phase xenon TPCs: for example, there is asymmetric dark matter (DM) with $m_\chi \sim$ GeV.

Furthermore, there are other potential signals of interest above the energy range of a WIMP scatters. For example, there is DM coupling through a complete basis of effective field theory operators (the standard WIMP signal is induced through only one such operator), two-neutrino double electron capture of ^{124}Xe, and neutrinoless double beta decay of ^{134}Xe and ^{136}Xe.

This dissertation presents work extending the sensitivity of LUX and LZ to rare events outside of the energy range used for the standard WIMP analysis. It does so through two paths of action: precise management of backgrounds that can hide or mimic high-energy signals of interest and optimization of a threshold lowering analysis technique.

Chapter 5 focuses on the most challenging high-energy background in this type of detector: radon. This element is present in the air causing plate out of its daughters on components during construction. The short-lived isotopes quickly decay away, but ^{210}Pb

(with a 22 year half life) and its progeny remain long after the detector has been closed and has started running. The LUX data were used to set a limit on the rate at which this isotope washes off of the TPC walls into the xenon, corresponding to an effective half life of > 4.4 years. The long time scale of this process was used to predict there would be minimal impact from ^{210}Pb surface contamination on the sensitivity of the LZ detector. Radon can also become absorbed in the xenon when it emanates from the detector components, themselves. Consequently, the LUX data were used to characterize the distribution of radon chain α decays occurring throughout the xenon. The results constrained the rate of radon chain β decays which are backgrounds for all rare event searches of interest.

To make the radon work possible, and all other high-energy analyses of the LUX data, strategies were developed to accurately select events based on the number of scintillation ($S1$) and ionization ($S2$) pulses observed in photomultiplier tube (PMT) waveforms. High-energy events tend to induce secondary processes that produce small spurious $S1$s and $S2$s that accompany the larger pulses of the primary events. Chapter 3 discusses development of an algorithm used to distinguish between the two categories of pulses. The algorithm was applied to the LUX background data to select single scatter events with just one primary $S1$ and $S2$, in this way, rejecting multiple scatter events and reducing the event rate in the energy range of ^{134}Xe and ^{136}Xe neutrinoless double beta decay by a factor of ~ 3.

Also benefiting the radon work, Chapter 4 outlines a calibration of the detector using a "Doke" method. The analysis identified gain parameters g_1 and g_2 used to convert $S1$ and $S2$ signals into units of energy via $E = W(S1/g_1 + S2/g_2)$. The work was unique in that it took advantage of the dependence of recombination on electric field magnitude—as opposed to event energy as is done in a typical Doke analysis—which varied widely throughout the TPC during LUX's 2014-16 science run. The results indicate a modest decrease in g_1 and g_2 occurring over the ~ 1.75 year length of the run, attributed to PMT photocathode aging.

Another significant source of backgrounds in dual-phase xenon TPCs is intrinsic contamination of detector components by primordial nuclides and cosmogenically activated isotopes. With this in mind, Chapter 6 describes construction of the Black Hills Underground Campus (BHUC) and installation of the high-purity germanium (HPGe) detectors at this site—a process in which the author was deeply involved. It describes programming of the automated liquid nitrogen system used to cool the detectors so they could perform continuous measurements of radiogenic contamination in potential construction materials. The lowest-activity materials were selected to build the LZ detector resulting in a prediction that just 0.8% of the WIMP background rate will come from the detector materials. The chapter discusses a subset of these assays of special interest to either LUX and LZ. Finally, it details the design of a powerful dual-crystal detector named Morvydd & Owain with sensitivity a factor of 2 greater than the next most powerful detector at the site. The design allowed for one of the crystals to slide forward to meet the other, optimizing sensitivity to very small samples by providing near-4π coverage of the sample by the crystals.

Chapter 7 describes a search for low-mass DM using the 2013 LUX dataset. A signal from this type of DM would be very low-energy ($\sim$keV) scatters that ionize only a few xenon atoms and seldom produce detectable scintillation signals. A novel machine learning technique was

developed to mitigated electrode backgrounds that limit the sensitivity of searches in this energy regime. An effective 5 tonne·day exposure was used to place strong limits on the scattering of low-mass DM particles with masses in the range $m_\chi \in 0.15$–10 GeV.

The LZ collaboration has greatly improve upon LUX in the design of the detector and sophistication of its WIMP search analysis. I am greatly looking forward to applying the techniques discussed in this dissertation to LZ data to enable pursuit of a wider range of physics.

Bibliography

[1] N. Aghanim et al. "Planck 2018 results. VI. Cosmological parameters". In: *Astron. Astrophys.* 641 (2020), A6. DOI: 10.1051/0004-6361/201833910. arXiv: 1807.06209 [astro-ph.CO].

[2] J H Oort. "The force exerted by the stellar system in the direction perpendicular to the galactic plane and some related problems". In: *Bull. Astron. Inst. Netherlands* 6 (1932), pp. 249–287. URL: https://cds.cern.ch/record/436532.

[3] F. Zwicky. "Die Rotverschiebung von extragalaktischen Nebeln". In: *Helvetica Physica Acta* 6 (Jan. 1933), pp. 110–127.

[4] Vera C. Rubin and W. Kent Ford Jr. "Rotation of the Andromeda Nebula from a Spectroscopic Survey of Emission Regions". In: *Astrophys. J.* 159 (1970), pp. 379–403. DOI: 10.1086/150317.

[5] K. G. Begeman, A. H. Broeils, and R. H. Sanders. "Extended rotation curves of spiral galaxies: dark haloes and modified dynamics". In: *Monthly Notices of the Royal Astronomical Society* 249.3 (Apr. 1991), pp. 523–537. ISSN: 0035-8711. DOI: 10.1093/mnras/249.3.523. eprint: https://academic.oup.com/mnras/article-pdf/249/3/523/18160929/mnras249-0523.pdf. URL: https://doi.org/10.1093/mnras/249.3.523.

[6] David M. Wittman et al. "Detection of weak gravitational lensing distortions of distant galaxies by cosmic dark matter at large scales". In: *Nature* 405 (2000), pp. 143–149. DOI: 10.1038/35012001. arXiv: astro-ph/0003014.

[7] Peter Schneider. "Detection of (dark) matter concentrations via weak gravitational lensing". In: *Mon. Not. Roy. Astron. Soc.* 283 (1996), pp. 837–853. DOI: 10.1093/mnras/283.3.837. arXiv: astro-ph/9601039.

[8] Douglas Clowe et al. "A direct empirical proof of the existence of dark matter". In: *Astrophys. J. Lett.* 648 (2006), pp. L109–L113. DOI: 10.1086/508162. arXiv: astro-ph/0608407.

[9] E Hubble. "A Relation Between Distance and Radial Velocity Among Extra-Galactic Nebulae From the Proceedings of the National Academy of Sciences". In: (1929).

[10] John C. Mather et al. "A Preliminary measurement of the Cosmic Microwave Background spectrum by the Cosmic Background Explorer (COBE) satellite". In: *Astrophys. J. Lett.* 354 (1990), pp. L37–L40. DOI: 10.1086/185717.

[11] George F. Smoot et al. "Structure in the COBE differential microwave radiometer first year maps". In: *Astrophys. J. Lett.* 396 (1992), pp. L1–L5. DOI: 10.1086/186504.

[12] R. Adam et al. "Planck 2015 results. I. Overview of products and scientific results". In: *Astron. Astrophys.* 594 (2016), A1. DOI: 10.1051/0004-6361/201527101. arXiv: 1502.01582 [astro-ph.CO].

[13] Daniel J. Eisenstein et al. "Detection of the Baryon Acoustic Peak in the Large-Scale Correlation Function of SDSS Luminous Red Galaxies". In: *Astrophys. J.* 633 (2005), pp. 560–574. DOI: 10.1086/466512. arXiv: astro-ph/0501171.

[14] Wayne Hu and Scott Dodelson. "Cosmic Microwave Background Anisotropies". In: *Ann. Rev. Astron. Astrophys.* 40 (2002), pp. 171–216. DOI: 10.1146/annurev.astro.40.060401.093926. arXiv: astro-ph/0110414.

[15] Jaco de Swart, Gianfranco Bertone, and Jeroen van Dongen. "How Dark Matter Came to Matter". In: *Nature Astron.* 1 (2017), p. 0059. DOI: 10.1038/s41550017-0059. arXiv: 1703.00013 [astro-ph.CO].

[16] Marco Battaglieri et al. *US Cosmic Visions: New Ideas in Dark Matter 2017: Community Report. US Cosmic Visions: New Ideas in Dark Matter 2017: Community Report*. Tech. rep. 102 pages + references. July 2017. arXiv: 1707.04591. URL: https://cds.cern.ch/record/2275381.

[17] Jonathan L. Feng. "Dark Matter Candidates from Particle Physics and Methods of Detection". In: *Annual Review of Astronomy and Astrophysics* 48.1 (2010), pp. 495–545. DOI: 10.1146/annurev-astro-082708-101659. eprint: https://doi.org/10.1146/annurev-astro-082708-101659. URL: https://doi.org/10.1146/annurev-astro-082708-101659.

[18] K.A. Olive. "Review of Particle Physics". In: *Chinese Physics C* 40.10 (Oct. 2016), p. 100001. DOI: 10.1088/1674-1137/40/10/100001. URL: https://doi.org/10.1088/1674-1137/40/10/100001.

[19] P. A. R. Ade et al. "Planck 2013 results. XVI. Cosmological parameters". In: *Astron. Astrophys.* 571 (2014), A16. DOI: 10.1051/0004-6361/201321591. arXiv: 1303.5076 [astro-ph.CO].

[20] P. S. Bhupal Dev, Anupam Mazumdar, and Saleh Qutub. "Constraining Non-thermal and Thermal properties of Dark Matter". In: *Front. in Phys.* 2 (2014), p. 26. DOI: 10.3389/fphy.2014.00026. arXiv: 1311.5297 [hep-ph].

[21] Giorgio Arcadi et al. "The waning of the WIMP? A review of models, searches, and constraints". In: *Eur. Phys. J. C* 78.3 (2018), p. 203. DOI: 10.1140/epjc/s10052-018-5662-y. arXiv: 1703.07364 [hep-ph].

[22] Gerard Jungman, Marc Kamionkowski, and Kim Griest. "Supersymmetric dark matter". In: *Physics Reports* 267.5 (1996), pp. 195–373. ISSN: 0370-1573. DOI: https://doi.org/10.1016/0370-1573(95)00058-5. URL: https://www.sciencedirect.com/science/article/pii/0370157395000585.

[23] Matthew J. Strassler and Kathryn M. Zurek. "Echoes of a hidden valley at hadron colliders". In: *Phys. Lett. B* 651 (2007), pp. 374–379. DOI: 10.1016/j.physletb.2007.06.055. arXiv: hep-ph/0604261.

[24] Matthew J. Strassler. "Possible effects of a hidden valley on supersymmetric phenomenology". In: (July 2006). arXiv: hep-ph/0607160.

[25] Benjamin W. Lee and Steven Weinberg. "Cosmological Lower Bound on Heavy Neutrino Masses". In: *Phys. Rev. Lett.* 39 (1977). Ed. by M. A. Srednicki, pp. 165–168. DOI: 10.1103/PhysRevLett.39.165.

[26] Pierre Jean et al. "Early SPI / INTEGRAL measurements of 511 keV line emission from the 4th quadrant of the Galaxy". In: *Astron. Astrophys.* 407 (2003), p. L55. DOI: 10.1051/0004-6361:20031056. arXiv: astro-ph/0309484.

[27] Céline Boehm et al. "Scalar dark matter candidates revisited". In: *Phys. Rev. D* 103.7 (2021), p. 075005. DOI: 10.1103/PhysRevD.103.075005. arXiv: 2010.02954 [hep-ph].

[28] Dan Hooper and Kathryn M. Zurek. "A Natural Supersymmetric Model with MeV Dark Matter". In: *Phys. Rev. D* 77 (2008), p. 087302. DOI: 10.1103/PhysRevD.77.087302. arXiv: 0801.3686 [hep-ph].

[29] Jonathan L. Feng and Jason Kumar. "Dark-Matter Particles without Weak-Scale Masses or Weak Interactions". In: *Phys. Rev. Lett.* 101 (23 Dec. 2008), p. 231301. DOI: 10.1103/PhysRevLett.101.231301. URL: https://link.aps.org/doi/10.1103/PhysRevLett.101.231301.

[30] Celine Boehm et al. "MeV dark matter: Has it been detected?" In: *Phys. Rev. Lett.* 92 (2004), p. 101301. DOI: 10.1103/PhysRevLett.92.101301. arXiv: astro-ph/0309686.

[31] R. E. Lingenfelter, J. C. Higdon, and R. E. Rothschild. "Is There a Dark Matter Signal in the Galactic Positron Annihilation Radiation?" In: *Phys. Rev. Lett.* 103 (2009), p. 031301. DOI: 10.1103/PhysRevLett.103.031301. arXiv: 0904.1025 [astro-ph.HE].

[32] David E. Kaplan, Markus A. Luty, and Kathryn M. Zurek. "Asymmetric Dark Matter". In: *Phys. Rev. D* 79 (2009), p. 115016. DOI: 10.1103/PhysRevD.79.115016. arXiv: 0901.4117 [hep-ph].

[33] Kathryn M. Zurek. "Asymmetric Dark Matter: Theories, Signatures, and Constraints". In: *Phys. Rept.* 537 (2014), pp. 91–121. DOI: 10.1016/j.physrep.2013.12.001. arXiv: 1308.0338 [hep-ph].

[34] Tongyan Lin, Hai-Bo Yu, and Kathryn M. Zurek. "On Symmetric and Asymmetric Light Dark Matter". In: *Phys. Rev. D* 85 (2012), p. 063503. DOI: 10.1103/PhysRevD.85.063503. arXiv: 1111.0293 [hep-ph].

[35] R. Foot. "Mirror dark matter: Cosmology, galaxy structure and direct detection". In: *Int. J. Mod. Phys. A* 29 (2014), p. 1430013. DOI: 10.1142/S0217751X14300130. arXiv: 1401.3965 [astro-ph.CO].

[36] Robert Foot and R. R. Volkas. "Explaining Omega(Baryon) approximately 0.2 Omega(Dark) through the synthesis of ordinary matter from mirror matter: A More general analysis". In: *Phys. Rev. D* 69 (2004), p. 123510. DOI: 10.1103/PhysRevD.69.123510. arXiv: hep-ph/0402267.

[37] D. S. Akerib et al. "First direct detection constraint on mirror dark matter kinetic mixing using LUX 2013 data". In: *Phys. Rev. D* 101 (1 Jan. 2020), p. 012003. DOI: 10.1103/PhysRevD.101.012003. URL: https://link.aps.org/doi/10.1103/PhysRevD.101.012003.

[38] Jim Alexander et al. "Dark Sectors 2016 Workshop: Community Report". In: Aug. 2016. arXiv: 1608.08632 [hep-ph].

[39] Lawrence J. Hall et al. "Freeze-In Production of FIMP Dark Matter". In: *JHEP* 03 (2010), p. 080. DOI: 10.1007/JHEP03(2010)080. arXiv: 0911.1120 [hep-ph].

[40] Teresa Marrodán Undagoitia and Ludwig Rauch. "Dark matter direct-detection experiments". In: *J. Phys. G* 43.1 (2016), p. 013001. DOI: 10.1088/0954-3899/43/1/013001. arXiv: 1509.08767 [physics.ins-det].

[41] Maria Beltran et al. "Maverick dark matter at colliders". In: *JHEP* 09 (2010), p. 037. DOI: 10.1007/JHEP09(2010)037. arXiv: 1002.4137 [hep-ph].

[42] Morad Aaboud et al. "Search for dark matter and other new phenomena in events with an energetic jet and large missing transverse momentum using the ATLAS detector". In: *JHEP* 01 (2018), p. 126. DOI: 10.1007/JHEP01(2018)126. arXiv: 1711.03301 [hep-ex].

[43] Tracy R. Slatyer. "Indirect Detection of Dark Matter". In: *Theoretical Advanced Study Institute in Elementary Particle Physics: Anticipating the Next Discoveries in Particle Physics*. 2018, pp. 297–353. DOI: 10.1142/9789813233348_0005. arXiv: 1710.05137 [hep-ph].

[44] Jennifer M. Gaskins. "A review of indirect searches for particle dark matter". In: *Contemp. Phys.* 57.4 (2016), pp. 496–525. DOI: 10.1080/00107514.2016.1175160. arXiv: 1604.00014 [astro-ph.HE].

[45] Louis E. Strigari. "Galactic Searches for Dark Matter". In: *Phys. Rept.* 531 (2013), pp. 1–88. DOI: 10.1016/j.physrep.2013.05.004. arXiv: 1211.7090 [astro-ph.CO].

[46] V. Chepel and H. Araujo. "Liquid noble gas detectors for low energy particle physics". In: *JINST* 8 (2013), R04001. DOI: 10.1088/1748-0221/8/04/R04001. arXiv: 1207.2292 [physics.ins-det].

[47] F. S. Ling et al. "Dark Matter Direct Detection Signals inferred from a Cosmological N-body Simulation with Baryons". In: *JCAP* 02 (2010), p. 012. DOI: 10.1088/1475-7516/2010/02/012. arXiv: 0909.2028 [astro-ph.GA].

[48] N. Wyn Evans, Ciaran A. J. O'Hare, and Christopher McCabe. "Refinement of the standard halo model for dark matter searches in light of the Gaia Sausage". In: *Phys. Rev. D* 99.2 (2019), p. 023012. DOI: 10.1103/PhysRevD.99.023012. arXiv: 1810.11468 [astro-ph.GA].

[49] Alis J Deason et al. "The local high-velocity tail and the Galactic escape speed". In: *Monthly Notices of the Royal Astronomical Society* 485.3 (Mar. 2019), pp. 3514–3526. ISSN: 0035-8711. DOI: 10.1093/mnras/stz623. eprint: https://academic.oup.com/mnras/article-pdf/485/3/3514/28168725/stz623.pdf. URL: https://doi.org/10.1093/mnras/stz623.

[50] R. Agnese et al. "Search for Low-Mass Weakly Interacting Massive Particles with SuperCDMS". In: *Phys. Rev. Lett.* 112.24 (2014), p. 241302. DOI: 10.1103/PhysRevLett.112.241302. arXiv: 1402.7137 [hep-ex].

[51] E. Aprile et al. "Dark Matter Search Results from a One Ton-Year Exposure of XENON1T". In: *Phys. Rev. Lett.* 121.11 (2018), p. 111302. DOI: 10.1103/PhysRevLett.121.111302. arXiv: 1805.12562 [astro-ph.CO].

[52] D.S. Akerib et al. "Results from a search for dark matter in the complete LUX exposure". In: *Phys. Rev. Lett.* 118.2 (2017), p. 021303. DOI: 10.1103/PhysRevLett.118.021303. arXiv: 1608.07648 [astro-ph.CO].

[53] D. S. Akerib et al. "Projected WIMP sensitivity of the LUX-ZEPLIN dark matter experiment". In: *Phys. Rev. D* 101.5 (2020), p. 052002. DOI: 10.1103/PhysRevD.101.052002. arXiv: 1802.06039 [astro-ph.IM].

[54] Marc Schumann. "Direct Detection of WIMP Dark Matter: Concepts and Status". In: *J. Phys. G* 46.10 (2019), p. 103003. DOI: 10.1088/1361-6471/ab2ea5. arXiv: 1903.03026 [astro-ph.CO].

[55] P.A. Zyla et al. "Review of Particle Physics". In: *PTEP* 2020.8 (2020), p. 083C01. DOI: 10.1093/ptep/ptaa104.

[56] Gerard Jungman, Marc Kamionkowski, and Kim Griest. "Supersymmetric dark matter". In: *Phys. Rept.* 267 (1996), pp. 195–373. DOI: 10.1016/0370-1573(95)00058-5. arXiv: hep-ph/9506380.

[57] P. Gondolo et al. "DarkSUSY: Computing supersymmetric dark matter properties numerically". In: *JCAP* 07 (2004), p. 008. DOI: 10.1088/1475-7516/2004/07/008. arXiv: astro-ph/0406204.

[58] Richard H. Helm. "Inelastic and Elastic Scattering of 187-Mev Electrons from Selected Even-Even Nuclei". In: *Phys. Rev.* 104 (1956), pp. 1466–1475. DOI: 10.1103/PhysRev.104.1466.

[59] J. Engel. "Nuclear form-factors for the scattering of weakly interacting massive particles". In: *Phys. Lett. B* 264 (1991), pp. 114–119. DOI: 10.1016/0370-2693(91)90712-Y.

[60] G. Belanger et al. "Dark matter direct detection rate in a generic model with micrOMEGAs 2.2". In: *Comput. Phys. Commun.* 180 (2009), pp. 747–767. DOI: 10.1016/j.cpc.2008.11.019. arXiv: 0803.2360 [hep-ph].

[61] J. D. Lewin and P. F. Smith. "Review of mathematics, numerical factors, and corrections for dark matter experiments based on elastic nuclear recoil". In: *Astropart. Phys.* 6 (1996), pp. 87–112. DOI: 10.1016/S0927-6505(96)00047-3.

[62] P. Toivanen et al. "Large-scale shell-model calculations of elastic and inelastic scattering rates of lightest supersymmetric particles (LSP) on I-127, Xe-129, Xe-131, and Cs-133 nuclei". In: *Phys. Rev. C* 79 (2009), p. 044302. DOI: 10.1103/PhysRevC.79.044302.

[63] D.S. Akerib et al. "First results from the LUX dark matter experiment at the Sanford Underground Research Facility". In: *Phys. Rev. Lett.* 112 (2014), p. 091303. DOI: 10.1103/PhysRevLett.112.091303. arXiv: 1310.8214 [astro-ph.CO].

[64] D.S. Akerib et al. "Improved Limits on Scattering of Weakly Interacting Massive Particles from Reanalysis of 2013 LUX Data". In: *Phys. Rev. Lett.* 116.16 (2016), p. 161301. DOI: 10.1103/PhysRevLett.116.161301. arXiv: 1512.03506 [astro-ph.CO].

[65] R.L. Platzman. "Total ionization in gases by high-energy particles: An appraisal of our understanding". In: *The International Journal of Applied Radiation and Isotopes* 10.2 (1961), pp. 116–127. ISSN: 0020-708X. DOI: https://doi.org/10.1016/0020-708X(61)90108-9. URL: http://www.sciencedirect.com/science/article/pii/0020708X61901089.

[66] Marlo Martin. "Exciton Self-Trapping in Rare-Gas Crystals". In: *The Journal of Chemical Physics* 54.8 (1971), pp. 3289–3299. DOI: 10.1063/1.1675342. eprint: https://doi.org/10.1063/1.1675342. URL: https://doi.org/10.1063/1.1675342.

[67] Keiko Fujii et al. "High-accuracy measurement of the emission spectrum of liquid xenon in the vacuum ultraviolet region". In: *Nuclear Instruments and Methods in Physics Research Section A: Accelerators, Spectrometers, Detectors and Associated Equipment* 795 (2015), pp. 293–297. ISSN: 0168-9002. DOI: https://doi.org/10.1016/j.nima.2015.05.065. URL: https://www.sciencedirect.com/science/article/pii/S016890021500724X.

[68] Carl Eric Dahl. "The physics of background discrimination in liquid xenon, and first results from Xenon10 in the hunt for WIMP dark matter". PhD thesis. Princeton U., 2009.

[69] Peter Sorensen and Carl Eric Dahl. "Nuclear recoil energy scale in liquid xenon with application to the direct detection of dark matter". In: *Phys. Rev. D* 83 (2011), p. 063501. DOI: 10.1103/PhysRevD.83.063501. arXiv: 1101.6080 [astro-ph.IM].

[70] Tadayoshi Doke et al. "Absolute Scintillation Yields in Liquid Argon and Xenon for Various Particles". In: *Jap. J. Appl. Phys.* 41 (2002), pp. 1538–1545. DOI: 10.1143/JJAP.41.1538.

[71] E. Aprile et al. "Observation of anticorrelation between scintillation and ionization for MeV gamma rays in liquid xenon". In: *Phys. Rev. B* 76 (1 July 2007), p. 014115. DOI: 10.1103/PhysRevB.76.014115. URL: https://link.aps.org/doi/10.1103/PhysRevB.76.014115.

[72] E. Conti et al. "Correlated fluctuations between luminescence and ionization in liquid xenon". In: *Phys. Rev. B* 68 (5 Aug. 2003), p. 054201. DOI: 10.1103/PhysRevB.68.054201. URL: https://link.aps.org/doi/10.1103/PhysRevB.68.054201.

[73] D. S. Akerib et al. "Discrimination of electronic recoils from nuclear recoils in two-phase xenon time projection chambers". In: *Phys. Rev. D* 102.11 (2020), p. 112002. DOI: 10.1103/PhysRevD.102.112002. arXiv: 2004.06304 [physics.ins-det].

[74] D.S. Akerib et al. "Tritium calibration of the LUX dark matter experiment". In: *Phys. Rev. D* 93.7 (2016), p. 072009. DOI: 10.1103/PhysRevD.93.072009. arXiv: 1512.03133 [physics.ins-det].

[75] D. S. Akerib et al. "Improved Measurements of the β-Decay Response of Liquid Xenon with the LUX Detector". In: *Phys. Rev. D* 100.2 (2019), p. 022002. DOI: 10.1103/PhysRevD.100.022002. arXiv: 1903.12372 [physics.ins-det].

[76] E. Aprile et al. "Simultaneous measurement of ionization and scintillation from nuclear recoils in liquid xenon as target for a dark matter experiment". In: *Phys. Rev. Lett.* 97 (2006), p. 081302. DOI: 10.1103/PhysRevLett.97.081302. arXiv: astro-ph/0601552.

[77] G. Anton et al. "Measurement of the scintillation and ionization response of liquid xenon at MeV energies in the EXO-200 experiment". In: *Phys. Rev. C* 101.6 (2020), p. 065501. DOI: 10.1103/PhysRevC.101.065501. arXiv: 1908.04128 [physics.ins-det].

[78] Akira Hitachi et al. "Effect of ionization density on the time dependence of luminescence from liquid argon and xenon". In: *Phys. Rev. B* 27 (9 May 1983), pp. 5279–5285. DOI: 10.1103/PhysRevB.27.5279. URL: https://link.aps.org/doi/10.1103/PhysRevB.27.5279.

[79] Shinzou Kubota et al. "Dynamical behavior of free electrons in the recombination process in liquid argon, krypton, and xenon". In: *Phys. Rev. B* 20.8 (1979), p. 3486. DOI: 10.1103/PhysRevB.20.3486.

[80] D. Akimov et al. "Measurements of scintillation efficiency and pulse shape for low-energy recoils in liquid xenon". In: *Phys. Lett. B* 524 (2002), pp. 245–251. DOI: 10.1016/S0370-2693(01)01411-3. arXiv: hep-ex/0106042.

[81] T. Doke. "Fundamental Properties of Liquid Argon, Krypton and Xenon as Radiation Detector Media". In: *Portugal. Phys.* 12 (1981), pp. 9–48.

[82] Akira Hitachi et al. "Effect of ionization density on the time dependence of luminescence from liquid argon and xenon". In: *Phys. Rev. B* 27 (1983), pp. 5279–5285. DOI: 10.1103/PhysRevB.27.5279.

[83] J.V. Dawson et al. "A study of the scintillation induced by alpha particles and gamma rays in liquid xenon in an electric field". In: *Nuclear Instruments and Methods in Physics Research Section A: Accelerators, Spectrometers, Detectors and Associated Equipment* 545.3 (2005), pp. 690–698. ISSN: 0168-9002. DOI: https://doi.org/10.1016/j.nima.2005.01.343. URL: https://www.sciencedirect.com/science/article/pii/S0168900205007503.

[84] Jeremy Mock et al. "Modeling Pulse Characteristics in Xenon with NEST". In: *JINST* 9 (2014), T04002. DOI: 10.1088/1748-0221/9/04/T04002. arXiv: 1310.1117 [physics.ins-det].

[85] D. S. Akerib et al. "Liquid xenon scintillation measurements and pulse shape discrimination in the LUX dark matter detector". In: *Phys. Rev. D* 97.11 (2018), p. 112002. DOI: 10.1103/PhysRevD.97.112002. arXiv: 1802.06162 [physics.ins-det].

[86] Jingke Xu et al. "Electron extraction efficiency study for dual-phase xenon dark matter experiments". In: *Phys. Rev. D* 99.10 (2019), p. 103024. DOI: 10.1103/PhysRevD.99.103024. arXiv: 1904.02885 [physics.ins-det].

[87] D.S. Akerib et al. "The Large Underground Xenon (LUX) Experiment". In: *Nucl. Instrum. Meth. A* 704 (2013), pp. 111–126. DOI: 10.1016/j.nima.2012.11.135. arXiv: 1211.3788 [physics.ins-det].

[88] D.S. Akerib et al. "Calibration, event reconstruction, data analysis, and limit calculation for the LUX dark matter experiment". In: *Phys. Rev. D* 97.10 (2018), p. 102008. DOI: 10.1103/PhysRevD.97.102008. arXiv: 1712.05696 [physics.ins-det].

[89] D. S. Akerib et al. "An Ultra-Low Background PMT for Liquid Xenon Detectors". In: *Nucl. Instrum. Meth. A* 703 (2013), pp. 1–6. DOI: 10.1016/j.nima.2012.11.020. arXiv: 1205.2272 [physics.ins-det].

[90] D.S. Akerib et al. "3D Modeling of Electric Fields in the LUX Detector". In: *JINST* 12.11 (2017), P11022. DOI: 10.1088/1748-0221/12/11/P11022. arXiv: 1709.00095 [physics.ins-det].

[91] COMSOL Inc. *COMSOL*. 2020. URL: http://www.comsol.com/products/multiphysics/.

[92] D. S. Akerib et al. "FPGA-based Trigger System for the LUX Dark Matter Experiment". In: *Nucl. Instrum. Meth. A* 818 (2016), pp. 57–67. DOI: 10.1016/j.nima.2016.02.017. arXiv: 1511.03541 [physics.ins-det].

[93] D.S. Akerib et al. "LUX trigger efficiency". In: *Nucl. Instrum. Meth. A* 908 (2018), pp. 401–410. DOI: 10.1016/j.nima.2018.07.094. arXiv: 1802.07784 [physics.ins-det].

[94] D.S. Akerib et al. "Position Reconstruction in LUX". In: *JINST* 13.02 (2018), P02001. DOI: 10.1088/1748-0221/13/02/P02001. arXiv: 1710.02752 [physics.ins-det].

[95] URL: https://www.hamamatsu.com.

[96] D.S. Akerib et al. "Extending light WIMP searches to single scintillation photons in LUX". In: *Phys. Rev. D* 101.4 (2020), p. 042001. DOI: 10.1103/PhysRevD.101.042001. arXiv: 1907.06272 [astro-ph.CO].

[97] C. H. Faham et al. "Measurements of wavelength-dependent double photoelectron emission from single photons in VUV-sensitive photomultiplier tubes". In: *JINST* 10.09 (2015), P09010. DOI: 10.1088/1748-0221/10/09/P09010. arXiv: 1506.08748 [physics.ins-det].

[98] B. López Paredes et al. "Response of photomultiplier tubes to xenon scintillation light". In: *Astropart. Phys.* 102 (2018), pp. 56–66. DOI: 10.1016/j.astropartphys.2018.04.006. arXiv: 1801.01597 [physics.ins-det].

[99] D. S. Akerib et al. "^{83m}Kr calibration of the 2013 LUX dark matter search". In: *Phys. Rev. D* 96.11 (2017), p. 112009. DOI: 10.1103/PhysRevD.96.112009. arXiv: 1708.02566 [physics.ins-det].

[100] D. S. Akerib et al. "Ultralow energy calibration of LUX detector using ^{127}Xe electron capture". In: *Phys. Rev. D* 96.11 (2017), p. 112011. DOI: 10.1103/PhysRevD.96.112011. arXiv: 1709.00800 [physics.ins-det].

[101] D.S. Akerib et al. "Low-energy (0.7-74 keV) nuclear recoil calibration of the LUX dark matter experiment using D-D neutron scattering kinematics". In: (Aug. 2016). arXiv: 1608.05381 [physics.ins-det].

[102] E. M. Boulton et al. "Calibration of a two-phase xenon time projection chamber with a ^{37}Ar source". In: *JINST* 12.08 (2017), P08004. DOI: 10.1088/1748-0221/12/08/P08004. arXiv: 1705.08958 [physics.ins-det].

[103] E. Aprile et al. "Signal Yields of keV Electronic Recoils and Their Discrimination from Nuclear Recoils in Liquid Xenon". In: *Phys. Rev. D* 97.9 (2018), p. 092007. DOI: 10.1103/PhysRevD.97.092007. arXiv: 1709.10149 [astro-ph.IM].

[104] Brian Lenardo et al. "Measurement of the ionization yield from nuclear recoils in liquid xenon between 0.3 - 6 keV with single-ionization-electron sensitivity". In: (Aug. 2019). arXiv: 1908.00518 [physics.ins-det].

[105] M. Szydagis et al. *Noble Element Simulation Technique v2.0*. Version v2.0.0. July 2018. DOI: 10.5281/zenodo.1314669. URL: https://doi.org/10.5281/zenodo.1314669.

[106] D. S. Akerib et al. "Improving sensitivity to low-mass dark matter in LUX using a novel electrode background mitigation technique". In: *Phys. Rev. D* 104.1 (2021), p. 012011. DOI: 10.1103/PhysRevD.104.012011. arXiv: 2011.09602 [hep-ex].

[107] D. S. Akerib et al. "Radiogenic and Muon-Induced Backgrounds in the LUX Dark Matter Detector". In: *Astropart. Phys.* 62 (2015), pp. 33–46. DOI: 10.1016/j.astropartphys.2014.07.009. arXiv: 1403.1299 [astro-ph.IM].

[108] D. S. Akerib et al. "Measurement of the Gamma Ray Background in the Davis Cavern at the Sanford Underground Research Facility". In: *Astropart. Phys.* 116 (2020), p. 102391. DOI: 10.1016/j.astropartphys.2019.102391. arXiv: 1904.02112 [physics.ins-det].

[109] Kreuzer M and McLaughlin J. *WHO Guidelines for Indoor Air Quality: Selected Pollutants*. 2010. URL: https://www.ncbi.nlm.nih.gov/books/NBK138712/.

[110] M. Szydagis et al. "Investigating the XENON1T low-energy electronic recoil excess using NEST". In: *Phys. Rev. D* 103.1 (2021), p. 012002. DOI: 10.1103/PhysRevD.103.012002. arXiv: 2007.00528 [hep-ex].

[111] D.S. Akerib et al. "Investigation of background electron emission in the LUX detector". In: *Phys. Rev. D* 102.9 (2020), p. 092004. DOI: 10.1103/PhysRevD.102.092004. arXiv: 2004.07791 [physics.ins-det].

[112] Eric W. Lemmon, Mark O. McLinden, and Daniel G. Friend. *NIST Chemistry WebBook, NIST Standard Reference Database Number 69*. Ed. by P.J. Linstrom and W.G. Mallard. DOI: https://doi.org/10.18434/T4D303.

[113] Adam Bailey. "Dark matter searches and study of electrode design in LUX and LZ". PhD thesis. Imperial Coll., London, Aug. 2016.

[114] A. Tomás et al. "Study and mitigation of spurious electron emission from cathodic wires in noble liquid time projection chambers". In: *Astropart. Phys.* 103 (2018), pp. 49–61. DOI: 10.1016/j.astropartphys.2018.07.001. arXiv: 1801.07231 [physics.ins-det].

[115] D. S. Akerib et al. "The LUX-ZEPLIN (LZ) radioactivity and cleanliness control programs". In: *Eur. Phys. J. C* 80.11 (2020), p. 1044. DOI: 10.1140/epjc/s10052-020-8420-x. arXiv: 2006.02506 [physics.ins-det].

[116] S. Agostinelli et al. "Geant4—a simulation toolkit". In: *Nuclear Instruments and Methods in Physics Research Section A: Accelerators, Spectrometers, Detectors and Associated Equipment* 506.3 (2003), pp. 250–303. ISSN: 0168-9002. DOI: https://doi.org/10.1016/S0168-9002(03)01368-8. URL: https://www.sciencedirect.com/science/article/pii/S0168900203013688.

[117] D. S. Akerib et al. "LUXSim: A Component-Centric Approach to Low-Background Simulations". In: *Nucl. Instrum. Meth. A* 675 (2012), pp. 63–77. DOI: 10.1016/j.nima.2012.02.010. arXiv: 1111.2074 [physics.data-an].

[118] Glen Cowan et al. "Asymptotic formulae for likelihood-based tests of new physics". In: *Eur. Phys. J. C* 71 (2011). [Erratum: Eur.Phys.J.C 73, 2501 (2013)], p. 1554. DOI: 10.1140/epjc/s10052-011-1554-0. arXiv: 1007.1727 [physics.data-an].

[119] Chris Kouvaris and Josef Pradler. "Probing sub-GeV Dark Matter with conventional detectors". In: *Phys. Rev. Lett.* 118.3 (2017), p. 031803. DOI: 10.1103/PhysRevLett.118.031803. arXiv: 1607.01789 [hep-ph].

[120] Masahiro Ibe et al. "Migdal Effect in Dark Matter Direct Detection Experiments". In: *JHEP* 03 (2018), p. 194. DOI: 10.1007/JHEP03(2018)194. arXiv: 1707.07258 [hep-ph].

[121] D.S. Akerib et al. "Results of a Search for Sub-GeV Dark Matter Using 2013 LUX Data". In: *Phys. Rev. Lett.* 122.13 (2019), p. 131301. DOI: 10.1103/PhysRevLett.122.131301. arXiv: 1811.11241 [astro-ph.CO].

[122] P. Sorensen et al. "The scintillation and ionization yield of liquid xenon for nuclear recoils". In: *Nucl. Instrum. Meth. A* 601 (2009), pp. 339–346. DOI: 10.1016/j.nima.2008.12.197. arXiv: 0807.0459 [astro-ph].

[123] E. Aprile et al. "Low-mass dark matter search using ionization signals in XENON100". In: *Phys. Rev. D* 94.9 (2016). [Erratum: Phys.Rev.D 95, 059901 (2017)], p. 092001. DOI: 10.1103/PhysRevD.94.092001. arXiv: 1605.06262 [astro-ph.CO].

[124] P. Agnes et al. "Low-Mass Dark Matter Search with the DarkSide-50 Experiment". In: *Phys. Rev. Lett.* 121.8 (2018), p. 081307. DOI: 10.1103/PhysRevLett.121.081307. arXiv: 1802.06994 [astro-ph.HE].

[125] E. Aprile et al. "Light Dark Matter Search with Ionization Signals in XENON1T". In: *Phys. Rev. Lett.* 123.25 (2019), p. 251801. DOI: 10.1103/PhysRevLett.123.251801. arXiv: 1907.11485 [hep-ex].

[126] D. Yu. Akimov et al. "The ZEPLIN-III dark matter detector: instrument design, manufacture and commissioning". In: *Astropart. Phys.* 27 (2007), pp. 46–60. DOI: 10.1016/j.astropartphys.2006.09.005. arXiv: astro-ph/0605500.

[127] V. N. Lebedenko et al. "Result from the First Science Run of the ZEPLIN-III Dark Matter Search Experiment". In: *Phys. Rev. D* 80 (2009), p. 052010. DOI: 10.1103/PhysRevD.80.052010. arXiv: 0812.1150 [astro-ph].

[128] D. Yu. Akimov et al. "WIMP-nucleon cross-section results from the second science run of ZEPLIN-III". In: *Phys. Lett. B* 709 (2012), pp. 14–20. DOI: 10.1016/j.physletb.2012.01.064. arXiv: 1110.4769 [astro-ph.CO].

[129] B. J. Mount et al. "LUX-ZEPLIN (LZ) Technical Design Report". In: (Mar. 2017). arXiv: 1703.09144 [physics.ins-det].

[130] S. J. Haselschwardt et al. "A Liquid Scintillation Detector for Radioassay of Gadolinium-Loaded Liquid Scintillator for the LZ Outer Detector". In: *Nucl. Instrum. Meth. A* 937 (2019), pp. 148–163. DOI: 10.1016/j.nima.2019.05.055. arXiv: 1808.05595 [physics.ins-det].

[131] D. S. Akerib et al. "Identification of Radiopure Titanium for the LZ Dark Matter Experiment and Future Rare Event Searches". In: *Astropart. Phys.* 96 (2017), pp. 1–10. DOI: 10.1016/j.astropartphys.2017.09.002. arXiv: 1702.02646 [physics.ins-det].

[132] Carlos H. Faham. "Prototype, Surface Commissioning and Photomultiplier Tube Characterization for the Large Underground Xenon (LUX) Direct Dark Matter Search Experiment". PhD thesis. Brown U., 2014. DOI: 10.7301/Z0QV3JV5.

[133] D. S. Akerib et al. "Signal yields, energy resolution, and recombination fluctuations in liquid xenon". In: *Phys. Rev. D* 95.1 (2017), p. 012008. DOI: 10.1103/PhysRevD.95.012008. arXiv: 1610.02076 [physics.ins-det].

[134] M. Szydagis et al. *NESTCollaboration/nest: New, flexible LXe NR yields and resolution model + G4 improvements + linear Noise + much more*. Version v2.0.1. Aug. 2019. DOI: 10.5281/zenodo.3357973. URL: https://doi.org/10.5281/zenodo.3357973.

[135] *Decay Chain Visualizations*. URL: https://metadata.berkeley.edu/nuclear-forensics/.

[136] J E Gaiser. "Charmonium spectroscopy from radiative decays of the J/psi and psi'". PhD thesis. Aug. 1982. URL: https://www.osti.gov/biblio/6237411.

[137] J. B. Albert et al. "Measurements of the ion fraction and mobility of α- and β-decay products in liquid xenon using the EXO-200 detector". In: *Phys. Rev. C* 92.4 (2015), p. 045504. DOI: 10.1103/PhysRevC.92.045504. arXiv: 1506.00317 [nucl-ex].

[138] Brianna J. Mount et al. "Black Hills State University Underground Campus". In: *Appl. Radiat. Isot.* 126 (2017), pp. 130–133. DOI: 10.1016/j.apradiso.2017.02.025.

[139] *Research*. 2021. URL: https://www.bhsu.edu/Research/Underground-Campus.

[140] Rick Bitter, Taqi Mohiuddin, and Matt Nawrocki. *LabVIEW: Advanced programming techniques*. Crc Press, 2006.

[141] Ben G Streetman and Sanjay Banerjee. *Solid State electronic Devices*. 5th. Prentice Hall, 2000.

[142] M.J. Berger et al. XCOM: Photon Cross Section Database (version 1.5), [Online]. Available: http://physics.nist.gov/xcom [2020, June 1]. National Institute of Standards and Technology, Gaithersburg, MD. 2010.

[143] W. L. Hansen and E. E. Haller. "A View of the Present Status and Future Prospecis of High Purity Germanium". In: *IEEE Transactions on Nuclear Science* 21.1 (1974), pp. 251–259. DOI: 10.1109/TNS.1974.4327469.

[144] Tony R Kuphaldt. *Electrons and "holes": Solid-state Device Theory: Electronics Textbook*. URL: https://www.allaboutcircuits.com/textbook/semiconductors/chpt-2/electrons-and-holes/.

[145] Glenn F Knoll. *Radiation Detection and Measurement*. John Wiley, 2020.

[146] R.W. Williams et al. "High Th/U ratios in subcontinental lithospheric mantle: mass spectrometric measurement of Th isotopes in Gaussberg lamproites". In: *Earth and Planetary Science Letters* 111.2 (1992), pp. 257–268. ISSN: 0012-821X. DOI: https://doi.org/10.1016/0012-821X(92)90183-V. URL: https://www.sciencedirect.com/science/article/pii/0012821X9290183V.

[147] Brian Peter Tennyson. "Two-Phase Liquid-Gas Xenon Time Projection Chambers: Theory, Applications, and Analysis". PhD thesis. Yale University, Sept. 2017.

[148] K. T. Lesko. "The Sanford Underground Research Facility at Homestake (SURF)". In: *Phys. Procedia* 61 (2015). Ed. by Frank Avignone and Wick Haxton, pp. 542–551. DOI: 10.1016/j.phpro.2014.12.001.

[149] "United Nations Scientific Committee on the Effects of Atomic Radiation". In: *UNSCEAR 2000 REPORT: SOURCES AND EFFECTS OF IONIZING RADIATION*. Vol. I, pp. 84–141. URL: https://www.unscear.org/unscear/en/publications/2000_1.html.

[150] D. S. Akerib et al. "LUX-ZEPLIN (LZ) Conceptual Design Report". In: (Sept. 2015). arXiv: 1509.02910 [physics.ins-det].

[151] P. S. Bhupal Dev, Anupam Mazumdar, and Saleh Qutub. "Constraining Non-thermal and Thermal properties of Dark Matter". In: *Front. in Phys.* 2 (2014), p. 26. DOI: 10.3389/fphy.2014.00026. arXiv: 1311.5297 [hep-ph].

[152] Kalliopi Petraki and Raymond R. Volkas. "Review of asymmetric dark matter". In: *Int. J. Mod. Phys. A* 28 (2013), p. 1330028. DOI: 10.1142/S0217751X13300287. arXiv: 1305.4939 [hep-ph].

[153] D.S. Akerib et al. "Technical Results from the Surface Run of the LUX Dark Matter Experiment". In: *Astropart.Phys.* 45 (2013), pp. 34–43. DOI: 10.1016/j.astropartphys.2013.02.001. arXiv: 1210.4569 [astro-ph.IM].

[154] D.S. Akerib et al. "Results on the Spin-Dependent Scattering of Weakly Interacting Massive Particles on Nucleons from the Run 3 Data of the LUX Experiment". In: *Phys. Rev. Lett.* 116.16 (2016), p. 161302. DOI: 10.1103/PhysRevLett.116.161302. arXiv: 1602.03489 [hep-ex].

[155] D.S. Akerib et al. "First Searches for Axions and Axionlike Particles with the LUX Experiment". In: *Phys. Rev. Lett.* 118.26 (2017), p. 261301. DOI: 10.1103/PhysRevLett.118.261301. arXiv: 1704.02297 [astro-ph.CO].

[156] E. Morikawa et al. "Argon, krypton, and xenon excimer luminescence: From the dilute gas to the condensed phase". In: *The Journal of Chemical Physics* 91.3 (1989), pp. 1469–1477. DOI: 10.1063/1.457108. eprint: https://doi.org/10.1063/1.457108. URL: https://doi.org/10.1063/1.457108.

[157] Peter K. Leichner et al. "Two- and three-body collision coefficients for Xe($^3P_1$) and Xe($^3P_2$) atoms and radiative lifetime of the $Xe_2(1_u)$ molecule". In: *Phys. Rev. A* 13 (5 May 1976), pp. 1787–1792. DOI: 10.1103/PhysRevA.13.1787. URL: https://link.aps.org/doi/10.1103/PhysRevA.13.1787.

[158] J. W. Keto, R. E. Gleason, and F. K. Soley. "Exciton lifetimes in electron beam excited condensed phases of argon and xenon". In: *The Journal of Chemical Physics* 71.6 (1979), pp. 2676–2681. DOI: 10.1063/1.438625. eprint: https://doi.org/10.1063/1.438625. URL: https://doi.org/10.1063/1.438625.

[159] P. Millet et al. "Time resolved study of the uv and near uv continuums of xenon". In: *The Journal of Chemical Physics* 69.1 (1978), pp. 92–97. DOI: 10.1063/1.436349. eprint: https://aip.scitation.org/doi/pdf/10.1063/1.436349. URL: https://aip.scitation.org/doi/abs/10.1063/1.436349.

[160] Walter Blum, Luigi Rolandi, and Werner Riegler. *Particle detection with drift chambers*. Particle Acceleration and Detection. Springer, Berlin, Heidelberg, 2008. ISBN: 978-3-540-76683-4, 978-3-540-76684-1. DOI: 10.1007/978-3-540-76684-1.

[161] F. Pedregosa et al. "Scikit-learn: Machine Learning in Python". In: *Journal of Machine Learning Research* 12.85 (2011), pp. 2825–2830. URL: http://jmlr.org/papers/v12/pedregosa11a.html.

[162] Ji Zhu et al. "Multi-class AdaBoost". In: *Statistics and its interface* 2 (Feb. 2006). DOI: 10.4310/SII.2009.v2.n3.a8.

[163] S. Yellin. "Finding an upper limit in the presence of unknown background". In: *Phys. Rev. D* 66 (2002), p. 032005. DOI: 10.1103/PhysRevD.66.032005. arXiv: physics/0203002.

[164] Matthew J. Dolan, Felix Kahlhoefer, and Christopher McCabe. "Directly Detecting Sub-GeV Dark Matter with Electrons from Nuclear Scattering". In: *Phys. Rev. Lett.* 121 (10 Sept. 2018), p. 101801. DOI: 10.1103/PhysRevLett.121.101801. URL: https://link.aps.org/doi/10.1103/PhysRevLett.121.101801.

[165] P. Agnes et al. "Low-Mass Dark Matter Search with the DarkSide-50 Experiment". In: *Phys. Rev. Lett.* 121.8 (2018), p. 081307. DOI: 10.1103/PhysRevLett.121.081307. arXiv: 1802.06994 [astro-ph.HE].

[166] R. Agnese et al. "Search for Low-Mass Dark Matter with CDMSlite Using a Profile Likelihood Fit". In: *Phys. Rev. D* 99.6 (2019), p. 062001. DOI: 10.1103/PhysRevD.99.062001. arXiv: 1808.09098 [astro-ph.CO].

[167] A.H. Abdelhameed et al. "First results from the CRESST-III low-mass dark matter program". In: *Phys. Rev. D* 100.10 (2019), p. 102002. DOI: 10.1103/PhysRevD.100.102002. arXiv: 1904.00498 [astro-ph.CO].

[168] E. Aprile et al. "Search for Light Dark Matter Interactions Enhanced by the Migdal Effect or Bremsstrahlung in XENON1T". In: *Phys. Rev. Lett.* 123.24 (2019), p. 241803. DOI: 10.1103/PhysRevLett.123.241803. arXiv: 1907.12771 [hep-ex].

[169] Christopher McCabe. "Astrophysical uncertainties of dark matter direct detection experiments". In: *Phys. Rev. D* 82 (2 July 2010), p. 023530. DOI: 10.1103/PhysRevD.82.023530. arXiv: 1005.0579 [hep-ph]. URL: https://link.aps.org/doi/10.1103/PhysRevD.82.023530.

[170] E. Aprile et al. "Search for WIMP Inelastic Scattering off Xenon Nuclei with XENON100". In: *Phys. Rev. D* 96.2 (2017), p. 022008. DOI: 10.1103/PhysRevD.96.022008. arXiv: 1705.05830 [hep-ex].

[171] P. Agnes et al. "First Results from the DarkSide-50 Dark Matter Experiment at Laboratori Nazionali del Gran Sasso". In: *Phys. Lett. B* 743 (2015), pp. 456–466. DOI: 10.1016/j.physletb.2015.03.012. arXiv: 1410.0653 [astro-ph.CO].